

Synthesis and Characterisation of Highly Active Nuclear Waste Simulants

Jessica Ann Shiels

Submitted in accordance with the requirements for the integrated degree of
Doctor of Philosophy and Master of Science

The University of Leeds

School of Chemical and Process Engineering

March 2019

Intellectual Property and Publication Declaration

I, the candidate, confirm that the work submitted is my own, except where work which has formed part of jointly authored publications has been included. Details of one second authored journal, two jointly first authored journals, and a conference proceeding publication are provided and the contributions of myself and the other authors to these works has been explicitly indicated below. Appropriate credit has been given within the thesis where reference has been made to the work of others.

Jointly authored journal publications and conference proceedings publications:

1. Paul N, Biggs S, Shiels J, Hammond R.B, Edmondson M, Maxwell L, Harbottle D, Hunter T.N. 2017. Influence of shape and surface charge on the sedimentation of spheroidal, cubic and rectangular cuboid particles. *Power Technology*, 322, 75-83. 2017.
2. Shiels J, Harbottle D, Hunter T.N. 2018. Synthesis and Characterisation of Caesium Phosphomolybdate and Zirconium Molybdate found in the Highly Active Storage Tanks at Sellafield. Waste Management Conference, Phoenix, US, 2018.
3. Shiels J, Harbottle D, Hunter T.N. 2018. Synthesis and Physical Property Characterisation of Spheroidal and Cuboidal Nuclear Waste Simulant Dispersions. *Journal of Material Science*, 11, 1235-1245.
4. Shiels J, Harbottle D, Hunter T.N. 2019. Permeability and Compressive Yield Stress Measurements of Spheroidal and Cuboidal Nuclear Waste Simulants. Article in preparation. 2019

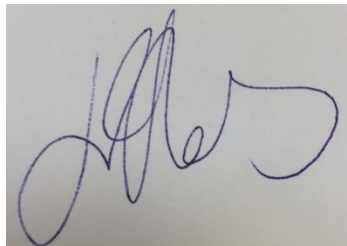
Within this thesis, Chapter 1 and 2 contain some relevant introduction based material from paper 2, 3 and 4. Chapter 3 contains kinetics, X-Ray Diffraction, Infrared Spectroscopy and Thermogravimetric Analysis data also presented in paper 3. Zeta potential and pH equilibrium measurements made for this research are published in paper 1 and 3, both of which are discussed in Chapter 4. Particle size data and some sedimentation behaviour presented in Chapter 4 is also published in paper 3. Chapter 5 forms the basis of paper 4 which is intended to be submitted before examination, with some compressive yield stress data that has been presented in paper 2.

The contribution of co-authors to publications 2,3 and 4 has been advisory, consistent with their role as academic supervisors of this PhD. Publication 1,

was primarily written by other authors, where both zeta potential and pH equilibrium data were collected for this thesis. I, the candidate, confirm that the experimental data acquisition, analysis and written work within this thesis has been my own and that any contributions from colleagues are explicitly referenced in the text.

This copy has been supplied on the understanding that it is copyright material and that no quotation from the thesis may be published without proper acknowledgement. The right of Jessica Ann Shiels to be identified as Author of this work has been asserted by her in accordance with the Copyright, Designs and Patents Act 1988.

Signed

A handwritten signature in blue ink, appearing to be 'J. Shiels', is centered on the page. The signature is fluid and cursive, with a large initial 'J' and a long, sweeping tail.

Jessica Shiels

2019

Acknowledgements

My first acknowledgement must go to Tim Hunter, had it not been for you I categorically would not of reached this point. You consistently made me feel this was achievable and supported me throughout. Dave Harbottle, thank you for your valuable input. To all the technicians, you literally make the department a pleasure to work in. Ben Douglas, thank you for all your help in the particles lab. Chris Bulman – you truly are the best lab tech and made lab work enjoyable!

To my colleagues at the University of Leeds, too numerous to mention, thank you. You ensured a daily smile on my face, provided appropriate distractions and made sure I never comfort ate alone. My office companions from B.12, 4.15 and G.29 – I will miss you all, to varying degrees... A few special mentions; Helen Freeman, for our lunchtime runs and life chats, Mike Johnson, our afternoon walks, James Goode, your rants about life, Alastair Baker, your positive influence on the atmosphere, Mo Jeraal, for just being you, Danny Theobald, your consistent annoyance (and big heart), Laura Elliott, for our adventures, Little Al, you babe. Finally, how could I forget the nuclear group for their regular motivation and to which without I wouldn't of learnt about bubbly flow.

A very special mention to my homies Charlotte Parrington and Toby Lord, I honestly don't believe I could of done this without you. From day one we clicked, forming an indestructible trio, dragging each other through the tough times and riding the good ones. It was probably that one run that got us through..

To my fellow Community First Responders, Samaritans and Mental Health Transport Assistants, thank you for helping me find my passion, drive and purpose. To those service users that I've interacted with during my time, you helped me in ways I can never repay. A special mention to Amy Woogler for being a truly amazing friend, Paul Jones (and Joe) for keeping me regularly fed and entertained and Ben McDougall for the new experiences you introduced me too – you guys rock.

Then there is my Cherub, Katie Chew, we have countless memories to look back on and more to make but thank you for your support (via prosecco) whilst we lived together. Of course I couldn't forget the Aireview massive group, Kate Quarmby, Jenny Quarmby and Hayley Nicholas over 20 years and still going strong, thank you for keeping me humble.

My Loughborough friends, where I started out on this academic journey; Kriti Singh, Dan Sedgwick, Toni Quius and Tom Cousins – The Best of People Love to Eat.

To my home slices Chelsea Mitchell (plus bump) and Rosh Patel, thanks for being your wild and wacky selves. I couldn't be prouder to call you my friends.

My godson Jax Walton, maybe one day you'll understand what I've written.

Tom Griffiths, possibly the strangest way I've made a friend but I'm so glad we connected. Zoe Andersen-Lawrence, thanks for being you and staying awesome! Alice Gornall, thanks for our various adventures over the years, including working at NNL!

To those I met at conferences, through the Brilliant club and at NNL, thank you for keeping my love for science alive when I thought it had gone.

Cathy Shiels and Anthony White (mum and dad), you supported me unwaveringly, allowing me to rant even when you had no idea what I was on about and how could I forget the financing when I started to struggle. To my family, you've always believed in me and pretended to understand when needed.

Finally to my friends not mentioned and partners, both old and new that put up tirelessly with my fluctuating moods, for those that helped me find the motivation to continue when I didn't feel I had any energy left and for those that continuously believed in me.

I DID IT!

Abstract

Caesium phosphomolybdate (CPM) and zirconium molybdate (ZM) are two known problematic fission products that precipitate out within the Highly Active Storage Tanks (HASTs) at Sellafield, UK. Currently these HASTs do not have an in situ monitoring system where the behaviour of these products can be directly observed. Therefore, non-radioactive simulants of CPM and ZM have been successfully synthesised and further characterised to aid behavioural understanding, specifically within a suspension, in the hope of assisting with the planning of future waste management strategy.

These fission products are potentially contributing to both mobility problems and 'hot-spots' with the HASTs, as a result of their suspension behaviours within the tanks, causing difficulty in re-suspension for onward processing and feasibly blocking pipes. Consequently, an understanding of their dispersion stability and behaviour is of crucial importance in limiting the potential for unexpected issues during Post Operational Clean Out (POCO).

Non-radioactive simulants of spheroidal CPM and two differing morphologies of zirconium molybdate, cuboidal (ZM-1) and wheatsheaf (ZMCA-1) were successfully synthesised; confirmed via Scanning Electron Microscopy (SEM), Powder X-ray Diffraction (PXRD) and Fourier Transform Infrared (FTIR) spectroscopy. The kinetics of the CPM synthesis was reported for the first time, where it was found to be a first order reaction in respect to phosphomolybdic acid. In addition, two supplied ZM simulants (ZM-2 and ZMCA-2) with an elongated bipyramid and wheatsheaf morphology, respectively were also analysed.

For the onward processing and immobilisation of these waste dispersions, centrifugal analysis was utilised to understand their suspension behaviours; sedimentation, compressive yield stress and permeability in both aqueous and 2 M nitric acid environments (mimicking current storage conditions). The application of the LUMiSizer® for sedimentation, compressive yield stress and permeability experiments and the methodology applied for investigating the permeability of the simulants is, as far as the author is aware, reported for the first time in this research. Furthermore, mixed dispersions of CPM and ZMCA-

2 were also investigated in depth for the first time where it was proposed that they have strong particle-particle interactions influencing their dispersion behaviour.

Overall, in comparing individual simulants CPM is reported to be the most challenging to re-suspend and keep in solution as a result of its high instability in both water and nitric acid. The suspension behaviour for different ZM simulants provided different results, highlighting the significant impact of ZM's morphology, where it is suggested a range will be present within the HASTs. When considering the mixed system of CPM:ZMCA-2 within both Milli-Q water and 2 M nitric acid regardless of the weight ratio of the simulants, an open difficult to compress bed network is formed, suggesting strong particle-particle interactions and high aggregation.

The key message from this research is that the systems are complex, unstable and likely to aggregate whether individually or mixed within the acidic conditions of the HASTs.

Table of Contents

Intellectual Property and Publication Declaration	ii
Acknowledgements	iv
Abstract	vi
Table of Contents	viii
List of Tables	xi
List of Figures	xii
List of Abbreviations	xix
Chapter 1 Introduction	1
1.1 Research Scope and Aims	2
1.1.1 Industrial Background and Applications	2
1.2 Specific Research Objectives	6
1.3 Thesis Delivery	8
Chapter 2 Literature Review	10
2.1 Nuclear Fuel Cycle	11
2.1.1 Nuclear Fuel Reprocessing	12
2.1.2 Highly Active Liquor Evaporation and Storage Plant	13
2.1.2.1 Highly Active Storage Tanks	14
2.1.2.2 Highly Active Liquor.....	19
2.1.3 Vitrification	21
2.2 Caesium Phosphomolybdate and Zirconium Molybdate.....	22
2.2.1 Caesium Phosphomolybdate.....	23
2.2.2 Zirconium Molybdate	26
2.2.3 Combined	30
2.3 Fundamental Aspects of Colloidal Synthesis, Stability and Dewatering.....	33
2.3.1 Particle Stability.....	34
2.3.2 Sedimentation	40
2.3.3 Compressive Yield Stress	47
2.3.4 Permeability	51
2.4 Conclusions	55
Chapter 3 Synthesis, Kinetics and Property Characterisation of Caesium Phosphomolybdate and Zirconium molybdate	57
3.1 Introduction	58
3.2 Materials and Methodology.....	60
3.2.1 Materials.....	60

3.2.2 Simulant Synthesis	61
3.2.2.1 Caesium Phosphomolybdate	62
Reaction Kinetics Experiments	64
3.2.2.2 Zirconium Molybdate	65
3.2.3 Characterisation Techniques and Methodologies	67
3.2.3.1 Scanning Electron Microscopy	67
3.2.3.2 Particle Density	68
3.2.3.3 Ultraviolet Spectroscopy	69
3.2.3.4 Powder X-ray Diffraction	71
3.2.3.5 Infrared Spectroscopy	73
3.2.3.6 Thermogravimetric Analysis	74
3.3 Results and Discussion	75
3.3.1 Synthesis, Morphology and Reaction Kinetics	75
3.3.2 Physical and Chemical Characterisation	85
3.4 Conclusions	93
Chapter 4 Dispersion Stability and Sedimentation Behaviour of Caesium Phosphomolybdate and Zirconium Molybdate – Influence of Charge, Shape, Size and Temperature.....	94
4.1 Introduction	95
4.2 Materials and Methodology	96
4.2.1 Materials	96
4.2.2 Characterisation Techniques and Methodologies	97
4.2.2.1 Particle Size Laser Diffraction Analysis	97
4.2.2.2 Zeta Potential Measurements	98
4.2.2.3 pH Investigations	100
4.2.2.4 Solubility Studies	100
4.2.2.5 Centrifugal Settling	100
4.3 Results and Discussion	104
4.3.1 Particle Size Distribution	104
4.3.2 Stability	109
4.3.3 Sedimentation	115
4.3.3.1 Procedure for Sedimentation Analysis	115
4.3.3.2 Stokes Estimation	118
4.3.3.3 Vesilind and Richardson-Zaki Plots.	122
4.3.3.4 Mixed System Settling Behaviour	129
4.3.3.5 Temperature Influence on Settling Behaviour	132

4.4 Conclusions	134
Chapter 5 Compressive Yield Stress and Permeability Investigations.....	136
5.1 Introduction	137
5.2 Materials and Methodology.....	138
5.2.1 Materials.....	138
5.2.2 Compressive Yield Stress	139
5.2.3 Permeability Studies	142
5.2.3.1 Resistance of the Membrane	144
5.2.3.2 Cake Permeability	147
5.2.3.3 Pressure Determination	150
5.3 Results and Discussion.....	152
5.3.1 Compressive Yield Stress	152
5.3.1.1 Analytical Procedure for Determining of Compressive Yield Stress	152
5.3.1.2 Compressive Yield Stress Results	155
5.3.2 Permeability	163
5.3.2.1 Analytical Procedure for Determining the Resistance of the Membrane	163
5.3.2.2 Analytical Procedure for Determining the Cake Resistance and Pressure	166
5.3.2.3 Cake Resistance Results	171
5.3 Conclusions	177
Chapter 6 Conclusions and Recommended Future Work	179
6.1 Recommended Future Work.....	183
References.....	186
Research Bibliography	200
Scientific Journal and Conference Paper Contributions	200
Oral and Poster Presentations Associated with this Thesis.....	200
Scholarships and Grants Associated with this Thesis	201
Appendix	202

List of Tables

Table 1 Zeta potential values in relation to the stability of a colloidal system	38
Table 2 Detailing the simulants investigated during this research including, their origin, morphology and what they will be referred to throughout this thesis.	60
Table 3 Stating the precursors used in the synthesis of caesium phosphomolybdate (CPM), zirconium molybdate (ZM-1) and zirconium citramolybdate (ZMCA-1), including their formula, purity and supplier.	61
Table 4 Reporting the density values for caesium phosphomolybdate (CPM), zirconium molybdate (ZM-1 and ZM-2) and zirconium citramolybdate (ZMCA-1 and ZMCA-2).....	85
Table 5 Summary of sedimentation experiments undertaken for this research, all in both Milli-Q water and 2 M nitric acid.....	103
Table 6 Weight % for caesium phosphomolybdate (CPM):zirconium citramolybdate (ZMCA-2) mixed dispersions	104
Table 7 Detailing the D10, D50 and D90 values for caesium phosphomolybdate (CPM) synthesised at 50 °C and 100 °C, titanium dioxide (TiO₂), zirconium molybdate (ZM-1 and ZM-2) and zirconium citramolybdate (ZMCA-1 and ZMCA-2). In addition to the polydispersity index for CPM synthesised at 50 °C and 100 °C.	106
Table 8 Presenting the equilibrium pH values for caesium phosphomolybdate (CPM) and zirconium molybdate (ZM-1 and ZM-2) and zirconium citramolybdate (ZMCA-1 and ZMCA-2). at 5 vol%.	112
Table 9 Symbols and their corresponding meanings from Equations (40) and (41), which are used to determine equilibrium compressive yield stress and equilibrium volume fraction of particle dispersion of a given sample.	141
Table 10 Summary of the symbols mentioned in Equations (42)-(46), their meaning and how they were determined for calculating the resistance of the membrane.	146
Table 11 Summary of the symbols mentioned in Equations (47)-(54), their meaning and how they were determined for calculating cake resistance.	150
Table 12 Summary of the symbols mentioned in Equations (55)-(57), their meaning and how they were determined for calculating pressure.....	151

List of Figures

Figure 1-1 Visual representation of the breakdown of Spent Nuclear Fuel (SNF).	4
Figure 1-2 A schematic illustration of how the Chapters of this thesis are presented.....	9
Figure 2-1 Basic schematic of the UK nuclear fuel cycle	11
Figure 2-2 Simplified flow diagram of the Highly Active Liquor Evaporation and Storage (HALES) plant, Sellafield, UK (Dobson and Phillips, 2006).	14
Figure 2-3 A 'new-side' Highly Active Storage Tank (HAST) positioned vertically, before it was commissioned with its cooling coils and agitation systems visible (Dobson and Phillips, 2006).....	15
Figure 2-4 Layout of jet ballasts and air-lifts in a 'new-side' Highly Active Storage Tank (HAST) (McArthur et al., 2005).	16
Figure 2-5 Schematic of proposed 'old-side' Highly Active Storage Tank (HAST) wash sequence (Edmondson et al., 2012).	17
Figure 2-6 Schematic and photo of 4:10th size inactive Highly Active Storage Tank (HAST) at the National Nuclear Laboratory (NNL), Workington, UK (Griffon, 2010-2011)	18
Figure 2-7 Scanning Electron Micrographs (SEM) of barium nitrate, strontium nitrate and barium nitrate & 4 mole% strontium (left to right) (Dunnett, 2015).	20
Figure 2-8 Schematic representation of CPM showing the Keggin cage, 12MoO_3 with a tetrahedral phosphate (PO_4^{3-}) group at the centre. Molybdenum being purple, oxygen red and phosphorus orange (Macheder, 2011).....	25
Figure 2-9 Depiction of the proposed three step mechanism of the formation of caesium phosphomolybdate, proposed by Paul (Paul, 2014).	26
Figure 2-10 Solubility curves for zirconium molybdate (ZM) at 3 M and 5 M concentrations of nitric acid (Zhang et al., 2013).	28
Figure 2-11 Representation of an CPM (caesium phosphomolybdate) -ZM (zirconium molybdate) conversion concentration-time profile (Bradley et al., 2004).....	29
Figure 2-12 Schematic of the second method Paul et al. (2015) attempted for the synthesis of zirconium citramolybdate (ZMCA) (Paul et al., 2015).	30
Figure 2-13 Sedimentation rate vs. volume fraction for caesium phosphomolybdate (CPM), zirconium molybdate (ZM) and titanium dioxide (TiO_2) (Paul et al., 2013).....	31

Figure 2-14 Yield stress vs. solid volume for samples of caesium phosphomolybdate (CPM), zirconium molybdate (ZM) and the mixed system (Dunnett et al., 2016).	32
Figure 2-15 Illustration of permanent, induced and instantaneous dipoles	36
Figure 2-16 Illustration of the interfacial double layer	37
Figure 2-17 General zeta potential verse pH curve (Silver-Colloids.com, 2012).....	39
Figure 2-18 Schematic of both stable and unstable dispersions with the grey circles representing individual particles	39
Figure 2-19 Zeta potential curve for zirconium molybdate (ZM) and titanium dioxide (TiO ₂) (Paul, 2014)	40
Figure 2-20 Forces acting on a spherical particle settling in a fluid	42
Figure 2-21 Illustration of the various potential settling regimes within a system dependent upon particle interactions with black spheres representing particles. Complete with settling velocity vs. time curve.	44
Figure 2-22 The effect of cylinder weight on the tilt angle (Liu and Joseph, 1993).....	47
Figure 2-23 An illustration of what is expected when a centrifugal force is applied and then increased on a settled sample for both stable and aggregated particles.....	49
Figure 2-24 Illustration of kaolin clay platelets compressing parallel to one another (Horpibulsuk et al., 2011).	50
Figure 2-25 Effects of interparticle pair potential on the compressive yield stress of flocculated alumina suspensions (Channell et al., 2000).....	51
Figure 2-26 Cake specific resistance vs pressure for a range of particle shapes with varying sizes including: spheres, cubes, platelets and needles (Bourcier et al., 2016).....	52
Figure 3-1 Schematic of the 500 ml jacketed reaction vessel, with overhead stirrer, precursor inlet, condenser, product outlet and heating oil set-up.....	62
Figure 3-2 Photo of dry solid caesium phosphomolybdate (CPM).	63
Figure 3-3 Schematic of the kinetics experiment procedure for the tracking of phosphomolybdic acid concentration in the synthesis of caesium phosphomolybdate (CPM).	65
Figure 3-4 Photo of dry solid zirconium molybdate (ZM-1).	66
Figure 3-5 Summary of the various synthesis routes of Highly Active Liquor (HAL) simulants conducted for this research.	67
Figure 3-6 Schematic of the inner workings of an Scanning Electron Microscope (SEM).	68

Figure 3-7 Schematic of the principle inner workings of an AccuPyc TM 1330 Pycnometer.....	69
Figure 3-8 Schematic of the principles of an Ultraviolet-Visible (UV-Vis) spectrophotometer.....	70
Figure 3-9 Calibration curve of the ultraviolet-visible (UV-Vis) absorbance values of phosphomolybdic acid at various concentrations, taken at wavelength 458 nm. Complete with line of best fit equation, error bars and an R ² value of 0.98.....	71
Figure 3-10 Schematic of the workings of an x-ray diffraction (XRD) analyser.	72
Figure 3-11 Schematic of the principles of Fourier Transform Infrared spectroscopy (FTIR).	74
Figure 3-12 Schematic of a thermogravimetric analysis (TGA) set-up.....	75
Figure 3-13 Scanning electron micrograph (SEM) images of caesium phosphomolybdate particles (CPM), complete with scale bars for comparison. The images were taken at different magnifications; a) 2k, b) 10k, c) 35k, d) 65k.....	76
Figure 3-14 Scanning electron micrograph (SEM) of caesium phosphomolybdate (CPM) synthesised at 25 °C, completed with relevant scale bar. The magnification being 25k.....	77
Figure 3-15 Rate of reaction graph showing first-order kinetics for the co-precipitation reaction of caesium nitrate and phosphomolybdic acid forming caesium phosphomolybdate (CPM) at 25 °C and 50 °C with corresponding reaction equation.	78
Figure 3-16 Scanning electron micrograph of: (a) and b)) zirconium molybdate (ZM-1); and (c) and d)) zirconium citramolybdate (ZMCA-1). The images magnifications being; a) 1.79k, b) 7k, c) 1.79k d) 7k.....	80
Figure 3-17 Scanning electron micrographs taken at various times during the tracking of zirconium molybdate (ZM-1) synthesis from a caesium phosphomolybdate (CPM) precursor over 10 days. The images magnifications being; Day 4) 12k, Day 6) 12k, Day 8) 12k, Day 10) 7k.	82
Figure 3-18 Scanning electron micrograph of: a) zirconium molybdate (ZM-2); and b) zirconium citramolybdate (ZMCA-2). The images magnifications being; 1a) 25k, 1b) 10k, 2a) 3.5k, 2b) 2.5k.....	83
Figure 3-19 X-ray Diffraction patterns for caesium phosphomolybdate (CPM), zirconium molybdate (ZM-1 and ZM-2) and zirconium citramolybdate (ZMCA-1 and ZMCA-2).....	87
Figure 3-20 Infrared (IR) spectra of caesium phosphomolybdate (CPM), zirconium molybdate (ZM-1 and ZM-2) and zirconium citramolybdate (ZMCA-1 and ZMCA-2).	89

Figure 3-21 Thermogravimetric analysis curves of caesium phosphomolybdate (CPM), zirconium molybdate (ZM-1 and ZM-2) and zirconium citramolybdate (ZMCA-1 and ZMCA-2). CPM shows a loss of 13 moles of water, ZM-1 a loss of 3, ZMCA-1 a loss of 5, ZM-2 a loss of 3 and ZMCA-2 a loss of 4.....	92
Figure 4-1 Schematic of the Mie Theory underlying principle.....	98
Figure 4-2 An illustration of a LUMiSizer® cell with light being transmitted through a settling sample with varying degrees of light being picked up by the sensor.	102
Figure 4-3 Scanning Electron Micrographs of titanium dioxide TiO ₂ and caesium phosphomolybdate (CPM) synthesised at 100 °C. The images magnifications being; a) 25k, b) 22k.	104
Figure 4-4 Particle size distributions of caesium phosphomolybdate (CPM) synthesised at 50 °C and 100 °C, titanium dioxide (TiO ₂), zirconium molybdate (ZM-1 and ZM-2) and zirconium citramolybdate (ZMCA-1 and ZMCA-2).....	105
Figure 4-5 Scanning electron micrograph of zirconium citramolybdate (ZMCA-2). The images magnifications being; 1b) 10k, 2b) 2.5k.	108
Figure 4-6 Scanning electron micrograph of: (c) and d)) zirconium citramolybdate (ZMCA-1). The images magnifications being; c) 1.79k d) 7k.....	109
Figure 4-7 Zeta potential curves for caesium phosphomolybdate (CPM), titanium dioxide (TiO ₂) and zirconium molybdate (ZM-1 and ZM-2) and zirconium citramolybdate (ZMCA-1 and ZMCA-2) measured in concentrations of 1000 ppm in 10 ⁻⁴ M in potassium nitrate solution.	110
Figure 4-8 Equilibrium pH (after 48 h) for caesium phosphomolybdate (CPM) and zirconium molybdate (ZM-1) and zirconium citramolybdate (ZMCA-1).	112
Figure 4-9 Solubility vs temperature graph for caesium phosphomolybdate (CPM), zirconium molybdate (ZM-1) and zirconium citramolybdate (ZMCA-1), in both 2 M nitric acid and Milli-Q water.	114
Figure 4-10 Schematic of the procedure used to analyse sedimentation data from raw Lumisizer transmission profiles to a bed height vs time plot where the zoomed in part of the plot shows the initial settling rate.	116
Figure 4-11 Vesilind plot of the natural log of the settling rate ($\ln \mu$) vs. volume fraction (ϕ) plot for caesium phosphomolybdate (CPM) in Milli-Q water. Complete with R ² value.	117
Figure 4-12 Richardson-Zaki plot for caesium phosphomolybdate (CPM) in Milli-Q water. Complete with linear relationship equation and R ² value.	118

Figure 4-13 Estimated Stokes' settling rates for caesium phosphomolybdate (CPM), titanium dioxide (TiO₂), zirconium molybdate (ZM-2) and zirconium citramolybdate (ZMCA-2) in both Milli-Q water (black) and 2 M nitric acid (red). 119

Figure 4-14 Experimentally determined settling rates for caesium phosphomolybdate (CPM), titanium dioxide (TiO₂), zirconium molybdate (ZM-2) and zirconium citramolybdate (ZMCA-2), all at 4 vol% in both Milli-Q water (black) and 2 M nitric acid (red). 120

Figure 4-15 Vesilind plot of the natural log of the settling rate ($\ln \mu$) vs. volume fraction (ϕ) for caesium phosphomolybdate (CPM), titanium dioxide (TiO₂), zirconium molybdate (ZM-2) and zirconium citramolybdate (ZMCA-2) in both Milli-Q water (black) and 2 M nitric acid (red). Complete with R² values. 123

Figure 4-16 Free settling velocities predicted from the Vesilind model for caesium phosphomolybdate (CPM), titanium dioxide (TiO₂), zirconium molybdate (ZM-2) and zirconium citramolybdate (ZMCA-2), in both Milli-Q water (black) and 2 M nitric acid (red). 124

Figure 4-17 Richardson-Zaki plots for caesium phosphomolybdate (CPM), titanium dioxide (TiO₂) zirconium molybdate (ZM-2) and zirconium citramolybdate (ZMCA-2) in both Milli-Q water (black) and 2 M nitric acid (red). Complete with linear relationship equations and R² values. 126

Figure 4-18 Experimentally determined settling rates for individual and mixed systems of caesium phosphomolybdate (CPM) and zirconium citramolybdate (ZMCA-2) at 1:3, 1:1 and 3:1 weight ratios at 4 vol% in Milli-Q water (black) and 2 M nitric acid (red). 129

Figure 4-19 Illustration of the potential interaction between spherical caesium phosphomolybdate (CPM, yellow circles) particles and wheatsheaf zirconium citramolybdate (ZMCA-2 grey 'bow ties'), with black arrow depicting the settling direction and red arrows depicting potential repulsions. 131

Figure 4-20 Experimentally determined settling rates for caesium phosphomolybdate (CPM)at both 25°C and 50°C with concentration of 4 vol% in Milli-Q water (black) and 2 M nitric acid (red). 133

Figure 5-1 Scanning Electron Micrograph (SEM) of kaolin, completed with scale bar. The magnification was 12k. 139

Figure 5-2 Illustration of a LUMiSizer® cell, labelled with the simulant dispersion (with various regions), the radial distance from centrifuge centre to bottom of bed, L , and the initial and equilibrium sediment height, H_0 , and H_{eq} , respectfully. 142

Figure 5-3 Unmodified to modified Microcon® Centrifugal Filters. 143

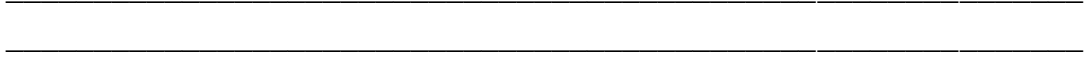
Figure 5-4 A illustration of the modified LUMiSizer® PA disposable cells complete with modified Microcon® Centrifugal Filters and simulant dispersion.....	144
Figure 5-5 Illustration of the permeability experimental steps.	148
Figure 5-6 Raw compressive yield stress profile for caesium phosphomolybdate (CPM) in Milli-Q water at 10 vol%. Plot is produced by the LUMiSizer® which utilises Space and Time resolved Extinction Profiles – Technology. The red profile being the first profile, progressing to the green, which is the last.	152
Figure 5-7 Sedimentation bed height vs. time plot for caesium phosphomolybdate (CPM) in Milli-Q water at 10 vol%. Change in shading represents the change in phases from settling to compression. Vertical dash lines correspond to an increase in centrifugal force, which is donated at the top of the plot. Both the initial and equilibrium heights (H_0 and H_{eq} , respectfully) are noted.	153
Figure 5-8 Plot of the equilibrium compressive yield stress vs. the equilibrium volume fraction of particle dispersion for caesium phosphomolybdate (CPM) in Milli-Q water at 10 vol%.	154
Figure 5-9 Sedimentation bed height vs. time plots for 25 vol% kaolin in water, 10 vol% caesium phosphomolybdate (CPM) in both Milli-Q water and 2 M nitric acid, and 16 vol% zirconium molybdate (ZM-2) and zirconium citramolybdate (ZMCA-2) in both Milli-Q water (black) and 2 M nitric acid (red). Vertical black dash lines correspond to an increase in centrifugal force.	155
Figure 5-10 Plots of equilibrium compressive yield stress vs. the equilibrium volume fraction of particle dispersion for; 25 vol% kaolin in water, 10 vol% caesium phosphomolybdate (CPM), 16 vol% zirconium molybdate (ZM-2) and zirconium citramolybdate (ZMCA-2) in both Milli-Q water (black) and 2 M nitric acid (red). Complete with lines of best fits, their equation and R^2 values.	157
Figure 5-11 Plots of equilibrium compressive yield stress vs. the equilibrium volume fraction of particle dispersion for individual and mixed systems of caesium phosphomolybdate (CPM) and zirconium citramolybdate (ZMCA-2) at 1:3, 1:1 and 3:1 weight ratios at 16 vol% in Milli-Q water (left, black) and 2 M nitric acid (right, red).	161
Figure 5-12 The radial position of the meniscus in the centrifuge tube vs. time, for an experiment determining the resistance of the Biodyne A membrane with Milli-Q water.	163
Figure 5-13 The height of the filtrate vs. time, for an experiment determining the resistance of the Biodyne A membrane with Milli-Q water.	164

Figure 5-14 The liquid height above the membrane vs. time, for an experiment determining the resistance of the Biodyne A membrane with Milli-Q water.....	164
Figure 5-15 Dimensionless value Y vs. time, for an experiment determining the resistance of the Biodyne A membrane with Milli-Q water. Shown with red line representing the gradient and constant, k_1	165
Figure 5-16 Plots showing the radial position of the meniscus in the centrifuge tube vs. time, the height of the filtrate vs. time and the liquid height above the membrane vs. time, for caesium phosphomolybdate (CPM) in Milli-Q water, respectfully.....	167
Figure 5-17 Dimensionless value y vs. time, for an experiment determining the cake resistance of caesium phosphomolybdate (CPM) in Milli-Q water. Shown with red line representing the gradient equivalent to constant, k_2	168
Figure 5-18 Specific cake resistance vs. rpm for caesium phosphomolybdate (CPM) in Milli-Q water.	169
Figure 5-19 Starting and ending pressures for the caesium phosphomolybdate (CPM) in Milli-Q water experiment at 1000, 2000, 3000 and 4000 rpm. With green arrow showing the median values which were used for calculations.....	170
Figure 5-20 Specific cake resistance vs. pressure for caesium phosphomolybdate (CPM) in Milli-Q water. Completed with corresponding rpm values.	171
Figure 5-21 Plots of specific cake resistances vs. pressure for; kaolin in water, caesium phosphomolybdate (CPM) in both Milli-Q water and 2 M nitric acid, zirconium molybdate (ZM-2) and zirconium citramolybdate (ZMCA-2) in both Milli-Q water (black) and 2 M nitric acid (red).....	172
Figure 5-22 Combined plot of specific cake resistance vs. pressure for mixed systems of caesium phosphomolybdate (CPM) and zirconium citramolybdate (ZMCA-2) at 1:3, 1:1 and 3:1 weight ratios at 16 vol% in both Milli-Q water (black) and 2 M nitric acid (red).....	176

List of Abbreviations

Abbreviation	Meaning
ABS	Acoustic Backscatter
AFM	Atomic Force Microscopy
AGR	Advanced Gas-Cooled Reactors
AAS	Atomic Absorption Spectroscopy
CPM	Caesium Phosphomolybdate
DLVO	Derjaguin, Landau, Verwey, and Overbeek
FTIR	Fourier Transform Infrared
HAL	Highly Active Liquor
HALES	Highly Active Liquor Evaporation and Storage Plant
HAST	Highly Active Storage Tank
HLW	High Level Waste
IR	Infrared
ICDD	International Centre for Diffraction Data
IEP	Isoelectric Point
LWR	Light Water Reactors
LED	Light-Emitting Diode
NNL	National Nuclear Laboratory
NDA	Nuclear Decommissioning Authority
PALS	Phase Analysis Light Scattering
PA	Polyamide
PDI	Polydispersity Index
PC	Polycarbonate
POCO	Post Operational Clean Out
POM	Polyoxometalate
RCA	relative centrifugal acceleration
SEM	Scanning Electron Microscope
STEP	Space and Time resolved Extinction Profiles
SNF	Spent Nuclear Fuel
THORP	Thermal Oxide Reprocessing Plant
TGA	Thermogravimetric Analysis
TEM	Transmission Electron Microscopy
UV-Vis	Ultraviolet-Visible
WVP	Waste Vitrification Plant
XRD	X-ray Diffraction
ZMCA-2	Zirconium Citramolybdate (provided by NNL)
ZMCA-1	Zirconium Citramolybdate (synthesised in this research)
ZM	Zirconium Molybdate
ZM-2	Zirconium Molybdate (provided by NNL)
ZM-1	Zirconium Molybdate (synthesised in this research)

Chapter 1 Introduction



This Chapter intends to cover the motivations behind this PhD thesis, including the scope of the research, specific objectives and how this thesis is structured.

1.1 Research Scope and Aims

This research aims to provide a better understanding of the behaviour of two specific problematic fission products precipitating out within Highly Active Storage Tanks (HASTs) at Sellafield. Currently, there is not enough behavioural understanding of the precipitation products; caesium phosphomolybdate (CPM) and zirconium molybdate (ZM) for effective Post Operational Clean-Out (POCO) strategic planning of the HASTs.

The HASTs do not have an *in situ* monitoring system, consequently the behaviour of the Highly Active Liquor (HAL) temporarily stored within them, containing both CPM and ZM compounds cannot be directly monitored. Therefore, non-radioactive simulants are required to aid behavioural understanding to assist with the planning of future waste management programs. In a broad summary, the research scope of this project was to characterise the nuclear waste simulants CPM and ZM to assist with this planning of future waste management programmes. In order for this to occur the simulants first needed to be synthesised, which therefore became an initial objective. It was then intended for multiple techniques to be utilised in both physical and chemical characterisation, particularly, when considering further understanding their stability, settling, compressive yield stress and permeability behaviours in different environments. Mixed systems of CPM and ZM are also of particular interest as very little research has been currently done in understanding them. Additionally, an understanding of the differences in characteristics of various morphologies of ZM, would be advantageous in preparing for worst case behaviour scenarios. Finally, a better understanding of the formation of both CPM and ZM could provide more extensive information on their potential ratios within the HASTs.

1.1.1 Industrial Background and Applications

The UK nuclear industry has made significant positive progress in the past decade, especially in regards to its political favourability and improving its

public perception. A factor for this is the current energy crisis, whereby the UK is challenged to provide secure and sufficient energy to meet increasing demands and do so from a clean reliable source, in order to combat climate change (Secretary of State for Trade and Industry, 2006, World Nuclear Association, 2018a). Previous energy demands have been satisfied predominately by fossil fuels in combination with nuclear power and renewable energy sources. However, the production of oil by the UK in the North Sea has been steadily declining since 1999 forcing the UK to either import fossil fuels or fund an alternative source of energy (Mearns, 2013). Nuclear power currently provides the UK with approximately 21% of its electricity from 15 reactors, yet nearly half of this capacity will be retired by 2025 (World Nuclear Association, 2018a). The UK has set targets to reduce carbon dioxide emissions by 80% using 1990 as a baseline. In order to achieve this target low-carbon dioxide emitting energy sources must become the dominant source of electricity, not fossil fuels (UK Government, 2008). The Committee on Climate Change consider that to achieve this reduction in carbon dioxide emissions the energy for the UK must come from the mix of following sources; 40% nuclear, 40% renewable, 15% carbon capture and storage, and 5% unabated gas-fired generation (Committee on Climate Change, 2012). As a result, the UK Government is now in full support of a UK new-build nuclear programme, with new reactors financed by the private sector (Secretary of State for Trade and Industry, 2006).

Despite the nuclear industry making positive progress, there is still a significant amount of legacy waste that needs to be addressed, in which we have a moral obligation to not leave for future generations. The industry originally began in Cumbria after the Second World War when the Windscale site in 1947 was established as part of the nuclear deterrent to produce weapon grade material (Biggs et al., 2009). Consequently, during the rapid progression of the nuclear civil energy industry, decommissioning and waste management were not comprehensively accounted for. A combination of bad practice, lack of planning and perhaps naivety in this has led to a mass of legacy waste and subsequently significant concerns still require addressing (Mort et al., 2013).

Reprocessing of Spent Nuclear Fuel (SNF) in the UK started in 1952 at the Windscale site when the First Chemical Separation Plant was commissioned to separate plutonium. This was a relatively small scale operation that progressively expanded until 1994 with the opening of the Sellafield Thermal Oxide Reprocessing Plant (THORP), which reprocesses spent oxide fuel for the UK and for several other countries, including Italy and Spain. At THORP, SNF is processed to allow 97% to be reused consisting of; 238-uranium, 235-uranium and 239-plutonium. However, a stream of concentrated highly active fission products (HAL) is also formed as waste from this process accounting for the remaining 3%, as shown visually in Figure 1-1 (World Nuclear Association, 2018b). THORP handles waste from both British Advanced Gas-Cooled Reactors (AGR) and Light Water Reactors (LWR) worldwide. Magnox SNF is treated at the Magnox Reprocessing Plant.

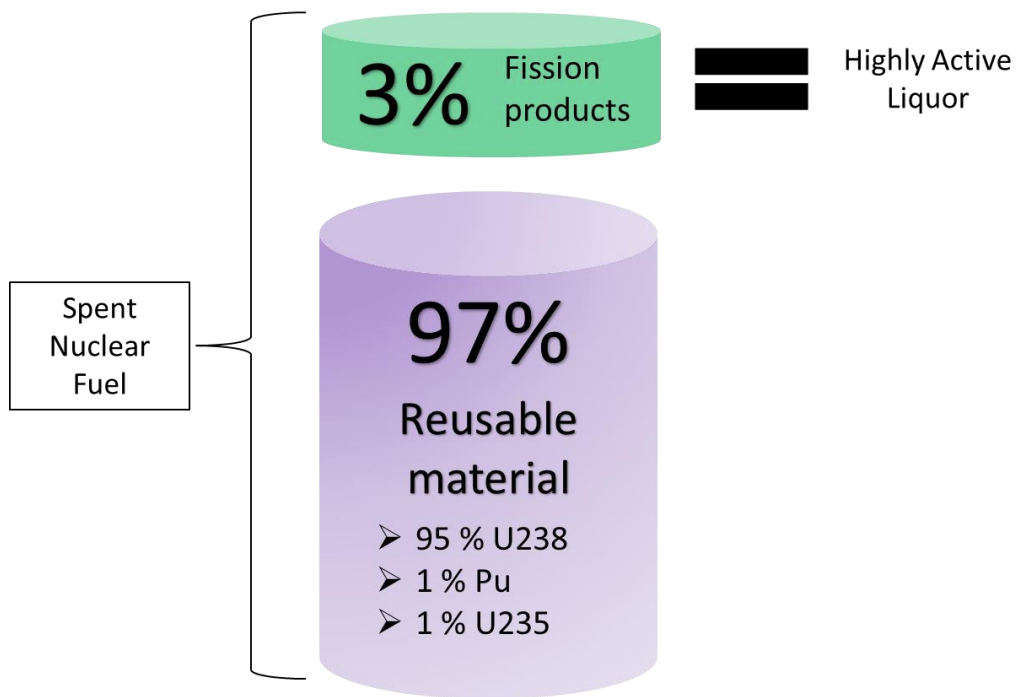


Figure 1-1 Visual representation of the breakdown of Spent Nuclear Fuel (SNF).

Waste from both these plants is treated in the Highly Active Liquor Evaporation and Storage (HALES) plant and is referred to as HAL, containing fission products to be stored temporarily in specially designed HASTs, before vitrification (Edmondson et al., 2012). As reprocessing is coming to an end both THORP and the HASTs will be slowly emptied and undergo POCO prior to eventual decommissioning (Nuclear Decommissioning Authority, 2017).

The HAL will undergo further processing in the form of vitrification before eventual geological disposal (Dunnett et al., 2014). Currently, however, there is not enough understanding of the behaviour of the solid precipitates within the HAL, therefore restricting the planning of both the onward processing of the liquor and POCO development (Edmondson et al., 2012). It has been predicted that there will be a solid bed of precipitated fission products within the HASTs and prospective POCO plans including re-suspending these beds, perhaps via a washout reagent (Edmondson et al., 2012). If this is to be the case, an understanding of the HAL product's stability in dispersions, their sedimentation behaviour and settled bed strength would be advantageous. Additionally, in considering the processing of the HAL for vitrification it may be of benefit to separate the solid and liquid water, through some sort of filtration. Therefore, it would be valuable to gain an understanding of the HALs filterability in determining whether this would be a viable option.

In addition, there are concerns about the potential for hotspots from precipitating highly active radioactive fission products within the HASTs which, in turn could potentially lead to corrosion of the tanks and a radioactivity leak. The HASTs maintain a constant temperature of 50 – 60 °C, whilst attempting to keep the HAL products suspended in a nitric acid medium (Dobson and Phillips, 2006). There have been several problematic fission products identified within the HAL. CPM ($\text{Cs}_3\text{PMo}_{12}\text{O}_{40} \cdot x\text{H}_2\text{O}$), is a known precipitation product that can convert to ZM ($\text{ZrMo}_2\text{O}_7(\text{OH})_2 \cdot x\text{H}_2\text{O}$), within the HASTs under the right conditions. The physical behaviour of CPM is of concern due to the presence of the radioactive isotopes 134-caesium and 137-caesium, which, if concentrated in a settled bed, could form the aforementioned hotspots within the HASTs (Edmondson et al., 2012). ZM is known to cause issues due to its mobility properties leading to potential problems with pipe blockages, which is a concern in regards to transferring it during POCO. The exact HAL composition within the HASTs is unknown and therefore the ratio of CPM to ZM is unknown, with the conversion potentially anywhere between 0 and 100%. Additionally, ZM is reported to take on different morphologies dependent on the conditions and additives of its synthesis. Therefore, a mix of ZM morphologies could be present within the HAL.

The primary focus of this research is to characterise CPM and ZM in relation to understanding their behaviours for the POCO planning of the HASTs, however there is also a broader scope of scientific interest. For example phosphomolybdates of alkali metals, have been studied in relation to using their reported cation-exchange properties for recovery of caesium and rubidium in solution (Krtil, 1960, Lento and Harjula, 1987, Bykhovskii et al., 2006, Bykhovskii et al., 2009, Bykhovskii et al., 2010). Therefore, studies into characterising CPM are of interest as they can help to understand behaviours of analogue systems, such as ammonium phosphomolybdate. ZM has been investigated in respect to its ability as a gel to produce the medical diagnostic agent ^{99m}Techetium, hence studies into ZM behaviour could also be of interest to this area (Evans et al., 1987, Monroy-Guzmán et al., 2003, Monroy-Guzman, 2008, Monroy-Guzman et al., 2011).

Additionally, the nature of the fission product's particle morphology is of general scientific interest, especially ZM, whose morphology encompasses a range of cuboidal shapes. For example the influence of particle shape when considering both sedimentation behaviour (Chong, 1979, Haider and Levenspiel, 1989, Loth, 2008, Gabitto and Tsouris, 2008) and permeability (Boskovic et al., 2005, Hakkinen et al., 2005, Wakeman, 2007, Beck et al., 2009, Bourcier et al., 2016, Perini et al., 2019), specifically in the fine chemical and pharmaceutical industry.

1.2 Specific Research Objectives

The specific research objectives within this thesis are as following:

- Synthesis of CPM and ZM in their non-radioactive forms, as the active material is too dangerous to handle, to provide material for characterisation. Additionally, ZM with another morphology was to be synthesised by the addition of citric acid, in order to compare shape influence on a range of physical, chemical and behavioural properties. For this reason the National Nuclear Laboratory (NNL) also provided two differing morphological simulants of ZM.
- Titanium dioxide (TiO₂) was to be used as a comparison material to the simulants and for some preliminary experiments, as the synthesis of

CPM and ZM did not yield large amounts of material for characterisation. TiO_2 is used extensively within other industries i.e. pharmaceuticals, cosmetics and paints. Therefore it is relatively well characterised. Additionally, it has previously been chosen as a suitable nuclear waste simulant in preceding studies, hence it being deemed an appropriate choice for this research (Paul et al., 2013, Bux et al., 2014).

- The kinetics of the formation of CPM were to be investigated at different temperatures. In addition, the development of the ZM morphology over time from its CPM precursor was to be tracked. This was to improve understanding of the formation of the compounds to gain a better idea of the ratio of CPM and ZM present in the HASTs.
- The simulants were to be characterised using; Scanning Electron Microscopy (SEM), Infrared (IR) analysis and X-ray Diffraction (XRD) which were to be used in addition with a Malvern Mastersizer® to confirm particle size. Additionally, density would be checked along with the water content of the simulants via thermogravimetric analysis (TGA).
- Zeta potential measurements were to be taken along with some equilibrium pH investigations to investigate stability of the simulants in a dispersion. Furthermore, the solubility of the simulants would be investigated to support the zeta potential measurements, as little has been done in investigating the solubility of specific HAST replicated conditions.
- The settling behaviours of CPM and ZM were to be investigated including the effects of temperature and pH (water and 2 M nitric acid) for both individual and mixed systems. As the ratio of CPM to ZM is unknown within the HASTs the settling of different ratios of CPM:ZM is important to understand, in order to gain insight into the potential range of behaviours of the possible combinations.
- In order to understand the way the simulants form a settled bed, compressive yield stress investigations were to be conducted on both single and mixed systems, in both water and 2M nitric acid.
- Finally, the permeability of these systems were also to be investigated, in order to understand the potential filterability of the simulants, which

could help to determine how viable a filtering option would be for POCO. For this an existing methodology was further developed (with Maksym Loginov), where kaolin was introduced as a preliminary material and for comparison to literature in validating the method.

1.3 Thesis Delivery

Chapter 1 is intended to introduce the relevance, scope and objectives of this research. Chapter 2 considers and discusses relevant literature related to this study, including those studies that have previously been conducted on both CPM and ZM, in addition to describing the components of the nuclear fuel cycle and covering some fundamental background science.

Chapter 3 presents and discusses the synthesis and kinetics of the non-radioactive simulants, followed by the results of a range of physical and chemical characterisation studies. The intention is for Chapter 3 to provide the foundations for the understanding of the experimental results presented in Chapter 4 and 5. The experiments designed for Chapter 4 and 5 were designed with the intention of providing more knowledge on how the dispersion properties of HAL may change once processing moves to a POCO stage. Chapter 4 focuses upon the surface charge, stability and settling behaviour of the simulants, considering both individual and mixed systems, in addition to the effects of pH. Compressive yield stress and permeability are investigated for both individual and mixed systems in different pH conditions in Chapter 5. Finally, Chapter 6 summarises the key conclusions made from this research and suggests potential ideas for future work.

Each of the results Chapters (Chapters 3, 4 and 5) consist of a brief 'Introduction' to reiterate the significance of the results they specifically present. This is followed by a 'Materials and Methodology' Section which presents all materials relevant to that Chapter, discusses in sufficient detail the basic principles of each piece of equipment employed and provides enough methodological detail for the experiments to be accurately repeated. The subsequent Section 'Results and Discussion' presents all the findings of the research related to that Chapter, including a discussion of their significance. Finally, a 'Conclusion' Section aims to bring all the results

together for that Chapter. Figure 1-2 presents a schematic of how the Chapters of this thesis are presented.

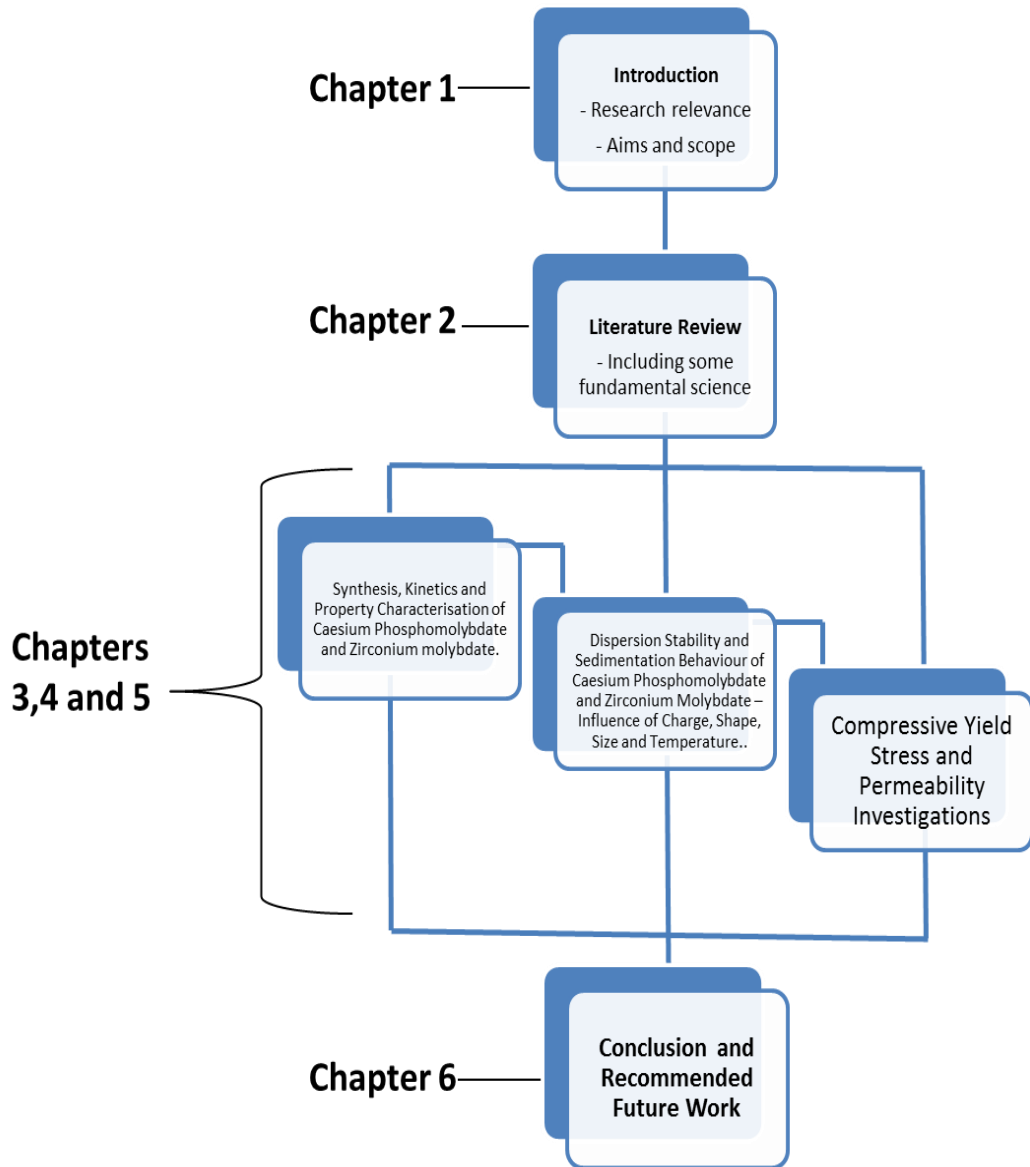
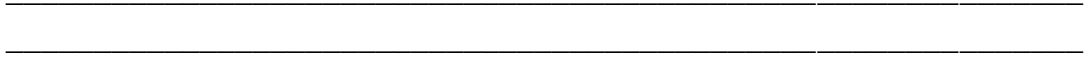


Figure 1-2 A schematic illustration of how the Chapters of this thesis are presented.

Chapter 2 Literature Review



The initial aim of this Chapter is to provide an insight into the nuclear fuel cycle (Section 2.1), focusing heavily on reprocessing (Section 2.1.1), which is the area most pertinent to this research. The main purpose of this Chapter, is to explore the studies that have preceded this research that have focused upon CPM and ZM (Section 2.2), therefore highlighting the areas of knowledge in which this research can contribute. Finally, relevant scientific theories (Section 2.3) combined with appropriate literature will be discussed, with the aim of assisting the understanding of the results presented in Chapters, 3, 4 and 5.

2.1 Nuclear Fuel Cycle

The nuclear fuel cycle is a succession of industrial processes, which commence from the mining of raw natural uranium, to its processing and use in a nuclear reactor, right through to its eventual waste disposal. Figure 2-1 shows a basic schematic of the UK nuclear fuel cycle.

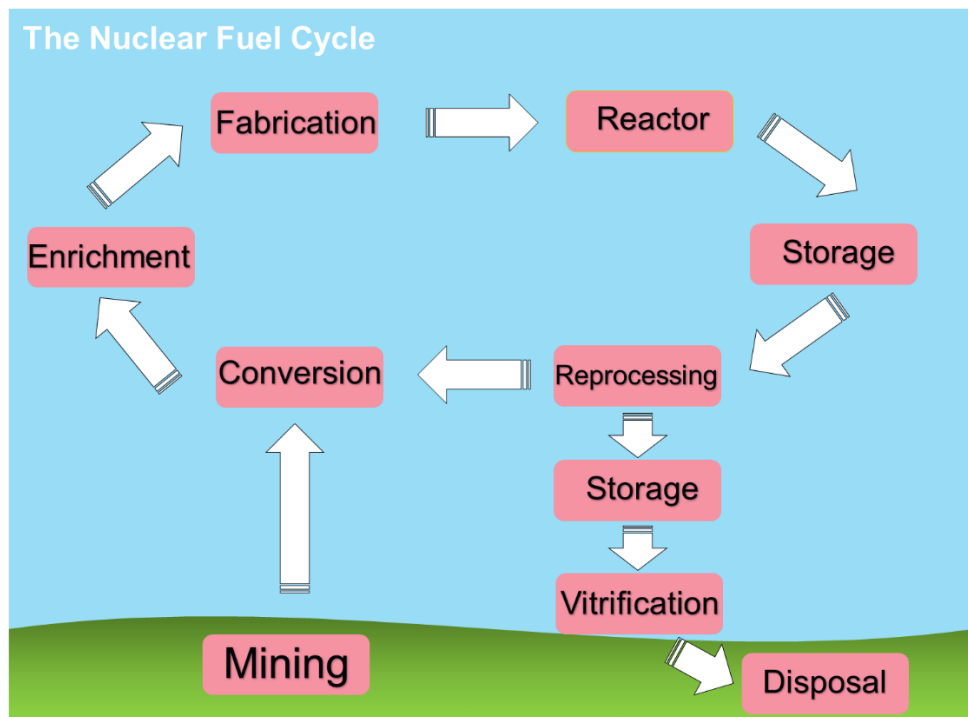


Figure 2-1 Basic schematic of the UK nuclear fuel cycle

Uranium is a naturally occurring radioactive metal that when in sufficiently high concentration can be mined from uranium ore for use as nuclear fuel (World Nuclear Association, 2017). There are several different techniques used to mine uranium dependent on where the ore is in comparison to the surface,

the governing body responsible for the mining (country dependent) and the economics of the technique. The freshly mined uranium ore must first undergo a process referred to as milling, fundamentally grinding the ore and separating the uranium from the rock. The unwanted 'rock' mainly ²³⁸-uranium hexafluoride still contains radioactivity, therefore is stored nearby the mine (World Nuclear Association, 2017). The remaining uranium undergoes chemical conversion and enrichment of the fissile ²³⁵-uranium to between 3-5%, as required for the specific reactor. The fuel is then fabricated in the specific form required for its designated reactor, more often than not in the form of ceramic pellets. The pellets are packed into fuel rods and arranged into a fuel assembly ready for insertion to the reactor.

After its use and removal from the reactor the used fuel is temporally stored to allow cooling. Currently, in the UK used fuel can either then be reprocessed or undergo long term storage with the view of eventual geological disposal (Nuclear Decommissioning Authority, 2010). It is this back 'portion' of the nuclear fuel cycle that is most pertinent to this research.

2.1.1 Nuclear Fuel Reprocessing

Reprocessing within the UK began in 1952, with the processing of Spent Nuclear Fuel (SNF) from the two air-cooled Windscale reactors, with the original aim being to separate out plutonium for weapons. Currently, reprocessing is not necessarily economically viable as uranium as a raw material is relatively cheap, however as the popularity of nuclear power increases, this cost will inevitably rise. SNF contains approximately 96% of the original uranium with less than 1% of this being ²³⁵-uranium the rest comprising of; 95% ²³⁸-uranium, 1% ²³⁹-plutonium and 3% fission waste products (World Nuclear Association, 2018b). Reprocessing involves separating the uranium and plutonium from these waste products (Bodansky, 2006). In the UK, this currently happens at both the Thermal Oxide Reprocessing Plant (THORP) and Magnox plant, where the SNF is first stored underwater to dissipate some of the heat before reprocessing, this can be from 180 days to 6 years dependent on the fuel type and reprocessing plant. Once cooled sufficiently the fuel is taken to the head end plant shear cave, where it is chopped up before being dissolved in concentrated nitric acid (Fountain et al., 2011). It is this dissolved solution that then undergoes

chemical separation and solvent extraction, processes that produce three highly active waste raffinates. The three raffinates include; plutonium, which is converted to plutonium oxide, uranium which is converted to uranium trioxide and fission products contained in nitric acid, which are stored within the Highly Active Storage Tanks (HASTs). Combined these raffinates contain nearly all the radioactivity that is processed at Sellafield (Mort et al., 2013).

2.1.2 Highly Active Liquor Evaporation and Storage Plant

The Highly Active Liquor Evaporation and Storage (HALES) plant at Sellafield consolidates and concentrates the raffinates from the separation processes of uranium and plutonium, through evaporation. The site receives the highly active raffinate from both the THORP plant and Magnox reprocessing plant. Currently, the HALES plant has four operating evaporators A-D, which have helped with the reprocessing pace before THORP was shut down (Edmondson et al., 2012). The process involves the highly active raffinate to be continually fed into the evaporator, with low operating pressures and temperatures reaching up to 60 °C (Edmondson et al., 2012). The feed flows into the evaporator vessels through a feed line, in addition to going through a feed cooler before being boiled. Any evaporated acid is then recycled and used at the start of the cycle. Water is then added to the highly concentrated acidic Highly Active Liquor (HAL) to reduce the 11 M nitric acid concentration to around 2/3 M (Edmondson et al., 2012). At this point the HAL will be sent on to the HASTs. The whole process can take up to 5 weeks. Figure 2-2 shows a simplified flow diagram of the HALES plant processes (Dobson and Phillips, 2006).

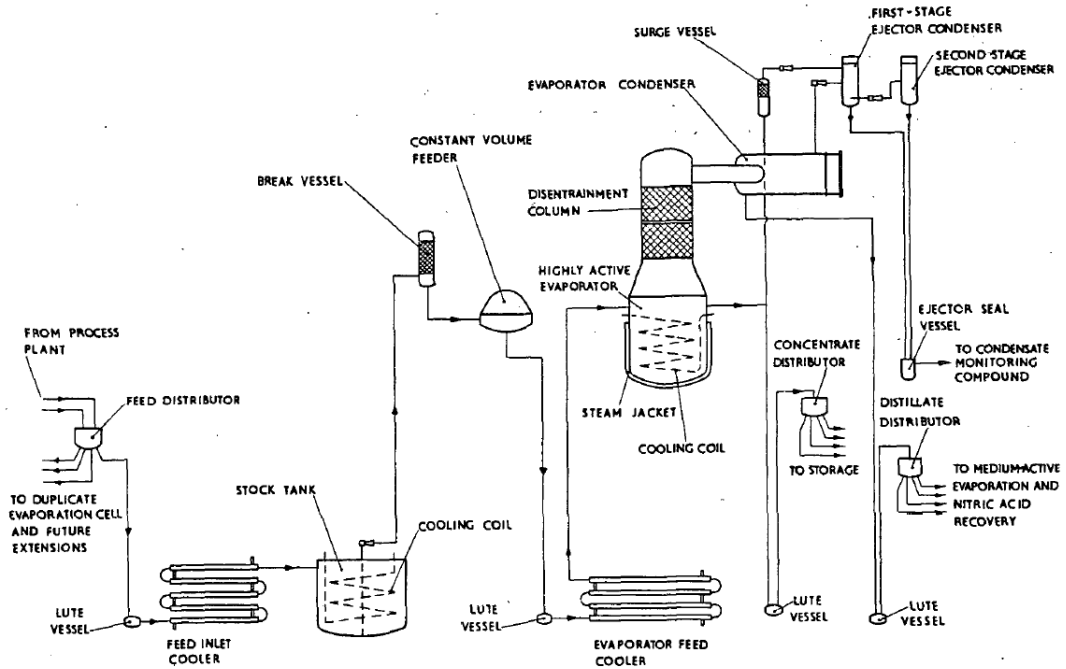


Figure 2-2 Simplified flow diagram of the Highly Active Liquor Evaporation and Storage (HALES) plant, Sellafield, UK (Dobson and Phillips, 2006).

2.1.2.1 Highly Active Storage Tanks

The twenty-one HASTs at Sellafield are an interim storage for the HAL, allowing radioactive heat to decay before it undergoes vitrification (Roth and Weisenburger, 2000). There are two types of HAST designs at Sellafield; eight 'old-side' and thirteen 'new-side' (Edmondson et al., 2012). The eight 'old-side' cylindrical 70 m³ stainless steel tanks are housed in underground concrete cells with their axis horizontal, built pre-1960s, have no inbuilt agitation system and contain up to three cooling coils (Dobson and Phillips, 2006). As reprocessing was progressing during the 1960s the volume of HAL was to increase and it was predicted that the 'new' HAL would be more active and precipitation of fission products within the tanks would increase. Therefore, the more modern stainless steel 'new-side' 150 m³ tanks were designed to have inbuilt agitation with seven jet ballasts and four airlift systems in addition to redundancy in cooling coils (Edmondson et al., 2012). Figure 2-3 shows a 'new-side' tank positioned vertically, before it was commissioned with its cooling coils and agitation systems visible.

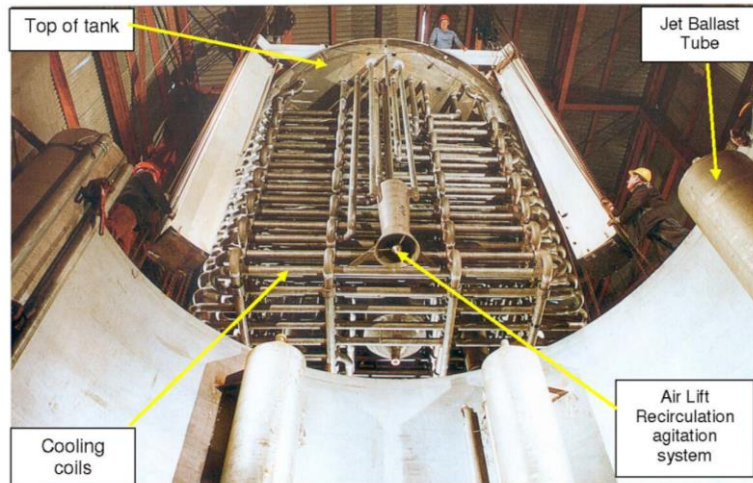


Figure 2-3 A 'new-side' Highly Active Storage Tank (HAST) positioned vertically, before it was commissioned with its cooling coils and agitation systems visible (Dobson and Phillips, 2006).

As the HAL is significantly radioactive, radioactive decay will occur, which in turn can heat the liquor causing it to boil, hence the requirement of a cooling system. The temperature is similar to that of the evaporators reaching up to 50 °C. Precipitation of solids can result in a settling bed which can inhibit heat transfer, block pipework, corrode steel and cause potential localised hot spots. The 'new-side' tanks contain seven cooling coils, five horizontal and two vertical, all acting independently, periodically isolated one at a time to test for activity via gamma pots. If they fail the activity test they can be isolated, as all coils are linked to a common delay tank, which prevents any excess activity getting back to the main cooling water system (McArthur et al., 2005). The 'new-side' tanks consist of six peripheral jet ballasts and one slightly larger central one, that are operated on a sequence basis taking up to 30 mins (McArthur et al., 2005). The air lifts are in place to attempt to keep any solids that have been re-suspended from resettling. Figure 2-4 shows the positions of these jet ballast and air-lifts.

the 'old-side' HASTs, which concluded; to be either ammonium carbamate or sodium carbonate. Figure 2-5, shows the proposed wash sequence of the 'old-side' HASTs into the 'new-side' tanks (Edmondson et al., 2012). Although the 'new-side' tanks are still being used they too will eventually need to undergo POCO although the hope is that with the inbuilt agitation systems the issue of solid settled beds will be less prevalent. In considering POCO it is vital to consider various processes to determine the most efficient and economically viable route in processing CPM and ZM. Therefore, a better understanding of the behaviour of both CPM and ZM will only be beneficial for POCO planning.

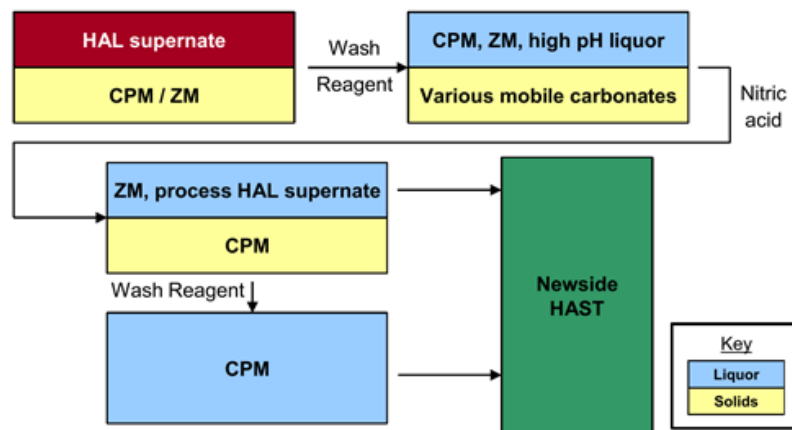


Figure 2-5 Schematic of proposed 'old-side' Highly Active Storage Tank (HAST) wash sequence (Edmondson et al., 2012).

In order to assist in predicting the behaviour of the solids in conjunction with the inbuilt agitation systems, a 4:10th replica of a 'new-side' HAST was constructed at the National Nuclear Laboratory (NNL), Workington, UK. Figure 2-6, shows both a schematic and photo of this HAST replica rig.

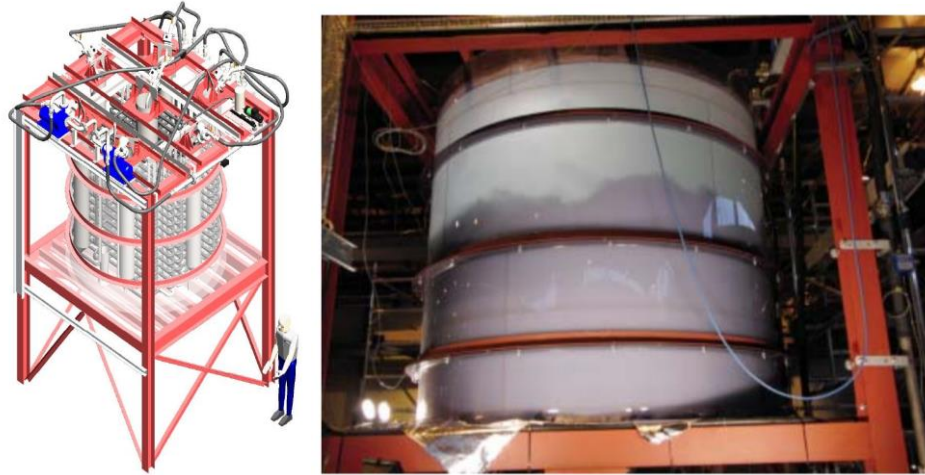


Figure 2-6 Schematic and photo of 4:10th size inactive Highly Active Storage Tank (HAST) at the National Nuclear Laboratory (NNL), Workington, UK (Griffon, 2010-2011)

Within the 4:10th replica rig, inactive simulants could be used in conjunction with the sequence of jet ballasts that occurs within the actual 'new-side' HASTs. The experimental results from this rig were applied to a computer model; GAHM Model for Jet Ballast Resuspension, which can help to predict the performance of the jets (McArthur et al., 2005). This model has been operational since 2001 and is being continually improved with data from the 4:10th tank studies, which is not all currently available publically. The air lifts are reported to keep suspended solids circulating providing that are successfully re-suspended by the jet ballasts. The accurate performance of the jet ballasts is not completely known due to the difficulty of replicating the exact conditions of the HASTs. Bux et al. (2014) utilised the 4:10th tank to test an *in situ* characterisation system; Acoustic Backscatter System (ABS). In this study ABS was used in measuring sediment bed erosion by impinging jet ballasts and the data was used for modelling and POCO planning. For this study barytes was used to predict a 'worst' case scenario as its properties were deemed to be less favourable than the actual fission precipitation products (Bux et al., 2014). Further understanding of the behaviour of the solids within the HASTs is crucially important to feed into the GAHM Model for Jet Ballast Resuspension for a more accurate simulation, especially in regards to settling and yield stress (McArthur et al., 2005).

2.1.2.2 Highly Active Liquor

HAL comprises of a number of fissions products several of which precipitate out in the nitric acid medium causing multiple issues within HASTs. The most problematic products include; barium/strontium nitrate, zirconium phosphates, CPM and ZM (Clelland, 1962). The amount of precipitate is dependent on the initial concentration of the fission product, the concentration of phosphate and the conditions in the tank; mainly the acidity (Clelland, 1962). There have been a number of studies that have investigated these precipitates, however, there is currently not a comprehensive understanding of their behaviour, hence the requirement for further research, such as with this project.

Barium nitrate ($\text{Ba}(\text{NO}_3)_2$) is the least soluble of the aforementioned solids and is most likely to crystallise in highly acidic environments, therefore causing more of an issue within the evaporators. The solubility of barium nitrate has been the focus of several studies (Greene, 1937, Zhirnov and Moiseenko, 1996, Hodgson et al., 2018). One of the first studies to publish data in regards to barium nitrate in concentrated nitric acid was conducted by Greene (1937), where he reported a logarithmic relationship of barium nitrate % to nitric acid%. Many years later Zhirnov and Moiseenko (1996) also investigated the solubility of $\text{Ba}(\text{NO}_3)_2$ with a focus upon its insolubility within the raffinates, where they reported a decrease in solubility as the concentration of nitric acid increased, a trend which was the same at both 30 °C and 60 °C. They reported that in order to maximise the degree of evaporation of the barium nitrate, the nitric acid concentration must be minimised, a condition that may not be plausible within the evaporators. The most recent study was published by Hodgson et al. (2018), studying the dissolution rate of barium nitrate in order to predict the time required to dissolve a settled bed, specifically in regards to the POCO of the HASTs. It was concluded that the rate of dissolution for barium nitrate would be slower than for other nitrates present within the HASTs and therefore it would be the limiting factor in respect to POCO.

The radioisotopes of barium typically have a very short half-life (ms-s range). Therefore, its solubility is more of a concern than its radioactivity. Some of its longer lived isotopes, in the form of nitrates co-precipitate with 90-strontium nitrate ($\text{Sr}(\text{NO}_3)_2$, half-life 29 years) to form a barium-strontium complex. This

complex contributes significantly to the heat output in the HASTs through radioactive decay, potentially causing hotspots (Mishina et al., 2010).

The composition and solubility of such barium-strontium precipitates within nitric acid have been extensively investigated (Mishina et al., 2010, Mishina et al., 2014a, Mishina et al., 2014b, Mishina et al., 2015). Strontium nitrate is reported to be more soluble than barium nitrate in nitric acid, until a concentration of ~ 7M nitric acid, where they then jointly precipitate. Mishina et al. (2015) reported that the nitric acid medium was crucial in the co-precipitation of the nitrates by being incorporated within their composition.

The morphology of both barium and strontium nitrate is reported to be cuboidal although their shapes are irregular, as can be seen in Figure 2-7 (Dunnett, 2015). When barium-strontium complexes are formed they provide a range of particle sizes. The morphology of the HAL simulants is of particular interest as it can potentially affect their behaviour.

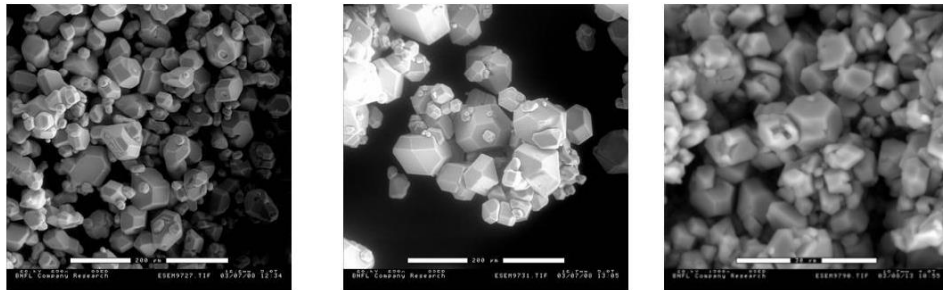


Figure 2-7 Scanning Electron Micrographs (SEM) of barium nitrate, strontium nitrate and barium nitrate & 4 mole% strontium (left to right) (Dunnett, 2015).

A large quantity of zirconium is formed through the fission of ²³⁵-uranium and ²³⁹-plutonium some of which goes on to form several different zirconium phosphates ($Zr(HPO_4)_2 \cdot nH_2O$). It is hypothesised that zirconium phosphate is the first product to precipitate out of the previously mentioned HAL products (Clelland, 1962). These phosphates do not directly cause a heat issue as zirconium is relative stable with an extremely long half-life. However, the phosphates do cause a mobility issue within the HAL, particularly as in high concentrations they can form a gel-like material, consequently increasing the viscosity of the HAL (Clearfield and Stynes, 1964). This gelatinous behaviour was reported when the crystal structure and ion exchange properties of

zirconium phosphates were investigated (Clearfield and Stynes, 1964). The structure is reported to be in a layered crystal consisting of zirconium atoms held by phosphate bridges strengthened by a hydrogen bond network. Zirconium phosphates are reported to be easily re-suspended after precipitation and therefore they don't pose as much of a concern as with other precipitation products (Dobson and Phillips, 2006).

Zirconium phosphate has also been studied as a catalyst and sodium zirconium phosphate as a material in immobilising nuclear waste (Segwa et al., 1987, Scheetz et al., 1994). The use of sodium zirconium phosphate was explored as an immobilisation material as a result of its ion exchange properties and structural flexibility (Scheetz et al., 1994). Future studies could investigate the possibility of utilising the zirconium phosphates within the HASTs to internally encapsulate nuclear waste.

Combined the HAL produces approximately 2 Watts/litre of heat and has an activity of up to 20 TBq/litre (Dunnett, 2015). Although only accounting for 3% of the SNF the HAL contains 99% of its radioactivity, hence it being both a hazardous and dangerous solution if not processed appropriately (Dobson and Phillips, 2006). This hazardous nature highlights the importance of fully comprehending the behaviour of the HAL products in order to plan safe onward processing. Although as discussed barium-strontium nitrate and zirconium phosphates cause issues within the HASTs, given the extensive literature a lot is currently known about them. However, less is known about both CPM and ZM and therefore these are more of a critical safety concern in regards to the planning of POCO of the HASTs. Section 2.2, details the issues and previous studies related to CPM and ZM, which are the HAL products this research is concerned with.

2.1.3 Vitrification

With the end disposal route of High Level Waste (HLW) being geological disposal the waste must first be in a suitable form and immobilised, vitrification is the internationally accepted technology for this (Roth and Weisenburger, 2000). The HAL contains a number of complex metal nitrates which are required to be converted into metal oxides, for easier handling. These metal oxides then undergo calcination, where they are evaporated and denitrated,

producing calcine, which is then mixed with borosilicate (Roth and Weisenburger, 2000). The mixing occurs in temperatures over 1000 °C to form the end product, an encapsulated glass block. This block is then allowed to cool and stored in containers before being sealed and stored. At Sellafield this process occurs at the Waste Vitrification Plant (WVP), which opened in 1990 (Harrison and Brown, 2018). As the POCO of HASTs progresses both CPM and ZM solids will need to be removed and undergo vitrification; however this will result in a stream of enriched molybdenum entering the WVP, which has a low solubility in borosilicate glass (Dunnett et al., 2014). Therefore, a new glass formation will need to be developed to counteract this effect (Dunnett et al., 2014). Increasing the characterisation and understanding of both CPM and ZM, could also assist with the formation of a new glass formation.

2.2 Caesium Phosphomolybdate and Zirconium Molybdate

There have been a number of studies that have looked into both CPM and ZM specifically relating to the issues they cause within the HASTs, the challenge they pose to the WVP and the *in situ* conversion of CPM to ZM (Bradley et al., 2004, Jiang et al., 2005, Edmondson et al., 2012, Paul et al., 2013, Paul et al., 2015, Dunnett et al., 2016). The issues they cause refer to CPM having the potential to cause 'hotspots' possibly affecting the integrity of the HASTs due to the presence of radioactive caesium (Edmondson et al., 2012). Where ZM causes mobility issues within the HAL when it is re-suspended by the jet ballasts in the HASTs and therefore potentially causing issues in future processing (Edmondson et al., 2012). This section aims to highlight the distinct lack of published studies focused on the stability, settling, compressive yield stress and permeability of these compounds. These aforementioned properties are critical in understanding in order to facilitate the onward processing of the HAL and the POCO of the HASTs. Additionally, there has been no literature focused on investigating the properties of a range of CPM:ZM mixed systems, which is the most likely situation present within the HASTs.

The relevant studies that focus upon both CPM and ZM, individually will first be discussed before the studies that have focused on both combined, thus highlighting the crucial gaps in literature this project aims to fill.

2.2.1 Caesium Phosphomolybdate

There have been relative few studies investigating CPM directly, although there are a number of analogues that have been studied, such as ammonium phosphomolybdate, which is a potential cation-exchange material for selective recovery of Cs (Krttil, 1960, Lento and Harjula, 1987). Indeed, CPM has also been synthesised itself for the same purpose, and as a photocatalyst for the photodegradation of dye pollutant (Bykhovskii et al., 2006, Bykhovskii et al., 2009, Bykhovskii et al., 2010, Ghalebi et al., 2016).

CPM is part of a family of salts referred to as polyoxometalates (POM), which consist of a polyatomic anion with three or more transition metal oxyanions linked via oxygen atoms (Dermeche et al., 2009, Patel and Pathan, 2012, Zhu et al., 2014, Ghalebi et al., 2016). POM's are of particular interest for their application in a range of fields, including medicine, electrochemistry and catalysis (Zhu et al., 2014). Typically, POM's are synthesised either via a solid state synthesis route (Kang et al., 2004, Paul et al., 2015, Ghalebi et al., 2016) or via ion exchange (Friesen .D.A et al., 2000, Bykhovskii et al., 2006, Srilatha et al., 2012, Patel and Pathan, 2012).

The physical behaviour of CPM in nuclear waste HAL is of concern due to the presence of the radioactive isotopes 134-caesium and 137-caesium, which if concentrated, could form potential hotspots within the HASTs (Edmondson et al., 2012). Paul et al. (2015) published a direct synthesis route to CPM, in order to study its morphology in nuclear HAL systems, this method was used in this research.

CPM formation within the HASTs is dependent on co-precipitation of caesium ions, Cs^+ and $[\text{PMo}_{12}\text{O}_{40}]^{3-}$. Phosphomolybdic acid ($\text{H}_3\text{PMo}_{12}\text{O}_{40}$) is known to be present within the HAL and is a pre-cursor to the formation of CPM, in addition to other POMs (Kang et al., 2004). CPM's formation is also heavily reliant on the molybdate concentration, with it needing to be 1.8 g/l of molybdate for the CPM to precipitate out (Dunnett, 2015). The caesium isotopes of particular issue are 134-caesium (2 year half-life) and 137-caesium (30 year half-life) as they contribute considerably to the heat output in the HASTs through radioactive decay, potentially causing hotspots similar to that of the barium-strontium complexes. As a result of its long-lived isotopes

several studies have focused on the removal of caesium from nuclear waste in order to decategorise the waste, allowing it to be disposed of via a more economic route (Carley-Macaulay et al., 1981, Brown et al., 1996, Dozol et al., 1999, Todd et al., 2004).

When exploring the literature, little is found in the way of studies exclusively focused on CPM and those research papers that are found often refer to CPM in addition to ZM. However, in 2006 an investigation into the varying composition of CPM was undertaken in Russia (Bykhovskii et al., 2006). They reported the variable composition of CPM to be a cubic body-centred lattice of formula $Cs_xH_{3-x}PO_4 \cdot 12MoO_3 \cdot nH_2O$ where $x = 0.8 - 3.0$ in nitric acid solutions, this corresponds to the Paul et al. (2015) published formula where, $x = 3$. Bykhovskii et al. (2006) also reported that in acidic conditions CPM was practically insoluble, which correlates with its predicted precipitation behaviour in the HASTs resulting in the problematic localised hot spots. Although a specific value for its solubility was not reported. Bykhovskii et al. (2009), conducted a further study built upon this looking at caesium pre-concentration by recovery from solutions in the form of phosphomolybdate. In this study the effect of the presence of other compounds or impurities was investigated on the recovery of the caesium through CPM in nitric acid. Ten different compounds were studied in a variety of conditions and it was found that all still promoted the recovery of caesium, although at varying degrees. It was also reported that once the caesium was recovered via the precipitate it could be concentrated further by dissolving in sodium hydroxide allowing caesium magnesium phosphate ($CsMgPO_4$) to precipitate out. Bykhovskii et al. (2010) used the knowledge gained from this previous study to help estimate the expected heat release during these same experiments.

In an another non-nuclear related study Ghalebi et al. (2016), studied the potential for CPM to be used as a photocatalyst for the photodegradation of dye pollutant. In this study CPM was synthesised via a solid-state reaction, using phosphomolybdic acid and caesium chloride, without the application of heat, utilising an ultrasonic bath for mixing. Once synthesised CPM was characterised via Scanning Electron Microscopy (SEM), Transmission Electron Microscopy (TEM), X-Ray Diffraction (XRD) and Fourier-Transform Infrared Spectroscopy (FTIR). Through directly comparing to

phosphomolybdic acid, it was found that CPM has less of a tendency to aggregate and subsequently produces smaller nanoclusters (Ghalebi et al., 2016). The investigation determined CPM to be a very stable and suitable catalyst.

POMs typically display a keggin structure, with a general formula of $[xM_{12}O_{40}]^n$, where X is most commonly phosphorous and M is most commonly molybdenum or tungsten (Dermeche et al., 2009, Srilatha et al., 2012, Patel and Pathan, 2012, Ghalebi et al., 2016). Ammonium phosphomolybdate was the first compound to be reported with a keggin structure in 1826 by Berzelius (Berzelius, 1826). Figure 2-8, illustrates the structure of CPM, which is reported to include 12 Keggin cages of MoO_3 with a tetrahedral phosphate (PO_4^{3-}) group at the centre and three caesium ($3Cs^+$) counter ions (Macheder, 2011). Macheder (2011) in his thesis titled 'Zirconium molybdate crystal growth and morphological control' focused on ZM, although he also investigated the breakdown of CPM at temperatures of 95 °C and in 3 M nitric acid. He used both SEM and TEM to determine that it took 4 h for the initial breakdown to start occurring.

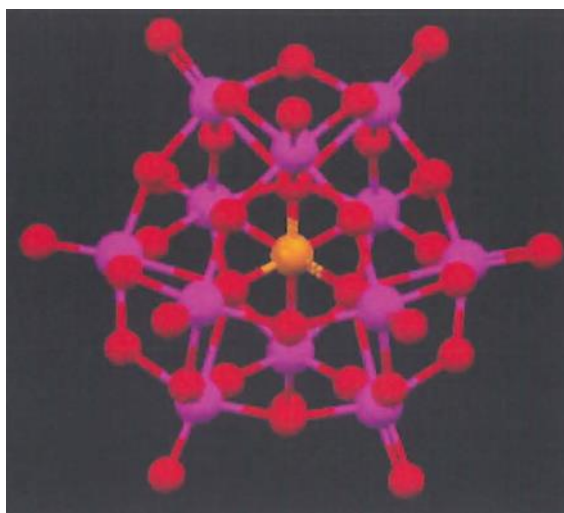
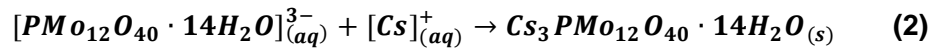
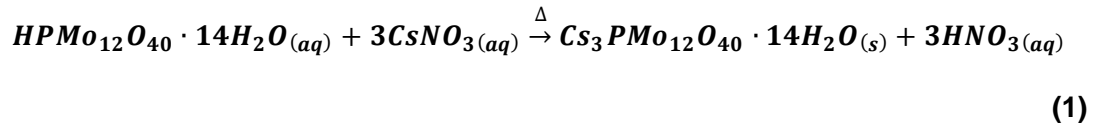


Figure 2-8 Schematic representation of CPM showing the Keggin cage, $12MoO_3$ with a tetrahedral phosphate (PO_4^{3-}) group at the centre. Molybdenum being purple, oxygen red and phosphorus orange (Macheder, 2011).

Paul et al. (2015) published a synthesis route to CPM via a double replacement reaction with two reactants; phosphomolybdic acid and caesium nitrate, dissociating and their respective ions forming CPM. Through this analysis Paul et al. (2015) published an Equation

(1) for the synthesis of CPM, in addition to a net ionic Equation (2).



Paul (2014) reported CPM to have an average particle size of 200 nm but surmised this to actually be a combination of much smaller particles, a three step mechanism of which can be seen in Figure 2-9. Where the initial step involves the formation of primary particles, the second for formation of CPM aggregates and the third formation of larger aggregates.

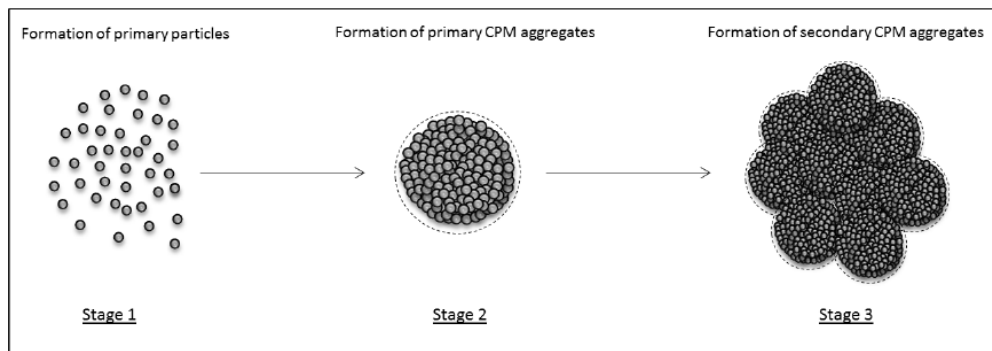


Figure 2-9 Depiction of the proposed three step mechanism of the formation of caesium phosphomolybdate, proposed by Paul (Paul, 2014).

2.2.2 Zirconium Molybdate

ZM has been the focus of several studies within literature, where it has been synthesised for various applications, such as a 99m-technetium generator (Evans et al., 1987, Monroy-Guzmán et al., 2003, Monroy-Guzman, 2008, Monroy-Guzman et al., 2011), a precursor for the formation of the negative thermal expansion material $ZrMo_2O_8$ (Lind et al., 2001, Varga et al., 2005) and predominately for nuclear waste based studies (Rao et al., 1986, Rao et al., 1990, Izumida and Kawamura, 1990, Doucet et al., 2002, Magnaldo et al.,

2004, Magnaldo et al., 2007, Usami et al., 2010, Vereshchagina et al., 2011, Xuegang et al., 2012, Paul et al., 2013, Zhang et al., 2013, Paul et al., 2015, Paul et al., 2017, Arai et al., 2018). Clearfield and Blessing (1972) were the first to publish a synthesis route for ZM, in order to characterise its ion exchange properties. Paul et al. (2015) further investigated this synthesis method, including using the addition of citric acid to alter the crystal morphology, the method of which was used in this research. ZM is known to cause issues within the nuclear industry, due to its mobility properties leading to potential problems with pipe blockages, for example (Edmondson et al., 2012).

Within the HASTs ZM is formed from CPM in combination with the nitric acid medium, zirconium ions and at elevated temperatures. Clearfield and Blessing (1972) were some of the first to discuss the synthesis of ZM through mixing of zirconium oxide dichloride and sodium molybdate before re-crystallising with hydrochloric acid in investigating its ion-exchange property. Rao et al. (1986) following on from this study investigated the formation of ZM under conditions encountered during reprocessing with varying concentrations of zirconium and molybdenum utilising Raman spectroscopy. They reported that complete precipitation of ZM occurs at conditions found within the HASTs; 3 M nitric acid. Other studies also investigated ZM and its precipitation in nitric acid, concluding with similar findings (Doucet et al., 2002).

Zhang et al. (2013), conducted a study specifically looking at the precipitation of ZM in Japan. This is one of the only studies that directly investigates the solubility of ZM. ZM's solubility was investigated in both 3 M and 5 M nitric acid from 70 °C to 100 °C, the results of which can be seen in Figure 2-10.

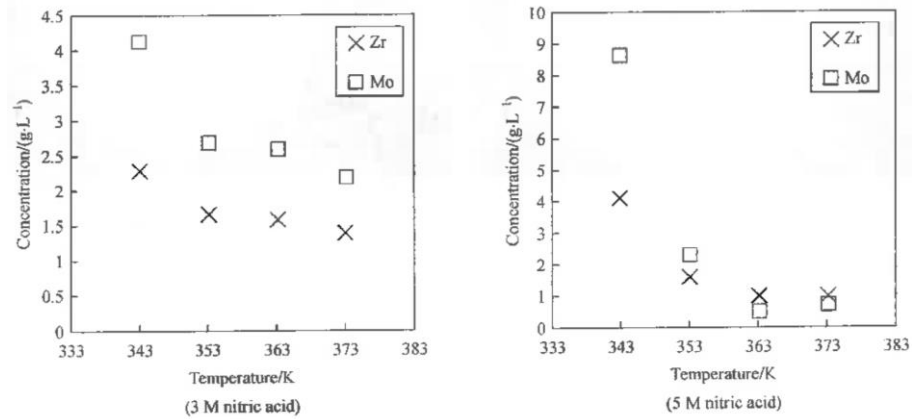


Figure 2-10 Solubility curves for zirconium molybdate (ZM) at 3 M and 5 M concentrations of nitric acid (Zhang et al., 2013).

As temperature increases the solubility is found to decrease, however at 70 °C the solubility in 5 M is higher than 3 M, a trend which reverses from 80 °C upwards. The values of solubility were very low, the highest value reading just over 4 g/L. Anything less than 1g/L is considered to be insoluble, so although these values are above this they are still very low. Consequently ZM is often referred to as being insoluble. In comparing the parameters used to the HASTs conditions both the acidity and temperature are higher and therefore the results of this study don't provide directly applicable solubility data. In addition, the authors did not discuss the solubility method they applied to achieve these results.

Bradley et al. (2004) first published the conversion of CPM to ZM within HAL, reporting high temperatures and low acidity as the optimum conditions. They investigated several parameters such as temperature, volume and concentration. Figure 2-11, is a published figure representing an example CPM-ZM conversation-time profile (Bradley et al., 2004). They concluded that heat promotes the breakdown of the CPM releasing molybdate ions that react with zirconyl ions. Therefore it is a two-step mechanism, not a direct conversion. This corresponds with Macheder (2011) reporting that CPM begins break down at high temperatures within 4 h.

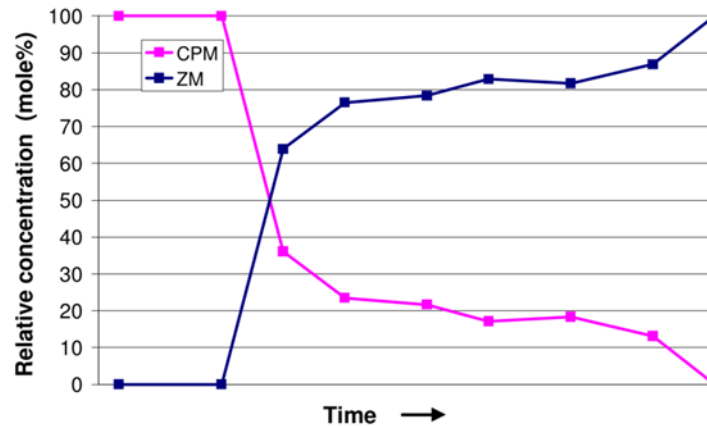
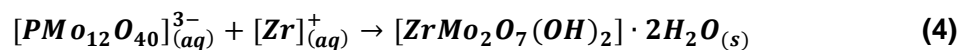
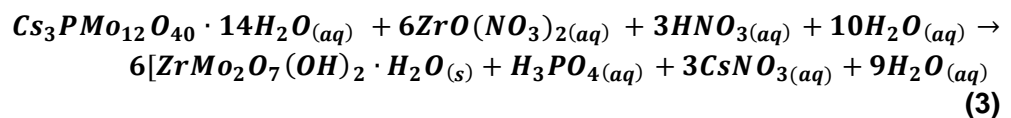


Figure 2-11 Representation of an CPM (caesium phosphomolybdate) -ZM (zirconium molybdate) conversion concentration-time profile (Bradley et al., 2004).

The conversion of CPM to ZM is still not fully understood. Paul et al. (2015) published an unbalanced chemical Equation (3) for the conversion and a net ionic precipitate Equation (4). Although this equation has been published, it has not been confirmed independently. However, it does provide a basis for the understanding of the conversion.



Macheder (2011) also investigated the use of additives in changing the morphology of ZM, investigating eleven organic compounds. In Macheder's (2011) thesis, an internal Sellafield document is referred to that was released in 2004, which is the first reported finding that ZM could exist in a non-cuboidal morphology. It was predicted that a different morphology could both alter and possibly improve dispersion behaviours. Therefore, in gaining an understanding of various morphologies of ZM, if one was deemed to display more advantageous properties over another, that morphology could be encouraged via doping.

Macheder (2011) found that over half of the chosen additives had no effect at all on the morphology of ZM, whilst four had a minor effect. From his studies he highlighted one organic compound, citric acid that did have a large effect on the morphology of ZM, causing an elongation of one of the axis, resulting in a reported rod-like structure. Once citric acid was identified as a viable additive several different concentrations were experimented with: 10, 20 and 40 mol% (Macheder, 2011). Paul et al. (2015) later developed the methodology for using citric acid at 20 mol% as an additive in manipulating the morphology of ZM to form a compound referred to as zirconium citratomolybdate (ZMCA). Paul et al. (2015) explored two methods in synthesising ZMCA, once of which can be seen in Figure 2-12. The first where the citric acid was added at the same time as the reactants and another where it was added at a 30 min delay to the reactants. It was determined that the second method provided the better product.

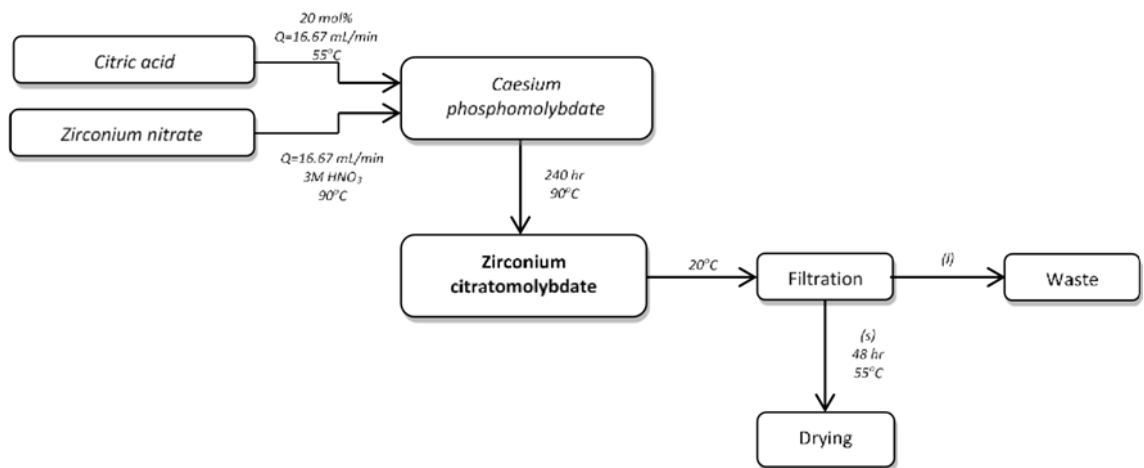


Figure 2-12 Schematic of the second method Paul et al. (2015) attempted for the synthesis of zirconium citramolybdate (ZMCA) (Paul et al., 2015).

2.2.3 Combined

Paul et al. (2013) published a study looking into both the sedimentation and rheological behaviour of CPM, ZM and titanium dioxide (TiO_2), Figure 2-13, shows the sedimentation rate vs. volume fraction graph published for this study.

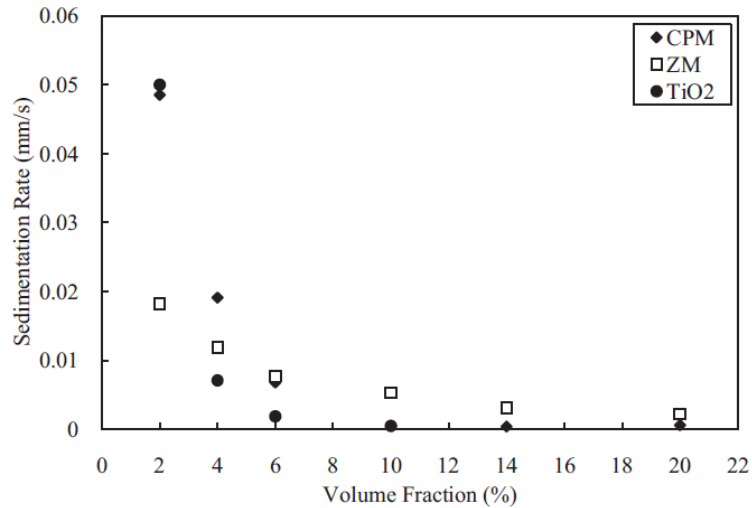


Figure 2-13 Sedimentation rate vs. volume fraction for caesium phosphomolybdate (CPM), zirconium molybdate (ZM) and titanium dioxide (TiO₂) (Paul et al., 2013).

For all simulants there is a decrease in settling as the volume fraction is increased. CPM has the faster settling rate compared to ZM for the lower volume fractions in addition to having a similar settling trend to titanium dioxide. This study provides a comparison for the settling of CPM and ZM as individual systems within water but does not investigate their settling behaviour in nitric acid (conditions expected within the HASTs) or when combined in a mixed system. Rheological studies were conducted on both CPM and ZM individually within nitric acid and water, reporting that the particles display Newtonian behaviour in water whereas within nitric acid the particles exhibit non-Newtonian behaviour. They concluded that further research is required into both the sedimentation and rheological behaviour of the HAL products. As previously mentioned in Sections 2.2.1 and 2.2.2 Paul et al. (2015) also investigated and published direct synthesis routes for both CPM and ZM which were applied in this research.

Dunnett et al. (2016) carried out some physical characterisation studies on both CPM and ZM and presented their findings in a conference paper. Their study looked at particle size, density, settling, voidage, viscosity, yield stress and ZM morphology. Their results were directly comparable to Paul et al. (2013) and (2015). This is the first published study that has considered the properties of CPM and ZM in a mixed system with a 50:50 mix analysed in their rheology, viscosity, yield stress and settling studies. Within the

conference paper detailed results weren't given for the properties of the mixed system but they were reported to be different from the single systems. It was reported that the mixed system behaved very similar to the ZM single system especially in terms of the rheology and viscosity measurements. For yield stress measurements on the mixed system it was found to be 90% reduced from the CPM yield stress even though only 50% of the CPM has been replaced, again suggesting the ZM dominates the properties of mixed systems, Figure 2-14 shows these results.

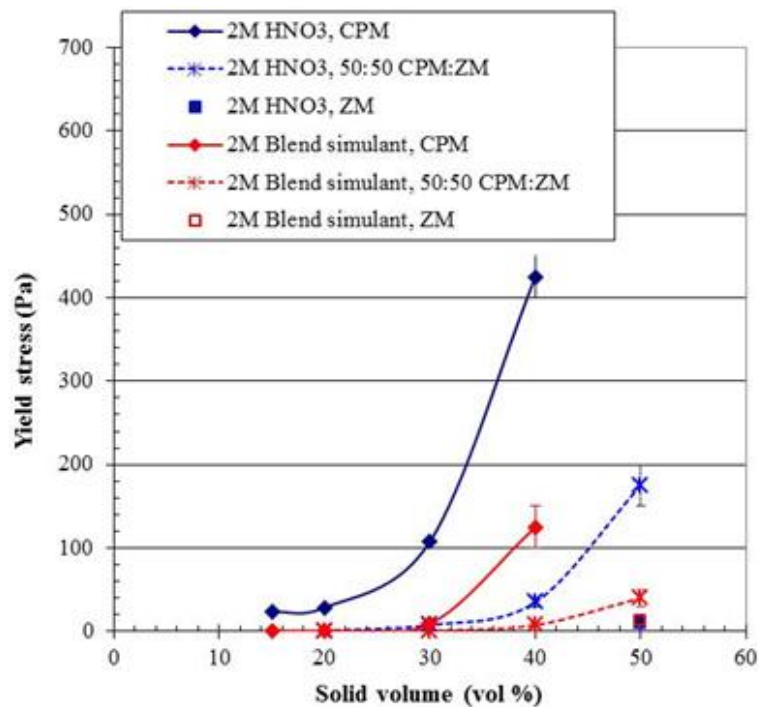


Figure 2-14 Yield stress vs. solid volume for samples of caesium phosphomolybdate (CPM), zirconium molybdate (ZM) and the mixed system (Dunnnett et al., 2016).

Given the complexity of CPM and ZM dispersion behaviour, there is a critical need to study their formation, characteristics and behaviour under a range of conditions. For example, there is no current information on the kinetics of CPM formation, or what impact storage temperature changes may have on growth rates and final morphology. Also, the main route for formation of ZM in nuclear operations is from metal substitution reactions with precipitated CPM, in the current holding tanks. While it is known that these conversion reactions are very slow kinetically (Paul et al., 2015), exact time scales for ZM precipitation by this route are not known, although it has been reported that an increase in temperature and an decrease in acidity promotes the conversion (Bradley et

al., 2004). Different wash reagents for both compounds have also been investigated with a suggestion that doping could be used to change the morphology of ZM, which has potential to be advantageous for transport or separation, depending on properties, such as sedimentation rate (Jiang et al., 2005, Edmondson et al., 2012). Consequently, a fuller understanding of the impact of ZM morphology on its dispersion behaviour is required, as the full consequence of varying morphology is unknown.

Additionally, it is crucial to understand the behaviour of the mixed systems, as the ratio of CPM:ZM within the HASTs is unknown. Currently, there is little understanding on the impact of dispersion behaviour mixed systems will have. In order to plan a successful POCO strategy, it is important to know the 'extremes' of potential behaviours that could be encountered to minimise unforeseen difficulties in handling and further processing of the HAL. Additionally, from the studies discussed in regards to both CPM and ZM, there is currently no published information on their permeability behaviour.

2.3 Fundamental Aspects of Colloidal Synthesis, Stability and Dewatering.

To comprehend the realistic conditions within the HASTs the precipitation behaviour of both CPM and ZM through an understanding of their stability and suspension properties are crucial. Additionally, in considering both future processing of both CPM and ZM in POCO and the potential requirement of a solid-liquid separation process, an understanding of both their compressive yield stress and permeability behaviour is required.

Furthermore, in considering the wider scientific community, the influence of particle properties such as surface charge, size and shape on sedimentation and permeability behaviour is of particular interest, to a number of different industries (Chong, 1979, Wiesner M et al., 1989, Liu and Joseph, 1993, Turney et al., 1995, Hlavacek and Remy, 1995, Waite et al., 1999, Channell et al., 2000, Pignon et al., 2000, Antelmi et al., 2001, Guan et al., 2001, Cabane et al., 2002, Hwang and Liu, 2002, Fan et al., 2004, Tomkins et al., 2005, Boskovic et al., 2005, Hakkinen A et al., 2005, Wakeman, 2007, Beck

et al., 2009, Lau and Chuah, 2013, Dogonchi et al., 2015, Bourcier et al., 2016, Perini et al., 2019)

2.3.1 Particle Stability

In order to understand the sedimentation behaviours of both CPM and ZM within a dispersion, a measure of their surface charge and therefore their stability is crucial. The surface charge of a particle cannot be directly measured. Therefore, zeta potential measurements are utilised in their place. In order to understand the relevance and importance of zeta potential measurements an understanding of basic colloidal theory is required.

The DLVO (Derjaguin, Landau, Verwey, and Overbeek) theory defines the simplest case of particle to particle interactions as a result of the balance between attractive van der Waals and repulsive electrostatic repulsions (Derjaguin and Landau, 1941, Verwey and Overbeek, 1948). The model only describes the most basic of systems and therefore fails against more complex systems. The DLVO theory bases the stability of a particle within a solution to be dependent on its total potential energy function V_T , see Equation (5).

$$V_T = V_A + V_R + V_S \quad (5)$$

Where, V_s is the potential energy due to solvent, V_A and V_R are the attractive (Van der Waals) and repulsive (electric double layer) contributions, respectfully. See Equations (6) and (7)

$$V_A = -A/(12\pi D^2) \quad (6)$$

$$V_R = 2\pi\epsilon\alpha\zeta^2 e^{(-kD)} \quad (7)$$

Where, A is the Hamaker constant, D is the particle separation, ϵ is the solvent permeability, α is the particle radius, ζ is zeta potential and k is a function of the ionic composition.

The potential energy of the solvent only contributes marginally to the total potential. Therefore, the DLVO theory essentially states that the stability of a

colloidal system is dependent upon the balance between the van der Waals and electric double layer, as a result of the Brownian motion of the particles. If two particles have significant repulsion an energy barrier will arise preventing them from approaching one another (Kaszuba et al. 2010). However, if the particles collide with enough energy the barrier can be overcome allowing the attractive forces to adhere them together. Essentially, if repulsive forces are more dominant than attractive forces, the colloidal system is said to be stable. Zeta potential is used to measure the stability of the systems in regards to the magnitude of the interactions between particles.

In addressing the surface chemistry of particles within a dispersion, fundamental parameters of the dispersed phase have to be considered, the interfacial chemistry and the actual extent of the interface (Fairhurst, 2013). Fine particles are largely unaffected by gravity, instead their particle to particle interactions and stability are governed by both attractive and repulsive inter-particle forces i.e. surface forces. The relevant surface forces to be discussed for this research are known as the van der Waals and the electrical double layer forces. The general factors that contribute to the behaviour of a dispersed system are: particle size and shape, surface properties, inter-particle interactions and particle-solvent interactions.

When a dispersion has a tendency to aggregate, this is as a result of van der Waals attractive forces between the particles. Van der Waals forces are also known as London or dispersion forces and are much weaker than chemical bonding (Hamaker, 1937). They exist as a result of the electrostatic attraction between temporary and induced dipoles formed due to movement of electrons (Bajd, 2006). Van der Waals forces can induce dipoles on surrounding molecules. Temporary dipoles are a result of electrons continuously moving so their exact location can never be certain, at a random point in time there could be an instantaneous, unpredictable 'pile-up' of electrons resulting in both electron-rich and electron-poor regions around the nucleus. Although this situation could exist for just 10^{-15} seconds it can polarise a neighbouring molecule, allowing their electron clouds to oscillate in sync with one another forming a net attractive force, i.e. van der Waals forces, as illustrated in Figure 2-15.

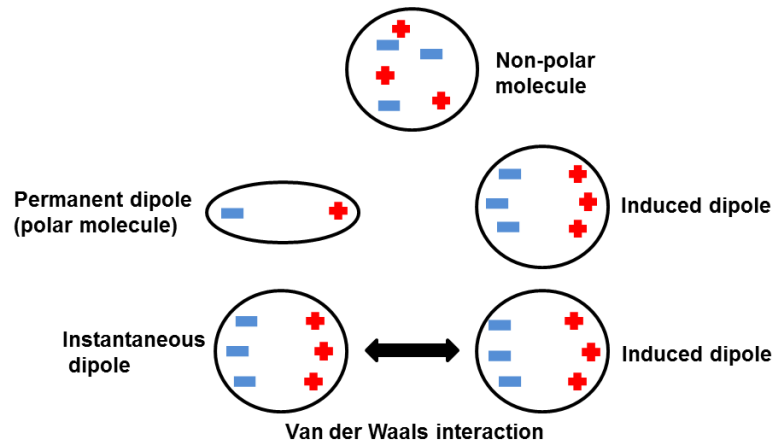


Figure 2-15 Illustration of permanent, induced and instantaneous dipoles

Equation (8), shows the Hamaker constant, A , which can be used to estimate the strength of the van der Waals interactions, where C is the attractive interaction strength and p is the number density of the molecules in the solid (Hamaker, 1937). When A is positive it represents an attractive interaction and when it is negative it represents a repulsive interaction.

$$A = \pi^2 C p_1 p_2 \quad (8)$$

As discussed the van der Waals forces provide an attractive force for particle interactions and for repulsive interactions the electric double layer theory can be applied. The double layer refers to two parallel layers of charge surrounding an object (Shaw, 1991). The first layer is referred to as the stern layer and comprises of ions of opposite charge to the surface charge of the object. The second layer is referred to as the diffuse layer which comprises of ions attracted to the surface charge through the coulomb force and electrically screens the stern layer (Shaw, 1991). It is termed the diffuse layer as it is made up of free ions that move under the influence of electric attraction, Figure 2-16 illustrates the diffuse double layer .

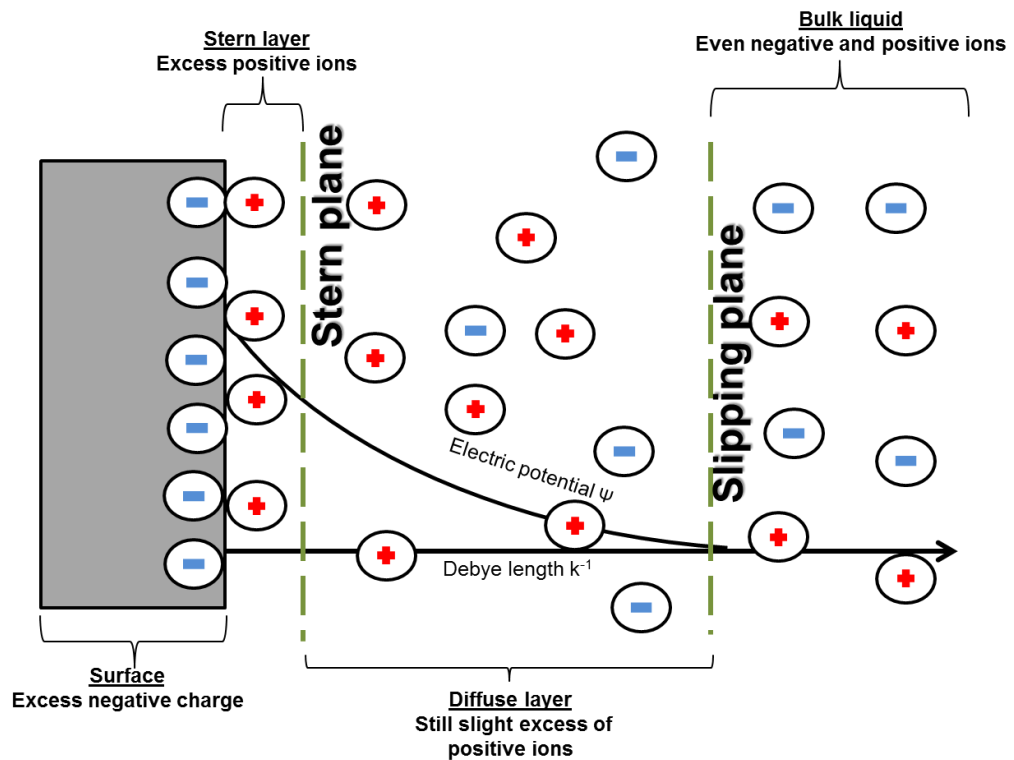


Figure 2-16 Illustration of the interfacial double layer

The thickness of the double layer is represented by the Debye length, k^{-1} , which is reciprocally proportional to the square root of the ion concentration, C , as seen in Equation (9).

$$k = 3.29 \sqrt{[C]} \quad (9)$$

The thickness of the layer will also be affected by an increase of the electrolyte concentration which will cause the layer to compress as there is an increase in counter-ions around the particle (Tindley, 2007). Within aqueous solutions, pH also has an impact on surface ionisation as low pH conditions promote positively charged surfaces, as a result of excess H^+ which can interact with the particles. Oppositely, high pH conditions promote negatively charged surfaces as a result of an increase in OH^- . When considering dispersions, the surface of each charged particle has sites available for oppositely charged counter ions. Consider that all charged particles in the solution have the electric double layer; therefore they are surrounded by a diffusive layer of counter ions which provides electrical stability. If particles have the same

charge a repulsive force (i.e. electrical double layer repulsive force) is felt as a result of the osmotic pressure gradient (Shaw, 1991).

It is extremely difficult to measure the surface charge/surface potential of a particle, therefore the zeta potential is often measured in its place. The zeta potential measures the particle charge and the immobile counter ions that surround it, approximately around the stern layer (Shaw, 1991). Zeta potential often serves as a measure of the stability of the colloidal system and is represented by symbol ζ , with units mV. Its magnitude whether positive or negative is proportional to the degree of repulsion between similarly charged particles (Shaw, 1991). A low value indicates attractive forces have overcome repulsive forces and aggregation may have occurred. A high value indicates the dispersion will resist aggregation with repulsive forces overcoming attractive forces, therefore indicating a stable colloid, see Table 1 for zeta potential stability ranges.

Table 1 Zeta potential values in relation to the stability of a colloidal system

Zeta potential (mV)	Stability
0 - ± 5	Aggregation
± 5 - ± 30	Instability
± 30 - ± 40	Moderate stability
± 40 - ± 60	Good stability
$> \pm 60$	Excellent stability

The isoelectric point (IEP) of a sample is the pH at which the particles have no net charge (although they still contain charge sites) and therefore when the zeta potential is equal to zero (Shaw, 1991). Particles attain a surface charge in water due to the polarisation effect of water with its permanent dipole. There are several factors that can affect the reliability of zeta potential including particle concentration, sedimentation behaviour and electrolyte concentration (Shaw, 1991). If a sample is too concentrated the viscosity of the solution will be affected therefore disrupting the mobility of the solution when an electrical field is applied. If a sample sediments rapidly or aggregates the zeta potential will vary significantly providing an unreliable reading. Increasing the electrolyte concentration will result in a compression of the zeta potential curve and

therefore a decrease in zeta potential, although the IEP shouldn't be affected. The general curve for zeta potential is expected to look similar to Figure 2-17.

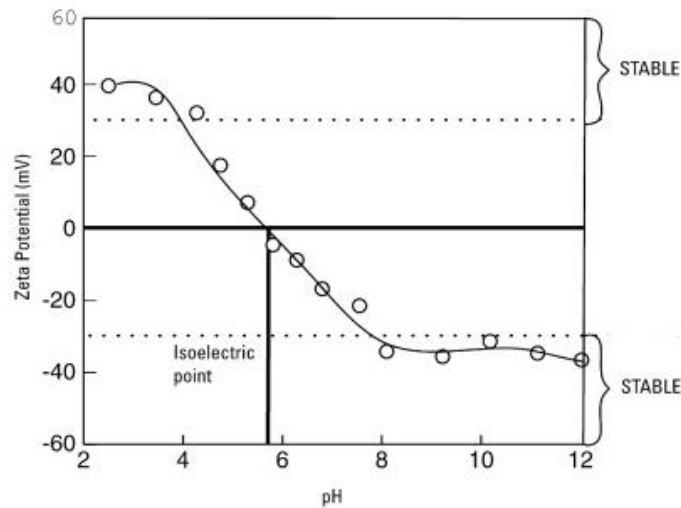


Figure 2-17 General zeta potential verse pH curve (Silver-Colloids.com, 2012)

Particles with zeta potentials more positive than +30 mV or more negative than -30 mV are considered stable, as shown in Table 1. This term stable refers to the particle's repulsive forces (generated from the electrical double layer) dominating. Once the zeta potential is within the unstable range, the particle's attractive forces (generated from the van der Waals forces) dominate, resulting in the particles aggregating. Figure 2-18, depicts a schematic of what is meant by the term stable and unstable, with the grey circles representing individual particles.

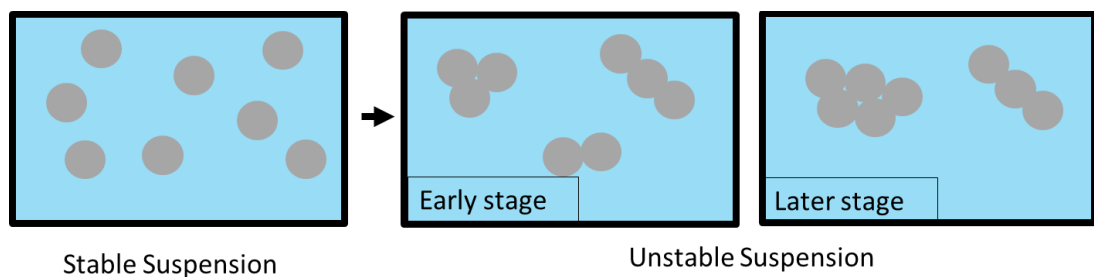


Figure 2-18 Schematic of both stable and unstable dispersions with the grey circles representing individual particles

As previously mentioned (Section 2.2) both CPM and ZM are reported to have low solubility in acidic conditions, which corresponds to their sedimentation behaviour within the HASTs (Zhang et al., 2013). Within Paul's (2014) thesis, there is a zeta potential curve for ZM, which can be seen in Figure 2-19. This shows the IEP for ZM to be around pH 4 and for it to increase in stability (>30

mV) as the pH decreases. One of the original aspects to this research will be producing a zeta potential curve for CPM. Additionally, a zeta potential curve for ZM will also be produced to compare to Paul's (2014), to see if the trend of stability at low pH is consistent. For this reason it is also beneficial to understand the natural equilibrium pH of both CPM and ZM.

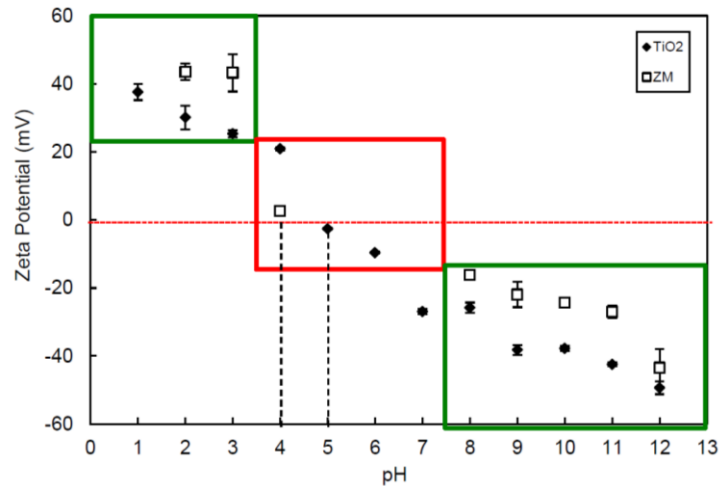


Figure 2-19 Zeta potential curve for zirconium molybdate (ZM) and titanium dioxide (TiO₂) (Paul, 2014)

2.3.2 Sedimentation

The settling behaviour of the HAL fission products, specifically CPM and ZM, is of great interest in direct relation to the current understanding of the conditions within the HASTs and in considering possible POCO strategies (Dunnett et al., 2016). If the products have a tendency to settle this could result in concentrated areas of radioactivity, referred to as hotspots, which could consequently damage the integrity of the tanks, resulting in a leak of radioactivity. Additionally, a settled bed would need to be eventually removed during POCO, therefore requiring re-suspension and/or washing out with a reagent. In either case an understanding of the dispersion stability of CPM and ZM in various pH environments would be beneficial in the planning of POCO strategy. For example, it may be more economically viable to use water as a re-suspension or washout reagent but if the fission products were to be unstable in this dispersion, it could potentially cause more issues longer term.

The term settling or sedimentation refers to the preference of particles within a system to settle out of a dispersion medium to form a solid bed. For particles to settle there must be an over ruling force acting upon them such as gravity,

centrifugal acceleration or electromagnetism. In order to understand sedimentation it is important to understand how particles move within a dispersion.

The random motion of particles within a fluid suspension as a result of collisions is referred to as Brownian motion (Einstein, 1956). As particles do not follow a set path or straight line their distance travelled cannot be calculated by simply knowing their initial and final positions. Therefore, other factors have to be considered such as temperature and particle size, in addition to diffusion of particles from high to low concentrated regions. Einstein was the first to define an equation for the mean square of displacement of a spherical particle in a given direction, x , as the result of Brownian motion, see Equation (10), where, k is the Boltzmann constant, T is the absolute temperature, μ is the fluid viscosity, α is the radius of the particle and t is time (Einstein, 1905, Einstein, 1956, Lemons and Gythiel, 1997).

$$\langle x^2 \rangle = \frac{kT}{3\pi\mu\alpha} t \quad (10)$$

In considering a perfectly spherical particle three forces are known to be acting upon it; gravitational force, F_g , buoyancy force, F_b , and drag force, F_d , as seen in Figure 2-20 (Clarke, 2009).

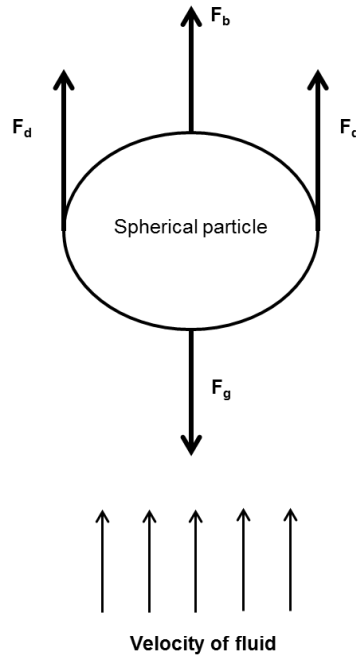


Figure 2-20 Forces acting on a spherical particle settling in a fluid

The gravitational force, F_g , is essentially the downwards pull of gravity, it is an attractive force and can be expressed several ways, see Equation (11). The expression shows that the mass of a body m , times its gravitational acceleration, g , is proportional to the gravitational force. In addition the force can also be expressed against the volume of liquid it displaces V , the density of the fluid ρ and the density of the particle ρ_p (Clarke, 2009).

$$F_g = mg = (\rho_p - \rho)gV \quad (11)$$

The buoyancy force, F_b , is an upwards force as a result of a pressure gradient and is parallel and opposite to the gravitational force. Equation (12), shows that the buoyancy force is proportional to gravitational acceleration, g , the volume of liquid it displaces V and the density of the fluid ρ (Clarke, 2009).

$$F_b = \rho gV \quad (12)$$

The drag force, F_d , is slightly more complicated and acts in a parallel direction to the particle's velocity. Equation (13) shows the

relationship between the F_d drag force, the drag coefficient C_D , area of particle A_p , density of the fluid ρ and settling velocity v_s^2 (Clarke, 2009).

$$F_d = \frac{C_D A_p \rho v_s^2}{2} \quad (13)$$

The drag coefficient is dependent on the Reynolds number, Re , which is a dimensionless quantity used to predict flow patterns (ref). The Reynolds number can be defined as can be seen in Equation (14) where ρ is the density of the fluid, u is the velocity of the fluid, d is the diameter of the sphere and μ is the viscosity of the fluid (Clarke, 2009).

$$Re = \frac{\rho u d}{\mu} \quad (14)$$

The relationship between the drag coefficient and the Reynolds number determines the flow of the fluid either turbulent or laminar. Laminar flow is considered to be ordered whereas turbulent flow is random.

Stokes' Law (Equation $\left[\frac{g(p_p - p_i) D^2}{18n} \right]$ (15)) is an expression that determines the settling velocity of a spherical particle by utilising its resisting drag force, the expression is valid for Reynolds number of less than 1 i.e. very small particles (Stokes, 1851, Miller, 1924). Where, V_s is the terminal settling velocity of the particle, g is the gravitational acceleration, p_p is the density of the setting particle, p_i is the density of the fluid, D is the diameter of the particle and n is the viscosity. Stokes' Law makes several assumptions such as: laminar flow, spherical particles, no temperature influence, homogenous material and that particles do not interact with one another.

$$V_s = \left[\frac{g(p_p - p_i) D^2}{18n} \right] \quad (15)$$

It is predicted that ZM would deviate from Stokes' law expected behaviour as a result of its non-spherical morphology (Macheder, 2011, Paul et al., 2013, Dunnett et al., 2016). For CPM despite its spherical shape, it is expected to

aggregate and therefore also deviate from Stokes' law expected behaviour (Paul et al., 2013).

When considering sedimentation, there are four regions that can be related to the settling velocity (or rate) of particles, these are illustrated in Figure 2-21 (Yang, 2003).

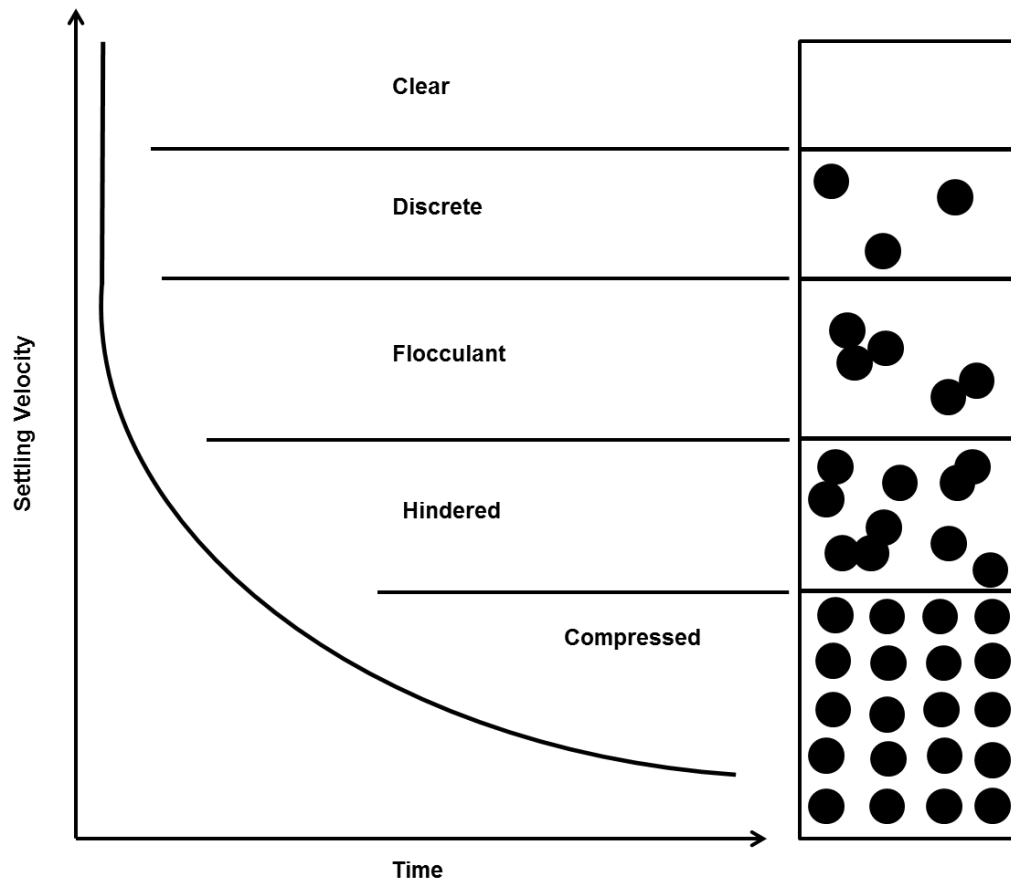


Figure 2-21 Illustration of the various potential settling regimes within a system dependent upon particle interactions with black spheres representing particles. Complete with settling velocity vs. time curve.

Discrete settling is when the particles within a dispersion act independently of one another, with no inter-particle forces; it is the simplest of the four regions, often a result of low concentrated solutions and can also be described as free settling (Yang, 2003). Flocculant settling is more dependent on the particle properties and how they interact, often governed by their tendencies to aggregate forming larger particles. In the hindered settling region the particles have a much stronger interaction with one another, dominating the behaviour of the region (Yang, 2003). This effect is increased at high concentration with the inter-particle forces restricting the movement of the particles, forcing some

to settle. The final region consists of compressive settling and has been much less studied; essentially it is the formation of a compressed bed (see Section 2.3.3).

As previously mentioned Stoke's Law provides a prediction of sedimentation rate for spherical particles in ideal conditions and relates to the 'free falling' of an individual particle (Stokes, 1851). Often systems are more complex than this and undergo hindered settling, which is expected for both CPM and ZM (Dunnett et al., 2016).

When hindered settling is predicted to occur there are a number of parameterised models that can be considered (Lester et al., 2005, Skinner et al., 2015, Usher et al., 2013) and other empirical settling models such as Vesilind (Vesilind, 1968), Steinour (Steinour, 1944), and Michaels and Bolger (Michaels and Bolger, 1962). The most widely used correlations are based on the Richardson and Zaki power-law relationship (Richardson and Zaki, 1954a). For the purpose of this research both the Vesilind model and the Richardson and Zaki power-law relationship are explored. For more information on the aforementioned models, refer to the relevant studies.

The Vesilind Equation (16), relates settling velocity, v_s to concentration, X , through the theoretical settling velocity, v_0 and settling parameter, k (Vesilind, 1968)

$$v_s = v_0 e^{-kX} \quad (16)$$

The Vesilind theory was developed to describe how the hindered settling tendency of a system negatively affects settling velocity. Both the theoretical settling velocity, v_0 and settling parameter, k , can be determined by using linear least-squares regression of $\log v_s$ against concentration X over a range of concentrations. This expression is typically applied to the study of sedimentation behaviour of sludges (Liu and Joseph, 1993, Stypka, 1998, Balbierz and Rucka, 2017, Bye and Dold, 1999, Stricker et al., 2007) including those relating to nuclear waste sludges (Johnson et al., 2016).

Richardson and Zaki investigated several materials with regards to sedimentation and liquid-solid fluidisation in which they devised

Equation, (17), which is still commonly used today for monodispersed particles in laminar flow (Richardson and Zaki, 1954a).

$$\frac{V}{V_s} = \varepsilon^n \quad (17)$$

The Richardson and Zaki equation relates V hindered settling velocity to the terminal settling velocity V_s , through the bed voidage and the Richardson-Zaki index, n . The model has been applied in several studies including those of non-spherical particles (Chong, 1979, Turney et al., 1995, Tomkins et al., 2005, Bargieł et al., 2013). Maude and Whitmore (Maude and Whitmore, 1958), considered the Richardson-Zaki index to be a function of particle shape, size and Reynolds number. They proposed a generalised equation of the Richardson-Zaki relationship (Equation (18)), where u is the settling rate, and ε , porosity. Therefore, linear settling rates $\ln(u)$ can be plotted to against the log of the porosity $\ln(1 - \Phi)$, to determine the n values.

$$\ln(u) = \ln u_0 + n \ln \varepsilon \quad (18)$$

When considering sedimentation, particle size, shape, density and strength of particle to particle interactions all have an influence. Many theories consider spherical particles, however often in industry different shaped non-spherical particles are found. The more a particle varies from a spherical shape the more factors such as orientation must be considered. When a sphere settles its orientation is irrelevant, for a non-spherical shape such as a rod shaped particle its orientation becomes more crucial. This is particularly prevalent when considering the varying cuboidal morphology of ZM.

Several studies have investigated the settling of non-spherical elongated particles, reporting that they will oscillate during their sedimentation, therefore settling with different orientations (Chong, 1979, Liu and Joseph, 1993, Turney et al., 1995, Fan et al., 2004, Tomkins et al., 2005, Lau and Chuah, 2013, Dogonchi et al., 2015). The most stable orientation of an elongated particle is said to be when it is horizontal and therefore perpendicular to the direction of flow (Fan et al., 2004, Lau and Chuah, 2013). Liu and Joseph (1993)

investigated the orientation of elongated cylindrical shapes, considering both their concentration and weight. They reported that in low concentrations the elongated particle will settle in its most stable orientation, increasing drag and therefore decreasing its settling rate. When concentration increases the particles start to settle vertically, therefore reducing drag and potentially increasing the settling rate. They also reported that in respect to weight, the heavier the cylindrical shape, the more likely they are to settle in the more stable horizontal position, demonstrated in Figure 2-22. This study highlights the various variables that need to be considered that can impact the orientation of elongated particles.

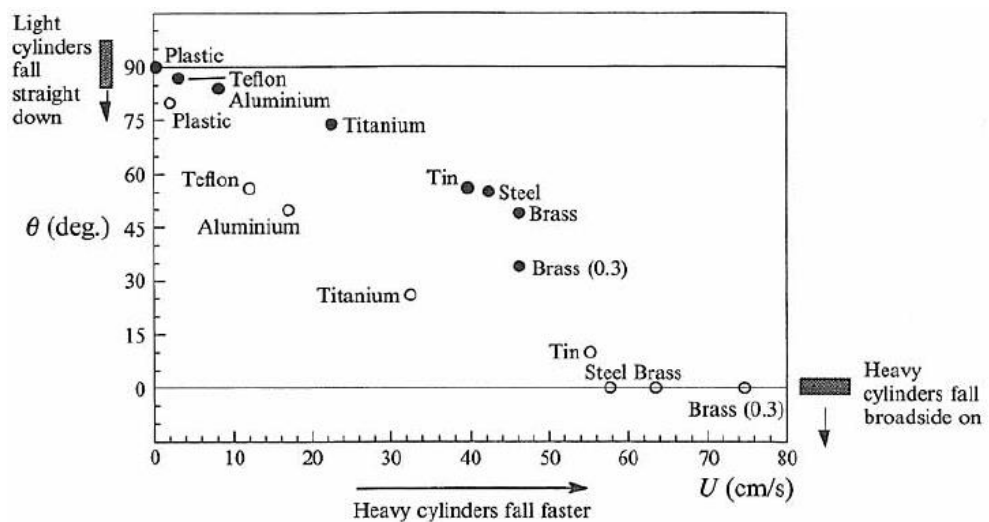


Figure 2-22 The effect of cylinder weight on the tilt angle (Liu and Joseph, 1993)

Even though Paul (2014) extensively studied CPM and ZM, the study only investigated them as individual systems (Paul, 2014). Only one study has been published looking at the settling properties of a combined mixed system of CPM and ZM (Dunnnett et al., 2016). This study only considered a 1:1 weight ratio mix and focused upon the amount of individual solid volume required to hinder settling. The lack of studies on mixed systems of CPM and ZM, highlights a gap in which this research can apply. Especially considering that the ratio of CPM:ZM within the HASTs is unknown, therefore a range of different mixed systems should be considered. In doing this a 'worst case' combination can be identified, therefore assisting in the extremes of POCO planning.

2.3.3 Compressive Yield Stress

The compressive yield stress of a material is 'an implicit function of the strength of the interparticle bridging forces' (Landman and White, 1994). Essentially, is it the maximum stress applied to a settled particle network, in which the network cannot be compressed (collapsed) any further. It is reported that for a range of systems, the compressive yield stress is independent of the compressive history of the material (Miller et al., 1996, Green and Boger, 1997). Therefore, the compressive yield stress can be determined via the application of a pressure or load onto the settled bed of a system.

There have been several methods developed in determining the compressive yield stress of a system, such as pressure filtration (Green and Boger, 1997, Green et al., 1998, Channell et al., 2000) and drying consolidation (Brown and Zukoski, 2003). The method chosen for this research was first developed by Buscall (Buscall, 1982) then developed with White (Buscall and White, 1987) utilising a multiple-step equilibrium sediment height technique via the application of centrifugal force. Both Miller et al. (1996) and Green and Boger (1997) did a comprehensive study into the various methodologies for determining compressive yield stress. Both studies concluded that each technique produces equivalent results, although Green and Boger (1997) reported centrifugation to be the easiest to implement. It was also reported that the compressive yield stress increases with the inverse square of particle size (Miller et al., 1996). The method utilised within this research is a multiple-step equilibrium sediment height technique via the application of centrifugal force published and detailed by Yow and Biggs (Yow and Biggs, 2013).

For a bed or particle network to be compressed, the bonds between the particles and/or aggregates must be broken and reformed (Channell et al., 2000). Therefore, the more force required to compress a network the stronger the interparticle forces are within a bed. In addition, the amount of bonds required to be broken within a network will have an effect on the compressive yield stress. Furthermore, the presence of aggregates is known to have an effect on the ability of the particle network to be compressed (Channell et al., 2000). Figure 2-23, shows a basic illustration of what is expected when a centrifugal force is applied and then increased on a settled sample for both stable and aggregated particles. This illustration demonstrates that a more

open network can often form when particles are strongly aggregated as they cannot be compressed further.

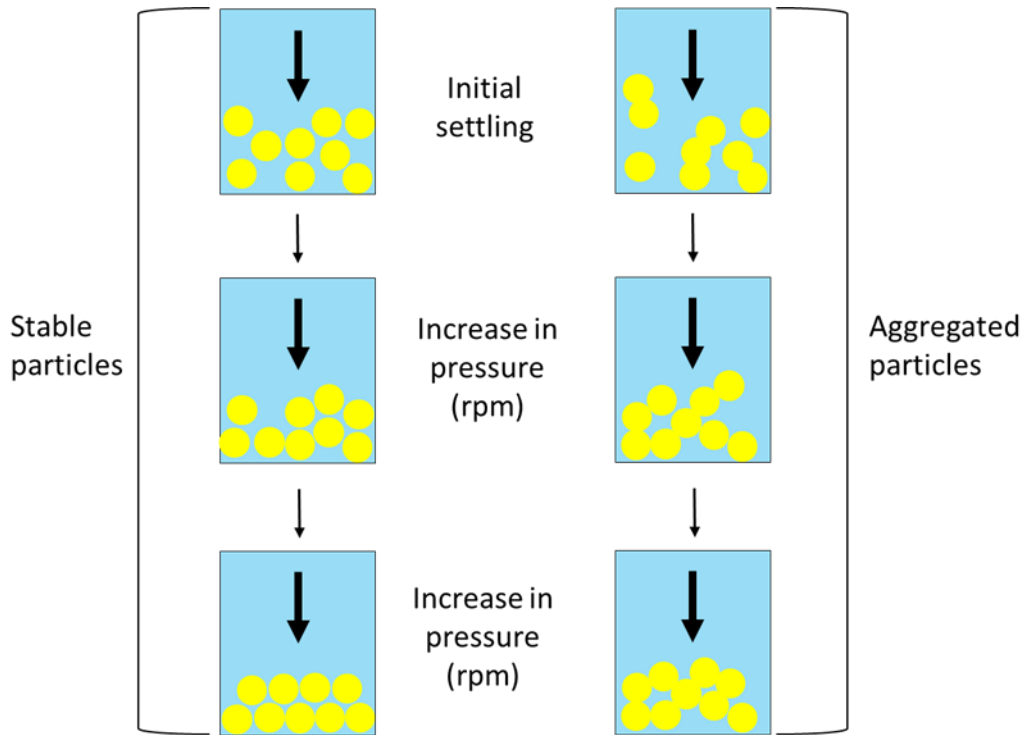


Figure 2-23 An illustration of what is expected when a centrifugal force is applied and then increased on a settled sample for both stable and aggregated particles.

A number of studies have looked into the compressibility of different clays, with the three most common being bentonite, illite and kaolinite (Mitchell, 1993). The compressibility of these clays is of particular interest as clays are often used in geoenvironmental practise to form waste containment barriers (Daniel, 1993). Therefore, an understanding of the effect of possible contaminants of their properties, specifically on their compressibility is of particular interest (Mitchell, 1960, Olson and Mesri, 1970, Sridharan and Rao, 1973, Moore C.A and Mitchell J.E, 1977, Chen et al., 2000, Angle and Gharib, 2017). It was found in these studies that the compressibility of kaolinite varied depending on the chemistry of the contaminant, contradicting the double layer theory. However, the reasoning behind this varied dependent on the study. Mitchell (1960) concluded that it was a result of large particle sizes with irregular surfaces, not collapsing parallel to one another. Other hypotheses were that the behaviour of the clay was controlled by mechanical factors (Olson and Mesri, 1970, Sridharan and Rao, 1973). Moore and Mitchell (1974) were however, one of the first to discuss the effects of van der Waals forces,

concluding that shear strength increased with attractive forces. Without the influence of contaminants kaolinite is said to settle with its clay platelets in a parallel fashion, as demonstrated by Figure 2-24 (Horpibulsuk et al., 2011).

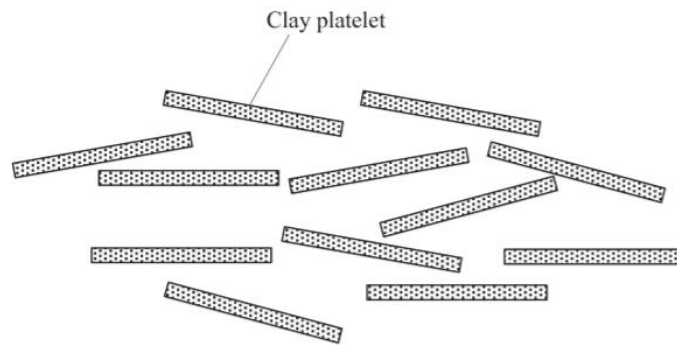


Figure 2-24 Illustration of kaolin clay platelets compressing parallel to one another (Horpibulsuk et al., 2011).

The stability and aggregation of a system has a significant effect on its compressive yield stress. Previously, aggregated alumina has been investigated as the behaviour of aggregated suspensions within a variety of industries can cause a number of issues (Channell et al., 2000). It was found that as the pH of the alumina system was increased, the interparticle potential becomes more attractive, forming aggregates and consequently becoming harder to compress, as shown in Figure 2-25. The study concluded that heterogeneities such as aggregates or large voids have a significant effect on the compressive yield stress of a system. Channell et al. (2000) also suggested that introducing heterogeneities by manipulating the system could be advantageous in regards to filtration.

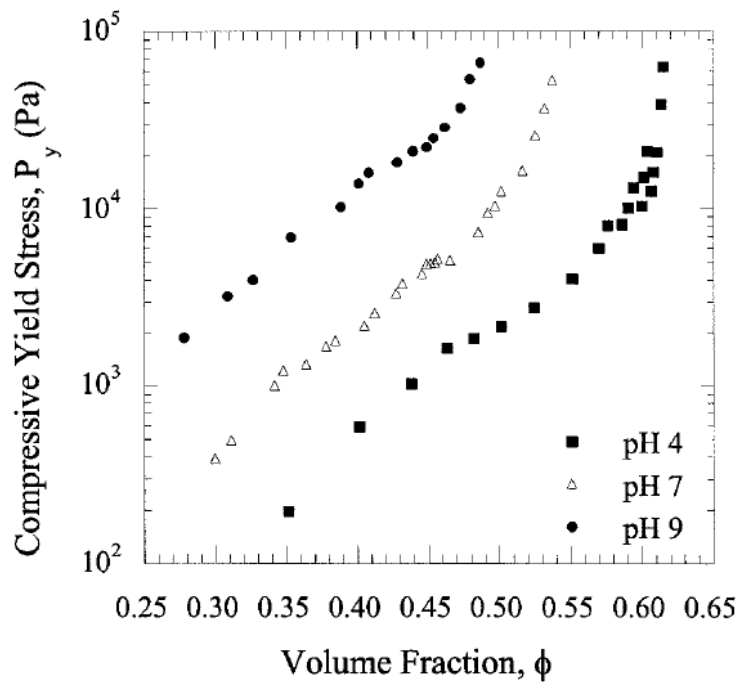


Figure 2-25 Effects of interparticle pair potential on the compressive yield stress of flocculated alumina suspensions (Channell et al., 2000).

2.3.4 Permeability

Solid-liquid separation techniques are utilised across a broad range of industries including; pharmaceuticals, oil and biotechnology. Permeability is effectively a measure of a dispersed material's ability to be filtered, consequently being separated into its corresponding solid and liquid components.

The filterability of both CPM and ZM are of direct interest in regards to the POCO planning of the HASTs and their subsequent handling in respects to further processing and vitrification. In general, if a solid is permeable it should be easy to filter, which could be a beneficial POCO technique applied to the HAL within the HASTs. This is in respect to the filtering of solid CPM and ZM from a potential wash out reagent to hypothetically separate the solid and liquid waste. The ultimate end disposal route for the CPM and ZM is vitrification (Section 2.1.3) before eventual geological disposal. Therefore all solids will need to be re-suspended in a suitable vitrification medium for this to occur (Dunnett et al., 2014). If the vitrification process isn't compatible with the POCO wash out reagent then filtration could be an option to separate the solids from the reagent pre-vitrification. Therefore, the study into the

permeability of CPM and ZM is a pro-active investigation, to gain an insight into whether this is a viable POCO option, as no previous studies have characterised this property.

Additionally, from a wider scientific perspective, the influence of particle properties on permeability is of interest, particularly to the fine chemical and pharmaceutical industries. Ideally, for an optimal filtration process the particles would be as large as possible, as near to spherical as possible, and have a monosize distribution (Wakeman, 2007). However, practically this optimum ideal is often not the case. In considering particle size, smaller particles are more likely to affect filter pores and consequently increase cake resistance (Tomas and Reichmann, 2002).

Particle size is said to have a larger effect on the permeability of a cake in comparison to particle shape, however the further a shape deviates from spherical the more impact on the resistance of the cake it has (Bourcier et al., 2016). Bourcier et al. (2016) investigated the permeability of a range of particle shapes with varying sizes including: spheres, cubes, platelets and needles, the results of which can be seen in Figure 2-26. These results were comparable to those found by Beck et al. (2009) in respect to spheroidal shapes particles displaying a higher resistance than both needle and polyhedral shaped particles.

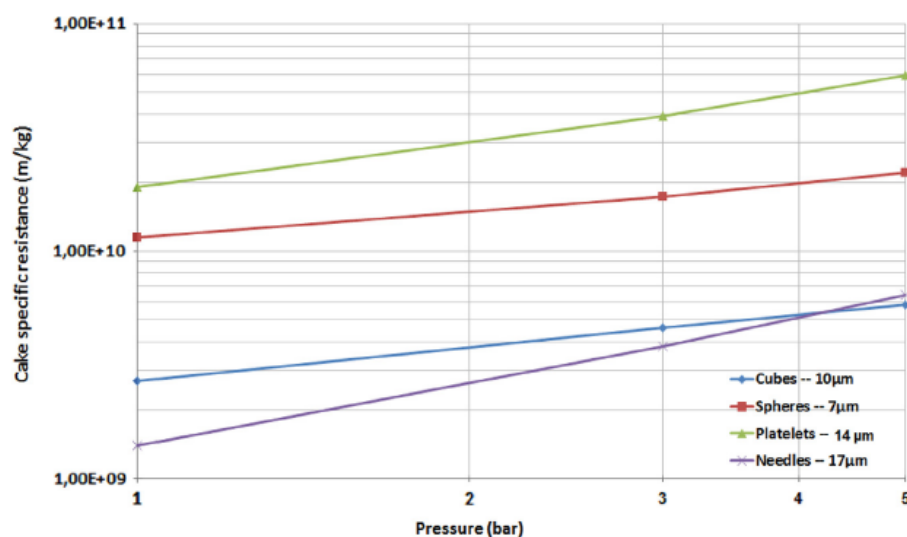


Figure 2-26 Cake specific resistance vs pressure for a range of particle shapes with varying sizes including: spheres, cubes, platelets and needles (Bourcier et al., 2016).

In considering the effect of particle shape on permeability there have been a number of studies that have investigated non-spherical particles (Boskovic et al., 2005, Hakkinen et al., 2005, Wakeman, 2007, Beck et al., 2009, Bourcier et al., 2016, Perini et al., 2019). Boskovic et al. (2005) investigated and compared the permeability of both spherical particles and cubic. They found that filtration efficiency is significantly different for cubic and spherical nanoparticles. Concluding that it was the nature of motion of the particles once settled on the filter medium that was the reason. Spherical particles could effectively roll or slide whereas cubes had a tendency to tumble.

Furthermore, a number of studies have investigated the impact of aggregated particles upon cake resistance (Wiesner et al., 1989, Hlavacek and Remy, 1995, Waite et al., 1999, Pignon et al., 2000, Antelmi et al., 2001, Guan et al., 2001, Cabane et al., 2002, Hwang and Liu, 2002). With the general consensus being that a more aggregated system will result in a more permeable system, due to increased particle size and the presence of more voids.

For the purpose of this research, permeability refers to the ease of the nuclear waste simulants to transmit a fluid through them when compressed as a solid bed. If a substance is referred to as highly permeable it essentially means it lets liquid pass through easily, if it is impermeable no fluid will be able to pass through. Porosity is closely linked to permeability, as it is a measure of the spaces in a material, whereas permeability is how close these spaces are linked. Darcy's law (Darcy, 1856) is typically used to calculate permeability, Equation (19), where ΔP is pressure loss, L is the bed depth, μ is the viscosity of the fluid, K is permeability of the bed and U_s is the velocity of the fluid flowing through the bed (Rushton et al., 1996).

$$-\frac{\Delta P}{L} = \frac{\mu}{K} U_s \quad (19)$$

As an alternative, cake (term used interchangeably with the solid bed) resistance, α , which is the inverse of permeability is often used, as shown in Equation (20) (Rushton et al., 1996). Where, ρ_s the density of the solid, ϵ is the porosity and k is again, the permeability. Typically, in a compressible cake, as the pressure is increased upon it, the

cake porosity decreases and therefore the cake resistance increases (Endo and Alonso, 2001).

$$\alpha = \frac{1}{k(1-\varepsilon)\rho_s} \quad (20)$$

There is a complex derivation and integration, Equation (21), that is formed from a combination of Equations (19)(19) and (20) of which there is the addition of the medium resistance, R_m . In addition, there is an assumption the pressure drop over the cake is the sum of the pressure drop over the cake and filter medium. Where V is the volume of liquid collected at time t , c is the mass of the dry cake per unit volume of filtrate and A is the filtering surface area. The derivation for this will not be discussed for this report, for more information see Rushton (1996). By plotting t/V vs V , a linear plot should occur where the slope is proportional to the average cake resistance and the intercept proportional to the medium resistance.

$$\frac{t}{V} = \frac{\mu c \alpha}{2A^2 \Delta P} V + \frac{\mu R_m}{A \Delta P} \quad (21)$$

The traditional way to determine permeability is a series of dead-end filtration tests (Lu et al., 1998, de Krester et al., 2001, Teoh et al., 2006). However, there are some practical restrictions with this method i.e. not good for small quantities, simultaneous analysis difficult and low pressure regions hard to measure (Loginov et al., 2014). For the HAL CPM and ZM simulants, dead-end filtration tests are not practical as the volume required for these tests is too high. Centrifugation is another alternative technique that has been commonly used, studied and modelled (Valleroy and Maloney, 1960, Green et al., 1996, Smiles, 1999, Chu and Lee, 2002, Barr and White, 2006, Usher et al., 2013, Fukuyama et al., 2013). Where three different approaches have been adopted;

- [1] Analysis of the height of the sediment; limitation due to applicability of chosen equations (Murase et al., 1989, Lee et al., 2003, Curvers et al., 2009, Loginov et al., 2012).

- [2] Analysis of the kinetics of centrifugal sedimentation-consolidation; complicated analysis due to creep phenomenon, sediment channelling and polydispersity of particles (Iritani et al., 1993, Iritani et al., 1994, Loginov et al., 2011, Loginov et al., 2012, Hwang et al., 2001).
- [3] Analysis of data of centrifugal filtration; simultaneous measurements of the filtrate volume, cake height and liquid height above the cake. Rarely used method due to rarity of specific centrifugal devices (Chu and Lee, 2002, Hwang et al., 2001, Hwang and Chou, 2006, Fukuyama et al., 2013).

Loginov et al. (2014) published a novel method of multistage centrifugation to determine filterability of various mineral suspensions (Loginov et al., 2014). Where their results were comparable to the traditional method of dead-end filtration tests. This methodology was developed upon for this research, with the assistance of Maksym Loginov to determine the permeability and therefore cake resistance for the HAL simulants; CPM and ZM.

Considering studies into the permeability of nuclear materials Féraud et al. (2013) published a novel test cell design that could be used within a glove box and therefore, with radioactive material (Feraud et al., 2013). Their new design allowed accurate pressure tracking in addition to measurement of the cake resistance. Further development of this system could be utilised in analysing potential samples of HAL, if there reaches a time where obtaining an active sample is possible. Bourcier et al. (2016) further utilised this test cell in investigating both the influence of particle size and shape properties on cake resistance and compressibility (Bourcier et al., 2016). Where it was concluded that cake filterability is impacted by both particle size and shape, therefore both need to be taken into consideration when considering the permeability of a material.

2.4 Conclusions

Through this literature review it has been demonstrated that further characterisation of the nuclear waste simulants CPM and ZM is crucial for future waste management strategies. Throughout Section 2.2 there were a number of studies discussed in regards to CPM and ZM, that have

characterised the simulants as individual systems. However, there has only been one investigation that considered them as a mixed system, although not in significant depth (Dunnett et al., 2016). It is a necessity to understand the suspension behaviour of CPM and ZM within a combined mixed system, as this is the most likely situation within the HASTs, therefore allowing for more realistic predictions of HAL behaviour.

Furthermore, there is little found in the way of the zeta potentials of both CPM and ZM, which could provide vital information on the stability of the simulants within different environments. Additionally, an understanding of their stability could help in predicting and explaining various suspension behaviours such as sedimentation and permeability. The sedimentation behaviour of the simulants is of great interest in considering the current understanding of the conditions within the HASTs i.e. if there is a settled bed of solids present. Moreover, if there were to be a settled bed, would it be easily re-suspended? Hence, there is a requirement to understand the compressive yield stress of the simulants.

The permeability of the nuclear waste simulants CPM and ZM has never before been investigated highlighting another gap within research that this project can address. Understanding their ability to be filtered could prove crucial in POCO planning of the HASTs and their subsequent handling in respects to further processing and vitrification. If the simulants are found to have a low permeability the option of filtration could be viable.

Overall, the more realistic an understanding of the current situation within the HASTs, the more streamline the POCO process will be, therefore decreasing cost and more importantly increasing safety.

**Chapter 3 Synthesis,
Kinetics and Property
Characterisation of
Caesium
Phosphomolybdate and
Zirconium molybdate**

3.1 Introduction

The Highly Active Liquor Evaporation and Storage (HALES) plant at Sellafield, UK, consolidates waste raffinates from the reprocessing of Spent Nuclear Fuel (SNF) through dissolution in nitric acid, before concentrating via evaporation (Edmondson et al., 2012). The waste Highly Active Liquor (HAL) is made up of several fission products, though this research focuses on two; caesium phosphomolybdate (CPM, $\text{Cs}_3\text{PMo}_{12}\text{O}_{40}\cdot x\text{H}_2\text{O}$) and zirconium molybdate (ZM, $[\text{ZrMo}_2\text{O}_7(\text{OH})_2]\cdot x\text{H}_2\text{O}$), which precipitate out during temporary storage within the HASTs before eventual vitrification (Dobson and Phillips, 2006). In order to aid behavioural understanding of these HAL precipitated dispersions, in the view of assisting with POCO planning and onward processing, characterisation is required on non-radioactive simulants.

Although there is not a substantial amount of studies directly investigating CPM, there are a number of analogues that have been studied, such as ammonium phosphomolybdate, which is a potential cation-exchange material for selective recovery of Cs (Krtil, 1960, Lento and Harjula, 1987). Indeed, CPM has also been synthesised itself for the same purpose, and as a photocatalyst for the photodegradation of dye pollutant (Bykhovskii et al., 2006, Bykhovskii et al., 2009, Bykhovskii et al., 2010, Ghalebi et al., 2016). The physical behaviour of CPM in nuclear waste HAL is of concern due to the presence of the radioactive isotopes ^{134}Cs and ^{137}Cs , which, if concentrated, could form potential hotspots within the HASTs (Edmondson et al., 2012). Paul et al. (2015) published a synthesis route to non-active CPM, in order to study its morphology in nuclear HAL systems, and this method was also used for this research.

There have been a number of studies that have focused upon ZM as a technetium-99m generator (Evans et al., 1987, Monroy-Guzmán et al., 2003, Monroy-Guzman, 2008, Monroy-Guzman et al., 2011), a precursor for the formation of the negative thermal expansion material ZrMo_2O_8 (Lind et al., 2001, Varga et al., 2005) and predominately for nuclear waste based studies (Rao et al., 1986, Rao et al., 1990, Izumida and Kawamura, 1990, Doucet et al., 2002, Magnaldo et al., 2004, Magnaldo et al., 2007, Usami et al., 2010, Vereshchagina et al., 2011, Xuegang et al., 2012, Zhang et al., 2013, Paul et

al., 2013, Paul et al., 2015, Paul et al., 2017, Arai et al., 2018). Within nuclear waste based studies ZM is the focus as a result of its mobility properties leading to potential problems with pipe blockages (Edmondson et al., 2012). Paul et al. (2015) published a synthesis method to ZM that was utilised in this research. In addition they described a method using the addition of citric acid to alter the crystal morphology, again this was utilised in this research.

A number of studies have focused upon both CPM and ZM, specifically relating to the issues they cause within the HASTs, the challenge they pose to the Waste Vitrification Plant (WVP) and the *in situ* conversion of CPM to ZM (Bradley et al., 2004, Paul et al., 2015, Dunnett et al., 2016). However, at present there have been no studies focusing on the kinetics of CPM formation and the impact of temperature. Additionally, the exact time scales for the *in situ* conversion of CPM to ZM is not known, although it has been reported that an increase in temperature and a decrease in acidity promote the conversion (Bradley et al., 2004).

Therefore, this Chapter presents the non-radioactive synthesis methodologies for these simulants, with an investigation into the kinetics of formation of CPM and tracking of the morphology of ZM. In addition to presenting a number of physical and chemical properties of the synthesised non-active CPM and ZM of various morphologies, some provided by the National Nuclear Laboratory (NNL) are also considered. Characterisation was both intended to confirm the identification of the simulants and provide information on certain properties which will assist in the analysis and discussion of results presented in future Chapters, 4 and 5.

3.2 Materials and Methodology

For ease of reading, a summary of the HAL simulants that have been characterised throughout this research is shown within Table 2, which details the samples, their origin, morphology and what they will be referred to throughout this thesis. The subsequent Sections 3.2.1 and 3.2.2 will elaborate further on the origin of these simulants.

Table 2 Detailing the simulants investigated during this research including, their origin, morphology and what they will be referred to throughout this thesis.

Sample	Origin	Morphology*	Notation
Caesium phosphomolybdate	Synthesised (Section 3.2.2.1)	Spheroidal	CPM
Zirconium molybdate	Synthesised (Section 3.2.2.2)	Cuboidal	ZM-1
Zirconium citramolybdate	Synthesised (Section 3.2.2.2)	Wheatsheaf	ZMCA-1
Zirconium molybdate	Provided (Section 3.2.1)	Cuboidal	ZM-2
Zirconium citramolybdate	Provided (Section 3.2.1)	Wheatsheaf	ZMCA-2

*morphology confirmed via SEM, Section 3.3.1

3.2.1 Materials

In order for the simulants to be characterised they first had to be synthesised, the methodology for this is discussed and depicted in Section 3.2.2. These nuclear waste analogues are costly to produce and do not yield a large volume of material (discussed Section 3.3.1) to allow for significant bulk characterisation. Consequently, this limitation of material volume dictated the choice of some of the experimental methods that were chosen for this research.

Additionally, the NNL provided two different non-radioactive ZM (ZM-2 and ZMCA-2) simulants, industrially synthesised by Johnson Matthey (Royston, UK) with differing morphologies that were also characterised alongside the ZM (ZM-1 and ZMCA-1) simulants that were synthesised for this project. The details of the precursors for the synthesis of the nuclear waste simulants (CPM, ZM-1 and ZMCA-1) are detailed in Table 3. Note that ZMCA refers to

zirconium citramolybdate, a term first published by Paul et al. (2015) in reference to the end product of a ZM synthesis route that incorporated citric acid. The exact conditions of the Johnson Matthey synthesis route were not provided, however it is known that the ZMCA-2 simulant was the product of a synthesis route incorporating citric acid, hence the notation.

Table 3 Stating the precursors used in the synthesis of caesium phosphomolybdate (CPM), zirconium molybdate (ZM-1) and zirconium citramolybdate (ZMCA-1), including their formula, purity and supplier.

Material	Formula	Purity	Supplier
Phosphomolybdic acid	$H_3PMO_{12}O_{40}$	Solid 80 %	Acros Organics
Caesium nitrate	$CsNO_3$	Solid 99.9%	Aldrich
Nitric acid	HNO_3	Solution 70%	Fisher Scientific
Zirconyl nitrate	$ZrO(NO_3)_2$	Solution 35 wt % in nitric acid	Sigma-Aldrich Co Ltd
Citric acid	$C_6H_8O_7$	Solid 99%	Fisher Scientific
Ammonium carbamate	$CH_6N_2O_2$	Solution 99%	Sigma-Aldrich Co Ltd

3.2.2 Simulant Synthesis

The synthesis of CPM, ZM-1 and ZMCA-1 were conducted in a 500 ml jacketed reaction vessel, which utilised silicon oil for heating, an over-head stirrer for agitation and a condenser under reflux for the cooling of any potential gaseous by-products. The vessel was fitted with an inlet for the precursor materials to be added and an outlet where the nuclear simulant products could be collected once synthesised. Figure 3-1 shows a schematic of this 500 ml jacketed reaction vessel set-up.

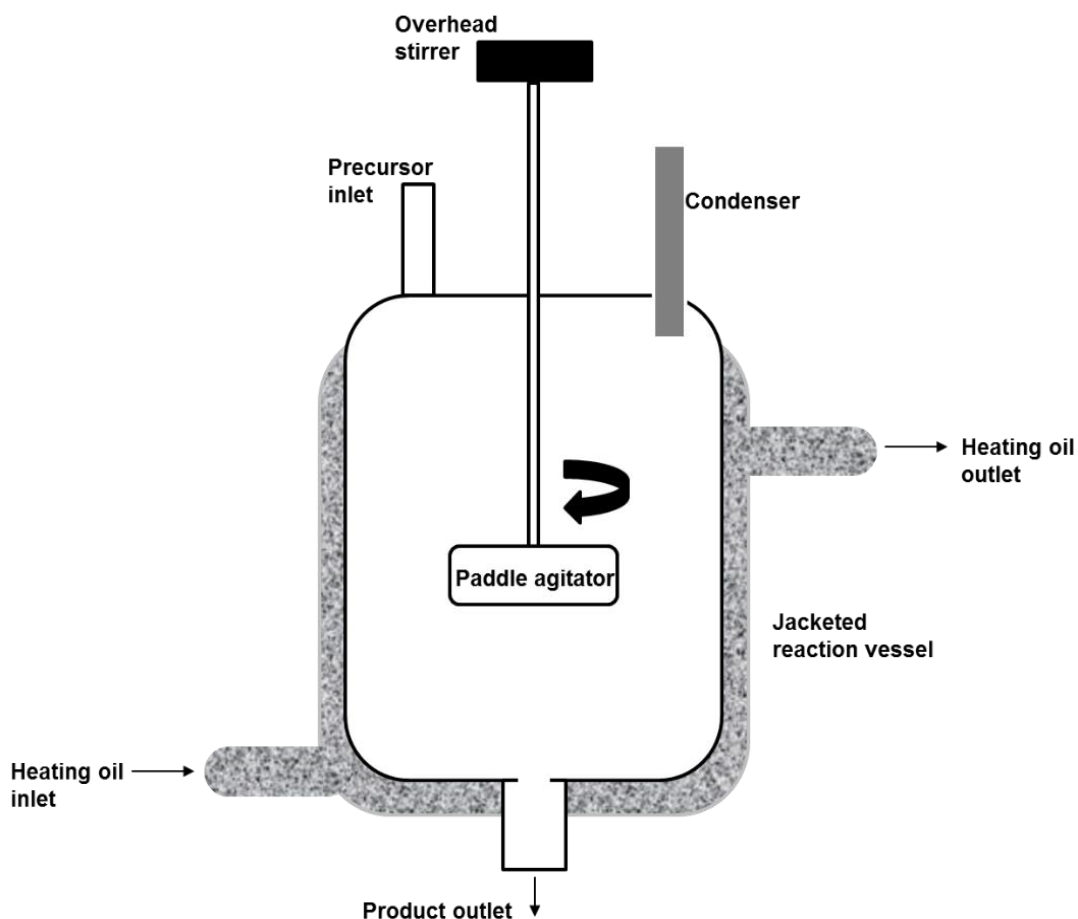
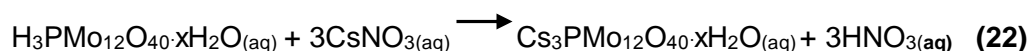


Figure 3-1 Schematic of the 500 ml jacketed reaction vessel, with overhead stirrer, precursor inlet, condenser, product outlet and heating oil set-up.

3.2.2.1 Caesium Phosphomolybdate

The synthesis of CPM involves a double replacement reaction with two reagents; phosphomolybdic acid ($\text{H}_3\text{PMo}_{12}\text{O}_{40}\cdot x\text{H}_2\text{O}$) and caesium nitrate (CsNO_3), as shown in Equation (22).



Separately, at a 1:3 molar ratio, equal volume solutions, 250 ml, of phosphomolybdic acid and caesium nitrate, were prepared by dispensing the solids independently into 2 M nitric acid solutions. These solutions were continuously stirred, separately at room temperature (25 °C) until all solids had fully dissolved, taking up to 1 h. The 250 ml caesium nitrate solution was then added to the empty 500 ml reaction vessel before being heated to 50 °C simultaneously being stirred at 100 rpm. When the temperature reached equilibrium the phosphomolybdic acid was added over a 1 h period at

approximately 4.5 ml/min. Once both solutions were within the vessel they were kept at 50 °C and stirred at 100 rpm for approximately 48 h. The methodology for this synthesis was originally established through an internally circulated document within the NNL, later published by Paul et al. (2015) and comparable to the work reported by Jiang et al. (2005) and Edmondson et al. (2012). During the 48 h reaction time, a yellow solid precipitated out which signified CPM had formed, Figure 3-2 shows this CPM solid.

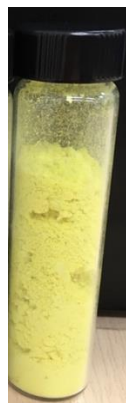
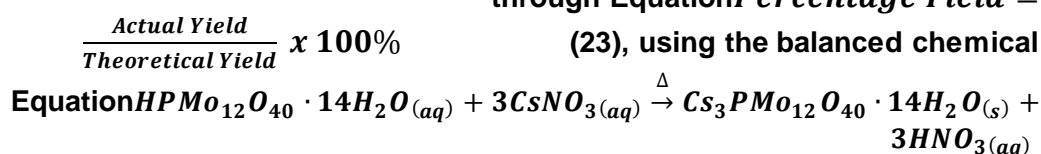


Figure 3-2 Photo of dry solid caesium phosphomolybdate (CPM).

In order to obtain the CPM solid the suspension was first drained through the product outlet before the solid was allowed to settle and the supernatant decanted, then the remnants of the supernatant were dried off with use of an oven set at 70 °C. The dry solid was then washed several times with Milli-Q water and dried again in an oven set at 70 °C. The final product was stored as a dry solid powder and used in characterisation experiments.

Additionally, the influence of temperature on the synthesis of CPM was investigated through the reaction being independently conducted at 25 °C and at 100 °C. The results of the synthesis at 100 °C are to be discussed in Chapter 4. For temperature investigations all other parameters were kept the same as the original synthesis method depicts.

The percentage yield for CPM synthesised at 50 °C was also calculated through Equation (23), using the balanced chemical



(1).

$$\textit{Percentage Yield} = \frac{\textit{Actual Yield}}{\textit{Theoretical Yield}} \times 100\% \quad (23)$$

In order to calculate the theoretical yield, the accurate mass of the reactants used in the synthesis; phosphomolybdic acid and caesium nitrate were recorded. Their respective equivalent in moles were then calculated by dividing the reactants mass by their molar mass. Stoichiometry was then used for each individual reactant to find the mass of product produced, where the limiting reactant was determined to be phosphomolybdic acid. The actual yield was taken to be the mass of the dry product, after washing and drying within the oven.

Reaction Kinetics Experiments

The reaction kinetics were investigated for the formation of CPM at both 25 °C and 50 °C, through the use of Ultraviolet-visible (UV-Vis) spectroscopy. In order to track the rate of the synthesis of CPM, a UV-Vis spectrophotometer (discussed in Section 3.2.3.3) was utilised in tracking the concentration of one of the reactants; phosphomolybdic acid (also the limiting reagent), as the other reactant, caesium nitrate, was found to not be significantly UV-Vis active. Before the synthesis was conducted, a calibration curve was generated for various diluted concentrations of phosphomolybdic acid versus their absorbance, taken at wavelength 458 nm. Once the synthesis had begun, regular 2 ml aliquots of the reaction solution were taken at varying time periods (~ every 20 min), which were then diluted by 100 within 2 M nitric acid. These aliquots were then centrifuged for 5 min at 2000 rpm in order to remove any CPM solid formed before the remaining supernatant underwent UV-Vis spectroscopy, a schematic of this experimental procedure is shown in Figure 3-3.

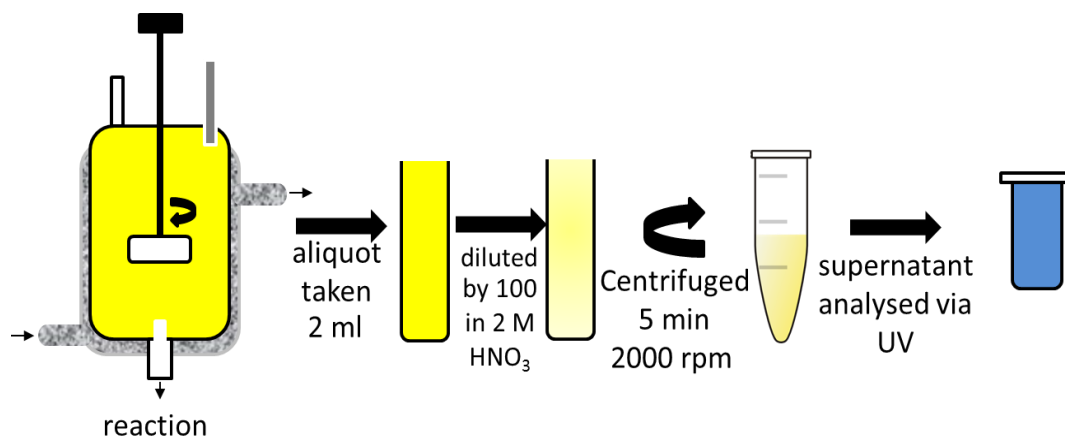
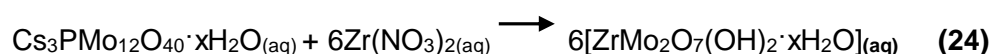


Figure 3-3 Schematic of the kinetics experiment procedure for the tracking of phosphomolybdic acid concentration in the synthesis of caesium phosphomolybdate (CPM).

The absorbance value of the supernatant at wavelength 458 nm was then compared to the calibration curve previously plotted for phosphomolybdic acid, to determine its concentration at that particular time. The corresponding concentrations were plotted against the time they were taken and the gradient taken of the plot in order to determine the rate constant.

3.2.2.2 Zirconium Molybdate

The conversion of CPM to ZM-1 also occurred in the 500 ml jacketed reaction vessel, shown in Figure 3-1. This synthesis method was also based on an internally circulated document within the NNL, later developed and published by Paul et al. (2015) and comparable to the work reported by Clearfield et al. (1972). A solution of zirconyl nitrate was dissolved in 6 M nitric acid, with a total volume of 250 ml, that was first conditioned by heating at 100 °C under reflux for 1 h, where the colour of the solution changed from milky white to transparent. This solution was then added at a 1:1 volume ratio to a 90 °C, 250 ml, stirring solution of CPM in 2 M nitric acid over 1 h at 15ml/5min and then left at this temperature for 2 weeks at 100 rpm. During this 2 week synthesis regular aliquots of the ZM-1 synthesis solution, were taken and dried for analysis to track the morphology change via SEM (discussed in Section 3.2.3.1). The reaction equation for the ZM-1 synthesis can be seen in Equation (24).



After the 2 week reaction time a white solid ZM-1 precipitated out, as shown in Figure 3-4.



Figure 3-4 Photo of dry solid zirconium molybdate (ZM-1).

In order to obtain the ZM-1, the suspension was first drained through the product outlet before the solid was allowed to settle and the supernatant decanted, then the remnants underwent an extensive washing procedure, first with 1 M ammonium carbamate, then with 2 M nitric acid and finally Milli-Q water before being oven dried at 70 °C and the ZM-1 solid powder used for analysis.

The same synthesis method for ZM-1 was repeated but with the addition of a 75 ml, 20 M citric acid solution being added to the CPM solution over 1 h at a rate of 6.25ml/5min once half of the zirconyl nitrate solution had been added. This method was published by Paul et al. (2015), with the intention of the ZM being formed having a different morphology to the original ZM-1. Paul et al. (2015) referred to this 'new' ZM as zirconium citramolybdate (ZMCA-1). Figure 3-5 shows an overview of the various synthesis routes discussed in this Section.

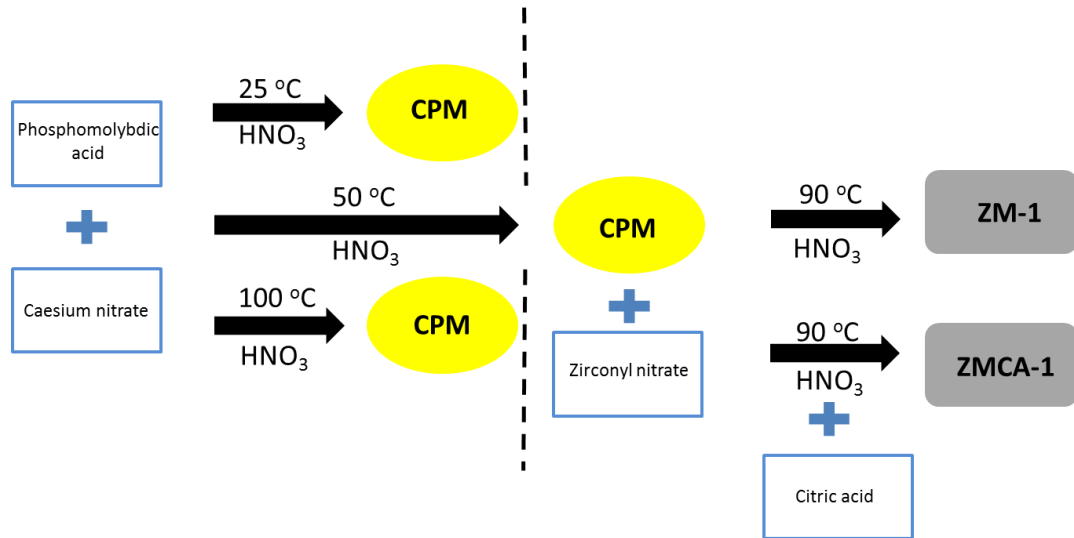


Figure 3-5 Summary of the various synthesis routes of Highly Active Liquor (HAL) simulants conducted for this research.

3.2.3 Characterisation Techniques and Methodologies

3.2.3.1 Scanning Electron Microscopy

Particle shape analysis was done through the use of both a SU8230 SEM (Hitachi, Krefeld, Germany) and a tabletop microscope TM3030Plus (Hitachi, Krefeld, Germany).

A SEM produces images via scanning a sample with a focused high-energy beam of electrons that can be utilised in obtaining information such as size and morphology of particles. The electrons are produced via a hot cathode source, for the Hitachi this is a tungsten filament, which when heated forms an electron cloud. The electrons are then directed through the use of oppositely charged plates and a series of electromagnetic lenses forming an incident beam composed of highly energised electrons. These electrons scan and interact with the sample producing characteristic x-rays in addition to secondary and backscattered electrons, which are detected and used to form an image of the sample. The secondary electrons are weak energy electrons formed when the incident beam knocks out an electron from the inner shell of an atom, referred to as inelastic scattering. A backscattered electron occurs when the incident beam collides with a nucleus of a sample atom and bounces back out, referred to as elastic scattering. Images taken of simulants for this research were from detected secondary electrons. Figure 3-6, shows a schematic of an SEM set-up.

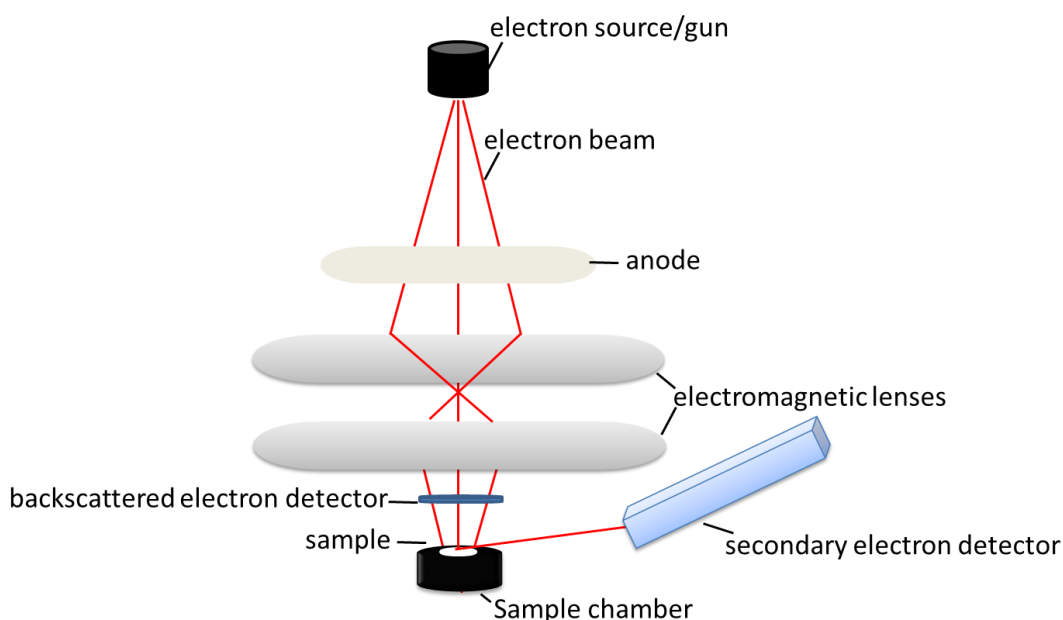


Figure 3-6 Schematic of the inner workings of an Scanning Electron Microscope (SEM).

The samples were prepared using a carbon based adhesive disk in which the dry ground up solid samples were placed. For the SU8230 SEM these samples were then platinum coated, for the tabletop microscope TM3030Plus they were left as they were. The SU8230 provided a higher resolution image as it has nearly 10 fold the magnification capability of the TM3030Plus. Therefore, the TM3030Plus was generally used as a quick check of the particle shapes before they were imaged accurately on the SU8230. Additionally, the TM3030Plus was used to analyse the aliquots taken during the ZM-1 synthesis, as it was easy to access for short time frames.

3.2.3.2 Particle Density

The density of the simulants is of importance to know as the values were used to calculate weight percentage concentrations and in some applied analysis equations. A AccuPycTM 1330 Pycnometer (micromeritics, Norcross, GA USA) was used to make these measurements, which utilises the pressure change of helium in a known calibrated volume to determine the density. In terms of sample preparation, first an empty sample cup is weighed, before the dry solid sample is placed within it, packing the cup at least two-thirds full.

Both the sample cup and the sample were then allowed to dry in an oven at 70 °C for ~ 4 h. The weight of the dry solid is then determined by subtracting the weight of the empty sample cup from the full. Once the sample cup and sample are placed within the pycnometer, the volume of the sample can be determined via displacement and hence the density can be calculated. Figure 3-7 shows a schematic of the principles of the AccuPyc™ 1330 Pycnometer.

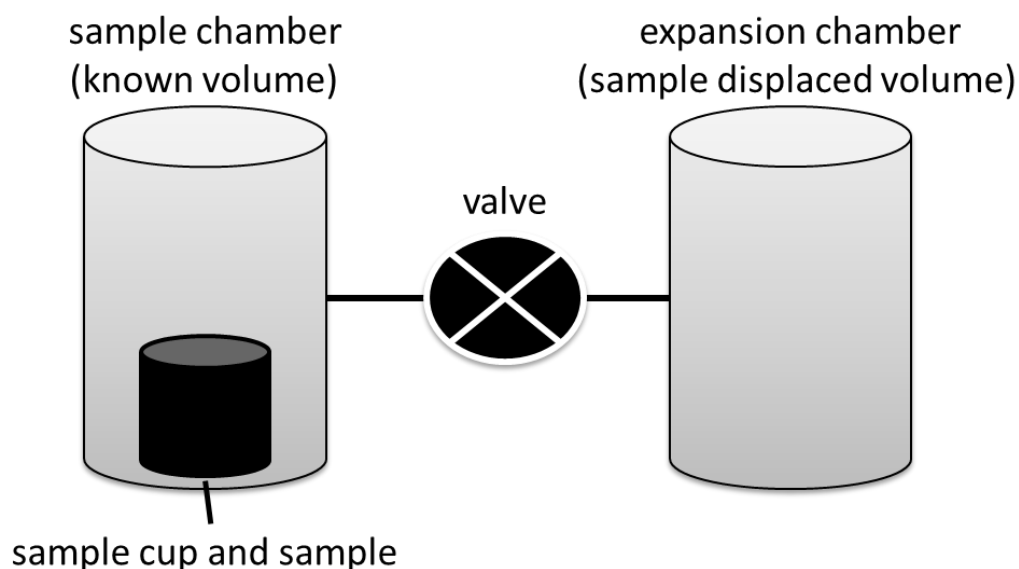


Figure 3-7 Schematic of the principle inner workings of an AccuPyc™ 1330 Pycnometer.

3.2.3.3 Ultraviolet Spectroscopy

In order to determine the kinetics of the synthesis of CPM, a UV-Vis spectrophotometer PE Lambda XLS (PerkinElmer, Waltham, UK) was utilised. The spectrophotometer was used to determine the concentration of phosphomolybdic acid.

A UV-Vis spectrophotometer utilises the UV-visible spectral region, with the UV region of light scanned being typically from 200 to 400 nm wavelengths, and the visible light from 400 to 800 nm. The instrument houses a UV-visible light source which releases a beam of light that is separated into its component wavelengths by a monochromator, in this case a prism. Each monochromatic beam in turn is split into two equal intensity beams by a half-mirrored device. One beam then passes through a cuvette containing a solution of the diluted sample. The other beam, passes through an identical cuvette containing only

the solvent, in this experiment 2 M nitric acid, which is referred to as the blank or reference. Figure 3-8 shows a schematic of a UV-Vis spectrophotometer.

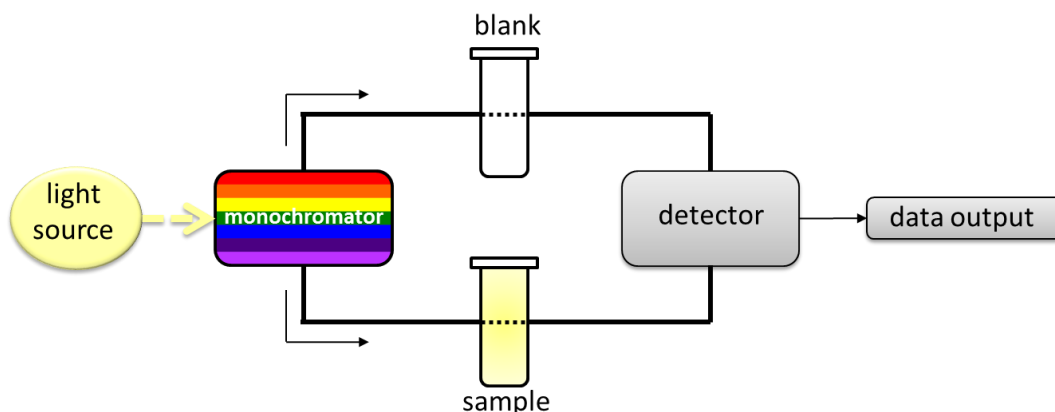


Figure 3-8 Schematic of the principles of an Ultraviolet-Visible (UV-Vis) spectrophotometer.

The intensity of light passing through the sample is then compared to the intensity of light passing through the blank. The ratio of these intensities is called the transmittance, usually expressed as a percentage, which can be easily converted to absorbance, A . The theory behind this is known as the Beer Lambert-Law, shown in Equation (25), where I_0 and I are the intensities of the blank and the sample respectively, ϵ is the molar absorption coefficient of the sample for a certain wavelength, L is the path length through the cuvette and c is the concentration of the sample.

$$\log \frac{I_0}{I} = \epsilon L C = A \quad (25)$$

Prior to the synthesis experiment being conducted a calibration curve was determined for the concentration of phosphomolybdic acid vs. absorbance. For this a phosphomolybdic acid solution was made up in 2 M nitric acid at the same starting concentration it would be for the CPM synthesis (Section 3.2.2.1). This concentration was then diluted by 100 with 2 M nitric acid, to avoid overloading the spectrometer detector. The absorbance was then recorded for this maximum concentration of phosphomolybdic acid, in addition to various percentage dilutions of this 'maximum' concentration (80, 60, 40, 20, 10%) also being recorded. From this data a calibration curve was plotted with an R^2 value of 0.98 and this can be seen in Figure 3-9.

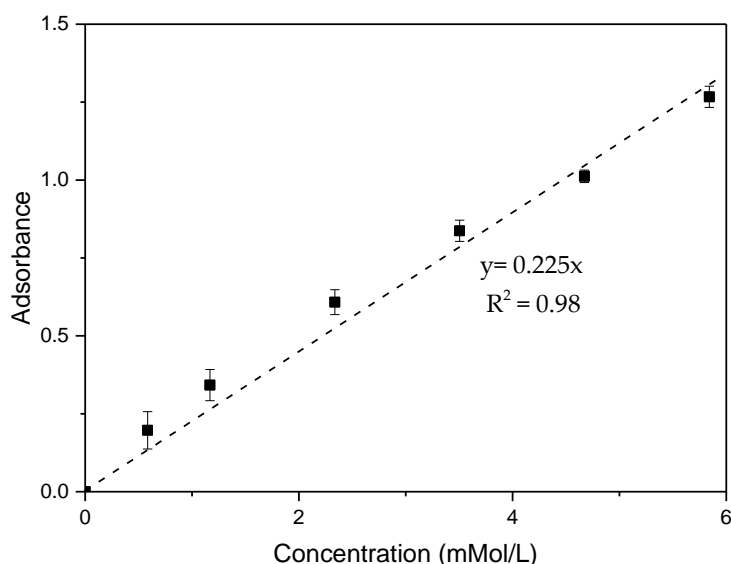


Figure 3-9 Calibration curve of the ultraviolet-visible (UV-Vis) absorbance values of phosphomolybdic acid at various concentrations, taken at wavelength 458 nm. Complete with line of best fit equation, error bars and an R^2 value of 0.98.

Once the calibration curve was plotted the aliquots of the CPM synthesis could be analysed, following the procedure discussed in Section 3.2.2.1. The concentration of the phosphomolybdic acid within that aliquot could then be determined and then plotted against the time it was taken to evaluate the kinetics of the CPM synthesis at both 25 °C and 50 °C. It should be noted that aliquots were analysed in triplicate (with an average standard deviation of 3% of the mean value) where an average of the results is reported. Standard deviation was calculated using the equation displayed in Appendix Fig. 3.

3.2.3.4 Powder X-ray Diffraction

A D8 x-ray diffraction analyser (Bruker, Coventry, UK) was used to analyse the crystalline structure of the samples, for both identification and comparative purposes of the simulants.

The majority of materials have an XRD pattern which is characteristic of their structure, essentially a fingerprint that can be utilised to identify a compound. The XRD technique utilises x-rays that are directed onto a solid powder which are then scattered via the lattice planes of the crystals which results in a diffraction plot where intensity is plotted against 2θ , the angle of the detector.

Once the diffraction pattern has been obtained it can be identified via comparison to The International Centre for Diffraction Data (ICDD) online database, if no match is found the pattern can be indexed and details of its lattice parameters determined. The diffraction pattern can also provide evidence of impurities, which are usually excess unreacted precursors. The x-rays are produced through the bombardment of a metal with electrons, in the case of the Bruker D8, copper is the metal used with an electron beam of 40 keV. The electrons are produced from a hot filament made of tungsten, similarly to an SEM electron source (Section 3.2.3.1). The copper source ($\text{Cu K}\alpha$) has a wavelength of 1.54 \AA , the energy of the radiation source is 1.6kW, and measurements were taken over the 2θ range $10\text{-}60^\circ$ with a step size of $0.032^\circ 2\theta$ and a scan speed of 0.2 s per step. An overall diffraction pattern is formed by the scattering of the bombarding x-rays (incident beam) off various layers of atoms within the solid and detecting the diffracted beam, shown in Figure 3-10.

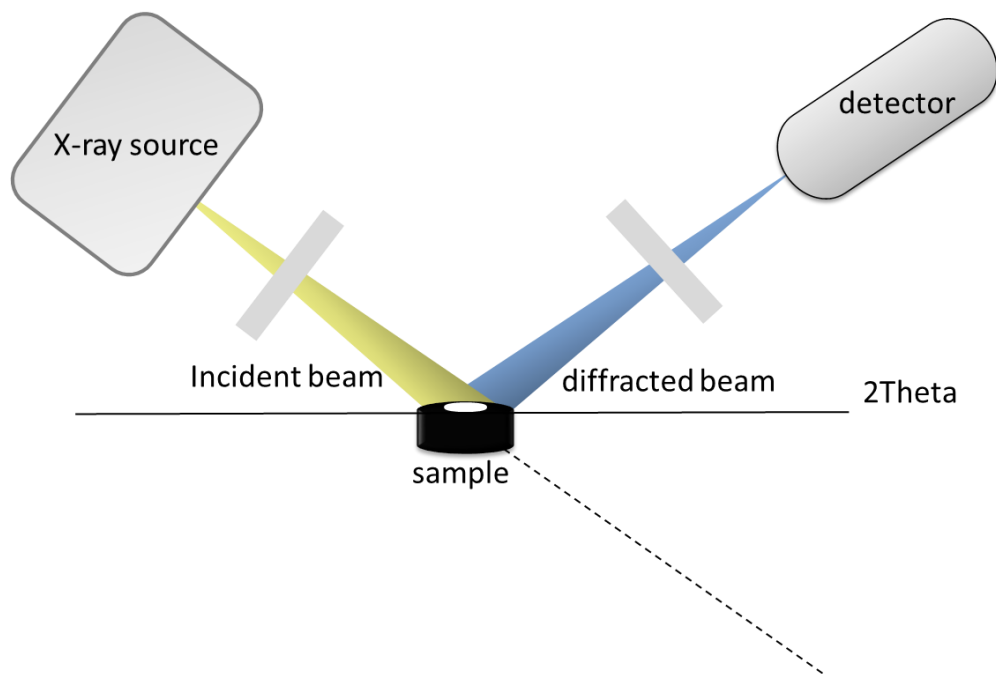


Figure 3-10 Schematic of the workings of an x-ray diffraction (XRD) analyser.

For the diffraction to occur the spacing between the atom layers must be close to the wavelength of the radiation utilised and the sample must be crystalline. When a peak occurs in the pattern it is representative of constructive interference i.e. two layers are in phase and will obey Bragg's Law Equation

(26), where, θ is the angle of incidence of the x-ray, n is an integer, λ is the wavelength, and d is the spacing between atom layers.

$$n\lambda = 2d\sin\theta \quad (26)$$

The samples were prepared by approximately 1 g of powder being tightly packed into a sample mount. The raw data for the diffraction pattern was then extracted before comparison to the ICDD online database.

3.2.3.5 Infrared Spectroscopy

The functional groups of the simulants were identified through Fourier Transform Infrared (FTIR) spectroscopy carried out using a Thermo iS10 (ThermoFisher, Waltham, UK) with a ZnSe ATR attachment, at a resolution of 4 cm^{-1} and 64 scans.

Infrared (IR) spectroscopy utilises the IR region of the electromagnetic spectrum similar to how UV-Vis spectroscopy (Section 3.2.3.3) utilises the UV and visible light regions. Essentially the IR instrument utilises light of multiple frequencies to shine at the sample to determine how much is absorbed, it does this using an IR light source, a beam splitter and both a fixed and moving mirror, shown in Figure 3-11. The detector can then formulate the results to work out the absorption at each wavelength. The peaks or troughs in the spectrum are indicative of functional groups of the compound, essentially allowing identification of the compound like a fingerprint. Resulting in an IR spectrum which is principally a graph showing IR light absorbance vs frequency.

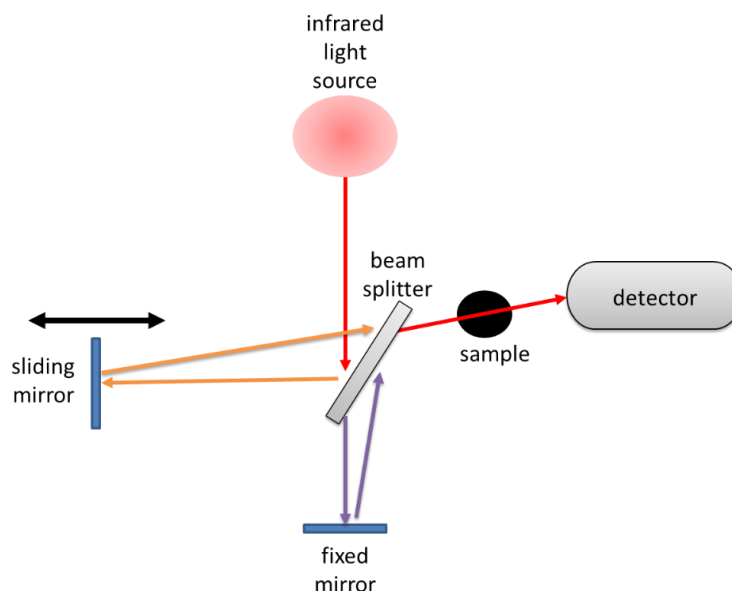


Figure 3-11 Schematic of the principles of Fourier Transform Infrared spectroscopy (FTIR).

Dry power samples were placed upon the sample holder before being clamped into place and the IR spectroscopy conducted.

3.2.3.6 Thermogravimetric Analysis

Thermal dehydration of the simulants, used to determine the amount of bound water was measured via thermogravimetric analysis (TGA), using a TGA/DSC 1100 LF (Mettler Toledo, Leicester, UK).

A TGA works by tracking the mass change of a sample over time with controlled temperature variations. Mass change at certain temperatures (usually < 400 °C) can be equated to the loss of loosely bound water molecules. In order to conduct the experiment a crucible, the material of which is dependent on the temperature profile used, is filled with a sample and is placed into the TGA on a precision balance along with an empty identical reference crucible. The crucibles are then heated within a furnace, during the experiment thermocouples underneath the crucibles monitor their temperature. The mass of the sample is continuously monitored throughout, with an inert purge gas flowing over the sample controlling the environment. Figure 3-12 shows a schematic of a TGA set-up.

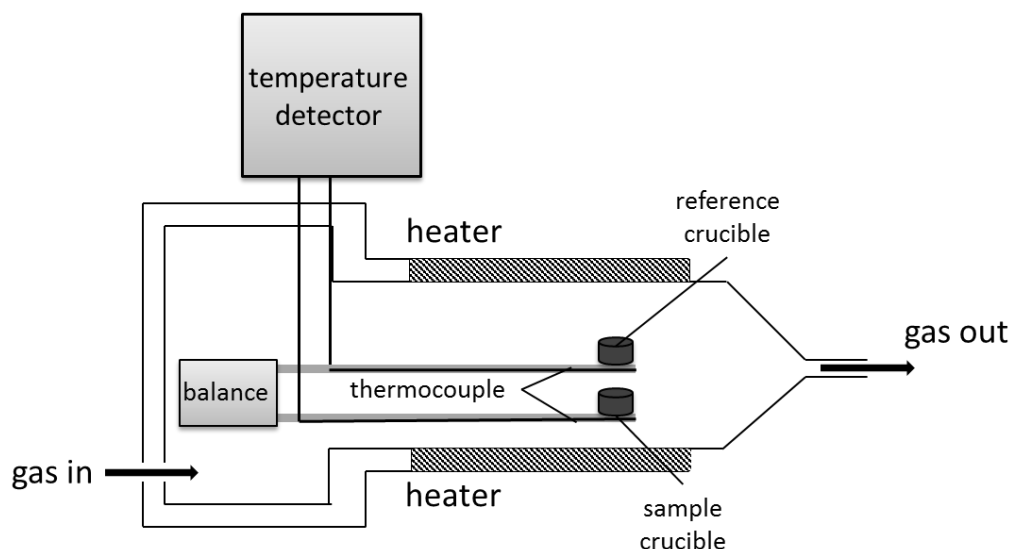


Figure 3-12 Schematic of a thermogravimetric analysis (TGA) set-up.

For each experiment, a 0.1 g sample was packed into an alumina crucible and heated using a temperature profile from 30 °C to 400 °C at a heating rate of 10 °C·min⁻¹ under a nitrogen gas atmosphere. Where the temperature profile is determined to be reproducible to within +/- 1 °C, established from multiple (triplicate) runs.

3.3 Results and Discussion

3.3.1 Synthesis, Morphology and Reaction Kinetics

The SEM images in Figure 3-13 present images, at various magnifications of CPM, which was synthesised at 50 °C in the 500 ml jacketed reaction vessel for 48 h. These images for are in agreement with those previously published with CPM exhibiting a spheroidal shape (Paul et al., 2015, Ghalebi et al., 2016, Dunnett et al., 2016). Image a) (Figure 3-13) shows clearly that the particles are not uniform in size even though they are comparable in their spheroidal morphology. The primary particle size visually observed from these images is ~300 nm with a range of larger agglomerates having sizes of up to ~2 µm. Image b) (Figure 3-13) shows a higher magnification image of the range of particles sizes. These spheroidal particles seem to be polycrystalline and consist of agglomerated nanoclusters. Images c) and d) (Figure 3-13) provide

a higher magnification of one of the individual spheroidal particles, where these nanoclusters can be seen on the roughened surface of a CPM particle.

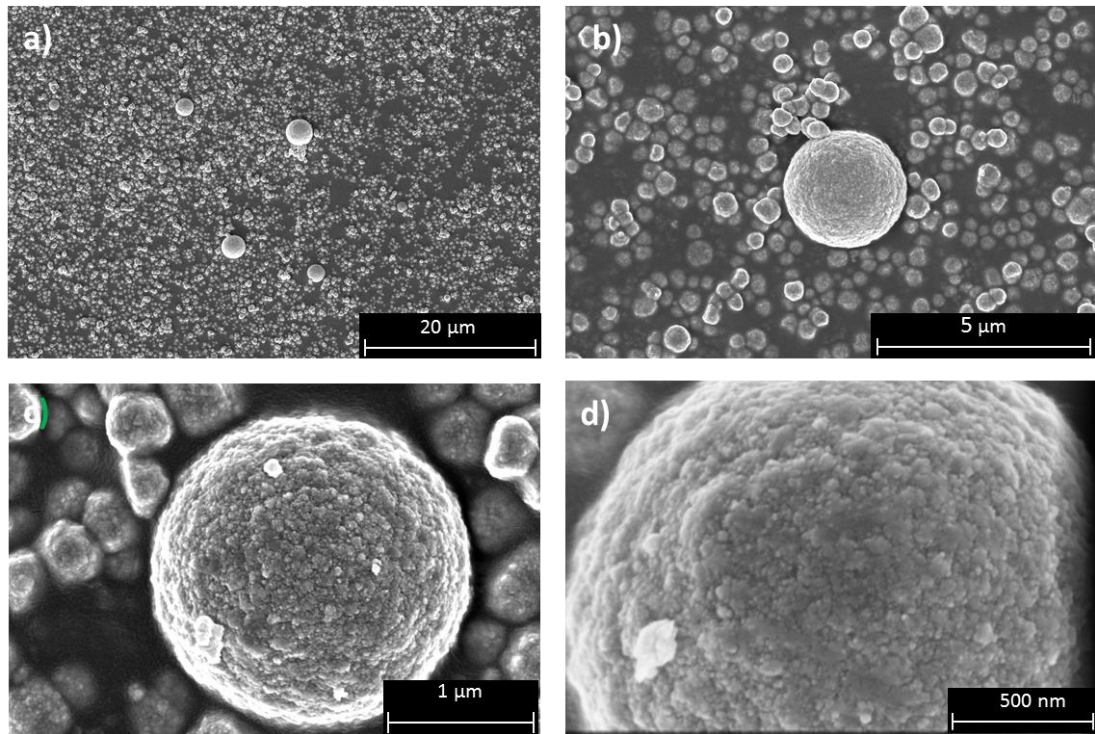


Figure 3-13 Scanning electron micrograph (SEM) images of caesium phosphomolybdate particles (CPM), complete with scale bars for comparison. The images were taken at different magnifications; a) 2k, b) 10k, c) 35k, d) 65k.

Paul (2014) proposed a three step mechanism for the formation of the overall CPM particles, which can be seen in, Section 2.2.1, Figure 2-9. In stage 1, the formation of the primary particles occurs, the size of which have yet to be determined by either Paul (2014) or this research. In stage 2 aggregation of these primary particles occurs through the attractive van der Waals forces in the system, forming a primary spheroidal CPM aggregate with a size of ~300 nm. Finally, in stage 3 these primary aggregates themselves form larger secondary aggregates, with an overall size of a few microns.

For the synthesis of CPM at 50 °C, a 79% yield was determined after synthesis, with the phosphomolybdic acid determined to be the limiting reagent. This is a high value considering the draining of CPM in solution from its original vessel, into the washing vessel and finally to where it was weighed in its drying vessel, all potentially contributing to mass loss. The formation of CPM at such a high percentage yield, over a relatively short reaction time, in

conditions similar to that of the HASTs, suggest it is likely to form easily in high quantities. If this is the case depending on its stability, hotspots within the tanks could potentially occur with the presence of highly radioactive caesium isotopes.

CPM was also synthesised at 25 °C to investigate the effect of temperature on its synthesis and morphology, Figure 3-14 shows an SEM image of these particles. The particles in the image display the expected spheroidal morphology of CPM and corresponds well to the CPM synthesised at 50 °C (Figure 3-13) (Paul et al., 2015, Dunnett et al., 2016, Ghalebi et al., 2016). This suggests that an application of heat is not actually required for successful synthesis to occur and that it does not alter the final particle morphology. Several studies that have synthesised CPM have also not applied heat and have successfully synthesised CPM (Jiang et al., 2005, Edmondson et al., 2012, Ghalebi et al., 2016). However, no previous study has directly compared the effect of temperature on the synthesis before.

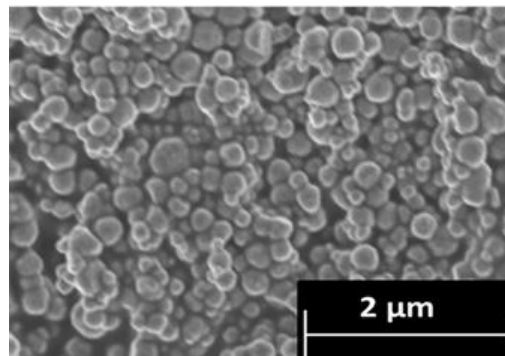


Figure 3-14 Scanning electron micrograph (SEM) of caesium phosphomolybdate (CPM) synthesised at 25 °C, completed with relevant scale bar. The magnification being 25k.

The origin of the application of the temperature 50 °C by Paul et al. (2015) appears to be from an internal document from NNL and is likely applied as this is the temperature of the HASTs, where it is both formed and stored. Although the application of temperature may not be required for the synthesis of CPM, it is the temperature in which it will form within the HASTs and therefore it will be the route utilised for the CPM experimented upon throughout this thesis, unless stated otherwise.

The synthesis of CPM involves a double replacement reaction with two reactants; phosphomolybdic acid ($\text{H}_3\text{PMo}_{12}\text{O}_{40}\cdot x\text{H}_2\text{O}$) and caesium nitrate (CsNO_3). This is discussed in detail by Paul et al. (2015). Phosphomolybdic acid is UV-Vis active, which allowed the precipitation kinetics of CPM to be tracked via measuring the phosphomolybdic acid decrease in concentration over time. Figure 3-15 shows the rate of reaction plot determined for the CPM synthesis conducted at both 25 °C and 50 °C, through tracking of the phosphomolybdic acid concentration.

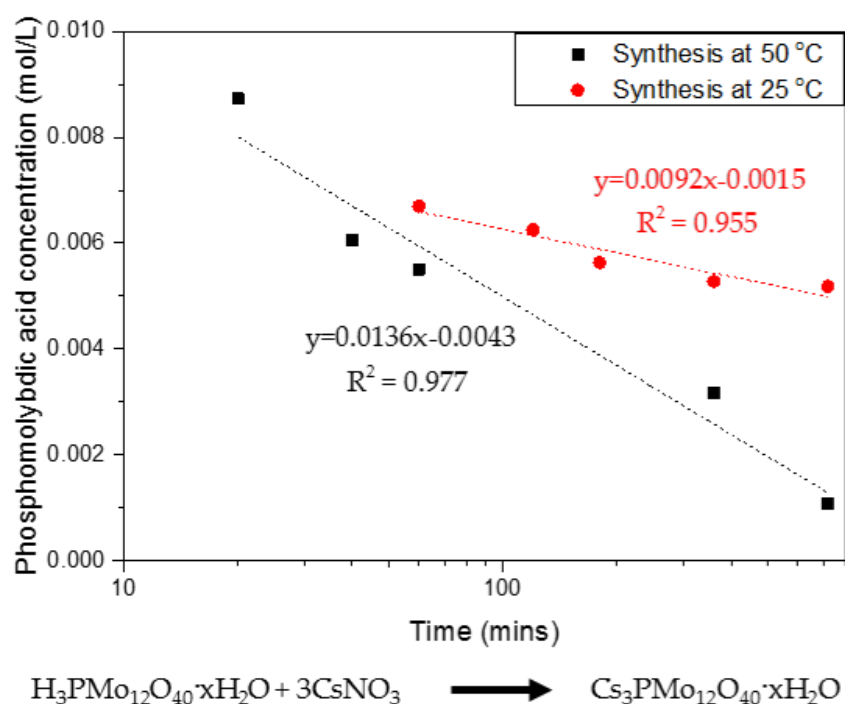


Figure 3-15 Rate of reaction graph showing first-order kinetics for the co-precipitation reaction of caesium nitrate and phosphomolybdic acid forming caesium phosphomolybdate (CPM) at 25 °C and 50 °C with corresponding reaction equation.

It was found to be a first-order reaction with respect to phosphomolybdic acid, which is in excess to the caesium nitrate, giving a rate constant of 0.04 min^{-1} for the reaction at 25 °C and of 0.09 min^{-1} for the reaction at 50 °C. This result demonstrates for the first time the fast kinetics at which CPM is formed within laboratory conditions. Previously published synthesis routes of CPM have not quoted exact reaction times, although it is implied that the reaction was completed quickly (Kang et al., 2004, Jiang et al., 2005, Edmondson et al.,

2012, Ghalebi et al., 2016). Paul et al. (2015), published reaction times of ~48 h, however at the higher temperature it is clear that the actual reaction is almost at completion within 2.5 h. This study is the first to directly investigate the speed of formation of CPM both without applied temperature and at 50 °C. While the reaction environment will differ within the HASTs as a result of the complex nature of the HAL, average temperatures are kept within 50–60 °C, suggesting a similar synthesis rate of CPM to that found at 50 °C could be feasible. This information could prove critical in understanding the amount of CPM formed within the HASTs. With the relative ease of formation, it is highly likely that due to the high relative proportions of caesium within the fission products, CPM will form easily and in high amounts. POCO planning can then consider a potential large quantity of radioactive CPM within the HASTs and design relevant processes with this in mind. Once the behaviour of CPM within dispersion is understood further in terms of its stability, settling and permeability (Chapters 4 and 5), POCO planning will have a range of 'worst case' scenarios to consider.

In large industrial processes the economics of synthesis procedures are incredibly important, therefore knowing CPM can form without the application of heat and over a short space of time, is an attractive aspect of the synthesis. This is because applying heat over prolonged periods of time can be costly. For the nuclear industry, if non-active CPM is going to be continually utilised in research and in large quantities, cost reduction is crucial. This study has demonstrated the simplicity of synthesising CPM, which could allow the nuclear industry to synthesise greater quantities for scale-up experiments. The more realistic the conditions experimented upon i.e. scale, temperature, pH, quantities, the more pertinent information that can be provided for POCO, again saving costs.

Figure 3-16 shows the SEM images of both ZM-1 (image a) and b)) and ZMCA-1 (image c) and d)). ZM is most commonly known to be discrete cuboidal in shape which is demonstrated in the images of ZM-1 (Macheder, 2011, Paul et al., 2015, Dunnett et al., 2016). The SEM images of ZMCA-1 show a shape somewhat resembling a sheaf of wheat, hence from here on in referred to as "wheatsheaf" morphology.

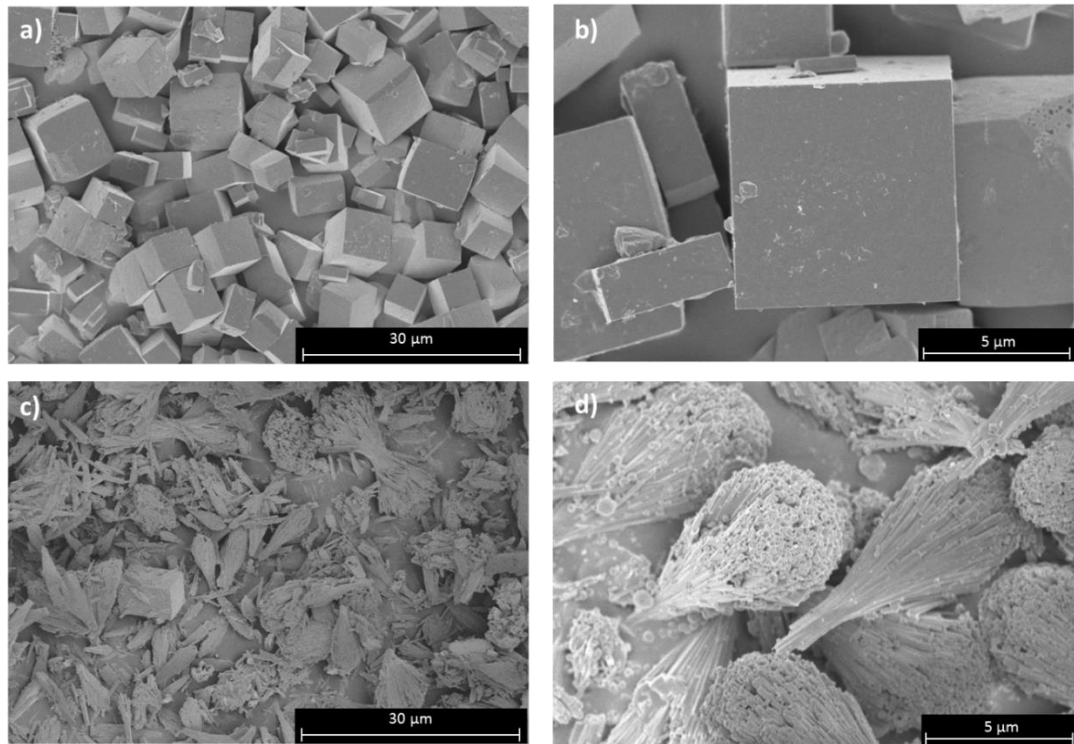


Figure 3-16 Scanning electron micrograph of: (a) and b) zirconium molybdate (ZM-1); and (c) and d) zirconium citramolybdate (ZMCA-1). The images magnifications being; a) 1.79k, b) 7k, c) 1.79k d) 7k.

Occasionally during the growth of a crystal, if subjected to parameters different to which it is usually formed within, two or more crystals can grow and essentially pass through each other (Jawson and Dove, 1956). This is a process known as crystal twinning. There are many ways in which a crystal can twin, for wheatsheaf morphology it is generally thought of as multiple twinned needles, which grow out and fuse together rather than staying as individual needles (Lussier et al., 2011). The mineral staurolite displays a similar wheatsheaf shape to that displayed by ZMCA-1 (Hurst et al., 2018). The twinning of crystals is a result of additive molecules and occurs by stabilization of one or more crystal faces (Wang et al., 1998). It is the addition of citric acid interacting with the molybdenum in solution, forming citratomolybdate complexes in the ZM synthesis that alters the expected cuboidal morphology of the particles (Macheder, 2011, Paul et al., 2015). The acid binds to certain faces of the ZM, reduces their growth, and therefore alters the particle aspect ratio (Samotus et al., 1991, Cruywagen et al., 1995, Zhou et al., 1997). For both Paul et al. (2015) and Macheder (2011), the use of citric acid to alter the morphology of ZM, produced rod-like particles, not the

wheatsheaf shape found in this research. However, both did find evidence of some twinning, just not as pronounced as for ZMCA-1. The wheatsheaf morphology for ZM has been referenced previously by Edmondson et al. (2012), where they attributed the shape to be a result of the presence of tellurium, an element not present in the synthesis of ZMCA-1.

It is clear that the formation of ZM is very sensitive to a number of parameters and is susceptible to additives that have a direct influence on its morphology. For this reason, it is important to increase understanding of a range of ZM morphologies to determine which shape has the most desirable behaviour properties, for potential doping. Additionally, there could well be a range of ZM morphologies present within the HASTs, so it is crucial to understand their behaviours in order to prepare for a range of POCO scenarios.

The conversion of CPM to ZM involves a two-step mechanism, first involving the breakdown of CPM, allowing free molybdate ions to react with the zirconyl ions, in the zirconyl nitrate solution (Bradley et al., 2004). Even though ZM has been synthesised in a number of studies, very few use CPM as a starting reagent (Bradley et al., 2004, Macheder, 2011, Paul et al., 2013, Paul et al., 2015, Dunnett et al., 2016, Paul et al., 2017). Of these studies only Macheder (2011) and Paul et al. (2015) make any reference to the time the conversion takes, both stating 'up to 14 days'. Therefore, the conversion of CPM to ZM-1 was qualitatively tracked, via SEM of intermediate structures over a period of ten days, the images of which are presented in Figure 3-17.

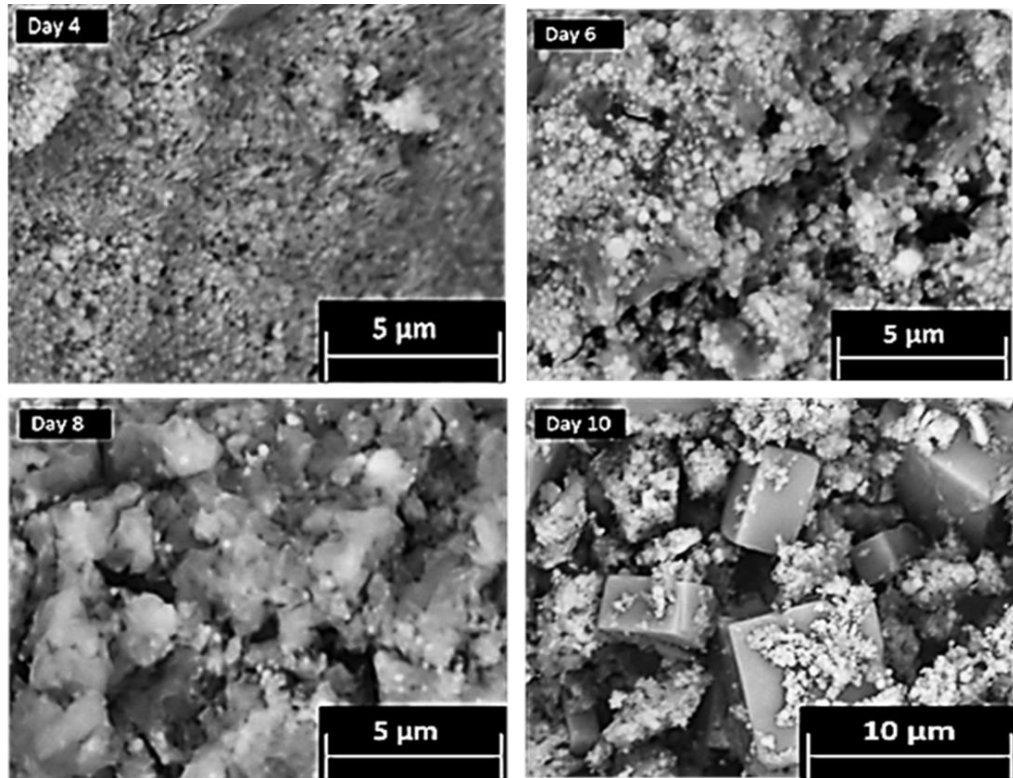


Figure 3-17 Scanning electron micrographs taken at various times during the tracking of zirconium molybdate (ZM-1) synthesis from a caesium phosphomolybdate (CPM) precursor over 10 days. The images magnifications being; Day 4) 12k, Day 6) 12k, Day 8) 12k, Day 10) 7k.

Through Days 0–6, it was observed that the particles remain predominantly spheroidal in their morphology and nanometre in size, representative of CPM. In addition, the solids all remained yellow in colour, visually a characteristic expected for CPM. For the solids precipitating out from Day 8 to Day 10, there appeared to be a mix of yellow and white solids suggesting that ZM-1 was beginning to form. The SEMs taken at Days 8 and 10 also suggest this, as the cuboidal micrometre particles that would be expected of ZM can be seen to appear, in addition to the spheroidal CPM particles coating the ZM-1. Once Day 10 was reached, the solids were washed with 1 M ammonium carbamate, which dissolved the CPM particles, resulting in the clear cuboidal particles, as seen in Figure 3-16 image a) and b) (Jiang et al., 2005, Edmondson et al., 2012). This sequence of SEM images demonstrates the length of time it takes for ZM to transform from CPM in a highly controlled environment. Additionally, the conversion yield from CPM to ZM remains low, estimated to be ~30–40%. An exact percentage yield couldn't be determined due to the extraction of regular aliquots of the reaction solution. The full conversion of CPM to ZM-

1 takes 10 days which, is much slower than CPM forming rapidly within hours as shown in the kinetics studies, suggesting that there could be a higher concentration of CPM in contrast to ZM within the HASTs. However, tank conditions and specific compositions of the HAL within the tanks are variable, and thus the ratio of CPM:ZM is extremely difficult to predict. Considering the amount of time that HAL is left in the tanks, which is often in the order of months, potentially large quantities of ZM could form that would need to be considered for POCO. This issue highlights the importance of understanding both systems individually and mixed. Due to the long periods of time for ZM-1 to form this allows for slow crystal growth and therefore in the case of ZMCA-1, allowing time for twinning to occur.

The NNL, provided two samples of ZM that had differing morphology to the traditional cuboidal shape expected by ZM, Figure 3-18 shows the SEM images of these provided ZM (ZM-2 and ZMCA-2) samples.

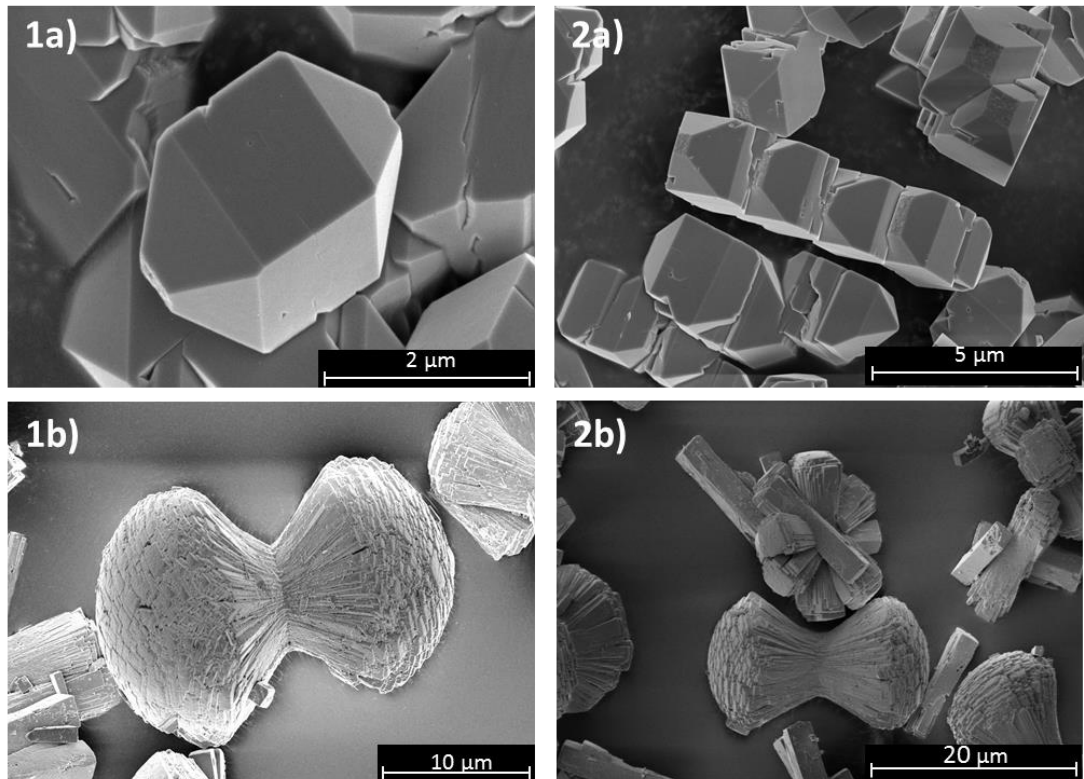


Figure 3-18 Scanning electron micrograph of: a) zirconium molybdate (ZM-2); and b) zirconium citramolybdate (ZMCA-2). The images magnifications being; 1a) 25k, 1b) 10k, 2a) 3.5k, 2b) 2.5k.

ZM-2, shown in Figure 3-18 (image 1 and 2 a)) displays an elongated square bipyramid shape with truncated 'pyramid tops'. Due to the uniqueness of this morphology it is difficult to determine whether this shape has previously been seen within literature. Square bipyramid shapes have previously been seen, specifically relating to nanoparticles of gold (Liu and Guyot-Sionnest, 2005, Navarro et al., 2012) and iron (Lu et al., 2016). Navarro et al. (2012), found that the formation of square bipyramid shapes was largely time dependent, finding seven days to be optimum for their gold nanoparticles. It has already been stated that ZM morphology is sensitive to a number of parameters, the exact conditions of the ZM-2 synthesis have not been provided, therefore an exact mechanism for this growth pattern is unknown. As with the wheatsheaf shape it is likely formed through a form of twinning, with certain faces growing at different rates due to being inhibited by an additive (Nelson, 2019).

ZMCA-2, Figure 3-18 (image 1b and 2 b)) shows a more pronounced wheatsheaf shape, comparable to that of ZMCA-1, the twinning of these crystals is more evident in image 2b. It is noted that both the ZM-2 and ZMCA-2 particles used were produced at an industrial scale with different reaction conditions to the laboratory synthesised ZM-1, and it is likely that the final morphology of the particles is sensitive to various factors, such as; concentration of the citric acid reactants added, potential trace contaminants or even different precursor materials (Macheder, 2011). As the chemistry of the HAL and the conditions of the HASTs are largely unknown, it is not unreasonable to suggest a mix of ZM morphologies could be present, and therefore ZM-2 or ZMCA-2 may represent a more realistic simulant particle shape than the well-defined cuboidal ZM-1. Additionally, depending on the morphology of the ZM and the properties it exhibits, doping the HAL to promote a morphology change before POCO could be advantageous (Edmondson et al., 2012). This complexity re-enforces the need to characterise various morphologies of ZM to investigate the potential differences in physical and chemical properties, in order to determine the potential 'extremes' of ZM's behaviour.

3.3.2 Physical and Chemical Characterisation

The densities of the simulants are given in Table 4. When compared to literature, values of 3.82 g/cm^3 were reported for CPM and values of 3.41 g/cm^3 for ZM (Paul et al., 2013, Dunnett et al., 2016). The CPM synthesised for this research has a higher density than this reported value, however it is not a significance difference. The densities for the ZM samples range from $3.61 - 3.82 \text{ g/cm}^3$, which is comparable to literature. The AccuPycTM 1330 Pycnometer achieves calibration to within $\pm 0.02 \%$ of true zero. Therefore density measurements presented have an uncertainty of $\pm 0.02 \%$ of their presented value.

Table 4 Reporting the density values for caesium phosphomolybdate (CPM), zirconium molybdate (ZM-1 and ZM-2) and zirconium citramolybdate (ZMCA-1 and ZMCA-2)

Simulant	Density (g/cm^3)
Caesium Phosphomolybdate (CPM)	4.15
Zirconium Molybdate (ZM-1)	3.67
Zirconium Molybdate (ZMCA-1)	3.73
Zirconium Molybdate (ZM-2)	3.61
Zirconium Molybdate (ZMCA-2)	3.82

Figure 3-19, shows the XRD patterns for CPM, ZM-1, ZMCA-1, ZM-2 and ZMCA-2. All the ZM and ZMCA patterns, were compared to The ICDD online database, where they correlated with the ICDD number 04-011-0171. Confirming in all these samples the simulant is ZM. All these ZM morphologies are reported to crystallise as a body-centred tetragonal lattice with space group $I41cd$, lattice parameters $a = b = 11.45 \text{ \AA}$, $c = 12.49 \text{ \AA}$ and angles $\alpha = \beta = \gamma = 90^\circ$. Although the morphologies of the ZM samples are all quite different, the XRD patterns show their bulk crystal structure remains the same. The XRD patterns for these samples also agree with those published within literature (Clearfield and Blessing, 1972, Paul et al., 2015, Paul et al., 2013). Whilst the pattern for CPM was not found in the ICDD database, it is in good correlation to the patterns for CPM found within literature (Bykhovskii et al., 2006, Paul et al., 2015). On analysis CPM is reported to crystallise in a cuboidal lattice with space group $Pn-3m$, lattice parameters $a = b = c = 11.79$

Å and angles $\alpha = \beta = \gamma = 90^\circ$. Lattice parameters presented, according to the XRD manufacturer, have uncertainty values of ± 0.0001 Å associated with them, whilst lattice angles presented have uncertainty values of $\pm 0.02^\circ$. As the patterns correlated well with both previous literature and the ICDD it was not deemed necessary for further analysis on this patterns. For a more in depth understanding of the crystalline structure of the nuclear waste simulants CPM and ZM, refer to Paul (2014).

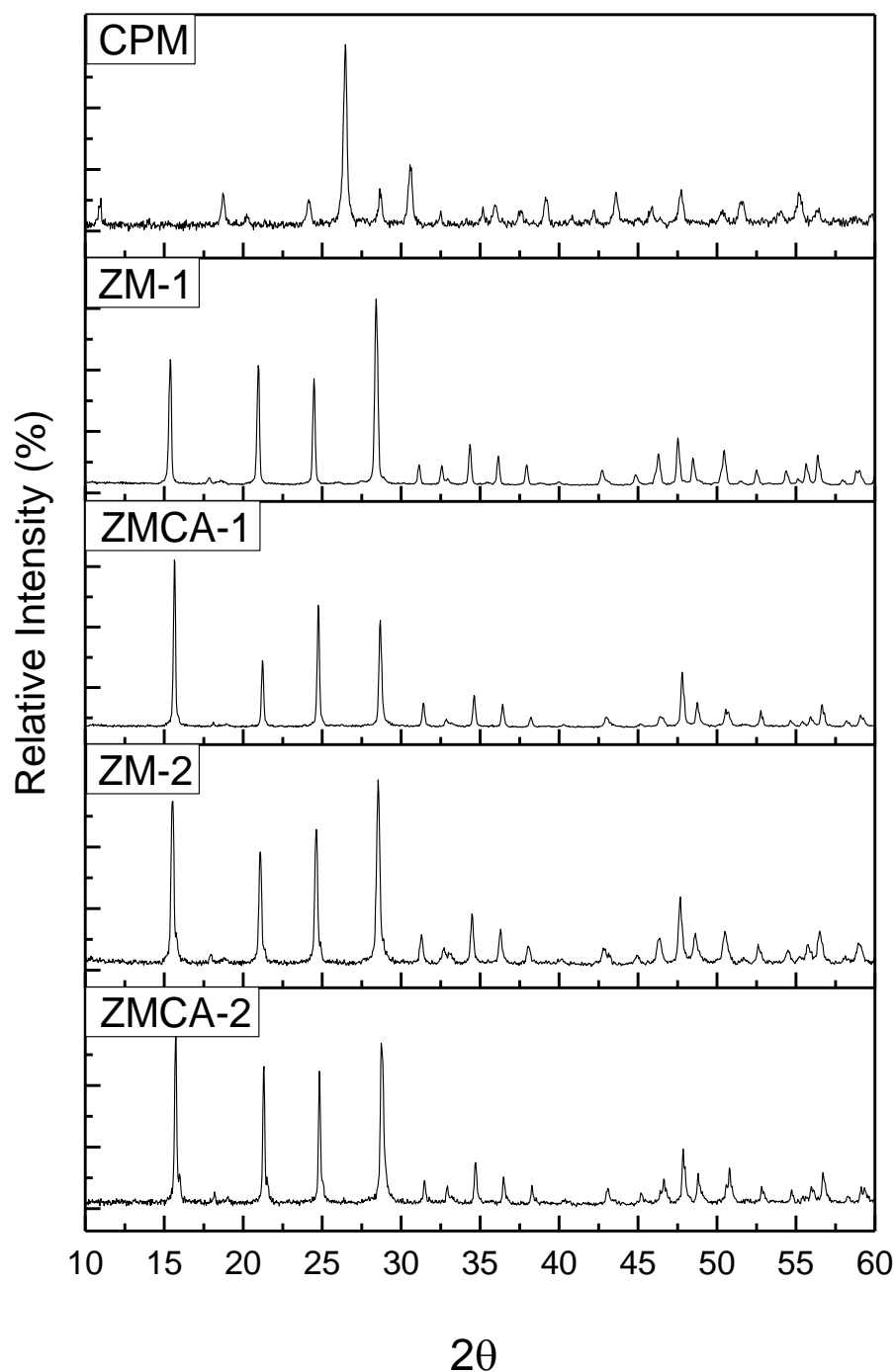


Figure 3-19 X-ray Diffraction patterns for caesium phosphomolybdate (CPM), zirconium molybdate (ZM-1 and ZM-2) and zirconium citramolybdate (ZMCA-1 and ZMCA-2).

IR analysis was used as a fast method for fingerprinting the synthesised compounds, in addition to comparing them to the provided simulants. Figure Figure 3-20, presents the FTIR spectra for CPM , ZM-1, ZMCA-1, ZM-2 and

ZMCA-2. The CPM spectrum published by Ghalebi et al. (2016), is in good agreement to the CPM spectrum published here. The spectrum published by Rao et al. (1990), is in good agreement to the ZM (ZM-1, ZMCA-1, ZM-2 and ZMCA-2) spectra shown in Figure 3-20. The spectra for all ZM samples show a band between 3000 cm^{-1} and 3300 cm^{-1} , which is representative of the O-H group, with the band at 1600 cm^{-1} representing the O-H-O bonds. The 'fingerprint' region is below 1000 cm^{-1} corresponding to metal to oxygen groups. If the sample was to be anhydrous, the IR spectrum would differ with no bands between $400 - 700\text{ cm}^{-1}$ (Rao et al., 1990). The ZM-1 and ZMCA-2 spectra differ slightly from the ZMCA-1 and ZM-2 spectrum with more intense bands around 1000 cm^{-1} , potentially equated to the presence of more bound water molecules present in the structures. The ZMCA-1 spectrum has slightly more intensity around the $3000 - 3500\text{ cm}^{-1}$ region suggesting the presence of more O-H groups. For the CPM spectrum, the higher region, from 1250 cm^{-1} upwards, is largely similar to the ZM spectra (representing the O-H and O-H-O groups with slight intensity differences). The 'fingerprint' region ($< 1000\text{ cm}^{-1}$) highlights clear differences in intensity from the ZM spectra, due to the main metal bonding, indicating IR probe analysis may potentially be useful as an *in situ* technique to determine compositional differences, in CPM:ZM mixtures. Although uncertainty values are not associated with the IR spectra, it was found that when repeating on fresh sample (three times) the spectra were accurately reproduced.

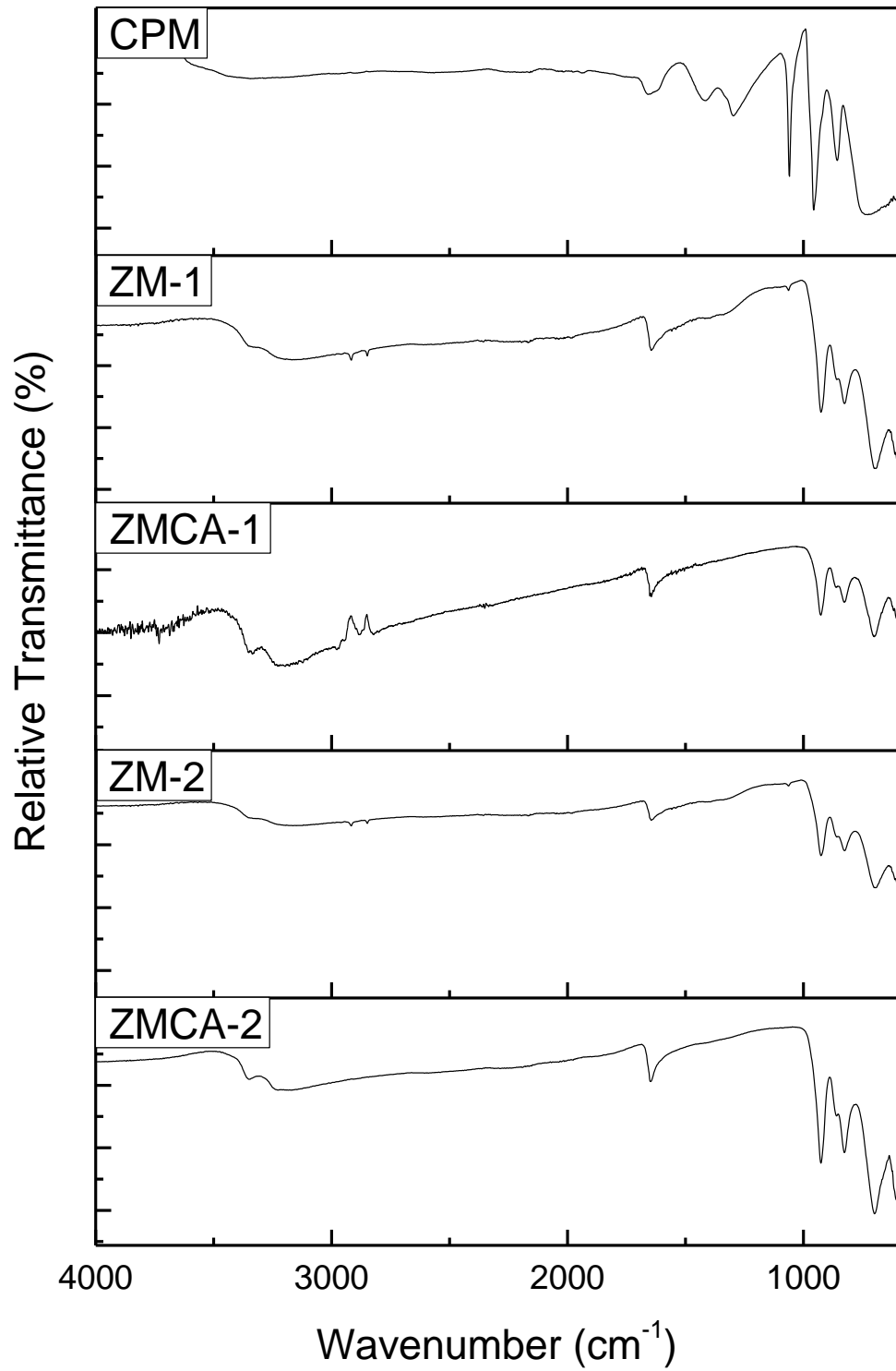


Figure 3-20 Infrared (IR) spectra of caesium phosphomolybdate (CPM), zirconium molybdate (ZM-1 and ZM-2) and zirconium citramolybdate (ZMCA-1 and ZMCA-2).

Figure 3-21 presents the TGA plots of CPM, ZM-1, ZMCA-1, ZM-2 and ZMCA-2, over a temperature range from 30 °C to 400 °C. For CPM, the water loss begins below 100 °C and continues until ~400 °C, with a total mass loss equating to 13 moles of water, therefore resulting in a chemical formula of: $\text{Cs}_3\text{PMo}_{12}\text{O}_{40}\cdot 13\text{H}_2\text{O}$. This value is in good agreement with the reported literature values, which are generally between 9 and 14 moles of water, dependent on the drying method chosen (Clearfield and Blessing, 1972). In the present study, CPM was dried using an oven at 70 °C for 12 h. Therefore, it is possible some of the initial water loss could potentially have been strongly adsorbed bound water, or water with extremely low binding energy, however given the length of drying time, it is not assumed to be from any free water.

In comparison, the dehydration process for all ZM morphologies has a clearer start and end temperature. For ZM-1, the mass loss starts around 100 °C and stops just before 200 °C, equating to 3 moles of water and a chemical formula of $\text{ZrMo}_2\text{O}_7(\text{OH})_2\cdot 3\text{H}_2\text{O}$, which is the same value reported in literature (Zhang et al., 2013). The TGA curve for ZM-2 is almost identical to that of ZM-1 and also correlates to a loss of 3 moles of water and a chemical formula of $\text{ZrMo}_2\text{O}_7(\text{OH})_2\cdot 3\text{H}_2\text{O}$. The dehydration process of ZMCA-2 is similar to ZM-1 and ZM-2, but appears to begin at a slightly slower rate and lower temperature, while again the mass loss stops just before 200 °C. This curve equates to a loss of 4 moles of water giving formula; $\text{ZrMo}_2\text{O}_7(\text{OH})_2\cdot 4\text{H}_2\text{O}$, showing a difference in bound water content between the ZM-1, ZMCA-2 and ZM-2 samples. For ZMCA-1 the mass loss appears to occur in a twostep process, the first from 100 – 150 °C, the second from 150 – 250 °C, in total equating to 5 moles of water, giving formula; $\text{ZrMo}_2\text{O}_7(\text{OH})_2\cdot 5\text{H}_2\text{O}$. It is expected that this may be a result of the citric acid incorporation, although, again differences in reaction conditions may also be a cause. The extra water present in ZMCA-1 is also consistent with the slight variation in the FTIR spectra (Figure 3-20) with the increased intensity around 3000 - 3500 cm^{-1} for ZMCA-1 compared to the other ZM simulants. It is highlighted that ZM-1 and ZM-2 both of which have a cuboidal shape, have 3 moles of water, whereas the higher aspect ratio ZM samples, ZMCA-1 and ZMCA-2, have 5 and 4, respectively. Suggesting that the higher aspect ratio ZM, potentially has different surface chemistry, which could influence its dispersion behaviour.

It should be considered that when quoting the number of moles of water as a whole number, that this value has been calculated and rounded up. Therefore, it may be more accurate to assume a range of moles of water rather than an exact value.

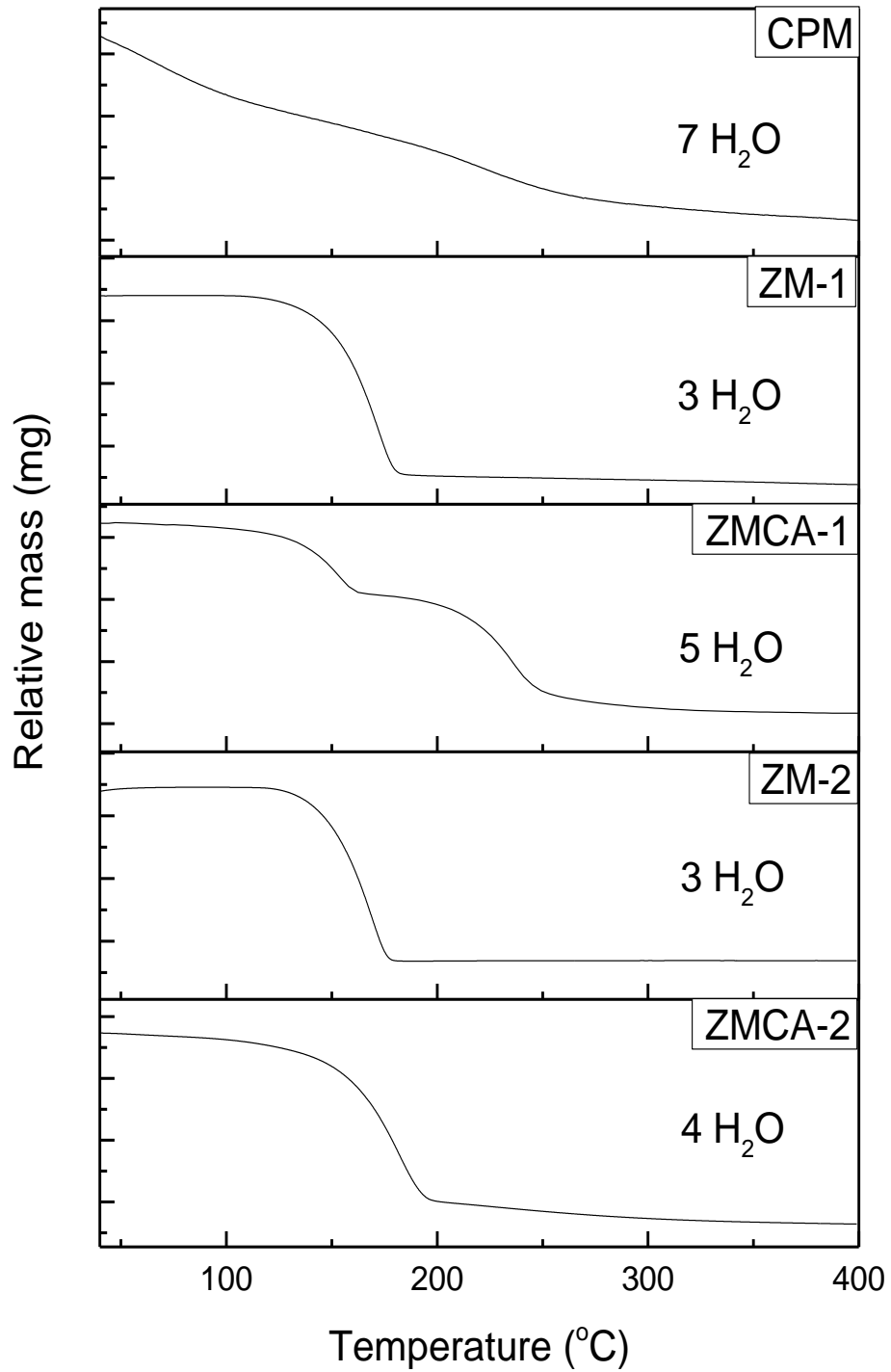


Figure 3-21 Thermogravimetric analysis curves of caesium phosphomolybdate (CPM), zirconium molybdate (ZM-1 and ZM-2) and zirconium citramolybdate (ZMCA-1 and ZMCA-2). CPM shows a loss of 13 moles of water, ZM-1 a loss of 3, ZMCA-1 a loss of 5, ZM-2 a loss of 3 and ZMCA-2 a loss of 4.

3.4 Conclusions

This Chapter has presented both results and discussion on the synthesis, kinetics and a range of properties of the non-radioactive simulants CPM and ZM. CPM, with spheroidal particle shape (synthesised at 25 °C, and 50 °C) ZM-1, with a cuboidal morphology and ZMCA-1 with a wheatsheaf morphology were successfully synthesised and characterised using SEM, XRD, IR and TGA. In addition, provided ZM-2 and ZMCA-2 were also characterised, with a square bipyramid and wheatsheaf shape, respectfully. CPM, was found to have formula, $\text{Cs}_3\text{PMo}_{12}\text{O}_{40} \cdot 13\text{H}_2\text{O}$, crystallise with space group $Pn-3m$ and have an IR spectrum comparable to literature. The reaction kinetics of CPM precipitation were investigated at various temperatures, finding it to be a first-order reaction with respect to the reactant phosphomolybdic acid, and able to form at room temperature. While the kinetics of CPM synthesis was very fast, ZM-1 formation from CPM was slow, being reported to convert only partially after ~10 days. The ease of formation of CPM compared to ZM suggests that within the HASTs there could be a larger proportion of CPM in comparison to ZM. Additionally, as the formation of ZM is sensitive to the effects of additives, it is likely that any ZM formed will contain a range of morphologies

The four ZM simulants varied not only in their morphologies but also their densities and water content. Characterising such a range of ZM morphologies means that the 'worst case' ZM properties can be identified, which will ultimately help with POCO planning. For all ZM simulants they were identical in terms of their crystal properties, with space group $I41cd$. Their IR spectra were also comparable, and compared well to literature. ZM-1 and ZM-2 had chemical formula of $\text{ZrMo}_2\text{O}_7(\text{OH})_2 \cdot 3\text{H}_2\text{O}$, ZMCA-2 of $\text{ZrMo}_2\text{O}_7(\text{OH})_2 \cdot 4\text{H}_2\text{O}$ and ZMCA-1 of $\text{ZrMo}_2\text{O}_7(\text{OH})_2 \cdot 5\text{H}_2\text{O}$. Noting that the lower aspect ratio ZM (ZM-1 and ZM-2) has lower water content than the higher aspect ratio ZM (ZMCA-1 and ZMCA-2), suggesting differences in surface chemistry relating to morphology.

Overall, the results highlight the complex morphology and various properties of these precipitated nuclear wastes, which will assist in the understanding of future results looking at their dispersion behaviours.

**Chapter 4 Dispersion
Stability and Sedimentation
Behaviour of Caesium
Phosphomolybdate and
Zirconium Molybdate –
Influence of Charge, Shape,
Size and Temperature.**

4.1 Introduction

An understanding of both the stability and settling behaviour of particulate suspensions is vital for a number of industries in order for them to optimise solid-liquid separation processes (Piazza, 2014). The Stoke's Law was designed to allow a prediction of sedimentation rates for spherical particles within ideal conditions (Stokes, 1851). However, a limitation of Stoke's Law is that it does not consider hindered settling, which is common for more complex particulate systems.

There are a number of parameterised models that have been designed to assist in predicting hindered settling (Lester et al., 2005, Skinner et al., 2015, Usher et al., 2013), in addition to empirical settling models such as Vesilind (1968), Steinour (1944), and Michaels and Bolger (1962). Where perhaps the most widely used correlations are based on the Richardson and Zaki (1954) power-law relationship.

The stability of a particulate system, particularly whether it will form aggregates plays a crucial part in understanding its sedimentation behaviour (Allain et al., 1995). Additionally, when considering the influence of particle properties on sedimentation behaviour, a number of studies have investigated the role of particle shape, specifically shapes deviating from spherical (Chong, 1979, Liu and Joseph, 1993, Turney et al., 1995, Fan et al., 2004, Tomkins et al., 2005, Lau and Chuah, 2013, Dogonchi et al., 2015). It is reported that non-spherical elongated particles, often oscillate during sedimentation and settle with different orientations, with the most stable orientation being when perpendicular to the direction of flow (Fan et al., 2004, Lau and Chuah, 2013). As highlighted in the previous Chapter, ZM has a range of morphologies, of which it would be beneficial to characterised in terms of understanding the potential differences in stability and sedimentation.

The previous Chapter presented a range of physical and chemical characterisation results for the individual simulants (CPM, ZM-1, ZM-2, ZMCA-1, ZMCA-2), predominantly in their dry solid form. These results were vital in providing the foundations upon which this Chapter was designed. It is crucial to further the knowledge of how the suspension properties of CPM and ZM may change once processing moves to a POCO stage, where the relative

concentrations of nitric acid may be diluted, potentially altering dispersion stability, amongst other properties. One major concern in regards to CPM and ZM is that during their storage within the HASTs, they precipitate out forming settled beds (Edmondson et al., 2012). Potentially resulting in localised heat spots, which could affect the integrity of the tanks. Currently, the ratio of CPM to ZM existing within the HASTs is unknown, within each of the 21 tanks there could be a ratio ranging from 0 – 100% of either CPM or ZM and any combination in-between. An understanding of mixed system settling behaviour will give a more realistic view of the current conditions within the HASTs and assist in the planning of future processing of the HAL. Therefore, the stability and settling behaviour of dispersions of the nuclear waste simulants both individually and mixed must be investigated, within both 2 M nitric acid and a more neutral medium; Milli-Q water. Any increase in the understanding of the potential behaviour of the HAL will hopefully aid in the assisting of the planning of future waste management strategy. Therefore, this Chapter presents stability and settling behaviour of individual CPM and ZM dispersions, with CPM at ambient and evaluated temperatures, in addition to mixed systems, in both 2M nitric acid and Milli-Q water.

4.2 Materials and Methodology

4.2.1 Materials

The simulants presented in Section 3.2 (Table 2) continued to be studied within this Chapter with the addition of CPM that was synthesised at 100 °C and a purchased sample of TiO₂.

As the synthesis of the simulants (CPM, ZM-1 and ZMCA-1) did not yield a large amount of material, the volume limitation meant some preliminary research for this project was conducted on the well-studied mineral oxide particle, TiO₂. TiO₂ in its anatase/rutile mixed form was purchased from Venator Materials PLC (formally Huntsmans Pigments Ltd.) with product code TS46424.

CPM was synthesised at 100 °C following the synthesis method described in Section 3.2.2.1, with all parameters remaining as stated apart from the increase of temperature.

In terms of any other additional reagents used in addition to those listed in Section 3.2.1 (Table 3), potassium hydroxide (KOH) and potassium nitrate (KNO_3) both supplied by Sigma-Aldrich Co Ltd were acquired for the zeta potential experiments, discussed in Section 4.2.2.2..

As a result of lack of material, ZM-1 and ZMCA-1 were not comprehensively studied in terms of all the experiments conducted within this Chapter.

4.2.2 Characterisation Techniques and Methodologies

4.2.2.1 Particle Size Laser Diffraction Analysis

A Mastersizer® 2000 (Malvern, Worcester, UK) was used to determine the particle size distribution of the simulants. The Mastersizer® utilises laser diffraction in measuring the size of the particles, its optimum particle measurement size being $< 100 \text{ nm}$ to $> 2 \text{ mm}$. Once the sample is within the loop system of the Mastersizer®, the intensity of the light-emitting diode (LED) scattered from the laser is measured and correlated to the particle size distribution. In order for the Mastersizer® software to do this, the Mie theory is utilised, which predicts the light scattering behaviour of all materials under all conditions (Eshel et al., 2004). The theory predicts particles of certain sizes can be determined by a 'fingerprint' scattering pattern correlating to that size, Figure 4-1 shows a schematic of the Mie theory principle. In the case of the Mastersizer®, the light scattering pattern is determined first and then back calculated to determine a particle size distribution. Caution should be taken when using the Mie theory to measure non-spherical particles, as it is based upon spherical particles. However, for the basis of this project the Mastersizer® technique was determined sufficient for a comparison of particle sizes between simulants.

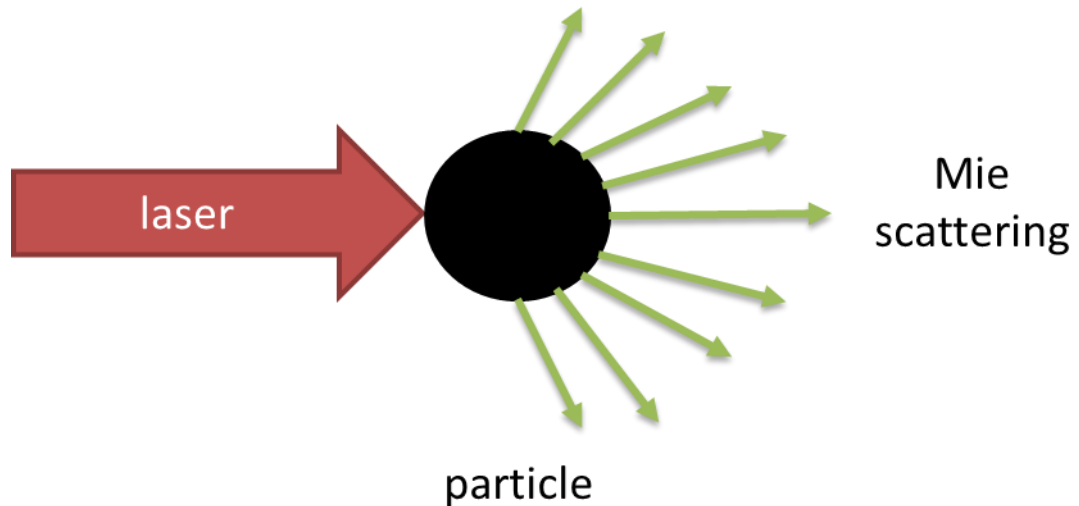


Figure 4-1 Schematic of the Mie Theory underlying principle.

The sample particles were dispersed within Milli-Q water and sonicated for 10 min before being added to the Mastersizer® until the 10% by volume value set on the software was met. The dispersed sample was then pumped around a loop system at 1500 rpm whilst being measured 10 times with each measurement over 10 s, with the software calculating the distribution of particle sizes. In addition, the D10, D50 and D90 values were determined by the Mastersizer® as the 10th, 50th and 90th percentiles of the cumulative distribution, respectively. These D values were therefore inclusive of any bimodal particle size distributions but were sufficient enough to provide comparative sample information. The Mastersizer® is reported by the manufacturer to be accurate to within +/- 0.6 % of the reported particle size.

Polydispersity Index

A Zetasizer Nano ZS (Malvern, Worcester, United Kingdom) was used to calculate the polydispersity index, which is a parameter determined from a Cumulants analysis of an intensity–intensity autocorrelation function. This was only for CPM simulants synthesised at 50 °C and 100 °C. More detail about the Zetasizer can be found in, Section 4.2.2.2.

4.2.2.2 Zeta Potential Measurements

The zeta potential of the simulants at various pH values were determined using a Zetasizer Nano ZS, which directly measures the electrophoretic

mobility and then uses this to calculate the zeta potential via an internal algorithm. The Zetasizer uses Laser Doppler micro-electrophoresis and a patented technique referred to as M3-PALS[®] (Phase Analysis Light Scattering). The Zetasizer utilises the presence of an electrical charge on a particle by applying an electric field in which it can interact with i.e. electrophoresis. When the electric field, E , is applied the particles within the dispersion are attracted to the electrode of opposite charge via a specific velocity, v . These values can be used to calculate the electrophoretic mobility, μ_e which in turn can be used to calculate the zeta potential, ζ . Equations (27) and (28) show the link between these terms. The electrophoretic mobility, μ_e is linearly related to zeta potential, ζ through the

$$\text{Henry equation (Equation } \zeta = \frac{4\pi\eta}{\varepsilon} f(ka)\mu_e \text{ (28)),}$$

where ε is the dielectric constant, n the viscosity and $f(ka)$ Henry's function (Henry and Lapworth, 1931) .

$$\mu_e = \frac{v}{E} \quad (27)$$

$$\zeta = \frac{4\pi\eta}{\varepsilon} f(ka)\mu_e \quad (28)$$

Henry's function is often accepted as 1.5 as a consequence of zeta potential measurements being taken in aqueous medium with an electrolyte (potassium nitrate for these experiments); this is known as the Smoluchowski approximation and this approximation was applied for all measurements (Shaw, 1991) .

Dispersions of the simulants were prepared with concentrations of 1000 ppm in a 10^{-4} M potassium nitrate solution. Nitric acid and potassium hydroxide solutions between 0.01 and 0.1 M were used to adjust the pH of the samples. For every sample, five measurements were taken and repeated on fresh samples 3 times, where an average of these results is presented. In all cases a DTS1070 cell was used and periodically calibrated through a standard solution to check for derogation of the cell. In measuring the pH a pre-calibrated Mettler Toledo MP225 pH meter was utilised. Where zeta potential results are presented an uncertainty value of +/- 0.12 mV is associated with them, as reported by the Zetasizer manufacturer.

4.2.2.3 pH Investigations

The Mettler Toledo MP225 pH meter was also used in several pH based experiments. Various concentrations of the synthesised simulants (CPM, ZM-1 and ZMCA-1) were made up in Milli-Q water and regularly monitored to determine if there was any change in their pH over time. Additionally, all HAL simulants had their equilibrium pH determined at a concentration of 5 vol%. Where pH values are reported an uncertainty value of +/- 0.01 pH is associated with them, as reported by Mettler Toledo.

4.2.2.4 Solubility Studies

A simple gravimetric analysis method was used for solubility studies of synthesised CPM, ZM-1 and ZMCA-1 in both Milli-Q water and 2 M nitric acid environments. In 20 ml vials the chosen solvent was saturated by the relevant simulant. Each of these vials were then placed on a shaker for 24 h at ambient temperature (25 °C) before being left for 12 h at the same temperature allowing the solids to settle. The supernatant was then emptied through the use of a pipette into pre-weighed vials and then weighed again before being placed in an oven at 70 °C. The vials were re-weighed over the course of several days until they gave a consistent value suggesting all liquid had been evaporated. Then the following Equations

$$m_{\text{vial+lid+solution}} - m_{\text{vial+lid}} \quad (29) \quad - \quad K_{\text{Solvent}} = \frac{m_{\text{solid}}}{m_{\text{solute}}}$$

(32) were used to calculate solubility in terms of mass of the solute per unit mass of solution, where m , is mass of the applicable subscript and k is the solubility. The experiment was conducted at three temperatures, 25 °C, 50 °C and 65 °C.

$$m_{\text{solution}} = m_{\text{vial+lid+solution}} - m_{\text{vial+lid}} \quad (29)$$

$$m_{\text{solid}} = m_{\text{vial+lid+solid}} - m_{\text{vial+lid}} \quad (30)$$

$$m_{\text{solute}} = m_{\text{solution}} - m_{\text{solid}} \quad (31)$$

$$K_{\text{Solvent}} = \frac{m_{\text{solid}}}{m_{\text{solute}}} \quad (32)$$

4.2.2.5 Centrifugal Settling

A LUMiSizer® (LUM GmbH, Berlin, Germany) was used to study the dispersion settling stability, where sedimentation studies for the simulants were conducted in triplicate (with an average standard deviation of 5% of the mean value) where an average of the results reported. Standard deviation was calculated using the equation displayed in Appendix Fig. 3. For aesthetic purposes, in presenting experimental results error bars were not plotted upon the figures associated with sedimentation.

The LUMiSizer® employs a centrifugal force (up to 4000 rpm) that can be utilised in measuring the settling rate (amongst other things) of solids within a dispersion, with the advantage of up to 12 samples being simultaneously measured. Additional benefits of the LUMiSizer® include the requirement of only a small quantity of material and the ability to set the temperature of the samples from 4 °C to 60 °C .The intensity of transmitted light, is detected as a function of time and sample height/length.

The LUMiSizer® measures the solids settling rate via applying centrifugal force and using LED light sources that emit light at different wavelengths to produce-transmission profiles at set time intervals. In order to do this the LUMiSizer® utilises STEP-Technology™ (Space and Time resolved Extinction Profiles). This technology allows the tracking of the whole sample instantaneously. Essentially the intensity of the light transmitted from the sample is detected and converted into transmission profiles. Figure 4-2, shows an illustration of a LUMiSizer® cell with light being transmitted through. When there is a solid bed not as much light can be transmitted, therefore the transmission percentage will be low. When this is tracked over time, the rate of settling can be calculated. The technique produces light transmission profiles that correspond to particle concentration, where low concentration is represented by high transmission, and vice versa.

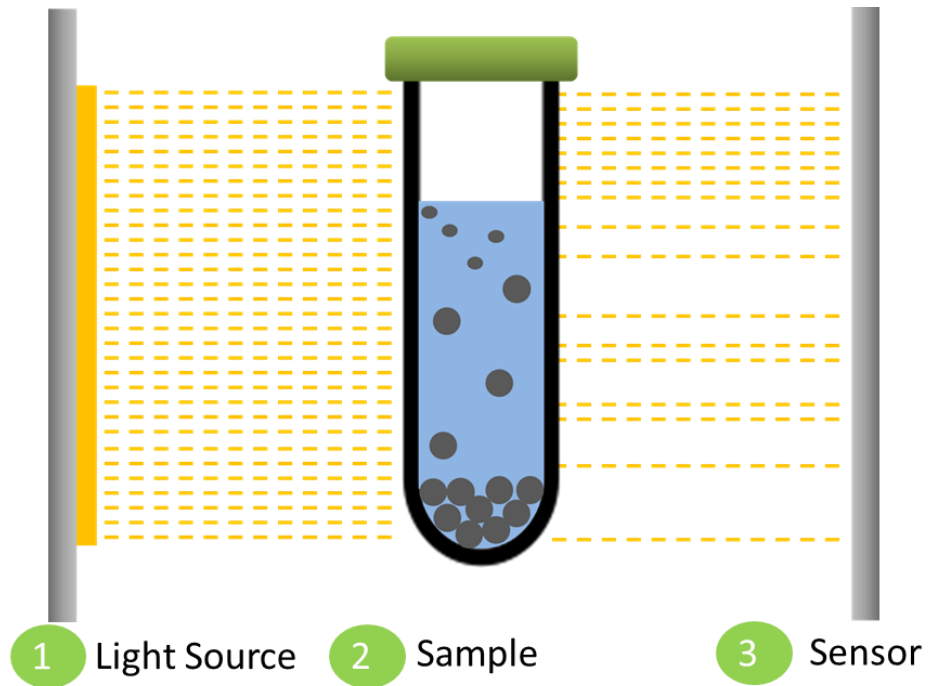


Figure 4-2 An illustration of a LUMiSizer® cell with light being transmitted through a settling sample with varying degrees of light being picked up by the sensor.

From the produced transmission profiles, a transmission percentage threshold is chosen and the data from this threshold extracted. It should be noted as a limitation of the technique when a specific threshold is chosen it represents a certain fraction of the particles at a certain size. A single threshold cannot capture the full behaviour of a polydispersed suspension. This extracted data can be used to plot the bed height vs. time, where the initial settling rate for each simulant at that specific rpm can be determined. The sedimentation rates can then be back calculated to estimate the settling rate at gravity, assuming linear dependence on *RCA* (relative centrifugal acceleration), using Equations $RCA=1.1118 \times 10^{-5} \times r \times rpm^2$ (33) and . Here, *r* is the radius of the instrument plate where the dispersion is housed (130mm for the LUMiSizer®) and rpm is the revolutions per minute of the experiment (Lerche and Sobisch, 2007). Section 4.3.3.1, presents this analytical process in respect to CPM in Milli-Q water, to aid understanding of its application.

$$RCA = 1.1118 \times 10^{-5} \times r \times rpm^2 \quad (33)$$

$$\frac{\text{Measured velocity}}{RCA} = \text{gravity velocity} \quad (34)$$

For the settling experiments the centrifuge speed was set between 500 and 2000 rpm at 25 °C or 50 °C, depending on the experiment. For clarity a summary of settling experiments that were undertaken is presented in Table 5. Transmission profiles were taken every 10 s with the total number of profiles equalling between 255 and 1000 (the maximum amount of profiles). LUMiSizer® polyamide (PA) disposable cells (110-134 xx) with 2.0 mm optical path length were used.

The Stokes (Stokes, 1851), Vesilind (Vesilind, 1968) and Richardson-Zaki (Richardson and Zaki, 1954c) theories were then utilised in analysing and comparing the settling rates of the simulants, all of which were discussed in Section 2.3.3.

Table 5 Summary of sedimentation experiments undertaken for this research, all in both Milli-Q water and 2 M nitric acid

Simulant	Concentration (vol%)
Caesium Phosphomolybdate (CPM)	2,4,8,12,16
Caesium Phosphomolybdate (CPM) at 50 °C	4
Titanium Molybdate (TiO ₂)	2,4,8,12,16
Zirconium Molybdate (ZM-2)	2,4,8,12,16
Zirconium Citramolybdate (ZMCA-2)	2,4,8,12,16
Mixed systems (CPM:ZMCA-2)	4

Mixed System Determination

Currently, there has only been one published investigated into CPM and ZM as a mixed system, which looked at a 50:50 mix (Dunnett et al., 2016). As there is an unknown ratio of CPM:ZM within the HASTs, it is crucial to understand their behaviour when mixed as well as individually. In order to prepare mixed dispersions of CPM and ZMCA-2, the weight ratios presented in Table 6, were used to form a total concentration of 4 vol%. In order to

calculate the total volume percent, the densities of both the simulants were used, Table 4 (Section 3.3).

Table 6 Weight % for caesium phosphomolybdate (CPM):zirconium citramolybdate (ZMCA-2) mixed dispersions

Weight % Ratio (CPM:ZMCA-2)
1:3
1:1
3:1

4.3 Results and Discussion

4.3.1 Particle Size Distribution

As both TiO₂ and CPM synthesised at 100 °C have been introduced for the first time in this Chapter, their SEM images are presented in Figure 4-3.

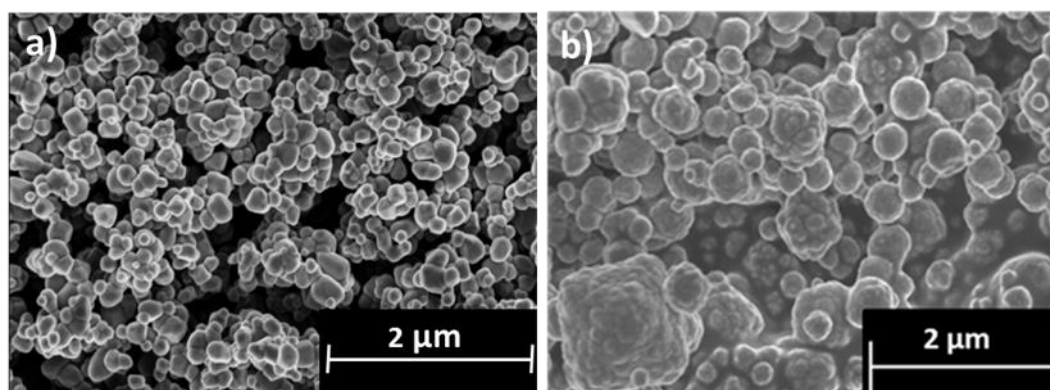


Figure 4-3 Scanning Electron Micrographs of titanium dioxide TiO₂ and caesium phosphomolybdate (CPM) synthesised at 100 °C. The images magnifications being; a) 25k, b) 22k.

The SEM image of TiO₂ seen in Figure 4-3 image a), demonstrates its spheroidal morphology, consisting of bound agglomerated clusters of nanocrystallites, which appear comparable to the morphology of CPM, and therefore an appropriate comparison material, from a morphological perspective. The density of TiO₂ is reported to be 4.23 g/cm³.

CPM was synthesised at 100 °C to investigate the effect of temperature on its morphology Figure 4-3 image b) shows the SEM images of these particles.

The particles in the image compare well initially in terms of the expected spheroidal shape of CPM. Accurate particle size comparison is difficult to make via SEMs, therefore the Mastersizer® laser diffraction technique was utilised to determine the particle size distribution data for all the simulants, the results of which can be seen in Figure 4-4.

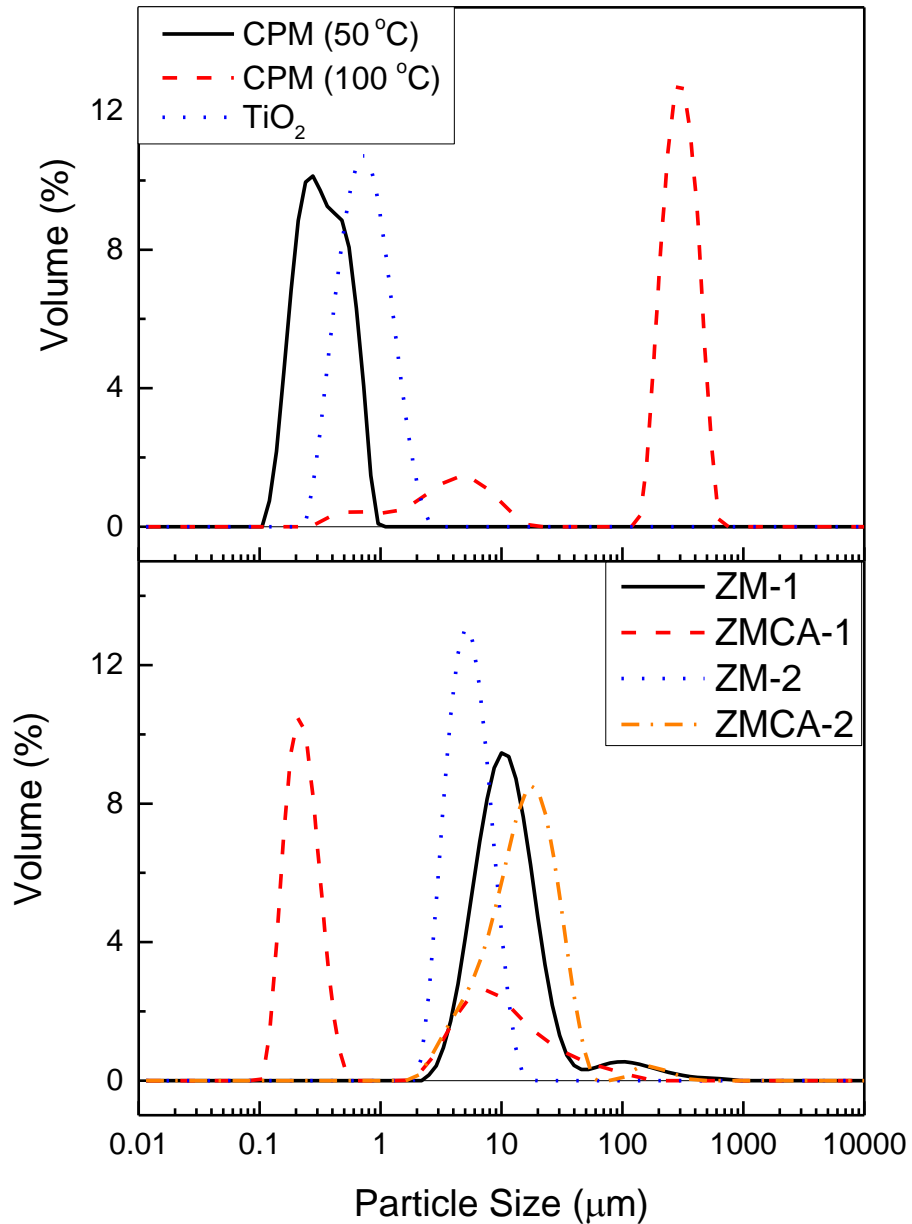


Figure 4-4 Particle size distributions of caesium phosphomolybdate (CPM) synthesised at 50 °C and 100 °C, titanium dioxide (TiO₂), zirconium molybdate (ZM-1 and ZM-2) and zirconium citramolybdate (ZMCA-1 and ZMCA-2).

Particle size distributions for each simulants were repeated in triplicate with only one distribution displayed per simulant in Figure 4-4, the reproducibility of these repeated spectra was within 1 % variation. To complement the particle size distribution data the 10th, 50th and 90th percentiles for each sample is provided in Table 7, in addition to the polydispersity index for both CPM simulants.

Table 7 Detailing the D10, D50 and D90 values for caesium phosphomolybdate (CPM) synthesised at 50 °C and 100 °C, titanium dioxide (TiO₂), zirconium molybdate (ZM-1 and ZM-2) and zirconium citramolybdate (ZMCA-1 and ZMCA-2). In addition to the polydispersity index for CPM synthesised at 50 °C and 100 °C.

Simulant	D10	D50	D90	PDI
Caesium Phosphomolybdate (CPM) at 50 °C	0.168	0.303	0.571	0.125
Caesium Phosphomolybdate (CPM) at 100 °C	3.295	249.72	399.221	0.558
Titanium Dioxide (TiO ₂)	0.375	0.687	1.326	-
Zirconium Molybdate (ZM-1)	4.994	10.123	23.958	-
Zirconium Molybdate (ZMCA-1)	0.152	0.272	15.789	-
Zirconium Molybdate (ZM-2)	2.98	4.89	8.245	-
Zirconium Molybdate (ZMCA-2)	5.167	14.476	30.704	-

When considering the particle size distribution data in Figure 4-4, noticeably the CPM synthesised at 50 °C, TiO₂, ZM-2, ZM-1 and ZMCA-2 exhibit essentially mono-modal size distributions with, respectively, increasing peak mean values of size. Whereas, the CPM synthesised at 100 °C and ZMCA-1 display bi-modal particle size distribution.

For the CPM synthesised at 100 °C, it was found that, although spheroidal particles were formed, as shown in Figure 4-4, there was an increase in large agglomerates and a greater range of particles varying in size and with irregular shape, especially compared to the CPM synthesised at 50 °C. A potential reason for the differences may be that the faster reaction kinetics that occur with an increase in temperature result in less time for the nanocrystallite clusters to form into self-similar spheroidal particles through diffusion interaction. Additionally, at 100 °C, it would be expected that formed CPM

would be less stable, as it is known to be a temperature range in which its breakdown should begin to occur (Bradley et al., 2004, Macheder, 2011). Hence, precipitates may partially re-solubilise, especially outer surfaces, leading to fusion of nanocrystallite clusters. It is therefore possible that over the 48 h time period of the synthesis that the higher temperature initially increased the rate of the reaction before becoming detrimental to CPM forming and promoting its breakdown. It is also known that in addition to an increase in temperature the acidity of the solution must also increase to fully breakdown the CPM, which may explain why the CPM in this sample only appears partially broken down.

The D50 value of CPM synthesised at 50 °C is 300 nm, which corresponds relatively well with the SEM images of CPM nanoclusters shown in Chapter 3 Figure 3-13. These SEM images show that these nanoclusters are made of smaller particles, which could be responsible for the D10 value. In addition, larger aggregates were shown to be present in the system through the SEM images, which could be responsible for the larger D90 value. In comparison, the CPM synthesised at 100 °C has a significantly higher D50 value of 250 μm , which is even larger than visually evident from the SEM images (Figure 4-3). Although individual crystallite sizes appear via SEM to be fairly similar to those formed at lower reaction temperatures, it is clear they cluster to a much greater degree and become extremely agglomerated, resulting in the high D50 value. The secondary smaller peak representing the finer particles ranging between 300 nm to 20 μm , likely represents both individual particles and smaller agglomerates. The polydispersity index (PDI) for CPM synthesised at 100 °C is 4.5 times larger than the CPM synthesised at 50 °C, which is attributed to the bimodal distribution of the CPM synthesised at 100 °C. For the remainder of this research only CPM synthesised at 50 °C will be discussed.

The TiO_2 simulant was predicted to have a slightly larger particle distribution than the CPM particles synthesised at 50 °C, due to agglomeration, as evidenced in the SEM images (Figure 4-3) and confirmed by the D50 value of ~ 700 nm for TiO_2 in comparison to the CPM D50 value of 300 nm.

For ZM-1 the cuboidal particles have a D50 value of 10 μm which is around 30 times larger than the CPM synthesised at 50 $^{\circ}\text{C}$. ZM-2 displays a smaller D50 of 5 μm and ZMCA-2 displays the largest D50 value of 14 μm . As ZM formation from CPM has been shown to be a slow reaction (Section 3.3.1), larger sized crystals are predicted to be formed, as generally slower reactions form larger crystals. Therefore, in comparing ZM-1 to ZM-2, if Johnson Matthey have attempted to speed up the reaction, it could have resulted in some smaller crystal formation. However, the exact reaction conditions are unknown. For ZMCA-2, as previously discussed significant twinning of the crystals is evident in the SEM images increasing the equivalent volume sphere diameter of the wheatsheaf shapes, as seen in Figure 4-5, repeated for ease of reading.

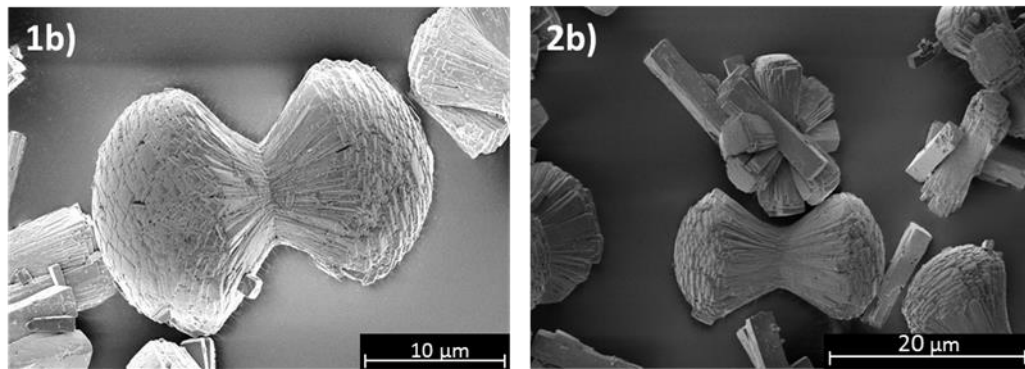


Figure 4-5 Scanning electron micrograph of zirconium citramolybdate (ZMCA-2). The images magnifications being; 1b) 10k, 2b) 2.5k.

When comparing all the simulants, ZMCA-1 has the smallest reported D50 value of 300 nm, even though it appears to have particles $\sim 10 \mu\text{m}$ via its SEM images, Figure 4-6 repeated for ease of reading. However, it does have a bimodal distribution and a D90 value of 16 μm . The exact reason for its bimodal distribution is unclear, however it is suggested on looking at the SEM images that there is a presence of a range of wheatsheaf sizes. There is potential that whilst within the loop of the Mastersizer®, some of the particle needles could break forming the small size fraction shown within its particle size distribution.

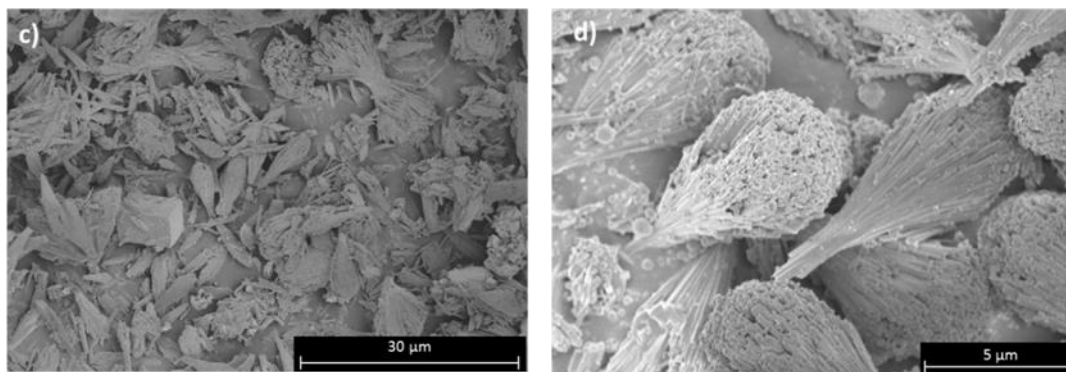


Figure 4-6 Scanning electron micrograph of: (c) and d) zirconium citramolybdate (ZMCA-1). The images magnifications being; c) 1.79k d) 7k.

In comparison to the literature, the CPM synthesised at 50 °C particle size is within a similar range when comparing to Paul et al. (2015). While the particle sizes for the ZM-1 and ZM-2 correlate with the ZM particle sizes found by Dunnett et al. (2016). ZMCA-1 and ZMCA-2 both have particle size values that don't compare to the literature, which is attributed to their unusual sheaf shape and high aspect ratio.

4.3.2 Stability

The zeta potentials of all simulants as a function of pH are shown in Figure 4-7. For CPM, the Isoelectric Point (IEP) could not be obtained confidently due to the observed variation at very low pH, likely because of the high effective counter ion concentration. However, through extrapolation, the IEP appears to be in the region of pH 1–1.5. The IEP for CPM has never been previously reported. TiO₂ had the highest IEP at just over ~pH 4, which compares well to previous literature on measurements of anatase and rutile mixtures (Mandzy et al., 2005, Liao et al., 2009). The IEP, for ZM-1, ZM-2 and ZMCA-2, was around pH 2.5, whereas for ZMCA-1 the IEP read to be around ~pH 4.

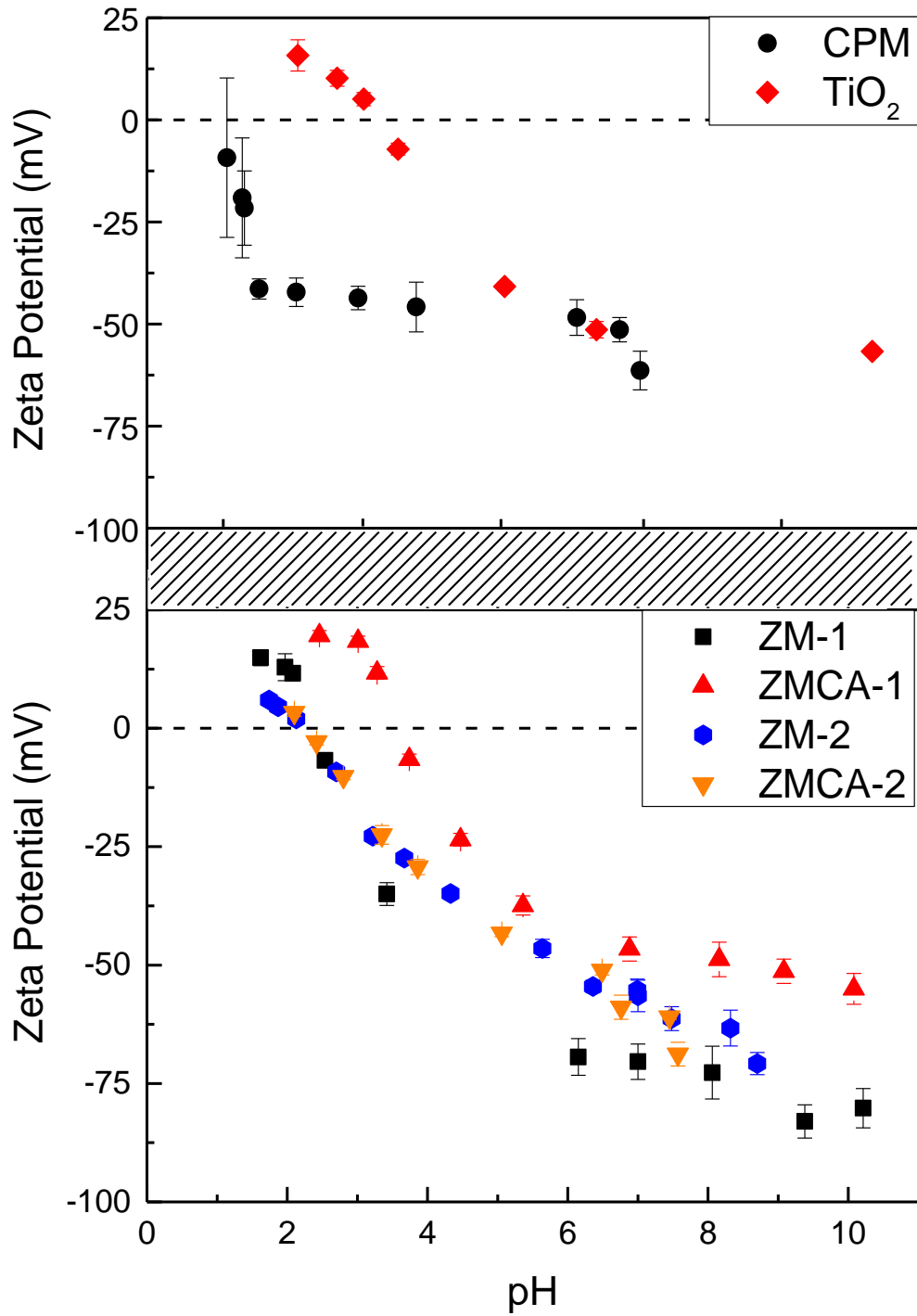


Figure 4-7 Zeta potential curves for caesium phosphomolybdate (CPM), titanium dioxide (TiO₂) and zirconium molybdate (ZM-1 and ZM-2) and zirconium citramolybdate (ZMCA-1 and ZMCA-2) measured in concentrations of 1000 ppm in 10⁻⁴ M in potassium nitrate solution.

The zeta potential data largely suggests that, in low pH conditions, such as those experienced in the HASTs, the ZM species will be positively charged (ZMCA-1 the most) thus likely charge stabilised, while the CPM may be close to an uncharged state or negatively charged. Therefore, considering CPM, given its IEP is very low, within acidic conditions it may aggregate, which is evident from its SEMs, Figure 3-13 (Section 3.3.1). It is worth considering that within the HASTs, the high acid concentration in the processing environments will mean that there is a high effective electrolyte concentration (resulting from acid counter ions), potentially collapsing the electric double layer around the particles, despite any native charge at low pH. Thus, it is important to study dispersion stability in both acidic and more neutral environments, the latter of which may represent conditions in POCO.

Even though XRD patterns (Figure 3-19) for all ZM samples matched, ZMCA-1 showed slight variation in its IR spectrum and TGA plot (Figure 3-21), suggesting there is potentially a difference in its surface chemistry. It is suggested that this difference could be a result of the surface adsorption of citric acid (Macheder, 2011, Paul et al., 2015, Paul et al., 2017). As a secondary effect of the citric acid (the primary being the influence on aspect ratio) it appears to alter the surface chemistry of the crystals, perhaps lowering affinity for hydroxide bonding leading to a slightly higher IEP.

Whilst there is little current literature in regards to the zeta potential of the nuclear waste simulants, similar negative potential trends have been found for SrMoO_4 particles across a broad pH range (Mukherjee et al., 2016). Additionally, studies conducted on molybdenite (MoS_2), a similar species to molybdate, have also measured low IEPs (Tabares et al., 2006, Lu et al., 2015). In regards to molybdenite, surface groups are thought to react with water forming MoO_4^{2-} ions which dominate the interaction potential.

A potential hypothesis for the IEP's of the simulants is that as CPM and ZM incorporate molybdenum into their chemical formulas, their surface molybdate groups may partially dissociate to form hydrates in water. The mechanism of which is conceivably through their bound water groups, which have been shown to exist via TGA (Figure 3-21). This mechanism could lead to strong

negative charges from OH^- groups and therefore the negative potentials for ZM shown in Figure 4-7. In addition, if the bound water formed hydrate groups on the simulant particles, the dispersions would potentially acidify from the release of the H^+ ions. Therefore, the synthesised simulants (CPM, ZM-1 and ZMCA-1), had their equilibrium pH measured at various concentrations, the results of which are shown in Figure 4-8.

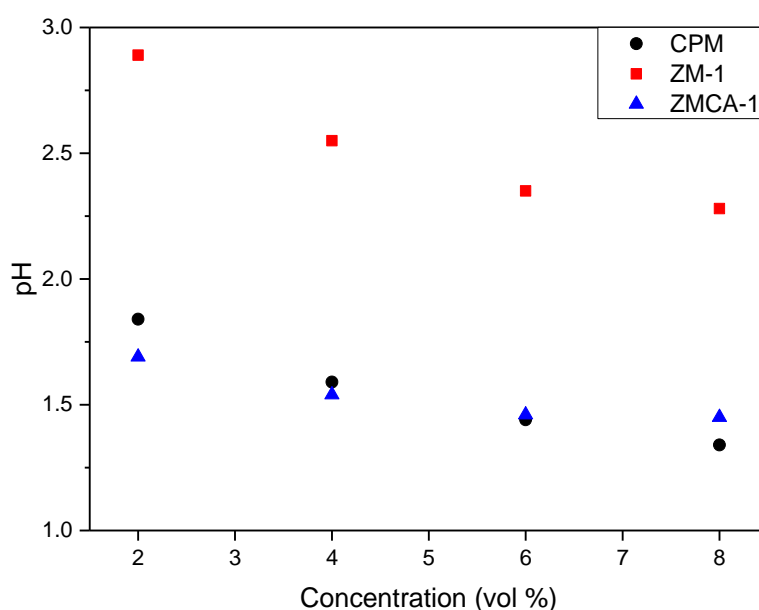


Figure 4-8 Equilibrium pH (after 48 h) for caesium phosphomolybdate (CPM) and zirconium molybdate (ZM-1) and zirconium citramolybdate (ZMCA-1).

The equilibrium pH for all simulants were also measured (at 5 vol%), with Table 8, displaying these results.

Table 8 Presenting the equilibrium pH values for caesium phosphomolybdate (CPM) and zirconium molybdate (ZM-1 and ZM-2) and zirconium citramolybdate (ZMCA-1 and ZMCA-2). at 5 vol%.

Simulant	Equilibrium pH
Caesium Phosphomolybdate (CPM)	1.51
Zirconium Molybdate (ZM-1)	2.45
Zirconium Molybdate (ZMCA-1)	1.50
Zirconium Molybdate (ZM-2)	2.13
Zirconium Molybdate (ZMCA-2)	1.26

For the concentration vs. pH graph, seen in Figure 4-8, it can be seen that as concentration increases the pH decreases, most notable for ZM-1. Both CPM and ZMCA-1 reach a region where their equilibrium pH values fall below pH 1.5 as their concentration goes beyond 4 vol%. As can be seen from the equilibrium pH results, all simulants have pH values that buffer < pH 3 for all concentrations. These low pH values suggest that 'acidification' is occurring, with the formation of the hydrate groups, leading to the release of H⁺ ions.

The equilibrium pH for CPM and ZMCA-1 is ~pH 1.5, for CPM this is near the extrapolated IEP, suggesting that even in Milli-Q water CPM would be unstable. For ZMCA-1, its IEP is much higher than its equilibrium pH, suggesting it will likely be positively charged and stable in Milli-Q water. The equilibrium pH for ZM-1 was slightly higher at pH ~ 2.4, near its IEP, suggesting instability in Milli-Q water. ZM-2 and ZMCA-2 have equilibrium pH values of ~2.1 and ~1.3, respectfully. For ZM-2 and ZMCA-2 both their IEP's are higher than their equilibrium pH, suggesting that they could be naturally positively charged with some potential partial aggregation and instability.

Through TGA, shown in Figure 3-21, ZM-1 and ZM-2 were shown to have fewer moles of water present in their chemical formula than both ZMCA-1 and ZMCA-2. Both ZM-1 and ZM-2 have equilibrium pH values > pH 2, whereas both ZMCA-1 and ZMCA-2 ≤ pH 1.5. Having less water available to form hydrate groups would consequently mean fewer H⁺ ions being released and therefore a higher equilibrium pH, as less acidification could occur.

It is noted that the pH of titania dispersions in Milli-Q water was close to neutral, although very slightly acidic due to the use of deionised Milli-Q water (~pH 5.5–6).

Initially, the solubility of the synthesised simulants (CPM, ZM-1 and ZMCA-1) were investigated to test if there was any measurable dissolution of the bulk particles, that could explain some of the zeta potential and equilibrium pH data. Additionally, the solubility of CPM and ZM has not previously been reported as an exact value for the HAST conditions, although it is widely accepted that both have low solubility (Bykhovskii et al., 2009, Zhang et al., 2013). The gravimetric method was simple to conduct and was done for CPM,

ZM-1 and ZMCA-1 in both Milli-Q water and 2 M nitric acid at three different temperatures; 25 °C (room temperature), 50 °C and 65 °C. Room temperature was chosen as a reference point, whereas the others correspond with temperatures experienced within the HALES plant and within the HASTs. Figure 4-9 shows the solubility curves for the various systems that were investigated.

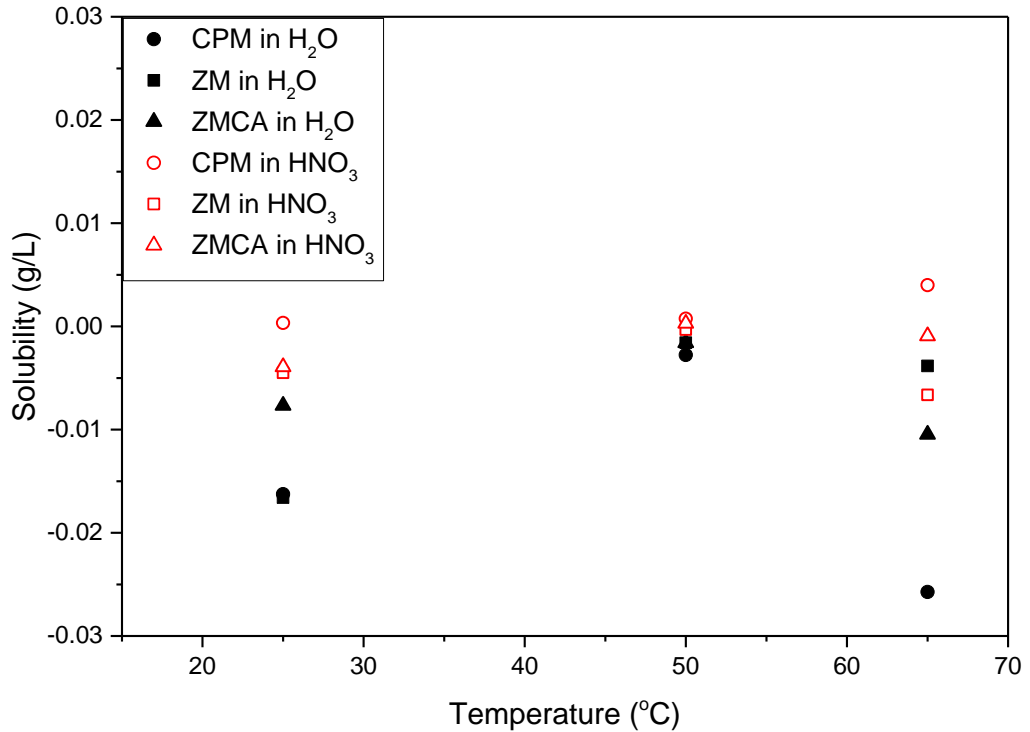


Figure 4-9 Solubility vs temperature graph for caesium phosphomolybdate (CPM), zirconium molybdate (ZM-1) and zirconium citramolybdate (ZMCA-1), in both 2 M nitric acid and Milli-Q water.

On initial inspection the results appear to have some significance however, all solubilities of all systems at every temperature vary a maximum of +/- 0.025 g of solute in 1 L of solvent from 0 g of solute in 1 L. It is not possible for a solubility to be a negative number which suggests this number could be a result of experimental error. This is even more plausible as the sample sizes were very small due to lack of synthesised material, which would contribute to the error. Even if considering the largest positive value of 0.004g/L this is still well below the 0.01g of solute in 1 L value required to class a substance as soluble. As mentioned in Section 2.2.2, a study conducted into the solubility

of ZM found the highest value to be 4 g/L which is 1000 times more than the value of 0.004 g/L for this study (Zhang et al., 2013). This study did not elaborate on their methodology and their conditions were different to those investigated in this research so it is difficult to determine why there is such difference. Figure 4-9 shows a general trend of an increase in solubility from room temperature to 50 °C, which is an expected trend for solubility. The increase in temperature correlates with an increase in kinetic energy that allows solids to be dissolved easier, therefore increasing the solubility. From 50 °C to 65 °C there is a general trend of a decrease in solubility which is consistent with the previous study's trend (Zhang et al., 2013). Using the results shown in Figure 4-9, the conclusions drawn from this solubility study are that CPM, ZM-1 and ZMCA-1 are insoluble and despite pH changes observed in the equilibrium pH, no measurable dissolution is occurring. Therefore, further confirming the hypothesis of the hydrate groups forming allowing the release of the H⁺ ions, being responsible for the low equilibrium pH values. The solubility could be investigated further to find an exact value with more advanced techniques such as Atomic Absorption Spectroscopy (AAS) or a reflection mode IR probe which could pick up peaks from sample supernatants to indicate the presence of the simulants.

4.3.3 Sedimentation

In order to understand the sedimentation results and analysis presented and discussed in this Section, a thorough example analytical process of the CPM in Milli-Q water data is detailed.

4.3.3.1 Procedure for Sedimentation Analysis

The LUMiSizer® STEP-Technology software produces transmission vs. position plots, as shown in Figure 4-10, a), for CPM in Milli-Q water at 4, 8 and 16 vol%. From these raw profiles, various data can be extracted (at a chosen threshold of 40% in this example) such as; time, (s), radial position of the meniscus (R , mm), temperature (°C) and speed (rpm). For this experiment, a threshold of 40% was chosen, as on analysis it was deemed the best representative threshold allowing for comparison of all samples. The position of the meniscus can be easily converted to bed height (H_b , mm) by Equation $H_b = R_0 - R(t)$ (35). The bed height can then be

plotted against time as shown in Figure 4-10, b), where the gradient of the line before it plateaus is equivalent to the initial settling rate, as shown in Figure 4-10, c). This settling velocity could then be converted to settling at gravity, using Equations shown in Figure 4-10 d) and discussed in Section 4.2.2.5.

$$H_b = R_0 - R(t) \quad (35)$$

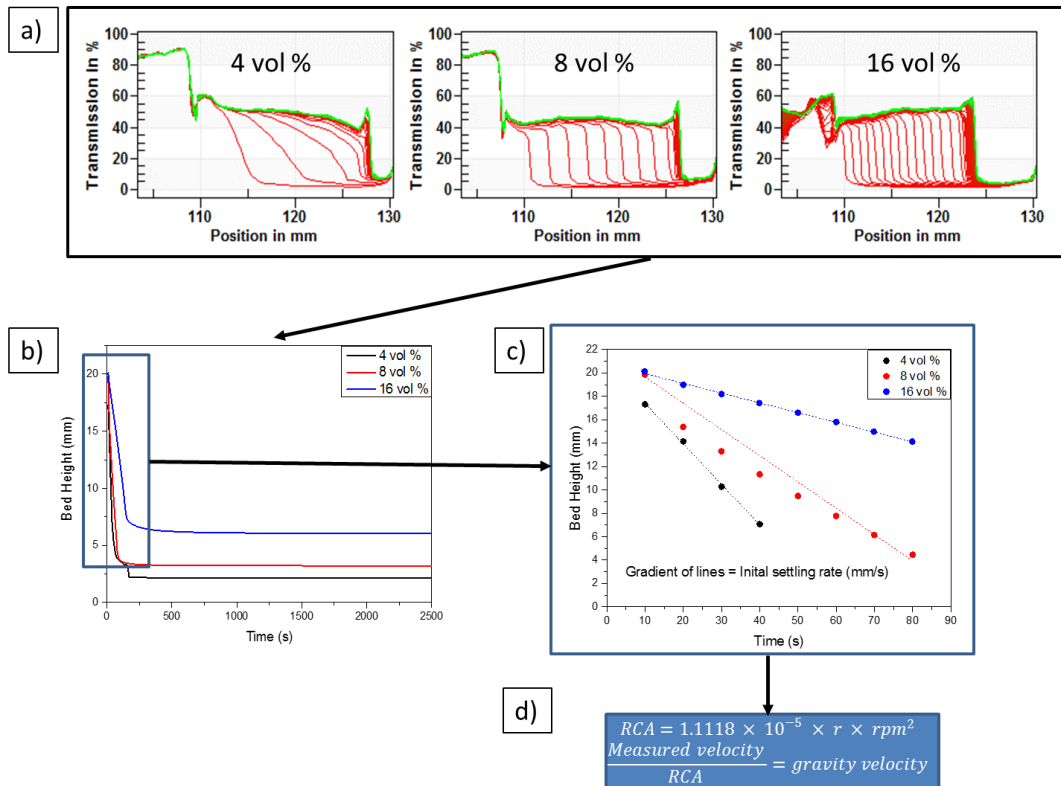


Figure 4-10 Schematic of the procedure used to analyse sedimentation data from raw Lumisizer transmission profiles to a bed height vs time plot where the zoomed in part of the plot shows the initial settling rate.

Once the settling rate for all the concentrations were converted to settling under gravity the values were plotted on a log settling rate vs. concentration graph. The Vesilind model shown by Equation $v_s = v_0 e^{-kX}$ (36), could then be fitted to the data; where settling velocity, v_s is related to concentration, X , through the theoretical settling velocity, v_0 and settling parameter, k (Vesilind, 1968).

$$v_s = v_0 e^{-kX} \quad (36)$$

Figure 4-11, displays the Vesilind plot with the natural log of the settling rate ($\ln \mu$) vs. volume fraction (ϕ) plot for CPM in Milli-Q water, complete with R^2 value.

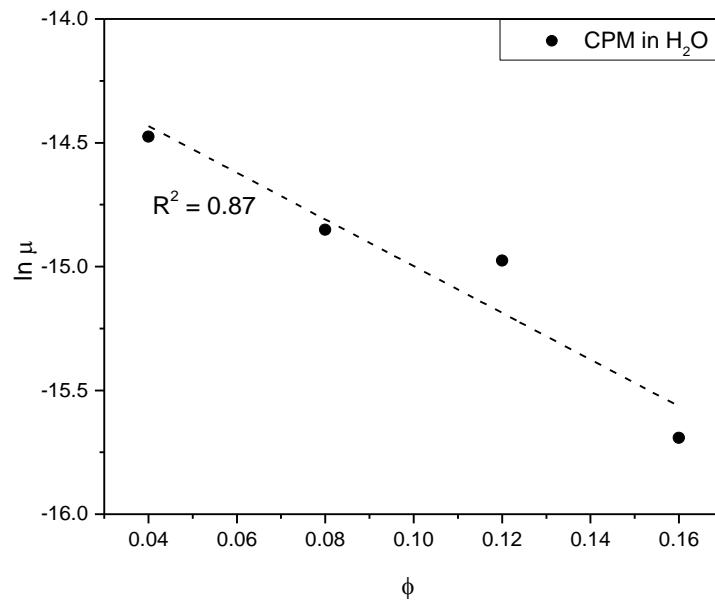


Figure 4-11 Vesilind plot of the natural log of the settling rate ($\ln \mu$) vs. volume fraction (ϕ) plot for caesium phosphomolybdate (CPM) in Milli-Q water. Complete with R^2 value.

The Richardson-Zaki, Equation $\frac{V}{V_s} = \epsilon^n$ (37),

relates V hindered settling velocity to the terminal settling velocity V_s , though the bed voidage and the Richardson-Zaki index, n (Richardson and Zaki, 1954b).

$$\frac{V}{V_s} = \epsilon^n \quad (37)$$

The linear form of this equation, Equation $\ln(u) = \ln u_0 + n \ln \epsilon$ (38), allows linear settling rates $\ln(u)$ to be plotted against the log of the porosity $\ln(1-\Phi)$, to determine the n values.

$$\ln(u) = \ln u_0 + n \ln \epsilon \quad (38)$$

Therefore, the Richardson-Zaki power-law hindered settling model could be applied to the data, where the natural log of the linear settling rates $\ln(u)$ is plotted against the log of the porosity $\ln(1 - \phi)$ as seen in Figure 4-12.

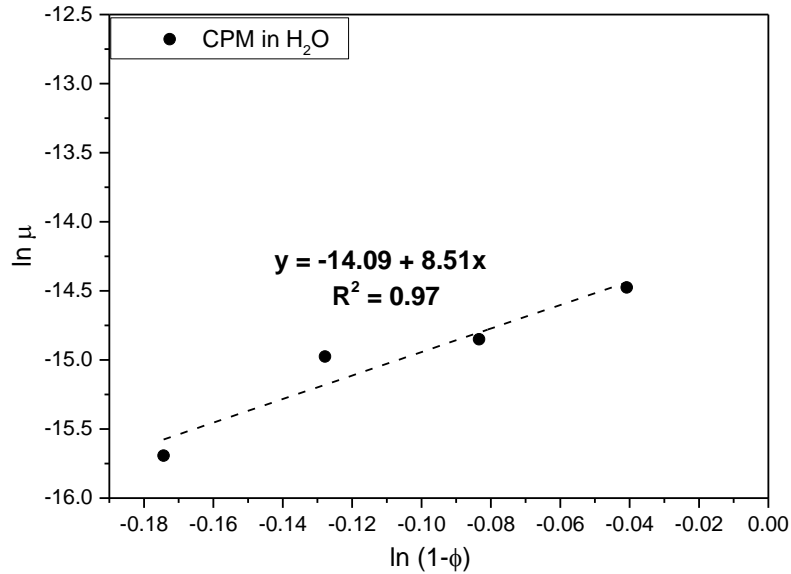


Figure 4-12 Richardson-Zaki plot for caesium phosphomolybdate (CPM) in Milli-Q water. Complete with linear relationship equation and R^2 value.

For the purpose of the sedimentation results (Section 4.3.3.3) both settling rate vs. concentration plots with the Vesilind fit and Richardson-Zaki plots are shown for the simulants. Bed height vs. time plots for CPM, TiO_2 , ZM-2 and ZMCA-2 are all displayed in Appendix Fig. 1.

4.3.3.2 Stokes Estimation

To estimate the expected differences in settling rates for the simulants the

$$\text{Stokes Equation } V_s = \left[\frac{g(p_p - p_i)D^2}{18n} \right] \quad (39) \text{ was used}$$

to theoretically estimate the free settling velocities for the simulants in both Milli-Q water and 2 M nitric acid (Stokes, 1851). Where, V_s is the terminal settling velocity of the particle, g is the gravitational acceleration, p_p is the density of the setting particle, p_i is the density of the fluid, D is the diameter of the particle and n is the viscosity.

$$V_s = \left[\frac{g(p_p - p_i)D^2}{18n} \right] \quad (39)$$

The D50 values provided in Table 7, were used for the particle diameter and density values from Table 4 were used. Water density and viscosity were taken as for standard temperature and pressure with a density of 998.21 kg/m³ and viscosity of 1 mPas. Fluid properties for the 2 M nitric acid solution were taken from literature with a density of 1070 kg/m³ and viscosity of 1.2 mPas (Rhodes and Hodge.Jr, 1929). Figure 4-13, shows displays the estimated Stokes' settling rates for the simulants.

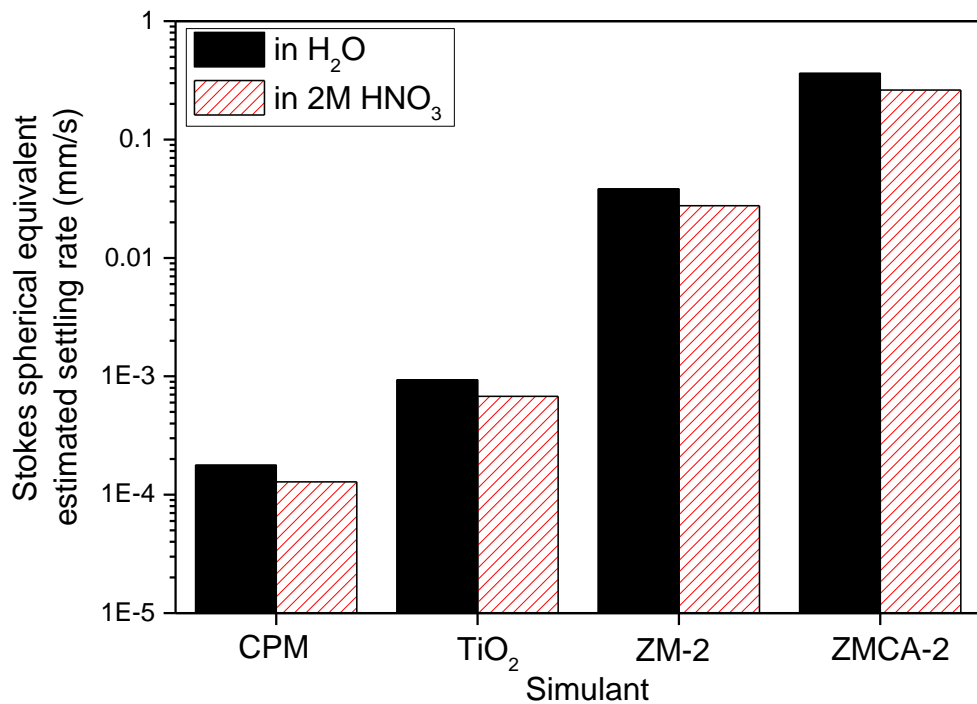


Figure 4-13 Estimated Stokes' settling rates for caesium phosphomolybdate (CPM), titanium dioxide (TiO₂), zirconium molybdate (ZM-2) and zirconium citramolybdate (ZMCA-2) in both Milli-Q water (black) and 2 M nitric acid (red).

The calculated rates plotted in Figure 4-13, indicate that all particles should have slightly lower settling rates in 2 M nitric acid (with a reduction of ~20%, from the increased density and viscosity of the fluid). Additionally, as the particle size distribution increases from CPM<TiO₂<ZM-2<ZMCA-2, the settling rate also increases. However, the Stokes equation does make an assumption that the particles are spherical, which both ZM-2 and ZMCA-2 are not. The Stokes equation does not take into consideration the increased drag associated with particles moving away from the typical spherical shape. It is accepted that as aspect ratios increase, their corresponding drag coefficients

also increase which would in turn hinder their settling rates (Haider and Levenspiel, 1989, Agarwal and Chhabra, 2007, Gabitto and Tsouris, 2008, Loth, 2008, Lau and Chuah, 2013, Dogonchi et al., 2015). This is more of an issue for ZMCA-2 due to its elongated sheaf shape. Therefore, it is expected that the simulant behaviour will deviate from Stokes settling theory, with CPM potentially settling the quickest as a consequence of its reported small particle size.

Figure 4-14 compares the experimentally determined settling rates of 4 vol% dispersions of the simulants to the Stokes estimation. It is not expected that these will directly correlate as they are within the normal hindered settling zones, but they represent realistic concentrations for the HASTs. Therefore, the comparison is more of a qualitative observation to indicate differences in stability in acidic conditions.

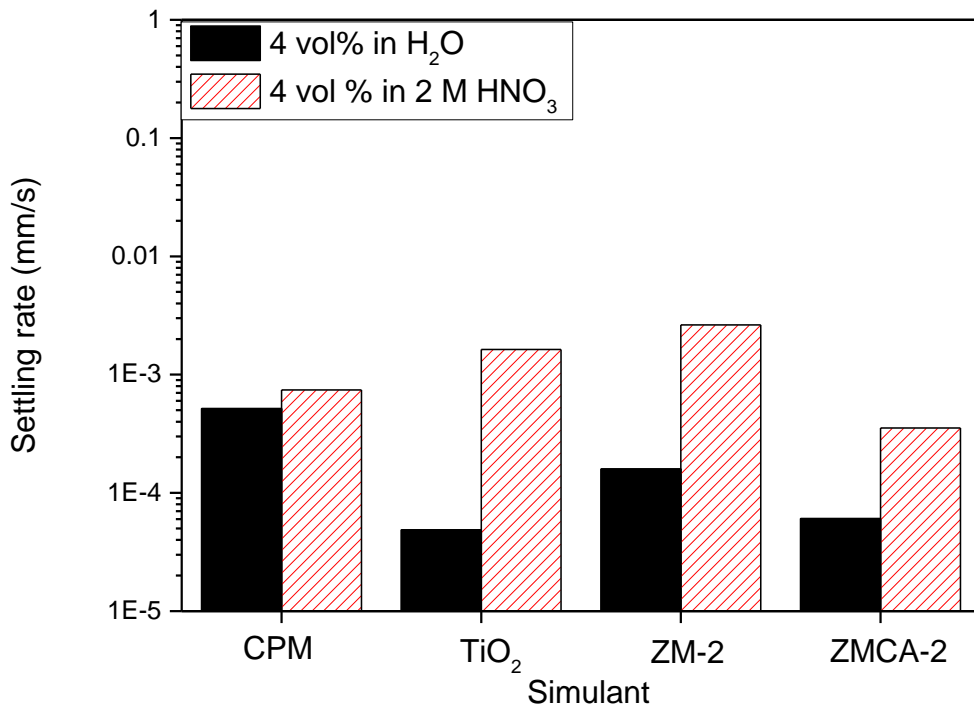


Figure 4-14 Experimentally determined settling rates for caesium phosphomolybdate (CPM), titanium dioxide (TiO₂), zirconium molybdate (ZM-2) and zirconium citramolybdate (ZMCA-2), all at 4 vol% in both Milli-Q water (black) and 2 M nitric acid (red).

For CPM the Stokes' law has been underestimated, however for TiO₂, ZM-2 and ZMCA-2 it has been overestimated. For all simulants their actual settling rate within acid is higher than in Milli-Q water, whereas the Stokes estimation predicted the reverse. This is because the Stokes equation does not take into account the pH of a fluid or the stability of the solids within it.

The difference in experimental settling rates for CPM is minimal for the two conditions, which would suggest similar levels of dispersion stability. As CPM has a naturally low equilibrium pH, it is assumed that in both conditions it is near its IEP, suggesting coagulation is occurring in both. Specifically within the 2 M nitric acid the nitrate counter ions would contribute to collapsing the electric double layer, destabilising the system. Therefore, it is expected that CPM is unstable at low pH, and consequently settles quickly, especially in comparison to the other simulants in water, as it does. TiO₂ in Milli-Q water settles slower than any other system, which coincides with the zeta potential data indicating good stability at neutral pH.

It is not just shape factor to consider in comparing the simulant's settling behaviour, their particle size also has an influence. It is known that on increasing particle sizes for spheres that their settling velocity also increases (Stokes, 1851, Gibbs et al., 1971). CPM is likely to be aggregated as demonstrated from the zeta potential and equilibrium pH data. Therefore its actual particle size is predicted to be much larger than the 300 nm measured in the Mastersizer®. Within the Mastersizer® cell the pH is more likely to be around neutral, as particle concentrations are within the ppm range thus, acidification is not observed. Therefore, the Mastersizer® data may not necessarily correlate to what we observe at higher concentrations for the sedimentation behaviour. This highlights the complexity of CPM as an individual system, where even after a number of experiments only now can a judgement call be made on its likely aggregation state and stability.

For ZM-2 and ZMCA-2 their representative drag coefficient will be larger than that of a sphere (Haider and Levenspiel, 1989, Lau and Chuah, 2013, Dogonchi et al., 2015), due to their irregular morphology. Therefore, they will likely settle slower than CPM. This is true for both ZM simulants, apart from ZM-2 in acid. ZM-2 has an equilibrium pH very close to its IEP of pH 2.5,

therefore within Milli-Q water it is predicted to be slightly positively charged although still within the unstable region. Within acid, it is likely the influence of the high electrolyte conditions that have significant impact on increasing the settling rate.

For TiO₂, ZM-2 and ZMCA-2 they all sediment at considerably higher rates in the acidic environment, indicating that the high electrolyte conditions lead to significant coagulations of the dispersions, likely through the collapse of the electric double layer. For ZMCA-2 the difference between the settling rates in both environments is less than that for ZM-2, as even though the IEP's are the same, ZMCA-2's equilibrium pH is lower. Therefore, in the Milli-Q water environment ZMCA-2 will be more positively charged than ZM-2 and consequently slightly more stable, settling slower. Additionally, due to its particle shape and size it will have a larger drag coefficient, as a consequence of its high aspect ratio. Therefore it will settle slower than ZM-2 and deviate from what Stokes law would predict (Haider and Levenspiel, 1989, Lau and Chuah, 2013, Dogonchi et al., 2015). The Stokes law is limited by making assumptions of spherical particles, low particle concentration and laminar flow, hence such deviation from predicted to actual settling rates. It is suggested that sedimentation behaviours are also influenced by particle charge, stability within a given medium and morphology.

It should be noted that, the presented settling data were taken at a single threshold of 40%. A single threshold represents a certain fraction of the particles, but it does not capture complete settling data, especially for polydisperse systems. For example, when the ZMCA-2 settling data were analysed at a range of thresholds, calculated linear settling rates vary by almost an order of magnitude (comparing 10% and 80% thresholds). While the 40% threshold was chosen as a fixed value to allow comparison of all samples, it appears this likely correlates to a fraction of the dispersion that is under the medium sizes. Therefore, caution should be taken when extracting data using light transmission as a means of observing a clear interface where there are a range of particle sizes. These issues are extenuated in centrifugal systems, as they tend to separate particles further under the centrifugal force. Although for the purpose of this study it is deemed sufficient from a comparative view point.

4.3.3.3 Vesilind and Richardson-Zaki Plots.

The Vesilind plot showing the natural log of the settling rates at gravity ($\ln \mu$) plotted against volume fraction (ϕ) in both Milli-Q water and 2 M nitric acid for CPM, TiO_2 , ZM-2 and ZMCA-2, can be seen in Figure 4-15, with corresponding R^2 values. Note there were some discrepancies found at 2 vol% for CPM, TiO_2 , and ZMCA-2, in addition to 4 vol% for ZM-2. Therefore, the settling rates for these values were not plotted, the reasons will be discussed in relation to the Richardson-Zaki data. Additionally, for ZM-2 due to experimental error no data for 2 vol % could be reported.

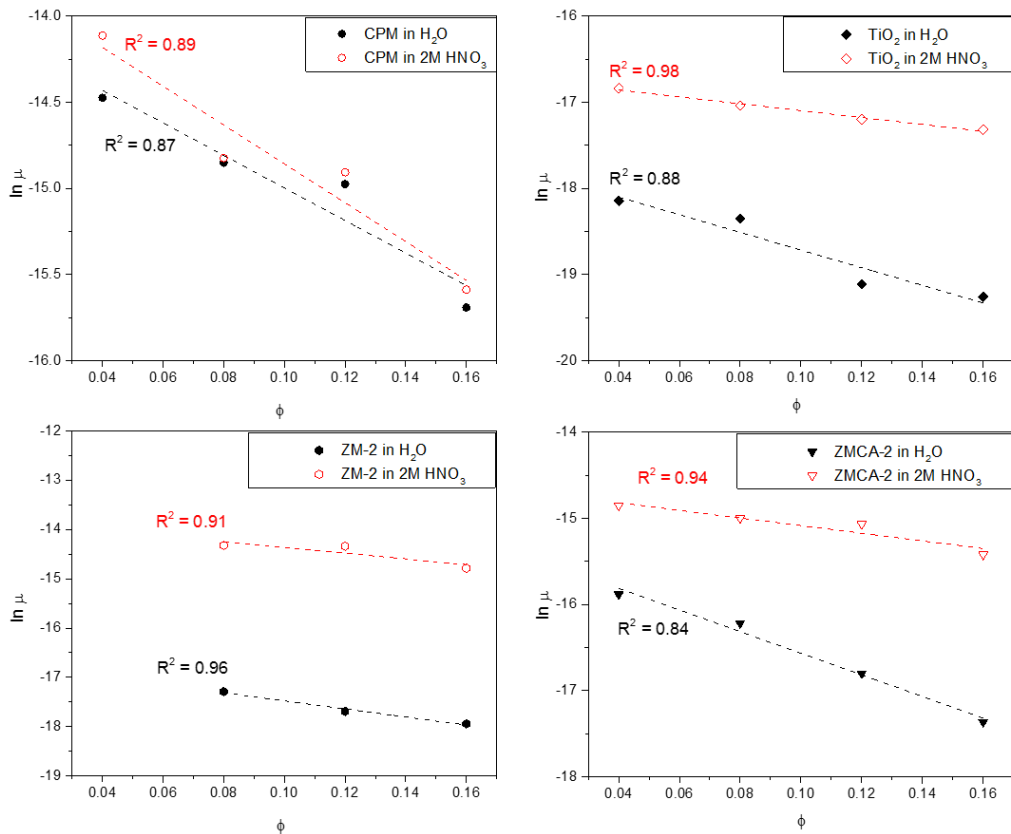


Figure 4-15 Vesilind plot of the natural log of the settling rate ($\ln \mu$) vs. volume fraction (ϕ) for caesium phosphomolybdate (CPM), titanium dioxide (TiO_2), zirconium molybdate (ZM-2) and zirconium citramolybdate (ZMCA-2) in both Milli-Q water (black) and 2 M nitric acid (red). Complete with R^2 values.

It can be seen in Figure 4-15 for all simulants that the settling rate decreases with an increase in concentration. A consequence of an increase in concentration results in more particle-particle interactions, therefore more opportunities for aggregation, hence increasing the size and drag force of the

particles and decreasing the settling rate. This correlation of a decrease in settling rate with increase of the concentration was also reported by Paul (2014) and Dunnett et al. (2016). The settling trends of the CPM in both conditions is very similar, as would be expected from the stability and Stokes discussion (Section 4.3.2 and 4.3.3.2). TiO_2 , ZM-2 and ZMCA-2 all clearly settle quicker in the acidic environment than within Milli-Q water, which was also reported by Paul (2014).

The Vesilind model is valid for the hindered settling region, which is appropriate for the simulants as they are expected to aggregate, as discussed in Section 4.3.2 and therefore settle within this region. Considering the R^2 values of the fits in Figure 4-15, all have R^2 values ≥ 0.84 . Suggesting a good fit with the Vesilind model. The free settling velocity predicted from the Vesilind model for each system is shown in Figure 4-16.

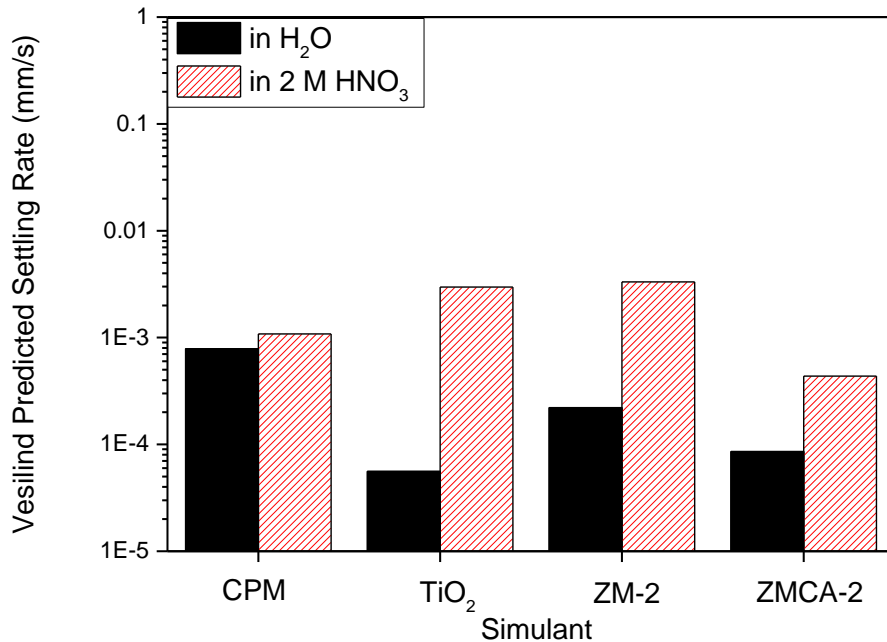


Figure 4-16 Free settling velocities predicted from the Vesilind model for caesium phosphomolybdate (CPM), titanium dioxide (TiO_2), zirconium molybdate (ZM-2) and zirconium citramolybdate (ZMCA-2), in both Milli-Q water (black) and 2 M nitric acid (red).

It is observed that CPM settles almost identically within both environments, as previously seen and discussed when considering the 4 vol % data (Figure 4-14). From this analysis it is further assumed that CPM is aggregated in both environments as previously concluded in Section 4.3.3.2.

There is significant difference in the settling rates of TiO₂, ZM-2 and ZMCA-2 in acid compared to in Milli-Q water highlighting again the significant impact of the high effective electrolyte concentration within acid.

Considering the morphology and size of ZM-2 in comparison to ZMCA-2, it is potentially easier for ZM-2 elongated square bipyramid shape particles to form aggregates and consequently increasing the overall particle size, hence ZM-2's faster settling rates, despite ZMCA-2 being reported to be three fold larger. Additionally, larger particle sizes can sometimes decrease the amount of particle-particle interactions as a result of a decrease in surface area available to interact (Vesaratchanon et al., 2008). With ZMCA-2 being a large wheatsheaf shape, even if unstable it may be difficult for it to form aggregates. The orientation of the ZMCA-2 could also impact the formation of large aggregates. Fan et al. (2004) reported that slender i.e. elongated non-spherical particles will oscillate during sedimentation, therefore settling with varying orientations rather than attempting to minimise their drag (by settling with a vertical orientation, parallel to the flow). When considering the orientation of an elongated particle the most stable orientation is considered to be when it is horizontal, therefore perpendicular to the direction of flow (Fan et al., 2004, Lau and Chuah, 2013). Liu and Joseph (1993) reported that in considering an increase of particle concentration, this perpendicular orientation, eventually changes so that the particle orientates vertically, therefore parallel to the flow. In the case of ZMCA-2 at the highest concentration of 16 vol% the slowest settling rate is observed, therefore suggesting a mix of both orientation and size effects influence its sedimentation behaviour.

For additional quantitative analysis, the sedimentation of the simulants for the range of concentrations in both Milli-Q water and acid were analysed using the Richardson-Zaki power-law hindered settling model, with data presented in Figure 4-17.

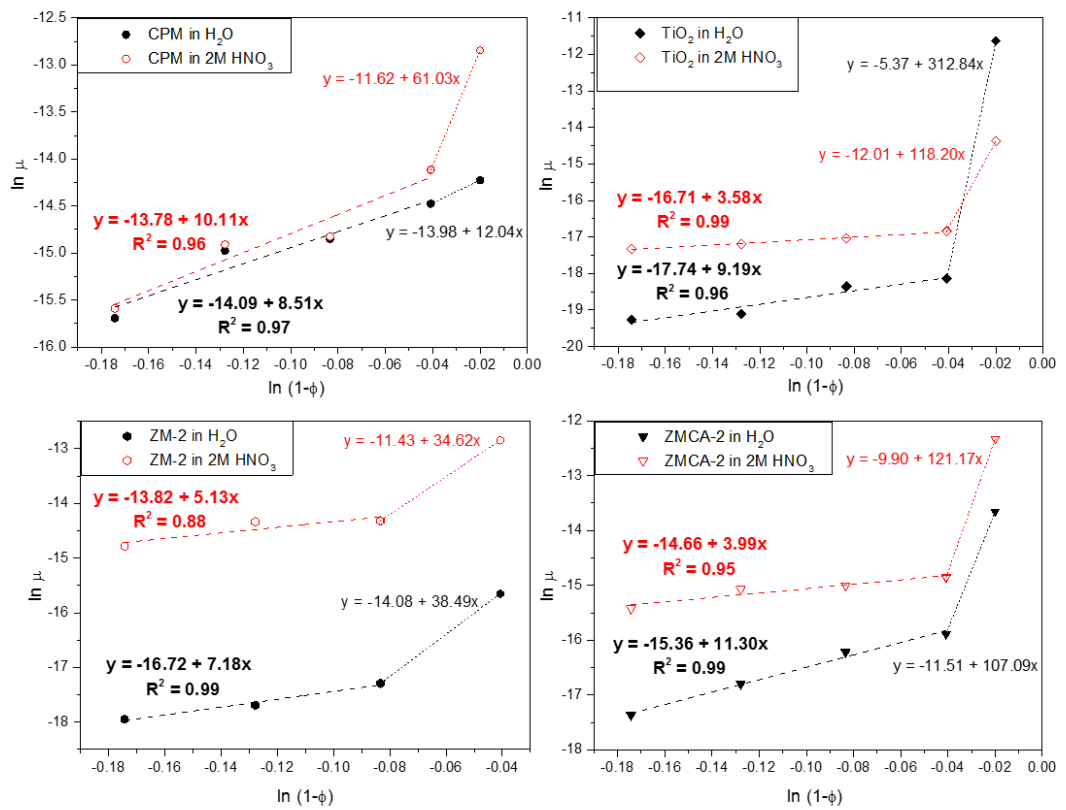


Figure 4-17 Richardson-Zaki plots for caesium phosphomolybdate (CPM), titanium dioxide (TiO_2) zirconium molybdate (ZM-2) and zirconium citramolybdate (ZMCA-2) in both Milli-Q water (black) and 2 M nitric acid (red). Complete with linear relationship equations and R^2 values..

The discrepancies for the 2 vol% concentrations and 4 vol% for ZM-2 previously mentioned are believed to be a result of two different regions of settling as shown by the two linear fits in Figure 4-17. Multiple settling regions have also been previously observed for aggregated systems such as kaolinite at 0.7 % (Michaels and Bolger, 1962) and for magnesium hydroxide over a similar volume % of around 2.4 (Johnson et al., 2016). The exact reasoning behind these multiple settling regions is uncertain, although there are a number of hypotheses. Michaels and Bolger (1962) attributed the two regions to be the formation of chains and networks of aggregates around a threshold concentration. Whereas Johnson et al. (2016) attributed the two regions to be the change from discrete aggregates settling to the hindered settling of the aggregates (essentially collective settling of the aggregates). The hypothesis suggest by Johnson et al. (2016) was first reported for calcium carbonate,

where two critical concentrations were observed, representing changes in settling regions (Allain et al., 1995). Allain et al. (1995) reported the initial critical concentration to represent the transition of discrete aggregates settling to hindered settling and the second to represent the gel point of the suspension.

In the case of the simulants, for both CPM and TiO_2 it is suggested that there are two different hindered settling regions. With the initial settling region being dominated by large aggregates, then the second region with a lower exponent where it is no longer clear what the average size of the aggregates are, because the spacing between them approaches the spacing between individual particles within the aggregates. Essentially the change in behaviour occurs for aggregates, when the inter-particle spacing between particles in aggregates starts to approach the length-scales of spacing between aggregates.

For the ZM simulants it is less likely to do with aggregation, especially as they have been reported to be more stable in Milli-Q water. However, it is suggested that in the less concentrated dispersion, the irregular particles are allowed a greater degree of freedom to re-orientate, which would therefore lead to more hindered settling effects and a rapid reduction in settling rate between the lower concentrations (4 vol % to 8 vol % for ZM-2 and 2 vol % to 4 vol % for ZMCA-2). This is especially the case for ZMCA-2, where once the concentration goes up to a certain threshold, the wheatsheaves no longer have the same degree of freedom to re-orientate, leading to a lower hindered settling exponent in the second settling region.

The exponent values associated with the fits can aid understanding on the coagulation of the simulants, in addition to the influence of particle shape. For non-agglomerated spherical dispersions, an exponent of ~ 4.65 would be expected (Richardson and Zaki, 1954a). The general fits on the second settling region for all simulants have R^2 values of ≥ 0.88 showing a good fit to the Richardson-Zaki power-law.

For spheroidal CPM, its exponent values were 8.51 and 10.11, in Milli-Q water and acid, respectively, while for the TiO_2 , its exponents were 9.19 and 3.58. For CPM the values are nearly double that expected for a spherical system,

inferring a high degree of aggregation in both systems. The fast settling rate and high exponent of CPM in both systems is consistent with its shape, size and instability previously discussed. The exponent value for TiO_2 is also doubled for a spheroidal system in Milli-Q water, reporting a similar exponent value to that previously reported of 8.8 (Turian et al., 1997). The high exponent in water suggests a degree of aggregation whereas the exponent value is < 4 in acid. Spheres give the lowest degree of drag and therefore the lowest exponents, consequently it should not be possible for this value to occur within a settling system. A potential possibility is that the system initially settles at 2 vol % then transitions to within the compression region.

For the ZM-2 and ZMCA-2 simulants, as discussed both show similar trends across the concentration regime measured, with their settling rates in acid being faster than that in Milli-Q water. Additionally, there are some similarities in the power-law exponent values, for ZM-2 in Milli-Q water it is 7.18 while for ZMCA-2 it is 11.30. These values are higher than expected for 'spherical' particles, which is expected due to the cuboidal and wheatsheaf shapes of the ZM (Bargiel et al., 2013). It has been previously reported that high exponent values occur from the enhanced drag on non-spherical particles due to their shape (Chong, 1979, Turney et al., 1995, Tomkins et al., 2005). Indeed, shape factor may help explain the exponent value for ZMCA-2, as the orientation of the elongated wheatsheaf/rod-like particles may have an additional effect on the drag, which will likely be greater if they adopt a horizontal orientation (Loth, 2008, Dogonchi et al., 2015). The exponent values are again both similar in acid, at 5.13 and 3.99 for ZM-2 and ZMCA-2, respectively. In this case the exponent values in Milli-Q water are higher than in acid, even though settling rates are lower. This behaviour may indicate that while agglomerates are smaller in Milli-Q water, they have a more open structure, which increases hindered settling effects. Additionally, in comparing the differences between ZM-2 and ZMCA-2 it may be the aggregated ZM-2 clusters actually have a reduced drag in comparison to the elongated and slightly more stable ZMCA-2 particles.

Therefore, in considering the settling results for the individual simulants in potential POCO environments, lower acidity wash waters may aid in stabilising

ZM dispersions, reducing issues of sedimentation on transfer, whereas effects on CPM will likely be minimal.

4.3.3.4 Mixed System Settling Behaviour

Figure 4-18, displays the settling rates for the mixed systems of CPM:ZMCA-2, at 1:3, 1:1 and 3:1 weight ratios with a total concentration of 4 vol% in Milli-Q water and 2 M nitric acid.

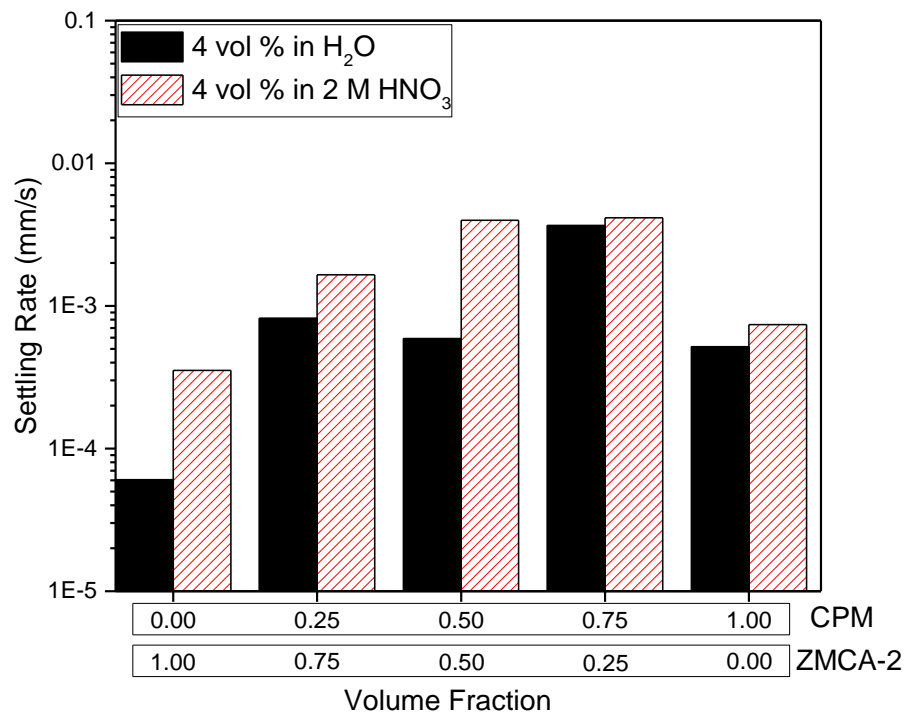


Figure 4-18 Experimentally determined settling rates for individual and mixed systems of caesium phosphomolybdate (CPM) and zirconium citramolybdate (ZMCA-2) at 1:3, 1:1 and 3:1 weight ratios at 4 vol% in Milli-Q water (black) and 2 M nitric acid (red).

There have been a number of studies investigating the settling of different sized spherical particles with the same density (Davies, 1968, Lockett and Bassoon, 1979, Mirza and Richardson, 1979, Greenspan and Ungarish, 1982, Kondrat'ev and Naumova, 2006, Kondrat'ev and Naumova, 2007, Krishnamoorthy, 2010) and with different densities (Masliyah, 1979, Patwardhan and Tien, 1985). However, there has been little done in the way of investigating the settling of a system, that has particles with different sizes, shapes, densities and surface charges.

On visual inspection of Figure 4-18 it is noted that each of the mixed systems settle quicker than the individual systems, suggesting that the different simulants are interacting.

The proposed theory of interaction is that ZMCA-2 is positively charged and that the aggregated CPM is slightly negatively charged; resulting in strong particle-particle interactions, forming heavy aggregates that results in the gravitation force dominating. Additionally, these larger aggregates could repel one another, increasing the settling rate. This theory is based upon the assumption that ZMCA-2 at low pH is positively charged and CPM is negatively charged. The IEP for CPM was not directly measured, so the value reported was extrapolated. Therefore, CPM and ZMCA-2 could be oppositely charged and consequently attracted to one another. Additionally, as a result of the irregular wheatsheaf shape of ZMCA-2, CPM aggregated particles could preferentially bind to one face over another dependent on concentration ratios. The attraction of the particles to one another could also impact the orientation of the wheatsheaf particle, especially CPM particles preferentially bind to one face over another. These large aggregated combined particles could then potentially repel each other. If they were to orientate in a more vertical position this could actually decrease the drag force and increase settling rate. Additionally, the aggregates formed could become so heavy that the gravitation force overrides any drag resistance.

Figure 4-19 illustrates a basic schematic of the aforementioned proposed theory.

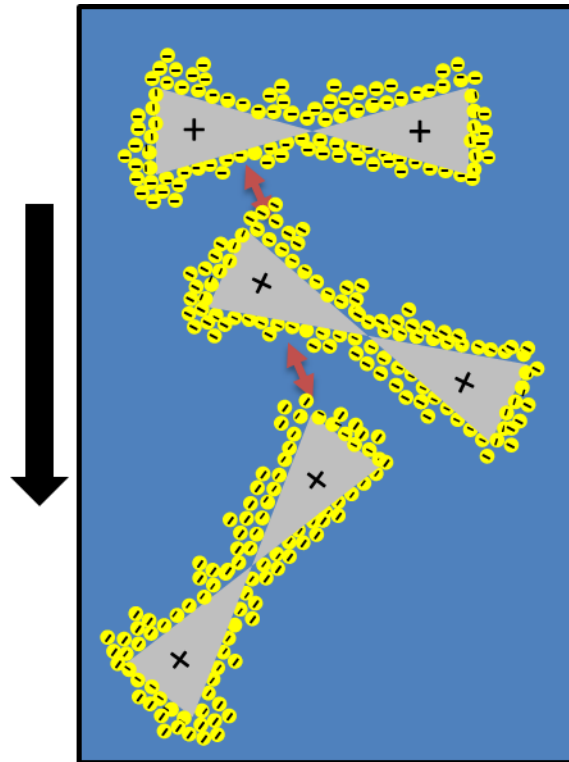


Figure 4-19 Illustration of the potential interaction between spherical caesium phosphomolybdate (CPM, yellow circles) particles and wheatsheaf zirconium citramolybdate (ZMCA-2 grey 'bow ties'), with black arrow depicting the settling direction and red arrows depicting potential repulsions.

Considering the suggested interaction theory and applying it to the results presented in Figure 4-18. The mixed system with the highest mass of CPM settled the fastest, with similar settling behaviour observed in both environments, a similar trend to that observed for pure CPM in both environments. It seems in mixing with some ZMCA-2, the particle-particle interaction potentially forces a less stable orientation of the large wheatsheaf shape, increasing the settling rate. Although overall the general behaviour of the CPM dominates these mixed systems, the settling is around an order of magnitude larger.

For the CPM:ZMCA-2 at a 1:1 weight ratio, the settling in acid is almost the same as the 3:1 ratio system, however there is a significant drop within Milli-Q water. If the interaction suggested were applied it could suggest that the drag force in Milli-Q water is increased with a higher presence of ZMCA-2, perhaps with the interacting particles forcing a more stable orientation.

Additionally, this could highlight the effects of high electrolyte concentration on the systems in acid, potentially collapsing the electric double layer around the particles, resulting in high levels of instability and increased settling rates.

Considering the CPM aggregates onto the ZMCA-2, creating large clusters, the settling data highlights the change in the structure formed is a complex interaction based on varying number densities of each species. This is even more of an important finding considering the HASTs, as the settling rates for the mixed systems within them could be faster than anyone has previously predicted.

Overall, the results of the mixed systems demonstrate that CPM and ZM do interact together, which will impact their dispersion behaviour. Further work is recommended in order to understand the interactions between the simulants, as the most likely scenario within the HASTs will be a range of ratios of the mixed systems.

4.3.3.5 Temperature Influence on Settling Behaviour

The settling rate of 4 vol% CPM in both Milli-Q water and 2 M nitric acid at both 25 °C and 50 °C, is shown in Figure 4-20. This experiment was conducted to compare the effects of temperature on settling rate, specifically the temperature which would be found within the HASTs. As can be seen an increase in temperature did significantly increase the settling rate over a magnitude of 1.5. Additionally, the difference between the settling rate of CPM in Milli-Q water and 2 M nitric acid lessened, meaning the temperature dominated over the effect of pH.

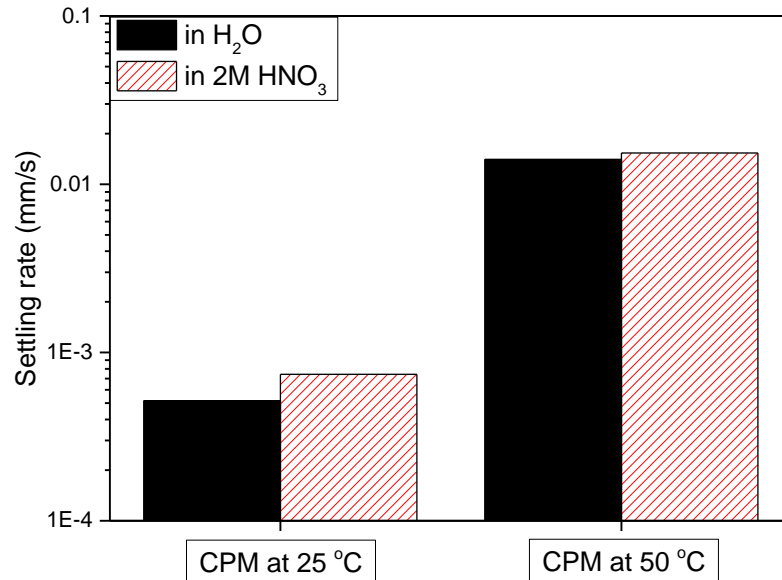


Figure 4-20 Experimentally determined settling rates for caesium phosphomolybdate (CPM) at both 25°C and 50°C with concentration of 4 vol% in Milli-Q water (black) and 2 M nitric acid (red).

Few studies have looked into the effect of temperature on settling rate, however there have been contradicting findings, seemingly it is the system that dictates whether the temperature increases or decreases the settling rate. One study found a decrease in temperature resulted in solids ‘crashing’ out of solution. Therefore the temperature actually promoted keeping the solids in suspension (Lau, 1994). This is reported to be a result of the increase in repulsive forces which are linearly proportional to an increase in temperature (van Olphen, 1977). Contradictory to this another study reported that for granular sludge that an increase in temperature increased the settling rate, which is what this research also found (Winkler et al., 2012). This is a result of the decrease in viscosity of the dispersion medium. Using the Stokes equation, the settling rates of CPM in the different temperature mediums could be estimated to confirm whether the difference is related to the viscosity of the medium. As discussed in Section 4.3.3.2, the actual settling rates vary from the Stokes estimation, however it is the change of the settling rate not the absolute value that is of concern. It was found that a reduction in viscosity resulted in an increase of settling rate by one order of magnitude, therefore implying the changes between 25 °C and 50 °C are viscosity related.

It is likely that each system has a temperature threshold, whereby the settling rate increases until a certain value has been reached. Although this cannot be confirmed for all the simulants, if a range of temperatures were investigated for CPM it could show that at a certain temperature the settling rate decreases. It is proposed that at 50 °C all the simulants would settle faster.

4.4 Conclusions

This Chapter has presented both results and discussion on the particle size, stability and sedimentation behaviour of the nuclear waste simulants both procured and synthesised for this research. TiO₂ as a commercially available alternative was introduced as a comparable simulant material to CPM as a result of its spheroidal morphology. CPM was synthesised at 100 °C and found to have a bimodal particle size distribution, with a PDI over 4 times larger than that of CPM synthesised at 50 °C, demonstrating the presence of large agglomerates and its potential breakdown at high temperature. Particle size distributions were found to be single modal and increase from CPM < TiO₂ < ZM-2 < ZM-1 < ZMCA-2, with ZMCA-1 displaying a bi-modal distribution. ZMCA-1 is suggested to differ as a result of a variation in its surface chemistry, from the addition of citric acid into its synthesis.

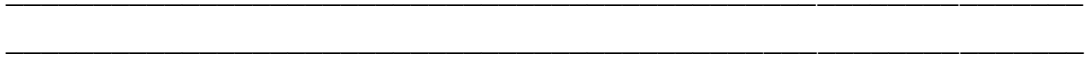
The dispersion stability of the simulants in Milli-Q water and 2 M nitric acid were observed by comparing zeta potential, solubility and pH measurements with centrifugal sedimentation analysis. All simulants were found to have low IEP values; however, acid group leaching reduced the natural pH of Milli-Q water suspensions to around or below these values. Therefore, in low pH conditions such as those experienced within the HASTs, the nuclear waste products are likely to be unstable and coagulate, especially CPM. All synthesised simulants were found to be insoluble and despite pH changes observed in the equilibrium pH, no measurable dissolution is occurring.

Stokes Law was applied to the simulants to predict settling behaviour and found to inaccurately estimate the settling rates, as a result of the complex behaviour they display within dispersions. CPM displayed similar settling behaviour in both environments, likely a consequence of both its low IEP and equilibrium pH. TiO₂, ZM-2 and ZMCA-2 all displayed similar behaviour,

settling quicker within the more acidic environment. Additionally at concentrations > 4vol%, there were only slight observed decreases in the settling rate with an increase in concentration. Their relatively low settling rates in Milli-Q water, suggest a degree of stability that decreases significantly in acid, assumed to be caused by coagulation from the collapse of the electric double layer. On analysing the results of the mixed system settling behaviour, it is clear that there is an interaction between CPM and ZMCA-2, resulting in faster settling rates for mixed systems over individual. Temperature was reported to increase the settling rate of CPM, suggesting rates reported for the various systems will be higher within the HAST conditions.

Overall, the results highlight the complex surface chemistry of these precipitated nuclear wastes, and imply their stability may be critically altered, depending on changes in acid levels as waste treatment moves to a POCO phase. In considering the settling results for the individual simulants in potential POCO environments, lower acidity wash waters may aid in stabilising ZM dispersions, reducing issues of sedimentation on transfer, whereas effects on CPM will likely be minimal. The settling behaviour of the mixed systems suggest that a generalised POCO methodology may be difficult if the conditions and ratios vary in each tank. To further the comprehension of the behaviours of the systems an understanding of their settled bed strength (compressive yield stress) and subsequently their permeability will assist, as presented in Chapter 5.

Chapter 5 Compressive Yield Stress and Permeability Investigations



5.1 Introduction

Solid-liquid separation techniques are vital for a number of industrial processes, where an understanding of the behaviour of particulate suspensions is crucial. This is particularly the case in respect of the management of waste slurries, where the separation of the waste into a liquor and manageable solids is a desirable outcome (Landman and White, 1994).

The previous Chapter concluded that the simulants (CPM, ZM-2 and ZMCA-) are relatively unstable within 2 M nitric acid and therefore the likelihood is that they will settle within the HASTs. Consequently, it would be advantageous to know how well packed the simulant beds formed are. Compressive yield stress is an implicit function of the strength of interparticle bridging forces, effectively the parameter which determines the strength of a settled bed (Landman and White, 1994). Over the years, a number of different methods have been utilised in determining the compressive yield stress, such as pressure filtration (Green and Boger, 1997, Green et al., 1998, Channell et al., 2000), drying consolidation (Brown and Zukoski, 2003) and centrifugation (Buscall, 1982, Buscall and White, 1987, Miller et al., 1996, Green and Boger, 1997, Yow and Biggs, 2013). The centrifugation methodology was chosen for this research, being both easy to implement and requiring a small sample volume.

The compressive yield stress of a settled bed can be linked to the permeability, as the more the particle network yields and compresses, the smaller the pore spaces for liquid to permeate through, therefore the higher the resistance of the cake (Buscall, 1982, Green and Boger, 1997, Channell et al., 2000, Antelmi et al., 2001). Typical experiments investigating permeability require large volumes of material, in dead-end filtration tests (Lu et al., 1998, de Krester et al., 2001, Teoh et al., 2006). However, an alternative technique utilising centrifugation has also been used (Valleroy and Maloney, 1960, Green et al., 1996, Smiles, 1999, Chu and Lee, 2002, Barr and White, 2006, Usher et al., 2013, Fukuyama et al., 2013). Where Loginov et al. (2014) published a novel method of multistage centrifugation in determining permeability that required a low volume of suspension material. This method was further developed during this research. Therefore, allowing both

compressive yield stress and permeability experiments to be conducted with the same technique. This is, as far as the author is aware, the first time the LUMiSizer® has been used to investigate both the compressive yield stress and permeability of a material individually within one study.

A number of studies have investigated the influence of particle size (Tomas and Reichmann, 2002, Wakeman, 2007, Bourcier et al., 2016), morphology (Boskovic et al., 2005, Hakkinen A et al., 2005, Wakeman, 2007, Beck et al., 2009, Bourcier et al., 2016, Perini et al., 2019) and stability (Wiesner M et al., 1989, Hlavacek and Remy, 1995, Waite et al., 1999, Pignon et al., 2000, Antelmi et al., 2001, Guan et al., 2001, Cabane et al., 2002, Hwang and Liu, 2002) on permeability behaviour. As the simulants (CPM, ZM-2 and ZMCA-2) have a range of particle sizes, morphologies and stabilities, it is of scientific interest to determine the influence these properties have on their ability to be filtered. Furthermore, very little has been done in the way of determining the permeability of a mixed particulate system.

In regards to the POCO of the HASTs, the HAL containing a mix of both CPM and ZM will most likely need to be re-suspended and/or washed out with an appropriate solution. Therefore, separating the solid and liquid waste forms, could be both required and financially beneficial for POCO and onward processing for vitrification. For filtering to be considered as a viable option, the permeability of these solid beds needs to be understood. Hence, the development of permeability experiments in this Chapter.

5.2 Materials and Methodology

5.2.1 Materials

There is one additional simulant introduced in this Chapter from those presented in Section 3.2 (Table 2), which is kaolin, a type of natural clay, the SEM image of which is shown in Figure 5-1. The SEM image shows the layered plate-like structure expected for kaolin. The reason for the introduction of kaolin, is that it was one of the materials studied by Loginov et al. (2014), who published a novel methodology that was utilised and developed to study permeability for this Chapter. Therefore, in terms of confirming the methodology for permeability was repeated accurately, kaolin was used as a

preliminary and comparative material. The kaolin suspension was both provided and prepared by Maksym Loginov (The Laboratory Science & Technology of Milk & Egg (STLO), Rennes, France) dispersing the kaolin powder (The mining company of kaolins of Morbihan, Kerbriant, France) in tap water at a 25 vol% concentration, with a reported density of $2.6\text{g}/\text{cm}^3$ for the solid.

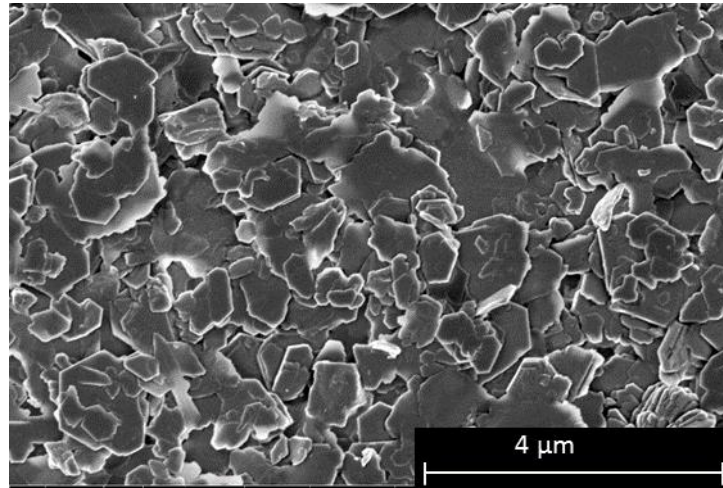


Figure 5-1 Scanning Electron Micrograph (SEM) of kaolin, completed with scale bar. The magnification was 12k.

As a result of lack of material, ZM-1 and ZMCA-1 were not studied for this Chapter. In addition, as kaolin was introduced as a preliminary material, it was decided that the compressive yield stress and permeability of TiO_2 would not be investigated. Therefore, kaolin at 25 vol%, CPM at 10 vol % , ZM-2 and ZMCA-2 at 16 vol % were the simulants selected for both compressive yield stress and permeability investigations. Additionally, mixed systems of CPM and ZMCA-2 at 16 vol%, with weight ratios of 1:3, 1:1 and 3:1 were also studied.

For both compressive yield stress investigations and permeability experiments, the simulants were dispersed in either Milli-Q water or 2 M nitric acid, to compare their behaviour in both conditions. For kaolin, as it was provided as a made up dispersion in water it was not tested in 2 M nitric acid.

5.2.2 Compressive Yield Stress

The LUMiSizer® was used for centrifugal-sedimentation based experiments from which the compressive yield stress properties could be determined. The experimental method was based upon that published by Yow and Biggs

(2013). A detailed explanation of how the LUMiSizer® works can be found in Section 4.2.2.5.

LUMiSizer® polycarbonate (PC) disposable cells (110-135XX) with a 2.0 mm optical path length were used for these compressive yield stress experiments. CPM at 10 vol%, ZM-2, ZMCA-2 and mixed systems (1:3, 1:1, 3:1 CPM:ZMCA-2 weight ratio) at 16 vol% dispersions were made up separately in both Milli-Q water and 2 M nitric acid. Kaolin at 25 vol% in water was provided (as previously mentioned in Section 5.2.1). The different starting vol % were chosen to ensure the simulants would be in the compressive region as shown from the settling experiments, without using excess material. All compressive yield stress experiments were conducted at 25 °C and conducted in triplicate (with an average standard deviation of 6% of the mean value) for each system with an average of the results taken. Standard deviation was calculated using the equation displayed in Appendix Fig. 3. Initially, the nuclear waste simulants were allowed to form a settled bed over a time frame of 100 min for CPM, ZMCA-2 and the mixed systems, 69 min for kaolin and 16 min for ZM-2. This settled bed was formed at 1000 rpm, with transmission profiles taken every 1 min. Subsequently, after the initial settled bed had been formed the rpm was increased by 500 rpm every 38 min for CPM, ZMCA-2 and the mixed systems, 28 min for kaolin and 16 min for ZM-2 until 4000 rpm (machine maximum), during which transmission profiles were taken every 15 s.

The following equations (40) and (41), were then applied to the raw data extracted from the LUMiSizer® in order to determine the equilibrium compressive yield stress, $P_y(\phi_{eq})$, and the equilibrium volume fraction of particle dispersion, ϕ_{eq} . Table 9 details each of the symbol's meaning and how they were determined.

$$P_y(\phi_{eq}) \approx \Delta\rho g \phi_0 H_0 \left(1 - \frac{H_{eq}}{2L}\right) \quad (40)$$

$$\phi_{eq} \approx \frac{\phi_0 H_0 \left[1 - \frac{1}{2L} \left(H_{eq} + g \frac{dH_{eq}}{dg}\right)\right]}{\left[\left(H_{eq} + g \frac{dH_{eq}}{dg}\right) \left(1 - \frac{H_{eq}}{L}\right) + \frac{H_{eq}}{2L}\right]} \quad (41)$$

Table 9 Symbols and their corresponding meanings from Equations (40) and (41), which are used to determine equilibrium compressive yield stress and equilibrium volume fraction of particle dispersion of a given sample.

Symbol	Meaning	Units	Determined via
$P_y(\phi_{eq})$	Equilibrium compressive yield stress	Pa	Calculated from Equation (40)
ϕ_0	Initial equilibrium volume fraction of particle dispersions	-	Set value per simulant
$\Delta\rho$	Density difference between particle and liquid	g/ml	Given by Table 4
g	Centrifugal acceleration at the bottom of the bed	-	Calculated
H_0	Initial sediment height	mm	Extracted from data
H_{eq}	Equilibrium sediment height	mm	Extracted from data
L	Radial distance from centrifuge centre to bottom of bed	mm	130 mm for LUMiSizer®
ϕ_{eq}	Equilibrium volume fraction of particle dispersion	-	Calculated from equation 41

In order to understand where the values stated in Equations (40) and (41), apply in terms of the compressive yield stress experiments, Figure 5-2, shows an illustration of a LUMiSizer® cell. This is labelled with the simulant dispersion (with various regions), the radial distance from centrifuge centre to bottom of bed, L , and the initial and equilibrium sediment height, H_0 , and H_{eq} , respectively. The initial equilibrium volume fraction of particle dispersions, ϕ_0 , density difference between particle and liquid, $\Delta\rho$ and the centrifugal acceleration at the bottom of the bed, g , are set values for each individual experiment. Section 5.3.1.1, details the analytical process step by step for determining compressive yield stress though this methodology applied to CPM at 10 vol% in Milli-Q water.

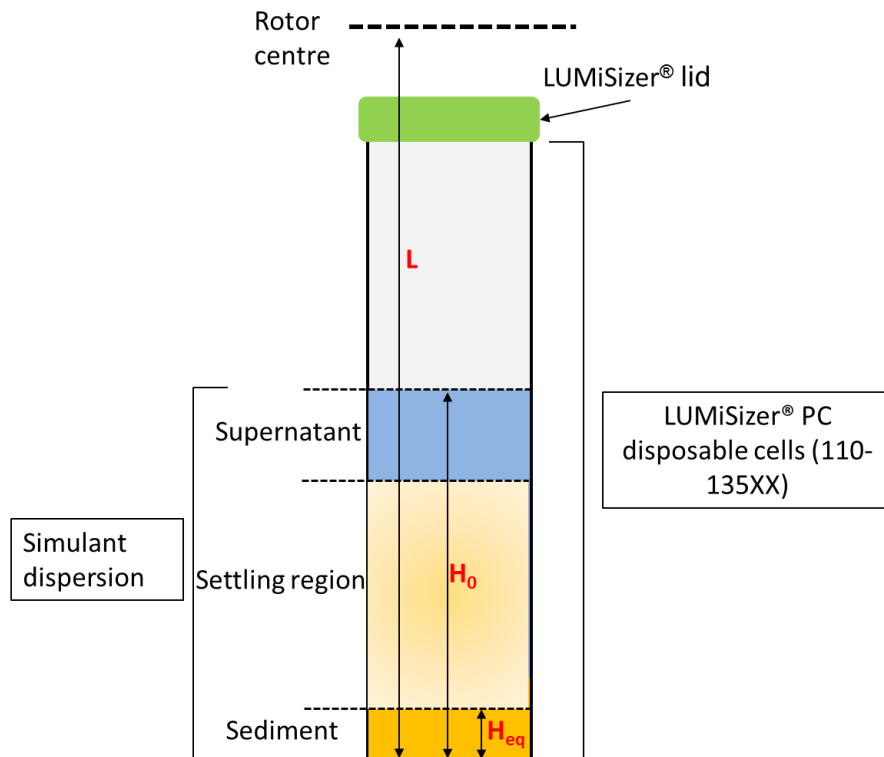


Figure 5-2 Illustration of a LUMiSizer® cell, labelled with the simulant dispersion (with various regions), the radial distance from centrifuge centre to bottom of bed, L , and the initial and equilibrium sediment height, H_0 , and H_{eq} , respectively.

5.2.3 Permeability Studies

The most common permeability experiments typically require materials with large volumes. However, with the development of the novel methodology from Loginov et al. (2014) it has been possible to investigate this property, again in both 2 M nitric acid and Milli-Q water environments for both individual and mixed systems.

The LUMiSizer® was used to study the permeability of the simulants with the experimental method developed upon that published by Loginov et al. (2014). Modified Microcon® Centrifugal Filters (Merck Millipore Ltd, Cork, Ireland) were provided by Maksym Loginov. Unmodified Microcon® Centrifugal Filters, consist of a polycarbonate (PC) sample tube, a polypropylene filter unit and a medical-grade silicone rubber O-Ring. They were modified by an extension of the sample tube height, as shown in Figure 5-3.

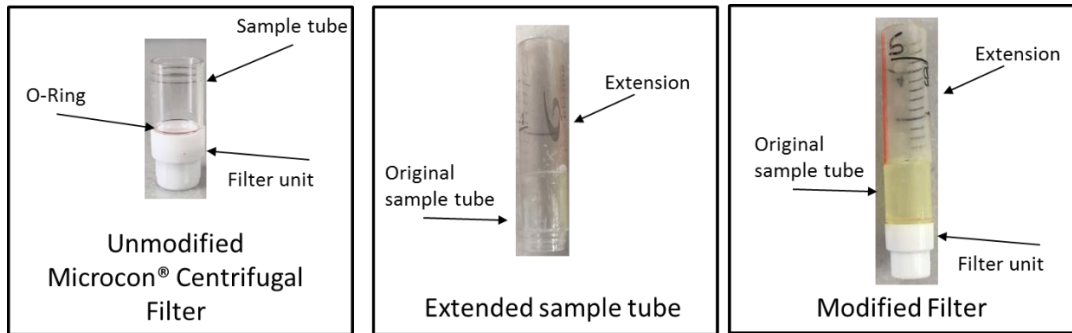


Figure 5-3 Unmodified to modified Microcon® Centrifugal Filters.

Loginov et al. (2014), previously used unmodified Microcon® Centrifugal Filters, the idea in extending the filters was so that the pressure upon the sample could be increased (as more sample could be placed within the tube). The modified Microcon® Centrifugal Filters were fitted with a nylon microfiltration membrane Biodyne A (Pall, USA) with pore size 0.2 μm , which was also provided by Maksym Loginov. The Biodyne A membrane was cut to size by the use of a cork borer (No.4, 8.75 mm). These modified centrifugal filter cells were then placed into modified LUMiSizer® PA disposable cells (110-335XX) with 10.0 mm optical path length, again these were provided by Maksym Loginov. Modification of the LUMiSizer® cells refers to the widening of the upper part of the cells to allow the modified Microcon® Centrifugal Filters to fit. Figure 5-4, shows an illustration of the modified LUMiSizer® PA disposable cells complete with modified Microcon® Centrifugal Filters and simulant dispersion.

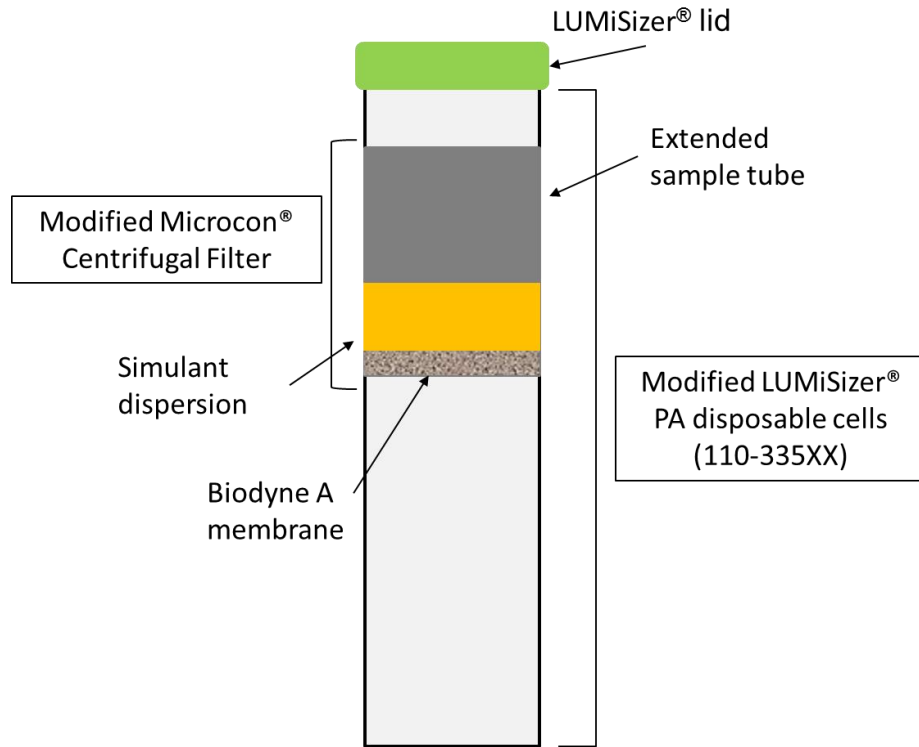


Figure 5-4 A illustration of the modified LUMiSizer® PA disposable cells complete with modified Microcon® Centrifugal Filters and simulant dispersion

All permeability experiments were conducted at 25 °C and were conducted in triplicate (with an average standard deviation of 5% of the mean value) with an average of the results taken. Standard deviation was calculated using the equation displayed in Appendix Fig. 3. The centrifuge speed was set between 500 - 4,000 rpm (depending on the experiment) and transmission profiles were taken every 10 s with the total number of profiles varying per simulant.

5.2.3.1 Resistance of the Membrane

Closely following the methodology published by Loginov et al. (2014), the initial step for the permeability experiments was to determine the resistance of the Biodyne A membrane. This was done by placing approximately 0.5 ml of Milli-Q water into the modified Microcon® sample tube, before placing into the modified LUMiSizer® cell and sealing with a lid. The sealed cell, was then placed into the LUMiSizer® and the centrifugal speed set at 500 rpm. Transmission profiles were recorded every 10 s and then the data extracted from these used to calculate the height of the filtrate, H_f . This was calculated through Equation (42), by taking the initial radial position of the meniscus, $R_{f,0}$,

from the measured radial position of the meniscus (filtrate surface) R_f at a given time, t , of centrifugation.

$$H_f = R_{f,0} - R_f(t) \quad (42)$$

The resistance of the membrane, r_m , was then determined by the analysis of the liquid permeation through the clean Biodyne A membrane. In order to calculate the resistance a sequence of equations were applied, that are detailed in this section. In Section 5.3.2.1, the analytical process step by step for determining the resistance of the membrane though this methodology is detailed. Equation (43), shows a constant, k_1 , that is dependent on the density, ρ_l , and viscosity, μ , of the filtrate, the radial position of the membrane, R_m , and the centrifugal rotation speed, Ω .

$$k_1 = \frac{\rho_l \Omega^2 R_m}{\mu r_m} \quad (43)$$

The constant, k_1 , shown in Equation (44), is determined by the slope of the plot Y which is a function of liquid height above the membrane, h , against centrifugation time, t .

$$Y = k_1 t \quad (44)$$

The dimensionless, Y , function is calculated through the height of the filtrate above the membrane, h , the initial height of the filtrate above the membrane, h_0 , and the radial position of the membrane, R_m , as shown in Equation (45).

$$Y \equiv \ln \left[\frac{2R_m - h}{h} \times \frac{h_0}{2R_m - h_0} \right] \quad (45)$$

The height of the filtrate above the membrane, h , is calculated via Equation (46), through the volume of the liquid added to the centrifugal filter, V_o , the cross-sectional area of the modified LUMiSizer® cells (110-335XX), S_c , and the cross-sectional area of the modified Microcon® Centrifugal Filters, S_F .

$$h = \frac{V_o - S_c H_f}{S_F} \quad (46)$$

Table 10, summaries the symbols mentioned in Equations (42)-(46), their meaning and how they were determined.

Table 10 Summary of the symbols mentioned in Equations (42)-(46), their meaning and how they were determined for calculating the resistance of the membrane.

Symbol	Meaning	Units	Determined via
H_f	Height of the filtrate	m	Calculated from Equation (42)
$R_{f,0}$	Initial radial position of the meniscus	m	Experimental value
$R_f(t)$	Radial position of the meniscus (filtrate surface)	m	Tracked during experiment
k_1	Constant	-	Calculated from slope of plot Y vs. t
ρ_l	Density of filtrate	Kg/m ³	Known value
Ω^2	Centrifugal rotation speed	Rad/s	Set per experiment
R_m	Radial position of the membrane (m)	m	0.072
μ	Viscosity of filtrate	PaS	Known value
r_m	Resistance of the membrane	m ⁻¹	1.8 x 10 ¹⁰
h	Liquid height above the membrane	m	Calculated through Equation (46)
h_0	Initial liquid height above the membrane	m	Calculated through Equation (46)
V_o	liquid added to the centrifugal filter	m ³	<u>Mass of liquid</u> Density of liquid
S_c	Cross-sectional area of the modified LUMiSizer cells (110-335XX)	m ²	6.30 x 10 ⁻⁵
S_F	Cross-sectional area of the modified Microcon® Centrifugal Filters	m ²	3.42 x 10 ⁻⁵

5.2.3.2 Cake Permeability

Once the resistance of the membrane was calculated the cake permeability, K , of each of the simulants could then be determined by the analysis of the liquid permeation through their solid settled bed/cake (Loginov et al. 2014). First, the simulant dispersion was placed into the modified sample tube and cell, complete with the Biodyne A membrane. The sample cake was then formed by the use of the centrifuge set at 1000 rpm over 6 h, which allowed the simulant to settle and form a solid cake on the membrane and the filtrate (either Milli-Q water or 2 M nitric acid) to filter through the membrane. Once the cake was formed its weight was recorded, then approximately 0.5 ml of either pure Milli-Q water or 2 M nitric acid was placed on top of the cake, the total weight of which was also recorded. The LUMiSizer® centrifugation was then set at the same constant rotation speed as it was for the initial cake formation stage, i.e. 1000 rpm. The height of the filtrate was then monitored until it became constant, taking a varying amount of time dependent on the simulant before it was compressed and the process repeated at increasing rpm (2000, 3000 and 4000). The step by step process is as follows:

1. Record weight of 'dry' cake,
2. Add 0.5 ml of pure Milli-Q water or 2 M nitric acid (experiment dependant), on top of the cake and record total weight,
3. Set rpm and allow experiment to run until the height of the filtrate becomes constant.
4. Increase rpm by 1000, to ensure cake is compressed before next step.
5. Then repeat steps 1-3 until the maximum rpm (4000 rpm) has been set.

Figure 5-5, demonstrates these steps visually.

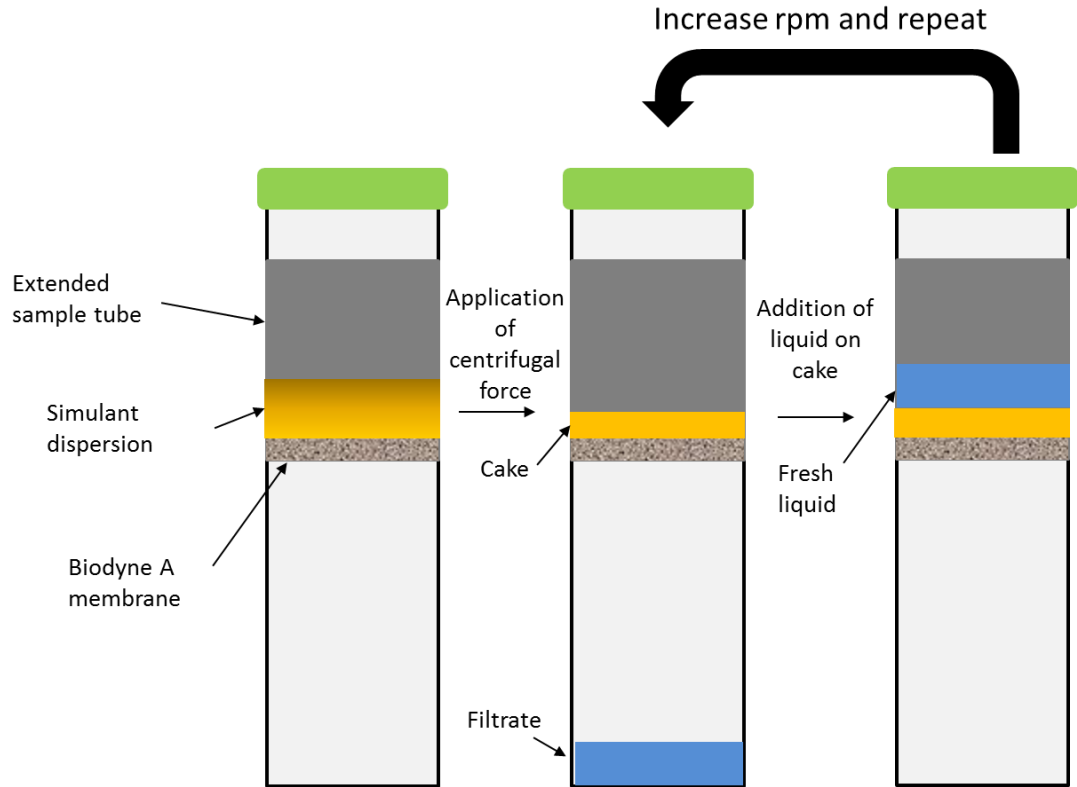


Figure 5-5 Illustration of the permeability experimental steps.

In order to actually calculate the cake permeability, K , a sequence of Equations (47)-(54) had to be applied to the experimental data (Loginov et al. 2014). A detailed step by step analytical procedure for determining permeability though the application of these equations applied to the CPM in Milli-Q data is provided (in Section 5.3.2.3). Equation (47), shows a constant, k_2 , that is dependent on the density, ρ_l , and viscosity, μ , of the filtrate (Milli-Q water or 2 M nitric acid), the centrifugal rotation speed, Ω , the radial position of the membrane, R_m , and the radial position of the cake surface, R_c .

$$k_2 = \frac{\rho_l \Omega^2 R_m}{\mu [r_m + \frac{R_m - R_c}{K}]} \quad (47)$$

Where k_2 , could be determined via the slope of the plot y vs. t , shown in Equation (48).

$$y = k_2 t \quad (48)$$

The dimensionless, y , function is calculated through the height of the filtrate above the membrane, h , the initial height of the filtrate above the membrane, h_0 , the radial position of the membrane, R_m and the radial position of the cake surface, R_c . This is shown by equation (49).

$$y \equiv \ln \left[\frac{R_m + R_c - h}{R_m - R_c + h} \chi \frac{R_m - R_c + h_o}{R_m + R_c - h_o} \right] \quad (49)$$

The radial position of the cake surface, R_c , had to be calculated through the use of Equation (50) and (51). Where the height of the filter cake, H_c , is dependent on the weight of suspension, m_o , the solid weight fraction of initial suspension, c_i , the density of the solid, ρ_s , the solid volume fraction in the filter cake, φ_∞ , and the cross-sectional area of the modified Microcon® Centrifugal Filters, S_F .

$$R_c = R_m - H_c \quad (50)$$

$$H_c = \frac{m_o c_i}{\rho_s \varphi_\infty S_F} \quad (51)$$

Once the above equations were utilised the specific cake resistance, α , could be calculated from the cake permeability, K , the density of the solid, ρ_s and the solid volume fraction in the filter cake, φ_∞ , as shown in Equation (52).

$$\alpha = \frac{1}{K \rho_s \varphi_\infty} \quad (52)$$

The solid volume fraction in the filter cake, φ_∞ , was calculated through the densities of both the solid ρ_s and the liquid ρ_l in addition to the solid weight fraction of the compressed filter cake, c_∞ , as shown in Equation (53).

$$\varphi_\infty = \frac{1}{\left(\frac{\rho_s}{\rho_l}\right) \left(\left(\frac{1}{c_\infty}\right) - 1\right) + 1} \quad (53)$$

The solid weight fraction of the compressed filter cake, c_∞ , was calculated through the weight of suspension, m_o , the solid weight fraction of initial suspension, c_i and weight of the filter cake, m_c , as shown in Equation (54).

$$c_\infty = \frac{m_o c_i}{m_c} \quad (54)$$

Table 11, summarises the symbols mentioned in equations (47)-(54), their meaning and how they were determined.

Table 11 Summary of the symbols mentioned in Equations (47)-(54), their meaning and how they were determined for calculating cake resistance.

Symbol	Meaning	Units	Determined via
K	Cake permeability	m^2	Calculated from Equation (47)
k_2	Constant	-	Determined from slope of y vs. t
R_c	Radial position of the cake surface	m	Calculated from Equation (50) and (51)
H_c	Height of the filter cake	m	Calculated from Equation (51)
m_o	Weight of suspension	kg	Measured value
c_i	Solid weight fraction of initial suspension	-	Known value
ρ_s	Density of solid	Kg/m^3	Known value
φ_∞	Solid volume fraction in the filter cake	-	Calculated from Equation (53)
α	Specific cake resistance	m/kg	Calculated from Equation (52)
c_∞	Solid weight fraction of compressed filter cake	-	Calculated from Equation (54)
m_c	Weight of the filter cake	kg	Measured value

5.2.3.3 Pressure Determination

The traditional way to present permeability data is specific cake resistance vs. pressure. This requires the rpm used in the permeability experiments to be converted appropriately to pressure. For this process a methodology was developed using the application of Equation (55). Where RCA is the relative centrifugal acceleration and r is the radius of the instrument plate where the dispersion is housed (130mm for the LUMiSizer®).

$$RCA = 1.1118 \times 10^{-5} \times r \times rpm^2 \quad (55)$$

The RCA can then be directly equated to acceleration, a , in Equation (56), where F , is force, and m is mass of the simulant (can be taken as the mass of dispersion added or the end cake mass).

$$F = m \times a \quad (56)$$

Once force, F , has been determined the pressure, P , can be calculated from Equation (57), where S_f is the cross-sectional area of the modified Microcon® Centrifugal Filters. The mass was taken at the start and end of each experiment, thus a starting and end force could be calculated and therefore a start and end pressure. For presentation of the data the median pressure was chosen.

$$P = \frac{F}{S_f} \quad (57)$$

A limitation of this chosen methodology is that the mass is assumed to be constant, which is not the case. However, it provides a straight forward methodology to determine pressure in which the simulants can be compared to one another.

Table 12, summarises the symbols mentioned in Equations (55)-(57), their meaning and how they were determined.

Table 12 Summary of the symbols mentioned in Equations (55)-(57), their meaning and how they were determined for calculating pressure.

Symbol	Meaning	Units	Determined via
RCA	Relative Centrifugal Acceleration	-	Calculated from Equation (55)
r	Radius	Cm	13 cm
RPM	Revolutions per minute	-	Varies per experiment
F	Force	N	Calculated from Equation (56)
m	Mass	Kg	Measured value
a	Acceleration	m/s ²	Equated to RCA
P	Pressure	Pa	Calculated from Equation (57)

5.3 Results and Discussion

5.3.1 Compressive Yield Stress

In order to understand the compressive yield stress results presented and discussed in this section, a detailed analytical procedure 'walkthrough' of Equations (40)-(41) applied to the experimental data of CPM in Milli-Q water at 10 vol% is detailed.

5.3.1.1 Analytical Procedure for Determining of Compressive Yield Stress

The LUMiSizer® STEP-Technology software produces transmission vs. position plots, as shown in Figure 5-6, for CPM in Milli-Q water at 10 vol%. From this raw profile, various data can be extracted and plotted, as explained in Section 4.3.3.1

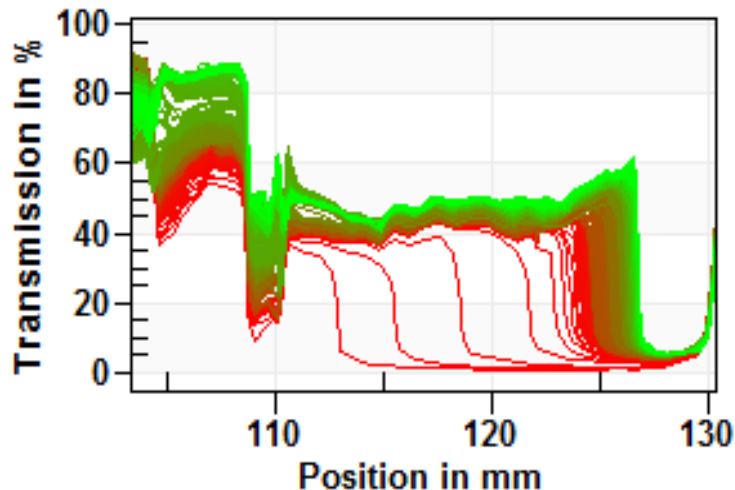


Figure 5-6 Raw compressive yield stress profile for caesium phosphomolybdate (CPM) in Milli-Q water at 10 vol%. Plot is produced by the LUMiSizer® which utilises Space and Time resolved Extinction Profiles – Technology. The red profile being the first profile, progressing to the green, which is the last.

Figure 5-7, shows a bed height vs. time plot of the CPM in Milli-Q water at 10 vol% data extracted from the raw profile shown in Figure 5-6 (the process of which was the same for determining the bed height vs. time graphs for sedimentation data in Section 4.3.3.1). This allows visualisation of what is occurring in the sample over time and with the increase in rpm. In addition, it

can be shown visually where both the initial and equilibrium heights (H_0 and H_{eq} , respectively) are extracted.

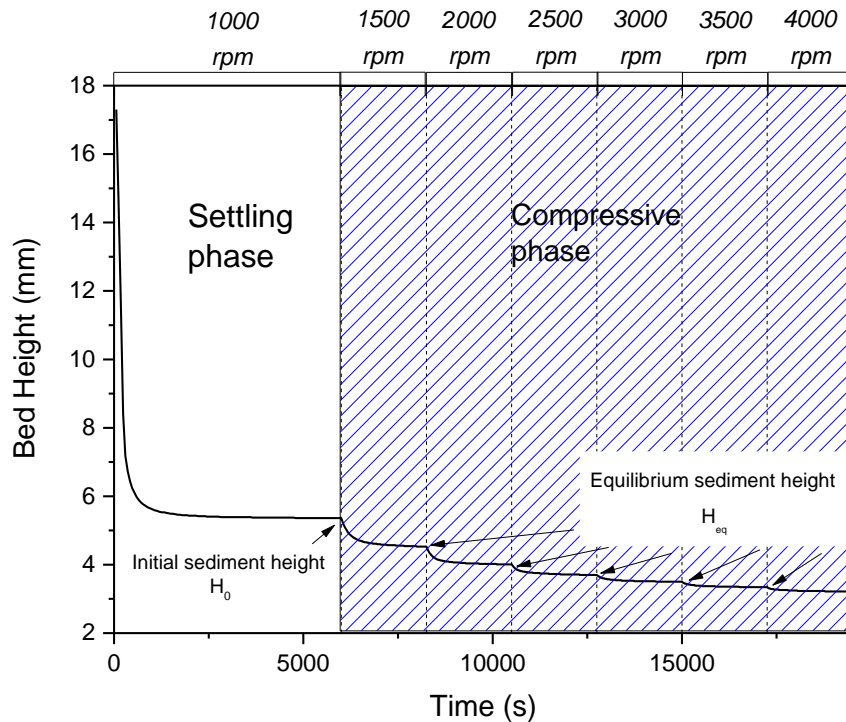


Figure 5-7 Sedimentation bed height vs. time plot for caesium phosphomolybdate (CPM) in Milli-Q water at 10 vol%. Change in shading represents the change in phases from settling to compression. Vertical dash lines correspond to an increase in centrifugal force, which is donated at the top of the plot. Both the initial and equilibrium heights (H_0 and H_{eq} , respectively) are noted.

Equations (40) and (41), presented in Section 5.2.2, utilise the raw data directly extracted from the transmission profiles, in respect to the initial, H_0 and equilibrium heights, H_{eq} of the settled simulant beds.

In applying these equations, to CPM in Milli-Q water at 10 vol%, the initial equilibrium volume fraction of particle dispersions, ϕ_0 , is 0.10 and the density difference, $\Delta\rho$, between CPM and water is, 3.15 g/ml. Inputting these values and the initial, H_0 and equilibrium heights, H_{eq} of the settled CPM bed (extracted from the transmission profiles), into Equations (40) and (41), allows a plot of the equilibrium compressive yield stress vs. the equilibrium volume fraction of particle dispersion to be formed. This is shown in Figure 5-8.

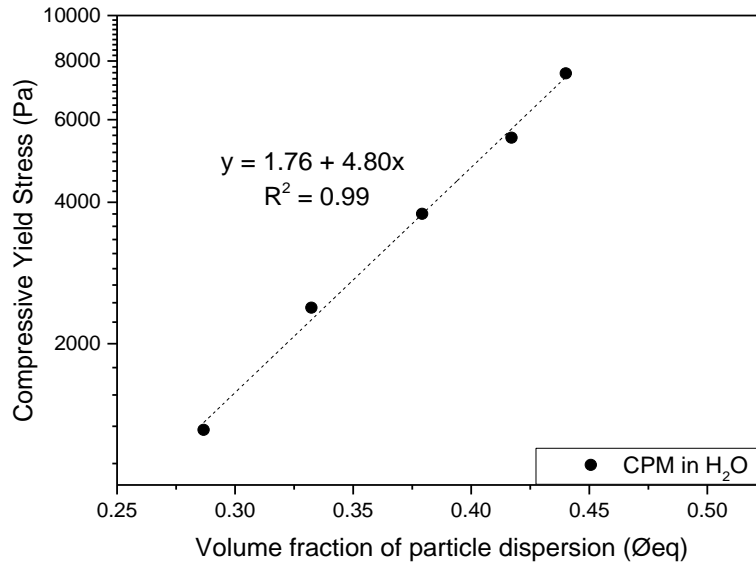


Figure 5-8 Plot of the equilibrium compressive yield stress vs. the equilibrium volume fraction of particle dispersion for caesium phosphomolybdate (CPM) in Milli-Q water at 10 vol%.

Presented in the next Section is the full set of final results for the compressive yield stress of all systems studied in this Chapter, displayed as plots of both bed height vs. time and the equilibrium compressive yield stress vs. the equilibrium volume fraction of particle dispersion.

5.3.1.2 Compressive Yield Stress Results

The bed height vs. time plots are shown for the simulants in Figure 5-9.

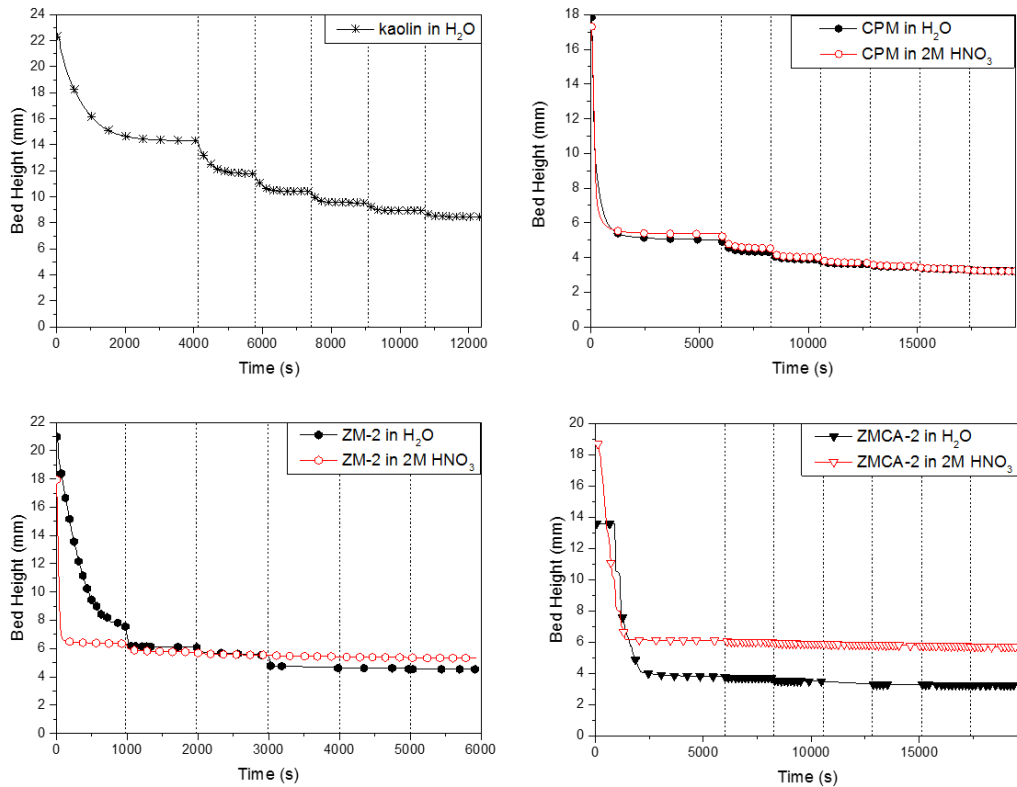


Figure 5-9 Sedimentation bed height vs. time plots for 25 vol% kaolin in water, 10 vol% caesium phosphomolybdate (CPM) in both Milli-Q water and 2 M nitric acid, and 16 vol% zirconium molybdate (ZM-2) and zirconium citramolybdate (ZMCA-2) in both Milli-Q water (black) and 2 M nitric acid (red). Vertical black dash lines correspond to an increase in centrifugal force.

For all simulants, an increase in applied centrifugal field resulted in further collapsing (lower bed height) of the particle network. This trend is most pronounced for kaolin and has previously been reported (Mitchell, 1960, Olson and Mesri, 1970, Sridharan and Rao, 1973, Chen et al., 2000, Angle and Gharib, 2017). Figure 2-24, in Section 2.3.3 illustrates the clay platelets of kaolin, compressing in a parallel fashion. As the pressure is increased upon the clay these platelets further compress upon one another therefore excluding liquid from the voids.

The settling behaviour analysed in Chapter 4, concluded that CPM behaves similarly in both Milli-Q water and 2 M nitric acid, this was determined to be a result of its low equilibrium pH 1.5 in water and its low Isoelectric Point (IEP) ~ pH 1. As a result of the low IEP, CPM is expected to be aggregated in both

environments, especially within the nitric acid where the nitrate counter ions would contribute to collapsing the electric double layer, destabilising the system. Therefore, on observing the bed height vs time compressibility plot, it is not unexpected that similar behaviour in both environments is once again witnessed. For both environments an increase in rpm results in a small but notable decrease in the bed height. This suggests the aggregated particles of CPM sediment into an initial open voluminous bed, that is compressed by excluding fluid from the aggregate voids once progressive pressure is applied.

From the plots shown in Figure 5-9, for the elongated square bipyramid shaped ZM-2 within Milli-Q water there is more compression observed than within 2 M nitric acid. It appears that initially within water a disordered network is formed, that can further compress with an increase in pressure. From the stability and settling results, it was suggested that ZM-2 would be more stable in water, than within acid, therefore consisting of slightly more discrete particles, which could rearrange under pressure. Furthermore, as found from the settling experiments, ZM-2 settles faster in 2 M nitric acid and it appears to form a harder to compress settled bed than within water as a result of the formation of strong aggregates unable to rearrange under pressure.

For the wheatsheaf shaped ZMCA-2 there is little observed change in bed height with increased rpm for the system within 2 M nitric acid, whereas within Milli-Q water the change is more noticeable. Due to the elongated shape it is possible that within water, where it has a relatively slow settling rate a more condensed bed can be formed. Whereas within acid ZMCA-2 appears to form dense aggregates that are very strong and unable to rearrange under compression.

Figure 5-10, shows the compressive yield stress plots of all the dispersions.

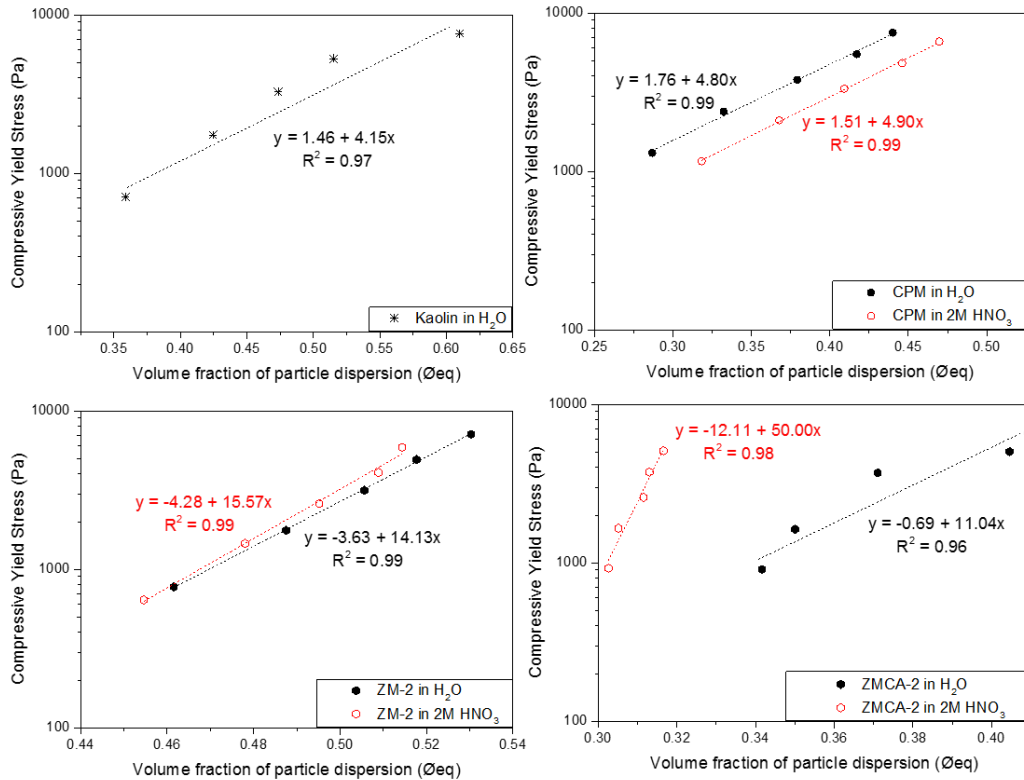


Figure 5-10 Plots of equilibrium compressive yield stress vs. the equilibrium volume fraction of particle dispersion for; 25 vol% kaolin in water, 10 vol% caesium phosphomolybdate (CPM), 16 vol% zirconium molybdate (ZM-2) and zirconium citramolybdate (ZMCA-2) in both Milli-Q water (black) and 2 M nitric acid (red). Complete with lines of best fits, their equation and R^2 values.

For the compressibility of the particle networks, for each simulant it can be seen that the equilibrium volume fractions increase with the compressive yield stress, which is as expected, as inferred from the bed height vs time plots in Figure 5-8. For all the simulants, the settled beds become more compressed as the liquid within the voids is expelled as higher pressures are exerted upon their settled bed. In general observation, for all the simulants there is a close fit of the trends with R^2 values all ≥ 0.96 . These close fit trends are expected for yield stress changes with volume fraction, if there are not significant surface changes. A log-linear plot allows for a visualising of data that is related according to an exponential relationship.

Considering kaolin is the most compressible system with the largest change in volume fraction of 0.25, it is believed that kaolin forms an initial open voluminous bed which when pressure is applied, fluid is excluded from the voids. The clay platelets of kaolin, without the influence of contaminants

compress in a parallel fashion, forming an ordered bed that is easy to compress. Angle and Gahrib (2017), also reported a similar range of volume fraction change, although they reported over a larger compressive yield stress range. This difference is suggested as a result of the different suspension medium and volume concentration. The study used model process water, with a concentration of 11 vol%.

For CPM, it can be seen that within 2 M nitric acid, the compressive yield stress is slightly lower than for the equivalent equilibrium volume fraction in Milli-Q water, although they both follow the same trend. The determined difference is very small considering the bed height plots, Figure 5-9 and is likely a result of experimental variance. The reported volume fraction values which are derived from the equilibrium height have an error of +/- 0.01, therefore the observed difference in Figure 5-10, represents the limit of experimental technique. As previously mentioned the IEP and natural equilibrium pH of CPM is reported to be low, therefore suggesting it aggregates and is unstable in both conditions. The compressive yield stress results are in agreement with the settling behaviour with ultimately, similar behaviour being shown for CPM in both systems. Paul (2014) reported for CPM in water that it was challenging to compress, as a result of requiring an increasing amount of compressive steps, which has also been observed here for both conditions. This suggests that the aggregates formed are strong and difficult to break, as increased pressure has a minor effect.

For ZM-2 the volume fraction range for the acid is slightly lower and the range is smaller, than within water. There is not much difference in volume fraction with an increase in pressure for either system, but generally volume fractions are slightly lower within acid, as expected when a network is more aggregated. It would appear that ZM-2 aggregates in acid, but under the initial 1000 rpm, the centrifugal force is great enough to compress the aggregates to a similar structure level as the un-aggregated ZM-2 in water. Hence, it may be the aggregates are not extremely large, which could be attributed to the unusual elongated square bipyramid shape. Therefore, despite differences in the settling rates, the strength of the particle network formed is comparable.

For ZMCA-2 the equilibrium volume fraction increases as the pH increases, meaning that in more acidic conditions the ZMCA-2 particles have a more open network, in comparison to the Milli-Q water system where a more dense bed is formed. As shown by ZMCA-2's zeta potential curve (Figure 4-7) in low pH conditions, the particles are unstable and are likely to settle quicker and as a result of their orientations they will potentially not settle in an ordered fashion, therefore forming a more open bed. Once settled within 2 M nitric acid, there is little change in the volume fraction with increased pressure, suggesting a strong particle network is formed quickly from the aggregates in these conditions. The particles in Milli-Q water do form a more compact structure, likely from the orientation of the elongated less aggregated particles under centrifugal force. The ZMCA-2 compressive yield stress data also highlights that the coagulation of the particles appears to form a stronger bed, despite the fact that it is more open.

In considering the HAL simulants, CPM forms, initially, the most open bed network, but is also the most compressible simulant, compressing over a volume fraction range of 0.2. Whereas, both ZM-2 and ZMCA-2 compress over a volume fraction of 0.1, half of that for CPM. Within Milli-Q water this was similar to that reported by Paul (2014), with CPM forming an open voluminous compressive bed and ZM forming a more dense, less compressible bed. Overall, the data illustrates that CPM dispersions are more challenging to compress, than ZM-2 and ZMCA-2.

Dunnett et al. (2016), found when measuring yield stress that the yield stress of liquors containing CPM were generally significantly higher than liquors containing ZM. Although not directly comparable, the trend for compressive yield stress was found to be different in this study, with all simulants compressing over a similar range of pressure. However, CPM was determined to be the most challenging to compress in comparison to ZM-2 and ZMCA-2.

In respect to the HASTs, it is suggested that CPM will be easily suspended, in comparison to ZM, in both water and nitric acid. Additionally, in considering a wash out reagent, water or nitric acid could be used for CPM as little difference is shown in its behaviour. For ZM-2, despite settling faster in 2 M nitric acid, its compressive yield stress behaviour is similar in both conditions,

whereas for ZMCA-2 a more open but less compressible network is formed. This highlights the effect of different ZM morphologies on the compressive yield stress, both behaviours need to be considered in determining the most advantageous POCO strategy. Finally, for the HAL simulants all compressive yield stresses were reported over a similar range, therefore despite compressive yield stress reportedly increasing with the inverse of particle size (Miller et al. 1996), it appears in the case of the simulants both stability and shape influence their compressive behaviour.

Figure 5-11, displays the compressive yield stress plots of the mixed systems of CPM and ZMCA-2, in both Milli-Q water and 2 M nitric acid, respectfully (bed height vs. times plots can be seen in Appendix Fig. 2).

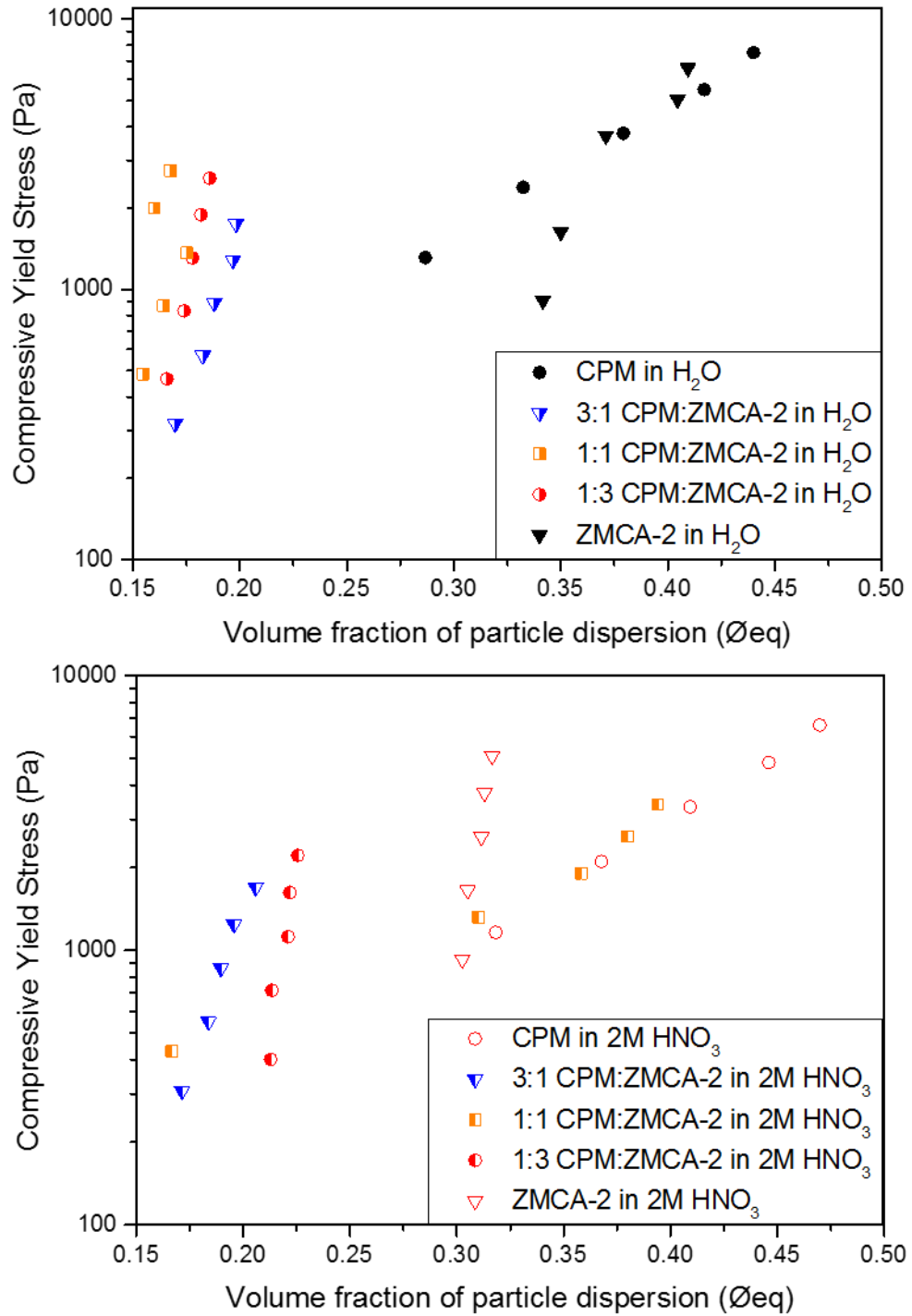


Figure 5-11 Plots of equilibrium compressive yield stress vs. the equilibrium volume fraction of particle dispersion for individual and mixed systems of caesium phosphomolybdate (CPM) and zirconium citramolybdate (ZMCA-2) at 1:3, 1:1 and 3:1 weight ratios at 16 vol% in Milli-Q water (left, black) and 2 M nitric acid (right, red).

First, in Milli-Q water it is observed that all the mixed systems form significantly more open networks than the individual systems, with volume fractions < 0.2 . Additionally, it can be seen that these open voluminous beds in water, are not very compressible, as there is very little change in volume fraction with pressure, therefore suggesting strong particle-particle interactions between both CPM and ZMCA-2. In comparing the systems in Milli-Q water, there is negligible differences regardless of the weight ratios, whether a higher mass of ZMCA-2 or a higher mass of CPM, the overall behaviour is comparable. In considering the settling rates of the systems, the 1:1 mix settled the slowest in water, followed by the 1:3 mix, then lastly the 3:1, which settled the fastest. This same trend of $1:1 < 1:3 < 3:1$ is actually observed in the compressive yield stress behaviour, with 1:1 forming the most open network, followed by the 1:3 mix and finally the 3:1.

Within the 2 M nitric acid environments, both the 1:3 and 3:1 (CPM:ZMCA-2) systems behave similarly to how they do in Milli-Q water, forming large open voluminous beds, larger than for the individual systems, that are difficult to compress. There is some variation in behaviour with the volume fractions increasing to < 0.23 , as opposed to < 0.2 within Milli-Q water. Additionally, when comparing to their behaviours in water, the 3:1 and 1:3 mixed systems have 'swapped', with 3:1 now having the more open bed compared to 1:3.

The 1:1 CPM:ZMCA-2 system within 2 M nitric does not appear to fit the trend. This system forms an initial open network which is highly compressible, over a volume fraction of 0.2. As discussed in Section 4.3.3.4, this system had a fast settling rate, suggesting high instability. The aggregates within this system appear to be easily compressible, perhaps even broken during the increase in pressure. This system also appears to follow the trend of the individual CPM system.

The behaviour, of the mixed systems highlight key differences in comparison to the individual simulants and consequently the importance of studying the systems together. It is likely that within the HASTs there will be some combination of CPM and ZM, therefore the settled beds are likely to be open and voluminous networks.

5.3.2 Permeability

In order to understand the permeability results presented and discussed in this section, a detailed example of the analytical procedure first published by Loginov et al. (2014) is given. Equations (42)-(54) are applied to the data of CPM in Milli-Q water for both the resistance of the membrane and the permeability.

5.3.2.1 Analytical Procedure for Determining the Resistance of the Membrane

Before any permeability experiments could begin the resistance of the membrane must be determined. First, the data was extracted from the LUMiSizer® transmission plots (discussed in Section 4.3.3.1), in the form of the radial position of the meniscus, R_f over time, t . This data was then plotted (although this is not necessary for the calculations, it helps with understanding of where the end result comes from), as shown in Figure 5-12.

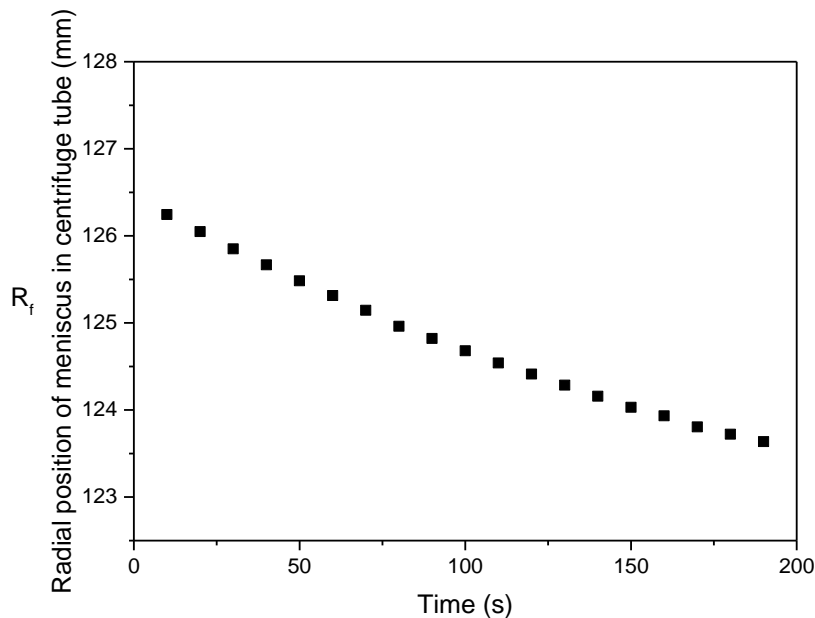


Figure 5-12 The radial position of the meniscus in the centrifuge tube vs. time, for an experiment determining the resistance of the Biodyne A membrane with Milli-Q water.

As the values for R_f are now known (and plotted) over time, t , the height of the filtrate, H_f , using Equation (42) can be determined and also plotted against time, t , as shown in Figure 5-13.

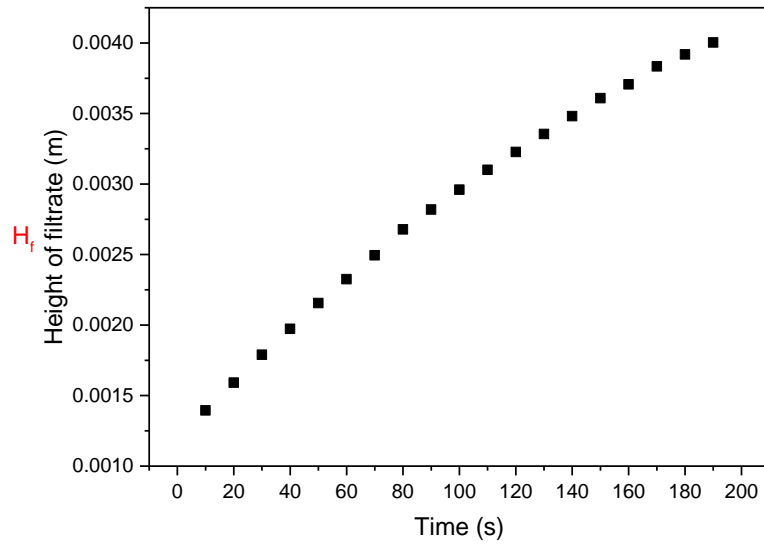


Figure 5-13 The height of the filtrate vs. time, for an experiment determining the resistance of the Biodyne A membrane with Milli-Q water.

Using these determined H_f values, Equation (46) could then be utilised in calculating the liquid height above the membrane, h . Where V_o is simply the mass of the Milli-Q water added to the sample tube divided by the density of Milli-Q water. Note that S_c and S_f remain the same for all simulants and V_o varies per experiment. After h was determined it could be plotted against time, as shown in Figure 5-14.

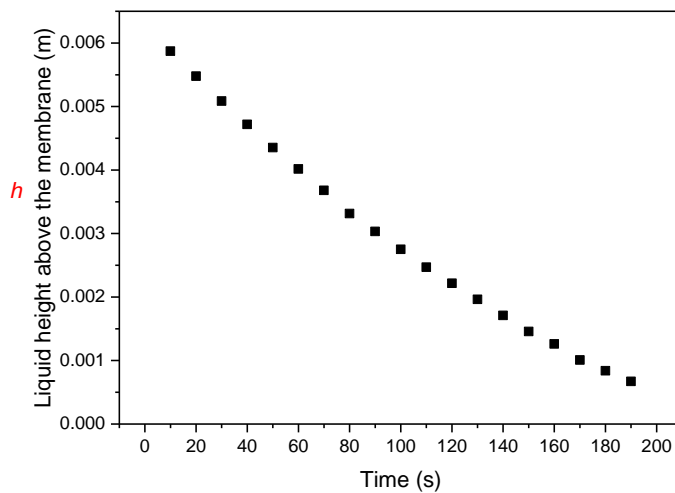


Figure 5-14 The liquid height above the membrane vs. time, for an experiment determining the resistance of the Biodyne A membrane with Milli-Q water.

Using these determined, h , values and substituting them into Equation (45), Y could be determined. The dimensionless Y function is calculated through the height of the filtrate above the membrane, h , the initial height of the filtrate above the membrane, h_0 , and the radial position of the membrane, R_m , as shown in Equation (45). Once Y had been calculated it was plotted against time (Figure 5-15), the gradient of the plot being equated to constant, k_1 . Overtime the Y vs time plot can deviate from linear as it is presumed the cell is cylindrical, whereas in reality it deviates from this (Loginov et al. 2014).

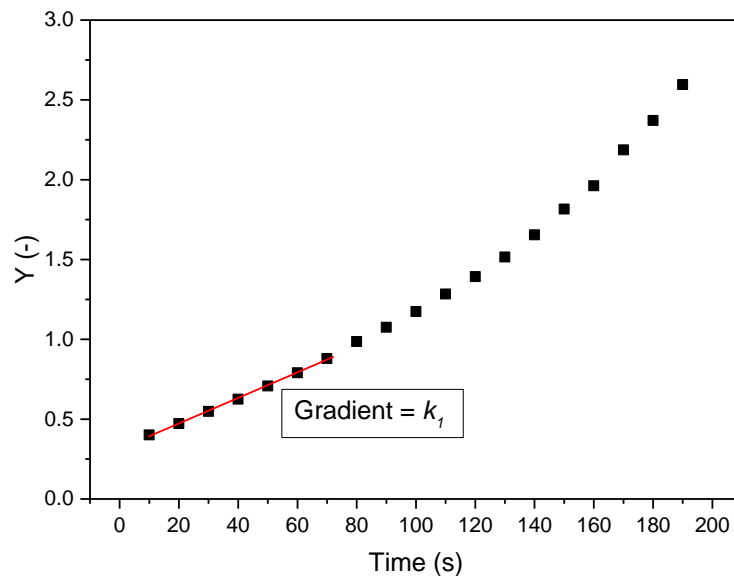


Figure 5-15 Dimensionless value Y vs. time, for an experiment determining the resistance of the Biodyne A membrane with Milli-Q water. Shown with red line representing the gradient and constant, k_1 .

Finally, once k_1 had been determined the resistance of the membrane, r_m , could be calculated, as shown by Equation (58). Where, ρ_l , is the density of the Milli-Q water and μ is its viscosity, both are fixed values. Ω is the centrifugal rotation speed, which requires the rpm used within the experiment to be converted to rad/s, which is done via Equation (59)

$$r_m = \frac{\rho_l \Omega^2 R_m}{\mu k_1} \quad (58)$$

$$1 \text{ rpm} = \frac{2\pi}{60} \text{ rad/s} \quad (59)$$

The resistant of the membrane, r_m , was found to be $1.8 \times 10^{10} \text{ m}^{-1}$, which is in the same order of magnitude of that reported by Loginov et al. (2014) for the same membrane. This value is considered insignificant in comparison to the resistance of the simulants filter cakes (Loginov et al. 2014).

5.3.2.2 Analytical Procedure for Determining the Cake Resistance and Pressure

The initial analysis of the cake resistance follows the same format as that for the resistance of the membrane determination. In this case the data is for CPM in Milli-Q water, Figure 5-16, displays the graphs of, R_f vs. t , H_f vs. t and h vs. t for this data set.

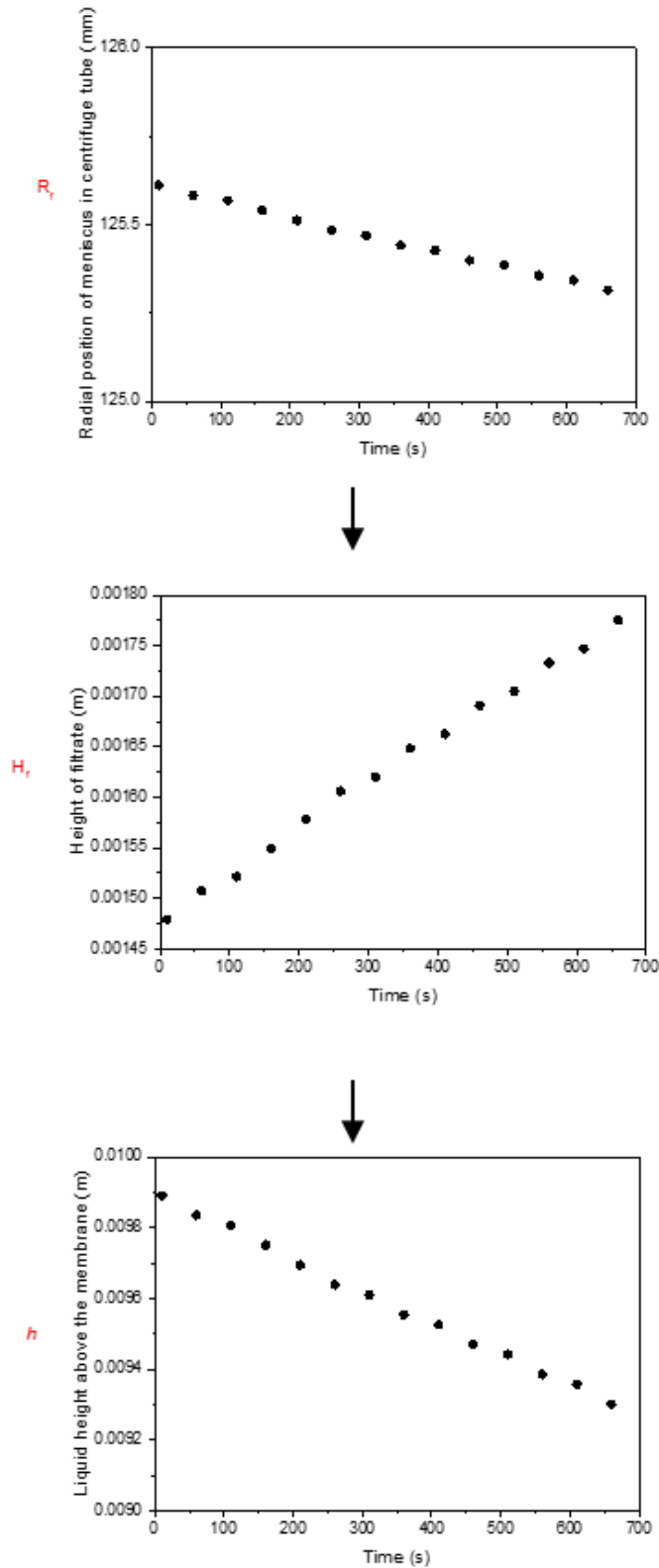


Figure 5-16 Plots showing the radial position of the meniscus in the centrifuge tube vs. time, the height of the filtrate vs. time and the liquid height above the membrane vs. time, for caesium phosphomolybdate (CPM) in Milli-Q water, respectively.

The determination of the cake resistance analysis deviates from the determination of the membrane resistance at this point, with use of Equation (47).

The radial position of the membrane, R_m , is known to be 0.072 m. The radial position of the cake surface, R_c , however, requires the use of the set of Equations (50) and (51).

Once y was determined it could be plotted against time as shown in Figure 5-17, for CPM in Milli-Q water, the gradient of the plot being equated to constant, k_2 , as shown in Equation (48).

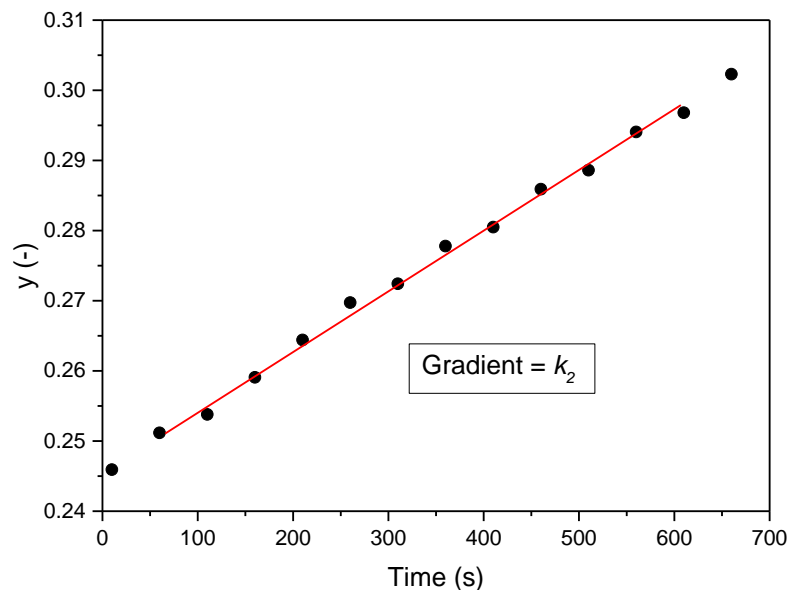


Figure 5-17 Dimensionless value y vs. time, for an experiment determining the cake resistance of caesium phosphomolybdate (CPM) in Milli-Q water. Shown with red line representing the gradient equivalent to constant, k_2 .

Then permeability, K , of CPM in Milli-Q could then be calculated by substituting the, k_2 , constant into Equation (60).

$$k_2 = \frac{\rho_l \Omega^2 R_m}{\mu [r_m + \frac{R_m - R_c}{K}]} \quad (60)$$

Once the permeability, K , was determined it could then be used to calculate the cake resistance, α , of the CPM in Milli-Q water at that particular rpm, as shown in Equation (52). The cake resistance, is the most typical way to present permeability data. The cake resistance, α , of the CPM in Milli-Q water could then be plotted against rpm, as shown in Figure 5-18.

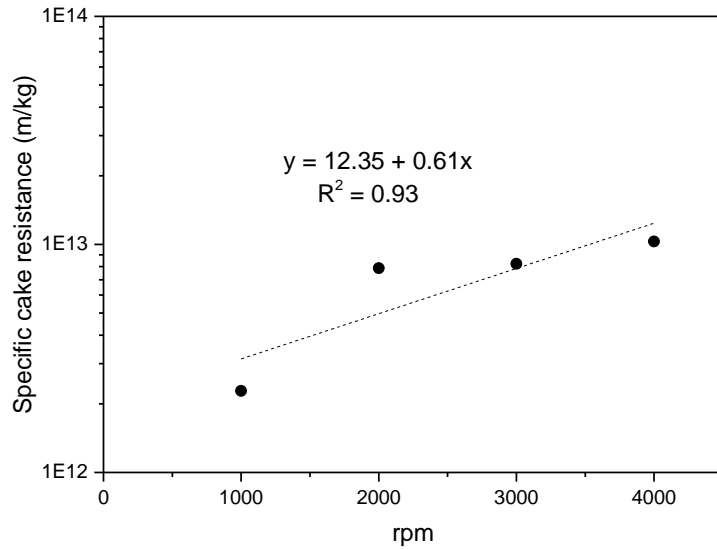


Figure 5-18 Specific cake resistance vs. rpm for caesium phosphomolybdate (CPM) in Milli-Q water.

A common way to present permeability data, is cake resistance against pressure. Therefore, the pressure had to be determined utilising Equations (61) and (62), repeated for ease of reading. Where, the acceleration of the centrifuge, a , can be linked to F , the force applied upon the cake, by m , the mass of the simulant.

$$F = m \times a \quad (61)$$

Once force, F , has been determined the pressure, P , can be calculated from Equation (62), where S_f is the cross-sectional area of the modified Microcon® Centrifugal Filters.

$$P = \frac{F}{S_f} \quad (62)$$

The mass of the simulant dispersion was taken at the start of the experiment, where it will be the heaviest and therefore result in the highest force and consequently the highest pressure. Additionally, the mass of the simulant cake was taken at the end of the experiment where it will be the lightest and therefore result in the lowest force and consequently the lowest pressure.

Figure 5-19, shows the assumed linear change of pressure over time for the CPM in Milli-Q water experiment at 1000, 2000, 3000 and 4000 rpm. For

presentation of the data, the median pressure was chosen. A limitation of this chosen methodology is that the mass is assumed to be constantly changing over time due to a constant rate of fluid loss. Although certainly for the initial part of the experiment the rate will be constant, as the experiment continues the rate will decrease slightly with a decrease in pressure. However, it provides a straight forward methodology to determine pressure in which the simulants can be compared to one another.

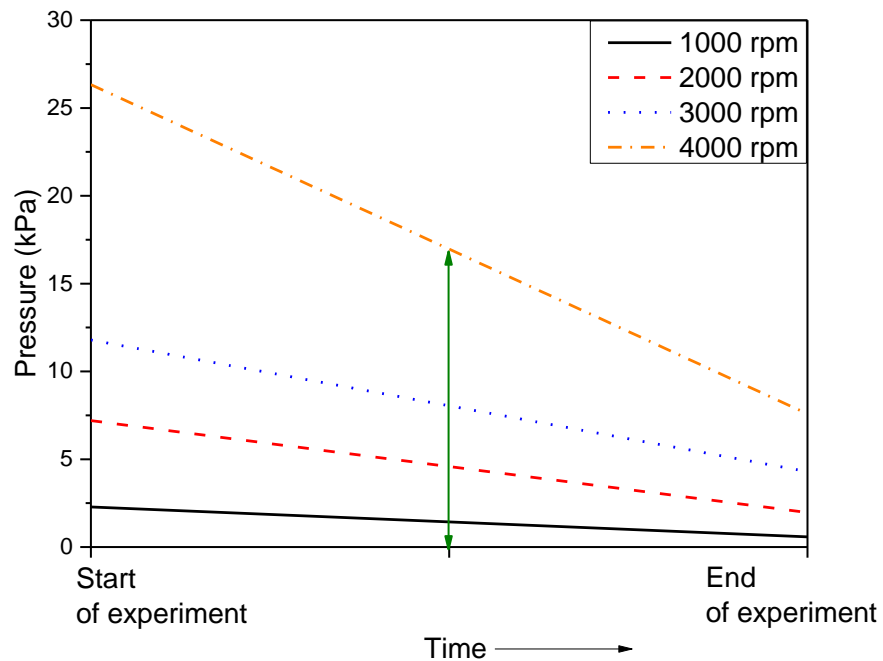


Figure 5-19 Starting and ending pressures for the caesium phosphomolybdate (CPM) in Milli-Q water experiment at 1000, 2000, 3000 and 4000 rpm. With green arrow showing the median values which were used for calculations.

Once the pressure for each experiment was calculated the specific cake resistance vs. pressure for CPM in Milli-Q water could be plotted, as is presented in Figure 5-20. This, is how all results in the proceeding sections will be presented.

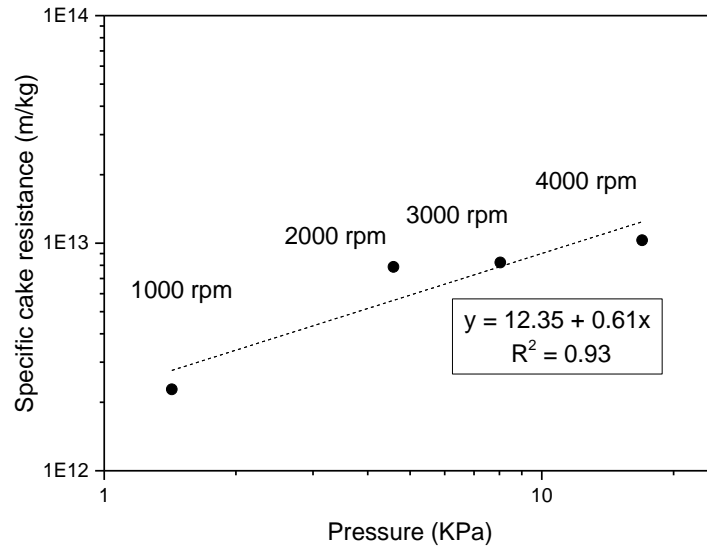


Figure 5-20 Specific cake resistance vs. pressure for caesium phosphomolybdate (CPM) in Milli-Q water. Completed with corresponding rpm values.

5.3.2.3 Cake Resistance Results

Figure 5-21, presents the cake resistance vs. pressure plots for all the individual simulants in this Chapter. All simulants follow the trend of an increase in pressure resulting in an increase in cake resistance. This is a result of the cakes being compressed at increasing pressures, therefore limiting the available pores for the liquid medium to permeate through (Tien and Bai, 2003, Vyas et al., 2000).

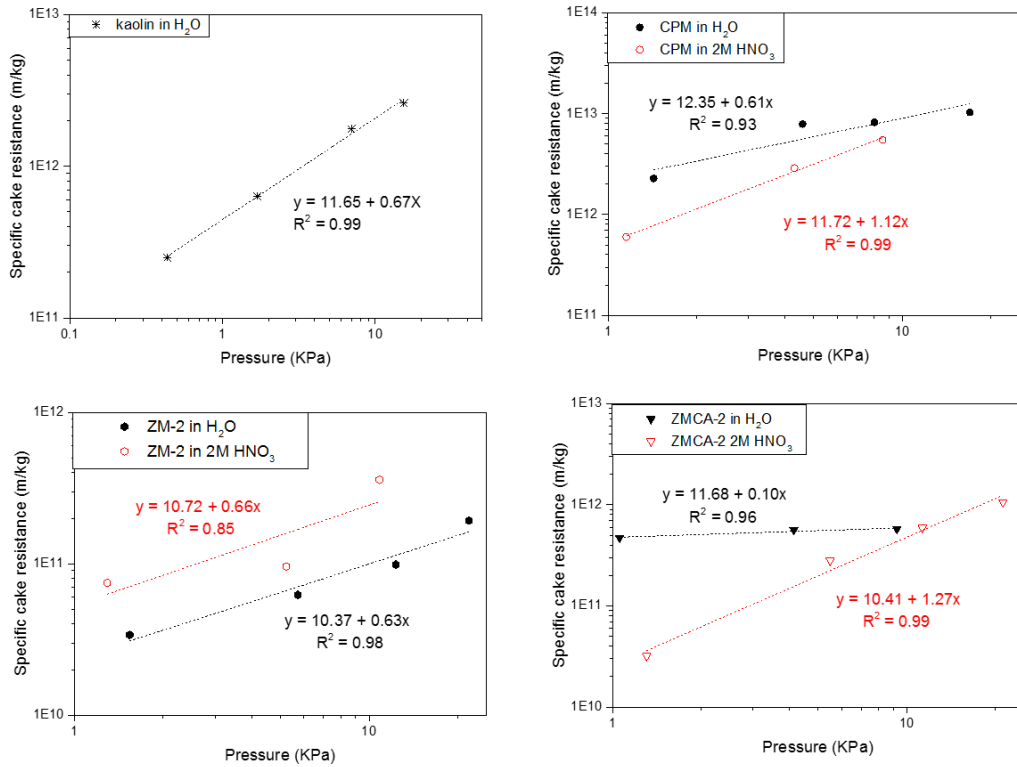


Figure 5-21 Plots of specific cake resistances vs. pressure for; kaolin in water, caesium phosphomolybdate (CPM) in both Milli-Q water and 2 M nitric acid, zirconium molybdate (ZM-2) and zirconium citramolybdate (ZMCA-2) in both Milli-Q water (black) and 2 M nitric acid (red).

Considering Kaolin, the specific cake resistance is comparable to that reported by Loginov et al. (2014). The resistance is spread over a range of 1 order of magnitude comparable to that published by Loginov et al. (2014). However the cake resistance overall is shifted slightly lower, by 0.3 orders of magnitude. The extensions of the Microcon® centrifugal filters, allowed for more sample into the tubes than the method presented by Loginov et al. (2014) and therefore a larger simulant cake could be formed. This methodology could be considered more accurate due to a larger cake mass, as thinner cakes are more likely to be disturbed by fresh filtrate.

As it was previously observed, the stability, sedimentation and compressive yield stress properties of CPM are almost undistinguishable when comparing their results in water to those within 2M nitric acid. Therefore, it was anticipated that CPM would also display similar trends in its permeability as its network structure in both environments appeared similar. However, at lower pressures this does not seem to be the case, although as pressure increases the trend

lines within both mediums seem to come closer together. Overall, the resistance of the CPM cake in acid is less than within water.

The compressive yield stress behaviour of a compound is linked to its permeability as the more the network yields and compresses, the smaller the pore space and therefore the higher the resistance (Buscall, 1982, Green and Boger, 1997, Channell et al., 2000, Antelmi et al., 2001). Therefore, the two experiments should give complementary data.

It is suggested that there is a slight degree of difference of the aggregation of CPM in the two environments. Where within acid more of the colloidal fines may be attached to larger particles, as a result of high effective electrolyte concentration decreasing the particle's stability. Therefore, with less fines present in the system a lower cake resistance would be found, as the presence of smaller particles are more likely to affect filter pores and consequently increase cake resistance (Tomas and Reichmann, 2002). However, the bulk densities of CPM in the two systems are considered comparable.

Regardless of the relatively small differences between the specific resistance in the two mediums (<0.5 orders of magnitude), they are collectively higher than both ZM simulants. This is because for CPM it is its spheroidal particle shape that dominates its cake resistance (Boskovic et al., 2005, Beck et al., 2009, Bourcier et al., 2016).

For ZM-2, the same trend of specific cake resistance vs. pressure is observed in both systems but with 0.5 order of magnitude difference. There is higher resistance observed within the settled bed of ZM-2 within 2 M nitric acid than within water. It has previously been found within a high electrolyte concentration that the collapse of the electric double layer, results in a higher cake porosity and lower specific filtration resistance of cake due to the aggregation of particles (and subsequent increase in particle size) (Wiesner et al., 1989, Antelmi et al., 2001, Hwang and Liu, 2002). However, in the case of ZM-2 within acid although determined to be unstable and likely to aggregate, it has a higher cake resistance than within water. It has previously been found that cakes formed from aggregates over a length of time have higher cake resistance (by over an order of magnitude) than those formed

instantly as a result of the strength of the structures formed (Waite et al., 1999). It is suggested that within acid the unusual ZM-2 shaped particle forms strong heterogeneous aggregated structures potentially resulting in increased tortuosity with the liquid flow. This is supported by the compressive yield stress displaying a small change of volume fraction of <0.5 orders of magnitudes with increased pressure.

For ZMCA-2, its cake resistance data shows an increase of cake resistance with an increase in pressure within acid but not within water. Within water ZMCA-2 is reported to be relatively stable, therefore once a settled cake is formed it will perhaps be difficult to change wheatsheaf orientations and consequently the permeability of the bed. It is likely the wheatsheaf shape that dominates the cake resistance (Bourcier et al., 2016). Within 2 M nitric acid ZMCA-2 is thought to be aggregated and aggregated particles are reported to decrease cake resistance, particularly if irregular packing of the aggregates occurs, forming larger pores (Antelmi et al., 2001). However, it is also reported that with increased pressure, deformations will occur in the aggregates resulting in some interparticle bond breakages, therefore, decreasing aggregate size and potentially releasing fines, increasing the cake resistance (Cabane et al., 2002). Which is the trend observed for ZMCA-2 within acid. The compressive yield stress data shows ZMCA-2 to be very difficult to compress within acid, however the release of fines, i.e. one needle from the wheatsheaf wouldn't necessarily affect the yield stress much but would impact the permeability.

In comparing the nuclear waste simulants, CPM has the highest overall cake resistance which is, likely a result of its size, as smaller particles tend to form less open particle beds (Endo and Alonso, 2001) and spheroidal shape (Boskovic et al., 2005, Beck et al., 2009, Bourcier et al., 2016). The overall trend of the cake resistance for the simulants CPM>ZMCA-2>ZM-2, is comparable to that found by Beck et al. (2009) where it was reported spherical particles have a higher cake resistance over needles > polyhedra.

When considering the filterability of a solid bed, CPM will be the most problematic of all individual simulant beds. Additionally, it is interesting to note that the ZM-2 has a higher resistance in 2 M nitric acid, whereas ZMCA-2 has

a higher resistance in Milli-Q water. This highlights once again that the morphology of ZM significantly influences its behavioural properties, requiring multiple morphologies to be characterised.

It should be noted that the method for permeability determination described has some limitations i.e particle segregation, cake deliquoring and low cake compressibility however, it does assist in evaluating the filterability of concentrated aggregated and moderately compressible systems which is appropriate for this research (Loginov et al. 2014).

Figure 5-22, displays the cake resistance vs. pressure plot for mixed systems of CPM and ZMCA-2, in both Milli-Q water and 2 M nitric acid.

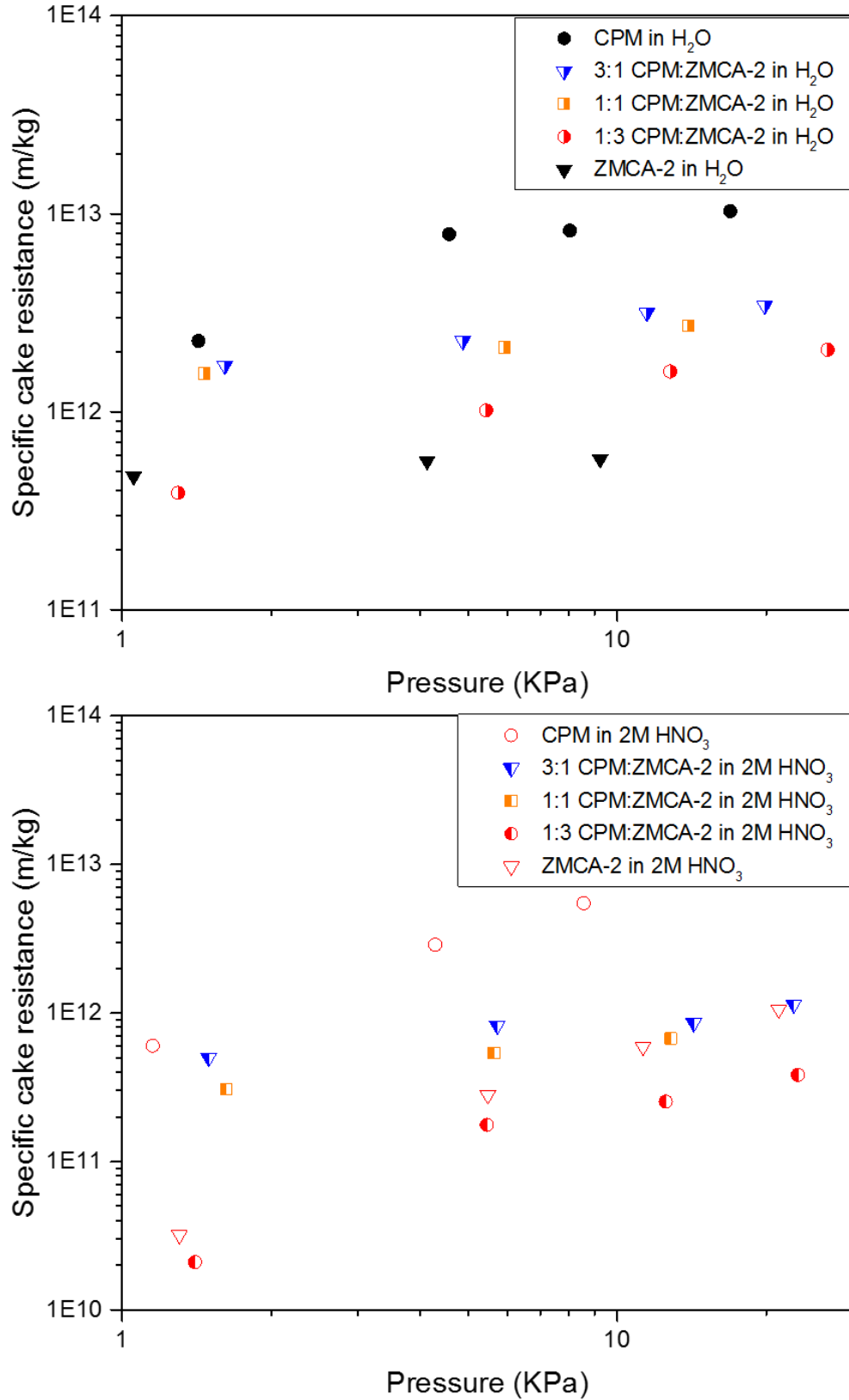


Figure 5-22 Combined plot of specific cake resistance vs. pressure for mixed systems of caesium phosphomolybdate (CPM) and zirconium citramolybdate (ZMCA-2) at 1:3, 1:1 and 3:1 weight ratios at 16 vol% in both Milli-Q water (black) and 2 M nitric acid (red).

It is observed that within 2 M nitric acid all the mixed systems have lower resistance than within Milli-Q water. Which, is a trend also observed for CPM and ZMCA-2 individually. Overall the highest resistance shown for the mixed system is not as high as that reported for CPM as an individual system. Additionally, the lowest resistance observed for the mixed systems, is lower than those values reported for either CPM or ZMCA-2 individually. As the mixed system is predicted to be aggregated a low cake resistance is expected.

In terms of comparing the different mixed systems the over cake resistance trend is 1:3<1:1<3:1 in 2 M nitric acid, and <1:3<1:1<3:1 in Milli-Q water. This trend shows that as the mass of ZMCA-2 decreases, the resistance is increased. However, it is clear overall the system medium is the more dominant factor. In considering a potential washout reagent regardless of the ratio of CPM:ZM within 2 M nitric acid a less resistant bed will form than within water. This suggests the particle interactions between the systems are allowing a more open pore network to form within nitric acid. Therefore, it is proposed that the HAL simulants will be easier to filter through 2 M nitric acid than water.

5.3 Conclusions

This Chapter has presented both results and discussion on the compressive yield stress and permeability of CPM, ZM-2, ZMCA-2 and mixed dispersions of CPM:ZMCA-2 in both Milli-Q water and 2 M nitric acid, in addition, to a mineral suspension of kaolin in water. This is, as far as the author is aware, the first time the LUMiSizer® has been used to investigate both the compressive yield stress and permeability of a material individually within one study. Overall, the compressive yield stress data and permeability data provided complementary data, that allowed for an in depth understanding of the behaviour of the individual and mixed particulate suspensions. Concluding these methodologies could be used in conjunction for future investigations.

As expected, kaolin was found to be the most compressible material and had both a compressive yield stress and permeability behaviour comparable to the literature. CPM was found to behave similarly in both environments in terms of its compressive yield stress, as expected from the settling data presented

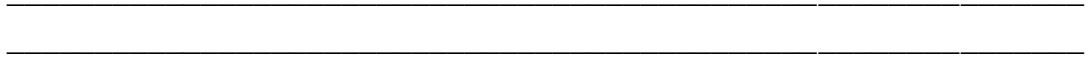
in the previous Chapter. However, there was a deviation in regards to its permeability behaviour with a lower cake resistance found within 2 M nitric acid. It was suggested a slightly more compact bed but with a more open pore network was formed within 2 M nitric acid.

ZM-2 displayed similar compressive yield stress behaviour in both conditions, despite having significantly different settling behaviours. It is observed that the strength of the particle network formed for ZM-2 seems independent of its settling behaviour, it is suggested that this is the result of its irregular elongated square bipyramid shape being unable to form a packed cohesive settled bed. Therefore, it forms in 2 M nitric acid a relatively strong particle network with less available pores, therefore displaying an increased cake resistance. For ZMCA-2 within 2 M nitric acid there is little change in the volume fraction with increased pressure, however there is change in its cake resistance suggesting the slight deformation of strong aggregates releasing fines. Within Milli-Q water a more compressible bed is formed. However as a result of the wheatsheaf shape orientation, the cake resistance of the bed changes little with increased pressure.

Furthermore, mixed systems of CPM:ZMCA-2 were also investigated where it is reported that within both Milli-Q water and 2 M nitric acid regardless of the weight ratio of the simulants, an open difficult to compress bed network is formed. Within 2 M nitric acid this network is slightly more packed with a lower cake resistance. The behaviour of the mixed systems deviates significantly from the behaviour of their individual counterparts suggesting there is a strong particle-particle interaction between the simulants.

Overall results highlight the differences in the behaviours of ZM morphologies and mixed systems in comparison to individual systems. When considering individual HAL systems, CPM is reported to be the most challenging to compress with the highest cake resistance. For mixed systems of CPM:ZMCA-2, they form an open bed network that displays a lower cake resistance in 2 M nitric acid. In considering a wash-out reagent that requires to be filtered, it is suggested that 2 M nitric acid would be preferable than water.

Chapter 6 Conclusions and Recommended Future Work



Research has successfully been conducted on non-radioactive simulants of two known problematic precipitated fission waste products CPM and ZM produced via the reprocessing of nuclear fuel and stored within HASTs before eventual vitrification.

CPM, with spheroidal particle shape and D50 value of 300 nm was successfully synthesised, confirmed by both IR spectrum and XRD pattern. This CPM was reported to have the formula, $\text{Cs}_3\text{PMo}_{12}\text{O}_{40}\cdot 7\text{H}_2\text{O}$, have low solubility and form via a first-order reaction with respect to phosphomolybdic acid in < 3 h. Furthermore, it was reported to form at both ambient (25 °C) and elevated temperatures (100 °C), confirmed via SEM. The speed and ease of the formation of CPM suggests it will be easily formed with the HASTs. The investigation into the kinetics and of the influence of temperature on the formation of CPM is reported for the first time, as far as the author is aware, in this study.

Additionally, ZM, with both a cuboidal morphology (ZM-1) and a wheatsheaf morphology (ZMCA-1) were successfully synthesised confirmed by both IR spectra and XRD patterns, with a D50 value of 10 µm and 300 nm, respectively. Both of these synthesised simulants were also found to be insoluble, with no measurable dissolution occurring. The formation of ZM-1 from CPM was reported to take ~10 days, suggesting a higher ratio of CPM:ZM will be present within the HASTs. Furthermore, two provided ZM simulants with a unique elongated square bipyramid shape with truncated 'pyramid tops' (ZM-2) and a wheatsheaf morphology (ZMCA-2) were also characterised. Displaying comparable IR spectra and XRD patterns, with a D50 value of 5 µm and 15 µm, respectively. The range of morphologies that ZM can form, suggest its formation is sensitive to a number of parameters and that a range of different particle shapes will be present within the HASTs. In comparing the determined bound water molecules of the ZM and ZMCA simulants, the ZMCA samples were reported to have more, suggesting a difference in surface chemistry attributed to the addition of citric acid within its synthesis.

The dispersion stability of the simulants were investigated as it was recognised to be a crucial characteristic in understanding their suspension

behaviours at different pH conditions. All HAL simulants were reported to have low IEP values, with CPM potentially being negatively charged and the ZM simulants being positively charged at low pH. Regardless of potential charge at low pH, all simulants are predicted to be unstable within the HAST conditions as a combination of their low IEP values and the surrounding high electrolyte content, collapsing the electric double layer. Additionally, it was reported that acid group leaching through the simulant's surface molybdate groups were found to reduce the natural pH of Milli-Q water suspensions to around or below their IEP.

Stokes Law was used to predict the settling rates of the simulants and found to be inaccurate, highlighting the complex settling behaviour of the dispersions. Therefore, both the Vesilind and Richardson and Zaki models were utilised in analysing the hindered settling of the simulant suspensions. The concentration of CPM correlation to its settling rate was found to be more pronounced than for other simulants due to instability and coagulation in both Milli-Q water and 2 M nitric acid environments. Overall, CPM displayed similar suspension properties in both conditions, especially for its sedimentation and compressive yield stress behaviours. In considering its permeability, it was reported to have a slightly lower cake resistance due to the aggregates within acid, attracting more of the suspension fines, as a result of high effective electrolyte concentration decreasing the particle's stability. Furthermore, CPM's settling rate was observed to increase with an increase of temperature from 25 °C to 50 °C, which is the temperature reported within the HASTs, as a result of the change in viscosity of the suspension medium. This temperature experiment was not conducted on all simulants but it is proposed that all simulants would show an increase in settling rate within the HASTs than reported through this research due to a decrease in viscosity of the liquor medium.

For the ZM-2 and ZMCA-2 simulants both displayed lower settling rates within Milli-Q water in comparison to 2 M nitric acid, a combination of the effect of the increase of drag force relating to their non-spherical morphology and their instability at low pH. Within both conditions, ZM-2 displayed similar compressive yield stress behaviour forming a more resistant bed within nitric acid suggesting a particle network with less pores than within Milli-Q water.

This is potentially a result of the irregular shape of the ZM-2 forming strong aggregates in nitric acid. ZMCA-2 displayed a less compressible bed within nitric acid with irregular packing of the aggregates occurring, forming larger pores and a lower cake resistance.

A novel method was developed for this research in measuring the permeability of small volumes of material, utilising the LUMiSizer®. Where, as far as the author is aware, is the first time the LUMiSizer® has been used to investigate the sedimentation, compressive yield stress and permeability of a material within one study. Consequently, providing a varied understanding of suspension behaviour for a range of materials.

Overall, in comparing individual simulants CPM is reported to be the most challenging to re-suspend and keep within solution as a result of its high instability in both water and nitric acid. The difference in suspension behaviour for ZM-2 and ZMCA-2 highlights the significant impact of ZM's morphology, where it is suggested a range will be present within the HASTs

An original aspect to the research presented in this thesis was that done upon mixed dispersions of CPM:ZMCA-2. It is unlikely that within the 21 HASTs there will be 100% of one or the other of the simulants, most likely there will be a mixed ratio. The settling rates, compressive yield stress and cake resistance of mixed dispersions all display different properties than those presented for their individual counterparts. Most interestingly, within both Milli-Q water and 2 M nitric acid regardless of the weight ratio of the simulants, an open difficult to compress bed network is formed, suggesting strong particle-particle interactions and high aggregation. It is proposed that CPM is negatively charged and ZMCA-2 is positively charged, therefore they attract one another forming large aggregates.

The key message from this research is that the systems are complex, unstable and likely to aggregate whether individually or mixed within the acidic conditions of the HASTs. POCO is an expensive procedure, even more so if the conditions prepared for are not what is encountered. The more information the planners are armed with, the less likely they are to encounter unexpected and potentially expensive issues. Investing in research and development, such as this project allows for further understanding of current conditions.

Successful POCO is crucial for safe and effective decommissioning, in which we have a moral obligation to provide, in dealing with this legacy waste.

This research is intended to further current understanding of the suspension behaviours of CPM and ZM both individually and as a mixed system in addition to highlighting areas which require future research. It is imperative to understand the extremes of behaviour of these suspensions, in respect of POCO and further processing of the HAL, which will limit the potential for unexpected conditions. Ultimately, the conditions of the HASTs are much more complicated than the conditions explored in this research but it is believed that the results reported will assist further the understanding of two of the most problematic reported fission products.

6.1 Recommended Future Work

In light of the aforementioned conclusions of this research several areas have been highlighted in respect to recommended future work.

First, as highlighted in Chapter 3, the formation of ZM could be further investigated in order to further the understanding of its formation and various morphologies. Through this research both IR and XRD has been shown to identify the individual compounds. Therefore, in tracking the synthesis of ZM an IR diamond probe could be utilised, a diamond probe would be able to handle both the temperature and acidity of the ZM reaction. Additionally, the reaction could be made to take place in an XRD capillary tube therefore directly monitoring the formation of the ZM morphology. Furthermore, Raman spectroscopy could be utilised in identifying and comparing the simulants, *in-situ*. Alternatively, as UV-Vis was successfully applied in tracking the synthesis of CPM, a UV-Vis probe could also be utilised. Furthering the understanding of both the formation of CPM and ZM, will allow more accurate scale-up of their non-active synthesis and a prediction of their ratios within the HASTs. If it was possible to obtain or synthesise a large volume of simulant material, easily and cheaply the properties of the systems could be investigated in bulk. Furthermore, in understanding the formation of ZM it could assist in predicting its morphology within the HASTs.

Within this research the behaviour of dispersions of the simulants individually and mixed were determined in both Milli-Q water and 2 M nitric acid. It was reported at low pH that all simulants were unstable and aggregated. Therefore, in considering a suitable wash-out reagent, investigations into the suspension behaviours of the simulants at a higher pH, could be beneficial. Specifically, as considering the zeta potential data for all the HAL simulants in this study, they are predicted to be stable at high pH which could be advantageous.

There is scope to examine the suspension behaviours of the various systems at different temperatures, considering the HAST conditions are around 50 – 60 °C. This would provide more realistic suspension behaviour data and explore the influence of temperature as a parameter on compressive yield stress and permeability. Furthermore, in considering once the HAL is removed from the HASTs there is potential it will be subjected to different temperatures, therefore an understanding of a change in behaviour with this parameter could be useful.

As it has been identified in this research, CPM and ZMCA clearly have some form of interaction. This could be further investigated through Atomic Force Microscopy (AFM), which is a technique that could be utilised in order to understand further the particle-particle interactions. This is a technique that has not currently been used for the analysis of either CPM or ZM. It potentially could complement the bulk data and provide more insight into the interactions between the systems both individually and mixed. It is possible to mount a particle onto a probe and use this to investigate its interaction with another chosen particle. Through these experiments the Hamaker constant could be determined which can then be used to understand the Van der Waals interactions of the particles and potentially model their aggregation tendency at low pH's, conditions which they experience in the HASTs. Once this has been determined computational fluid dynamics could be utilised in modelling the interaction between the systems for a more accurate prediction of their behaviour within the HASTs.

As this is the first time mixed systems have been explored in any depth, it is recommended that they are investigated further. Specifically, when

considering CPM and various morphologies of ZM and in understanding the impact of a suspension of mixed ZM morphologies upon its properties.

This research has focused on the potential storage behaviour of the HAL simulants, as well as further onward processing. In order to complement this research pipe flow behaviour could be investigated.

In comprehensively understanding the behaviour of CPM and ZM within the HASTs a full replication of the conditions would be ideal, however that would include over 90 elements, which would be both impractical and expensive. However, it is recommended to conduct studies with a range of HAL simulants to gain more accurate insight into the realistic conditions. Additionally, it is suggested to do time based studies, over prolonged periods (i.e. 3 weeks, 3 months, 3 years) to see the effect this has on the behaviour of the simulants. Finally, it would be advantageous to conduct studies on radioactive material to determine if the non-active simulants behave similarly to their chemically analogous counterparts.

References

- AGARWAL, N. & CHHABRA, R. P. 2007. Settling velocity of cubes in Newtonian and power law liquids. *Powder Technology*, 178, 17-21.
- ALLAIN, C., CLOITRE, M. & WAFRA, M. 1995. Aggregation and Sedimentation in Colloidal Suspensions. *Physical Review Letters*, 74, 1478-1481.
- ANGLE & GHARIB 2017. Effects of sand and flocculation on dewaterability of kaolin slurries aimed at treating mature oil sands tailings. *Chemical Engineering Research and Design*, 125, 306-318.
- ANTELM, D., CABANE, B., MEIRELES, M. & AIMAR, P. 2001. Cake Collapse in Pressure Filtration. *Langmuir*, 17, 7137-7144.
- ARAI, T., ITO, D., HIRASAWA, I., MIYAZAKI, Y. & TAKEUCHI, M. 2018. Encrustation Prevention of Zirconium Molybdate Hydrate by Changing Temperature, Nitric Acid, or Solution Concentration. *Chemical Engineering & Technology*, 41, 1-17.
- BAJD, F. 2006. Van der Waals Forces. Ljubljana: Univeristy of Ljubljana.
- BALBIERZ, P. & RUCKA, K. 2017. Sludge settling characterization for the mathematical modelling of sidestream treatment processes. *E3S Web of Conferences 17*. EDP Sciences
- BARGIEŁ, MONIKA, TORY & M., E. 2013. Extension of the Richardson–Zaki equation to suspensions of multisized irregular particles. *International Journal of Mineral Processing*, 120, 22-25.
- BARR, J. & WHITE, L. R. 2006. Centrifugal Drum Filtration: I. A Compression Rheology Model of Cake Formation. *ALChE Journal*, 52, 545-556.
- BECK, R., HÄKKINEN, A., MALTHE-SØRENSEN, D. & ANDREASSEN, J.-P. 2009. The effect of crystallization conditions, crystal morphology and size on pressure filtration of l-glutamic acid and an aromatic amine. *Separation and Purification Technology*, 66, 549-558.
- BERZELIUS 1826. Beitrag zur näheren Kenntniss des Molybdäns. *Annalen der Physik*, 82, 369-392.
- BIGGS, S., FAIRWEATHER, M., YOUNG, J., HYATT, N. & LIVENS, F. 2009. The Diamond Univeristy research consortium: nuclear waste characterisation, immobilisation and storage. *Environmental Remediation and Radioactive Waste Management*. Liverpool, UK.
- BODANSKY, D. 2006. Reprocessing spent nuclear fuel. *Physics Today*. American Institute of Physics.
- BOSKOVIC, L., ALTMAN, I. S., AGRANOVSKI, I. E., BRADDOCK, R. D., MYOJO, T. & CHOI, M. 2005. Influence of Particle Shape on Filtration Processes. *Aerosol Science and Technology*, 39, 1184-1190.
- BOURCIER, D., PIERRE FERAUD, J., COLSON, D., MANDRICK, K., ODE, D., BRACKX, E. & PUEL, F. 2016. Influence of particle size and shape properties on cake resistance and compressibility during pressure filtration. *Chemical Engineering Science*, 144, 176-187.
- BRADLEY, D. F., QUAYLE, M. J., ROSS, E., WARD, T. R. & WATSON, N. 2004. Promoting the conversion of caesium phosphomolybdate to zirconium molybdate. *ATALANTE Conference on Nuclear Chemistry for Sustainable Fuel Cycles*. Nimes, France.

- BROWN, G. N., BRAY, L. A., CARLSON, C. D., CARSON, K. J., DESCHANE, J. R., ELOVICH, R. J., HOOPES, F. V., KURATH, D. E., NENNINGER, L. L. & TANAKA, P. K. 1996. Comparison of Organic and Inorganic Ion Exchangers for Removal of Cesium and Strontium from Simulated and Actual Hanford 241 -AW-'I 01 DSSF Tank Waste.
- BROWN, L. A. & ZUKOSKI, C. F. 2003. Experimental Tests of Two-Phase Fluid Model of Drying Consolidation. *ALChE Journal*, 49, 362-372.
- BUSCALL, R. 1982. The elastic properties of structured dispersions: a simple centrifuge method of examination. *Colloids and Surfaces*, 5, 269-283.
- BUSCALL, R. & WHITE, L. R. 1987. The Consolidation of Concentrated Suspensions Part 1 .-The Theory of Sedimentation. *Journal of Chemical Society, Faraday Transactions 1*, 83, 873-891.
- BUX, J., HUNTER.T, PAUL.N, DODDS.J, RHODES.D, PEAKALL.J & BIGGS.S 2014. In Situ Characterization of Mobilization, Dispersion and Re-Settling in Impinging Jet Ballast Tanks with an Acoustic Backscatter System – 14097. *Waste Management*. Phoenix, Arizona, USA.
- BYE, C. M. & DOLD, P. L. 1999. Evaluation of Correlations for Zone Settling Velocity Parameters Based on Sludge Volume Index-Type Measures and Consequences in Settling Tank Design. *Water Environment Research*, 71, 1333-1344.
- BYKHOVSKII, D. N., KOL'TSOVA, T. I. & KUZ'MINA, M. A. 2006. Phases of variable composition in crystallization of cesium phosphomolybdate. *Radiochemistry*, 48, 429-433.
- BYKHOVSKII, D. N., KOL'TSOVA, T. I. & ROSHCHINSKAYA, E. M. 2009. Cesium preconcentration by recovery from solutions in the form of phosphomolybdate. *Radiochemistry*, 51, 159-164.
- BYKHOVSKII, D. N., KOL'TSOVA, T. I. & ROSHCHINSKAYA, E. M. 2010. Reduction of Radioactive Waste Volume Using Selective Crystallization Processes. *Radiochemistry*, 52, 530-536.
- CABANE, B., MEIERELES, M. & AIMAR, P. 2002. Cake collapse in frontal filtration of colloidal aggregates: mechanisms and consequences. *Desalination*, 146, 155-161.
- CARLEY-MACAULY, K. W., GUTMAN, R. G., HOOPER, H. W., JENKINS, J. A., TURNER, WACE, R. R., CHAUVET, R., GAUCHON, J. P. & DIPPEL, T. 1981. Radioactive Waste: Advanced Management Methods for Medium Active Liquid Waste. Brussels, Luxembourg.
- CHANNELL, G. M., MILLER.K.T & ZUKOSKI.C.F 2000. Effects of Microstructure on the Compressive Yield Stress. *AICHe Journal*, 46, 72-78.
- CHEN, ANANDARAJAH A & INYANG H 2000. Pore Fluid Properties and Compressibility of Kaolinite. *Journal of Geotechnical and Geoenvironmental Engineering*, 126, 798-807.
- CHONG, Y. S., RATKOWSKY.D.A, EPSTEIN.N 1979. Effect of Particle Shape on Hindered Settling in Creeping Flow. *Powder Technology*, 23, 55-66.
- CHU, C. P. & LEE, D. J. 2002. Dewatering of Waste Activated Sludge Via Centrifugal Field. *Drying Technology*, 20, 953-966.
- CLARKE, J. 2009. Theory of sedimentation and centrifugation.
- CLEARFIELD, A. & BLESSING, R. H. 1972. The preparation and crystal structure of a basic zirconium molybdate and its relationship to ion

- exchange gels. *Journal of inorganic and nuclear chemistry*, 34, 2643-2663.
- CLEARFIELD, A. & STYNES, J. A. 1964. The preparation of crystalline zirconium phosphate and some observations on its ion exchange behaviour. *Journal of inorganic and nuclear chemistry*, 26, 117-129.
- CLELLAND, D. W. Concentration and Storage of Highly-Active Wastes from the First Stages of the United Kingdom Civil Nuclear Power Programme. In: INTERNATIONAL ATOMIC ENERGY AGENCY, ed. Symposium on the treatment and storage of high level radioactive wastes 1962 Vienna.
- COMMITTEE ON CLIMATE CHANGE 2012. The need for a carbon intensity target in the power sector. London: Committee on Climate Change.
- CRUYWAGEN, J. J., ROHWER E.A & G.F.S, W. 1995. Molybdenum(IV) complex formation- 8 equilibria and thermodynamics quantities for the reactions with citrate. *Polyhedron*, 14, 3481-3493.
- CURVERS, D., SAVEYN, H., SCALES, P. J. & VAN DER MEEREN, P. 2009. A centrifugation method for the assessment of low pressure compressibility of particulate suspensions. *Chemical Engineering Journal*, 148, 405-413.
- DANIEL, D. 1993. *Geotechnical practice for waste disposal*, London, Chapman & Hall.
- DARCY, H. 1856. Les Fontaines Publiques de la Ville de Dijon. *Dalmont, Paris*.
- DAVIES 1968. The Experimental Study of the Differential Settling of Particles in Suspension at High Concentrations. *Powder Technology*, 2, 43-51.
- DE KRESTER, R. G., USHER, S. P., SCALES, P. J., BOGER, D. V. & LANDMAN, K. A. 2001. Rapid Filtration Measurement of Dewatering Design and Optimization Parameters. *ALChE Journal*, 46, 1758-1769.
- DERJAGUIN, B. & LANDAU, L. 1941. Theory of the stability of strongly charged lyophobic sols and of the adhesion of strongly charged particles in solutions of electrolytes. *Acta Physicochimica U.S.S.R*, 633-662.
- DERMECHE, L., THOUVENOT, R., HOCINE, S. & RABIA, C. 2009. Preparation and characterization of mixed ammonium salts of Keggin phosphomolybdate. *Inorganica Chimica Acta*, 362, 3896-3900.
- DOBSON & PHILLIPS, C. 2006. High Level Waste Processing in the U.K. – Hard Won Experience that can Benefit U.S. Nuclear Cleanup Work. *Waste Management Tucson, Arizona, USA*.
- DOGONCHI, A. S., HATAMI, M., HOSSEINZADEH, K. & DOMAIRRY, G. 2015. Non-spherical particles sedimentation in an incompressible Newtonian medium by Padé approximation. *Powder Technology*, 278, 248-256.
- DOUCET, F. J., GODDARD, D. T., TAYLOR, C. M., DENNISS, I. S., HUTCHISON, S. M. & BRYAN, N. D. 2002. The formation of hydrated zirconium molybdate in simulated spent nuclear fuel reprocessing solutions. *Physical Chemistry Chemical Physics*, 4, 3491-3499.
- DOZOL, J. F., SIMON, N., LAMARE, V., ROUQUETTE, H., EYMARD, S., TOURNOIS, B., DE MARC, D. & MACIAS, R. M. 1999. A Solution, for Cesium Removal from High-Salinity Acidic or Alkaline Liquid Waste: The Crown Calix[4]Arenes. *Separation Science and Technology*, 34, 877-909.

- DUNNETT, B. 2015. Formation and properties of solids formed during during evaporation and storage of highly active liquor.
- DUNNETT, B., GRIBBE, N. & SHORT, R. 2014. A new glass fomulation for the vitfirifcation of high molybdenum waste. *NNL Science*, 12-16.
- DUNNETT, B., WARD.T, ROBERTS.R & CHEESEWRIGHT.J 2016. Physical properties of highly active liquor containing molybdate solids *ATALANTE Conference on Nuclear Chemistry for Sustainable Fuel Cycles*. Montpellier, France Procedia Chemistry.
- EDMONDSON, M., MAXWELL, L. & WARD, T. R. 2012. A methodology for POCO of a highly active facility including solids behaviour. *Waste Management*. Phonenix, Arizona, USA.
- EINSTEIN, A. 1905. On the movement of small particles suspended in stationary liquids required by the molecular-kinetic theory of heat. *Annalen der Physik*, 17, 549 - 560.
- EINSTEIN, A. 1956. *Investigations on the theory of the Brownian movement*, USA, Dover Publications, INC.
- ENDO, Y. & ALONSO, M. 2001. Physical Meaning of Specific Cake Resistance and Effects of Cake Properties in Compressible Cake Filtration *Filtration and Seperation* 38, 43-46.
- ESHEL, LEVY.G.J, MINGELGRIN.U & SINGER.M.J 2004. Critical Evaluation of the Use of Laser Diffraction for Particle size Distribution Analysis *Soil Science Society of America*, 68, 736-743.
- EVANS, J. V., MOORE, W., SHYING, M. E. & SODEAU, J. M. 1987. Zirconium Molybdate Gel as a generator for Technetium-99m I. The Concept and its evalutaion *Applied Radiation and Isotopes*, 38, 19-23.
- FAIRHURST, D. 2013. An Overview of the Zeta Potential - Part 1: The Concept. *American Pharmaceutical Review*.
- FAN, L., MAO.ZS & YANG.C 2004. Experiment on Settling of Slender Particles with Large Aspect Ratio and Correlation of the Drag Coefficient. *Industrial and Engineering Chemistry Research*, 43, 7664-7670.
- FERAUD, J., BOURCIER, D., ODE, D. & PUEL, F. 2013. New filterability and compressibility test cell design for nuclear products. *Nuclear Engineering Design*, 265, 288-293.
- FOUNTAIN, T., ZARGES, T., HUDSON, I. & WRIGHT, T. 2011. Sellafield Plan.
- FRIESEN .D.A, MORELLO .L, HEADLEY .J.V & LANGFORD .C.H 2000. Factors influencing relative efficiency in photo-oxidations of organic molecules by Cs₃PW₁₂O₄₀ and TiO₂ colloidal photocatalysts. *Journal of Photochemistry and Photobiology*, 133, 213-220.
- FUKUYAMA, R., TANAKA, T., JAMI, M. S. & IWATA, M. 2013. Analysis of centrifugal dewatering: consolidation behavior with and without supernatant. *Proc. of FILTECH*, 112.
- GABITTO, J. & TSOURIS, C. 2008. Drag coefficient and settling velocity for particles of cylindrical shape. *Powder Technology*, 183, 314-322.
- GHALEBI, H. R., SOHEIL, A. & AFZAL, K. 2016. Keggin type of cesium phosphomolybdate synthesized via solid-state reaction as an efficient catalyst for the photodegradation of a dye pollutant in aqueous phase. *Journal of Molecular Catalysis A: Chemical*, 415, 96-103.

- GIBBS, MATTHEWS M.D & LINK D 1971. The Relationship between Sphere Size and Settling Velocity. *Journal of Sedimentary Petrology*, 41, 7-18.
- GREEN, M. D. & BOGER, D. V. 1997. Yielding of Suspensions in Compression. *Industrial & Engineering Chemistry Research*, 36, 4984-4992.
- GREEN, M. D., EBERL, M. & LANDMAN, K. A. 1996. Compressive yield stress of flocculated suspensions: determination via experiment. *Materials, Interfaces and Electrochemical Phenomena*, 42, 2308-2318.
- GREEN, M. D., LANDMAN, K. A., DE KRESTER, R.G & BOGER, D. V. 1998. Pressure Filtration Technique for Complete Characterization of Consolidating Suspensions. *Industrial & Engineering Chemistry Research*, 37, 4152-4156.
- GREENE, C. H. 1937. The Solubility of Barium Nitrate in Concentrated Nitric Acid. *Journal of the American Chemical Society*, 59, 1186-1188.
- GREENSPAN & UNGARISH 1982. On hindered settling of particles of different sizes *International Journal of Multiphase Flow*, 8, 587-604.
- GRIFFON, J. 2010-2011. Technology Development and Delivery Summary. Sellafield Ltd.
- GUAN, J., AMAL, R. & WAITE, T. D. 2001. Effect of aggregate size and structure on specific resistance of biosolids filter cakes. *Water Science and Technology*, 44, 215-220.
- HAIDER & LEVENSPIEL 1989. Drag Coefficient and Terminal Velocity of Spherical and Nonspherical Particles. *Powder Technology*, 58, 63-70.
- HAKKINEN, POLLANEN K, KARJALAINEN M, RANTANEN J, LOUHI-KULTANEN & NYSTROM L 2005. Batch cooling crystallization and pressure filtration of sulphathiazole: the influence of solvent composition. *Biotechnology and Applied Biochemistry*, 41, 17-28.
- HAMAKER, H. C. 1937. The London-Van Der Waals attraction between spherical particles. *Physica*, 4, 1058-1072.
- HARRISON, M. T. & BROWN, G. C. 2018. Chemical durability of UK vitrified high level waste in Si-saturated solutions. *Materials Letters*, 221, 154-156.
- HENRY, D. C. & LAPWORTH, A. 1931. The Cataphoresis of Suspended Particles. Part I. - The Equation of Cataphoresis. *Proceedings of the Royal Society of London A*133, 106-129.
- HLAVACEK, M. & REMY, J. F. 1995. Simple Relationships among Zeta Potential, Particle Size Distribution, and Cake Specific Resistance for Colloid Suspensions Coagulated with Ferric Chloride. *Separation Science and Technology*, 30, 549-563.
- HODGSON, B., WARD, T. R., DUNNETT, B., PYKE, C & CHEESEWRIGHT, J. 2018. Dissolution Rates of Barium Nitrate in Water and Weak Nitric Acid Solutions Under Stirred and Stagnant Conditions. *Journal of Solution Chemistry*, 47, 1858-1874.
- HORPIBULSUK, S., YANGSUKKASEAM, N., CHINKULKIJNIWAT, A. & DU, Y. J. 2011. Compressibility and permeability of Bangkok clay compared with kaolinite and bentonite. *Applied Clay Science*, 52, 150-159.
- HURST, V. J., DONNAY, J. D. H. & DONNAY, G. 2018. Staurolite twinning (With Plates V-VI.). *Mineralogical Magazine and Journal of the Mineralogical Society*, 31, 145-163.

- HWANG, K.-J. & CHOU, K.-H. 2006. Effect of Cake Compression on the Performance of Centrifugal Dewatering. *Drying Technology*, 24, 1263-1270.
- HWANG, K.-J., CHU, W.-T. & LUI, W.-M. 2001. A Method to Determine the Cake Properties in Centrifugal Dewatering. *Separation Science and Technology*, 36, 2693-2706.
- HWANG, K.-J. & LIU, H.-C. 2002. Cross-flow microfiltration of aggregated submicron particles. *Journal of Membrane Science*, 201, 137-148.
- IRITANI, E., HATTORI, K. & MURASE, T. 1993. Analysis of dead-end ultrafiltration based on ultracentrifugation method. *Journal of Membrane Science*, 81, 1-13.
- IRITANI, E., HATTORI, K. & MURASE, T. 1994. Evaluation of Dead-end Ultrafiltration Properties by Ultracentrifugation Method. *Journal of Chemical Engineering of Japan*, 27, 347-362.
- IZUMIDA, T. & KAWAMURA, F. 1990. Precipitates Formation Behavior in Simulated High Level Liquid Waste of Fuel Reprocessing. *Journal of Nuclear Science and Technology*, 27, 267-274.
- JAWSON & DOVE 1956. Twinning Properties of Lattice Planes. *Acta Crystallographica*, 9, 621-626.
- JIANG, J., MAY, I., SARFIELD, M. J., OGDEN, M., FOX, D. O., JONES, C. J. & MAYHEW, P. 2005. A Spectroscopic Study of the Dissolution of Cesium Phosphomolybdate and Zirconium Molybdate by Ammonium Carbamate. *Journal of Solution Chemistry*, 34, 443-468.
- JOHNSON, M., PEAKALL, J., FAIRWEATHER, M., BIGGS, S., HARBOTTLE, D. & HUNTER, T. N. 2016. Characterization of Multiple Hindered Settling Regimes in Aggregated Mineral Suspensions. *Industrial & Engineering Chemistry Research*, 55, 9983-9993.
- KANG, Z., WANG, Y., WANG, E., LIAN, S., GAO, L., YOU, W., HU, C. & XU, L. 2004. Polyoxometalates nanoparticles: synthesis, characterization and carbon nanotube modification. *Solid State Communications*, 129, 559-564.
- KASZUBA, M., CORBETT, J., WATSON, F. M. & JONES, A. 2010. High-concentration zeta potential measurements using light-scattering techniques. *Philos Trans A Math Phys Eng Sci*, 368, 4439-51.
- KONDRAT'EV, A. S. & NAUMOVA, E. A. 2006. Hindered settling velocity of a bimodal mixture of spherical solid particles in a Newtonian fluid. *Theoretical Foundations of Chemical Engineering*, 40, 387-392.
- KONDRAT'EV, A. S. & NAUMOVA, E. A. 2007. Calculation of the hindered settling velocity of a bimodal mixture of solid particles of arbitrary shape in a Newtonian fluid. *Theoretical Foundations of Chemical Engineering*, 41, 216-220.
- KRISHNAMOORTHY 2010. Sedimentation model and analysis for differential settling of two - particle - size suspensions in the Stokes region. *International Journal of Sediment Research* 25, 119-133.
- KRITIL, J., KOURIM.V, 1960. Exchange properties of ammonium salts of 12-heteropolyacids. Sorption of caesium on ammonium phosphotungstate and. *Journal of Inorganic and Nuclear Chemistry*, 12, 367-369.
- LANDMAN, K. A. & WHITE, L. R. 1994. Solid/liquid separation of flocculated suspensions. *Advances in Colloid and Interface Science*, 51, 175-246.
- LAU 1994. Temperature effect on settling velocity and deposition of cohesive sediments. *Journal of Hydraulic Research*, 32, 41-51.

- LAU, R. & CHUAH, H. K. L. 2013. Dynamic shape factor for particles of various shapes in the intermediate settling regime. *Advanced Powder Technology*, 24, 306-310.
- LEE, S. J., CHU, C. P., TAN, R. B. H., WANG, C. H. & LEE, D. J. 2003. Consolidation dewatering and centrifugal sedimentation of flocculated activated sludge. *Chemical Engineering Science*, 58, 1687-1701.
- LEMONS, D. & GYTHIEL, A. 1997. Review of Paul Langevin's 1908 paper 'On the Theory of Brownian Motion'. *Am.J.Phys*, 65, 1079-1081.
- LENTO, J. & HARJULA, R. 1987. Separation of Cesium from Nuclear Waste Solutions with Hexacyanoferrate(II)S and Ammonium Phosphomolybdate. *Solvent Extraction and Ion Exchange*, 5, 343-352.
- LERCHE, D. & SOBISCH, T. 2007. Consolidation of concentrated dispersions of nano- and microparticles determined by analytical centrifugation. *Powder Technology*, 174.
- LESTER, D., USHER, S. & SCALES, P. 2005. Estimation of the hindered settling function $R(?)$ from batch-settling tests. *ALChE Journal*, 51, 1158-1168.
- LIAO, D. L., WU, G. S. & LIAO, B. Q. 2009. Zeta potential of shape-controlled TiO₂ nanoparticles with surfactants. *Colloids and Surfaces A: Physicochemical and Engineering Aspects*, 348, 270-275.
- LIND, C., WILKINSON, A. P., RAWN, C. J. & PAYZANT, E. A. 2001. Preparation of the negative thermal expansion material cubic ZrMo₂O₈. *Journal of Materials Chemistry*, 11, 3354-3359.
- LIU, M. & GUYOT-SIONNEST, P. 2005. Mechanism of Silver(I)-Assisted Growth of Gold Nanorods and Bipyramids. *Journal of Physical Chemistry*, 109, 22192-22200.
- LIU, Y. J. & JOSEPH, D. D. 1993. Sedimentation of particles in polymer solutions. *Journal of Fluid Mechanics*, 255, 565-595.
- LOCKETT & BASSOON 1979. Sedimentation of Binary Particle Mixtures *Power Technology*, 24, 1-7.
- LOGINOV, M., CITEAU, M., LEBOVKA, N. & VOROBIEV, E. 2012. Evaluation of low-pressure compressibility and permeability of bentonite sediment from centrifugal consolidation data. *Separation and Purification Technology*, 92, 168-173.
- LOGINOV, M., LEBOVKA, N. & VOROBIEV, E. 2014. Multistage centrifugation method for determination of filtration and consolidation properties of mineral and biological suspensions using the analytical photocentrifuge. *Chemical Engineering Science*, 107, 277-289.
- LOGINOV, M., VOROBIEV, E., LEBOVKA, N. & LARUE, O. 2011. Compression-permeability characteristics of mineral sediments evaluated with analytical photocentrifuge. *Chemical Engineering Science*, 66, 1296-1305.
- LOTH, E. 2008. Drag of non-spherical solid particles of regular and irregular shape. *Powder Technology*, 182, 342-353.
- LU, J. F., TSAI, Y. Y. & TSAI, C. J. 2016. Shape dependence of the electrochemical properties of α -Fe₂O₃ particles as anode materials for lithium ion batteries. *RSC Advances*, 6, 26929-26935.
- LU, W.-M., HUANG, Y.-P. & HWANG, K.-J. 1998. Methods to determine the relationship between cake properties and solid compressive pressure. *Separation and Purification Technology*, 9, 9-23.

- LU, Z., LIU, Q., XU, Z. & ZENG, H. 2015. Probing Anisotropic Surface Properties of Molybdenite by Direct Force Measurements. *Langmuir*, 31, 11409-18.
- LUSSIER, A. J., HAWTHORNE, ABDU, S., HERWIG, V. K., MICHAELIS, P. M. & AGUIAR, S. K. 2011. The crystal chemistry of 'wheatsheaf' tourmaline from Mogok, Myanmar. *Mineralogical Magazine* 75, 66-68.
- MACHEDER, B. 2011. *Zirconium molybdate crystal growth and morphological control (thesis)*. PhD Thesis Univeristy of Bristol.
- MAGNALDO, A., MASSON, M. & CHAMPION, R. 2007. Nucleation and crystal growth of zirconium molybdate hydrate in nitric acid. *Chemical Engineering Science*, 62, 766-774.
- MAGNALDO, A., NOIRE, M. H., ESBELIN, E., DANCAUSSE, J. P. & PICART, S. 2004. Zirconium molybdate hydrate precipitates in spent nuclear fuel reprocessing. *ATALANTE Conference on Nuclear Chemistry for Sustainable Fuel Cycles*. Nimes, France.
- MANDZY, N., GRULKE, E. & DRUFFEL, T. 2005. Breakage of TiO₂ agglomerates in electrostatically stabilized aqueous dispersions. *Powder Technology*, 160, 121-126.
- MASLIYAH, J. 1979. Hindered settling in a multi-species particle system. *Chemical Engineering Science*, 34, 1166-1168.
- MAUDE, A. D. & WHITMORE, R. L. 1958. A generalized theory of sedimentation. *British Journal of Applied Physics*, 9, 477-482.
- MCARTHUR, G., TINSLEY, T. & MCKENDRICK, D. 2005. Development of a Liquid Jet Sludge Re-suspension Model (used on Pulse Jets or Jet Ballasts) *Paper number 480a, Proceeding 2005 AIChE Annual Meeting*.
- MEARNS, E. 2013. UK North Sea Oil Production Decline. *Energy, Environment and Policy* [Online]. Available from: <http://euanmearns.com/uk-north-sea-oil-production-decline/> 2018].
- MICHAELS, A. S. & BOLGER, J. C. 1962. Settling Rates and Sediment Volumes of Flocculated Kaolin Suspensions. *Industrial & Engineering Chemistry Fundamentals*, 1, 24-33.
- MILLER, C. The Stokes-Einstein Law for Diffusion in Solution. *Proceedings of the Royal Society of London. Series A, Containing Papers of a Mathematical and Physical Character*, 1924. The Royal Society, 724-749.
- MILLER, K. T., MELANT, R. M. & ZUKOSKI, C. F. 1996. Comparison of the Compressive Yield Response of aggregated Suspensions: Pressure Filtration, Centrifugation, and Osmotic Consolidation. *Journal of the American Ceramic Society*, 79, 2545-2556.
- MIRZA & RICHARDSON 1979. Sedimentation of suspensions of particles of two or more sizes *Chemical Engineering Science*, 34, 447-454.
- MISHINA, N. E., AKHMATOV, A. A., ZILBERMAN, B. Y., SHADRIN, A. Y. & SOLYARSKAYA, E. I. 2010. Solubility and Coprecipitation of Barium and Strontium Nitrates in HNO₃ Solutions and Multicomponent Systems. *Radiochemistry*, 52, 523-529.
- MISHINA, N. E., ZILBERMAN, B. Y., KOL'TSOVA, T. I., LUMPOV, A. A. & PUZIKOV, E. A. 2014a. Composition of precipitates of barium and strontium nitrates crystallizing from nitric acid solutions. *Radiochemistry*, 56, 252-261.

- MISHINA, N. E., ZILBERMAN, B. Y., LUMPOV, A. A., KOL'TSOVA, T. I., PUZIKOV, E. A. & GAVSHINA, D. Y. 2015. Coprecipitation of barium and strontium nitrates in the course of crystallization from nitric acid solutions and simulated high-level PUREX process raffinate. *Radiochemistry*, 57, 504-512.
- MISHINA, N. E., ZILBERMAN, B. Y., LUMPOV, A. A., KOLTSOVA, T. I., PUZIKOV, E. A. & RYABKOV, D. V. 2014b. Nitric acid adduct formation during crystallization of barium and strontium nitrates and their coprecipitation from nitric acid media. *Journal of Radioanalytical and Nuclear Chemistry*, 304, 387-393.
- MITCHELL 1993. *Fundamentals of soil behavior*, New York, Wiley.
- MITCHELL, J. E. "The application of colloidal theory to the compressibility of clays." Interparticle forces in clay-water-electrolyte systems, 1960 Melbourne, Australia. Commonwealth Scientific and Industrial Research Organization.
- MONROY-GUZMÁN, F., DÍAZ-ARCHUNDIA, L. V. & CONTRERAS RAMÍREZ, A. 2003. Effect of Zr:Mo ratio on ^{99m}Tc generator performance based on zirconium molybdate gels. *Applied Radiation and Isotopes*, 59, 27-34.
- MONROY-GUZMAN, F., RIVERO GUTIERREZ, T., LOPEZ MALPICA, I. Z., HERNANDEZ CORTES, S., ROJAS NAVA, P., VAZQUEZ MALDONADO, J. C. & VAZQUEZ, A. 2011. Production optimization of ⁹⁹Mo/^{99m}Tc zirconium molybdate gel generators at semi-automatic device: DISIGEG. *Applied radiation and isotopes*, 70, 103-11.
- MONROY-GUZMAN, F. D.-A. L. V., HERNÁNDEZ-CORTÉS S, 2008. ⁹⁹Mo/^{99m}Tc Generators Performances Prepared from Zirconium Molybdate Gels. *Journal of Brazilian Chemistry Society*, 19, 380-388.
- MOORE C.A & MITCHELL J.E 1977. Electromagnetic forces and shear strength. *Geotechnical*, 24, 627-636.
- MORT, P., ASKEW.G, PALETHORPE.S, BOWEN.B & HASTINGS, J. J. 2013. Technical challenges needs and opportunities in decommissioning of the Sellafield Site. *In: LTD, S. (ed.) Decommissioning Directorate*.
- MUKHERJEE, J., DUTTA, D. P., RAMAKUMAR, J. & TYAGI, A. K. 2016. A comprehensive study on the uptake of dyes, Cu(II) and radioactive ¹³⁷Cs(I) by sonochemically synthesized strontium/yttrium tungstate and molybdate nanoparticles. *Journal of Environmental Chemical Engineering*, 4, 3050-3064.
- MURASE, T., IWATA, M., ADACHI, T., GMACHOWSKI, L. & SHIRATO, M. 1989. An Evaluation of Compression-Permeability Characteristics in the Intermediate Concentration Range by Use of Centrifugal and Constant-Rate Compression Techniques. *Journal of Chemical Engineering of Japan*, 27, 378-384.
- NAVARRO, J. R., MANCHON, D., LEROUGE, F., COTTANCIN, E., LERME, J., BONNET, C., CHAPUT, F., MOSSET, A., PELLARIN, M. & PAROLA, S. 2012. Synthesis, electron tomography and single-particle optical response of twisted gold nano-bipyramids. *Nanotechnology*, 23, 145707.
- NELSON, S. A. 2019. *Twinning, Polymorphism, Polytypism, Pseudomorphism* [Online]. New Orleans, Louisiana: Tulane University

- Available: <https://www.tulane.edu/~sanelson/eens211/twinning.htm>
[Accessed 2019].
- NUCLEAR DECOMMISSIONING AUTHORITY 2010. Geological Disposal An overview of the generic Disposal System Safety Case.
- NUCLEAR DECOMMISSIONING AUTHORITY 2017. Draft Business Plan Cumbria
- NUCLEAR DECOMMISSIONING AUTHORITY & SELLAFIELD LTD. 2018. *End of reprocessing at Thorp signals new era for Sellafield* [Online]. GOV.UK. Available: <https://www.gov.uk/government/news/end-of-reprocessing-at-thorp-signals-new-era-for-sellafield> [Accessed 2019].
- OLSON & MESRI 1970. Mechanisms Controlling Compressibility of Clays. *Journal of the Soil Mechanics and Foundations Division*, 96, 1863-1878.
- PATEL, A. & PATHAN, S. 2012. Keggin-type cesium salt of first series transition metal-substituted phosphomolybdates: one-pot easy synthesis, structural, and spectral analysis. *Journal of Coordination Chemistry*, 65, 3122-3132.
- PATWARDHAN & TIEN, C. 1985. Sedimentation and Liquid Fluidization of Solid Particles of Different Sizes and Densities *Chemical Engineering Science*, 40, 1051-1060.
- PAUL, N. 2014. *Characterisation of highly active nuclear waste simulants (thesis)*. PhD, The University of Leeds.
- PAUL, N., BIGGS, S., EDMONDSON, M., HUNTER, T. N. & HAMMOND, R. B. 2013. Characterising highly active nuclear waste simulants. *Chemical Engineering Research and Design*, 91, 742-751.
- PAUL, N., BIGGS, S., SHIELS, J., HAMMOND, R. B., EDMONDSON, M., MAXWELL, L., HARBOTTLE, D. & HUNTER, T. N. 2017. Influence of shape and surface charge on the sedimentation of spheroidal, cubic and rectangular cuboid particles. *Powder Technology*, 322, 75-83.
- PAUL, N., HAMMOND, R. B., HUNTER, T. N., EDMONDSON, M., MAXWELL, L. & BIGGS, S. 2015. Synthesis of nuclear waste simulants by reaction precipitation: Formation of caesium phosphomolybdate, zirconium molybdate and morphology modification with citratomolybdate complex. *Polyhedron*, 89, 129-141.
- PERINI, G., SALVATORI, F., OCHSENBEIN, D. R., MAZZOTTI, M. & VETTER, T. 2019. Filterability prediction of needle-like crystals based on particle size and shape distribution data. *Separation and Purification Technology*, 211, 768-781.
- PIAZZA, R. 2014. Settled and unsettled issues in particle settling. *Rep Prog Phys*, 77, 056602.
- PIGNON, F., MAGIN, A., PIAU, J. M., CABANE, B., AIMAR, P., MEIERELES, M. & LINDNER, P. 2000. Structural characterisation of deposits formed during frontal filtration. *Journal of Membrane Science*, 74, 189-204.
- RAO, B. S. M., GANTNER, E., MULLER, H. G., REINHARDT, J., STEINERT, D. & ACHE, H. J. 1986. Solids formation from synthetic fuel reprocessing solutions characterisation of zirconium molybdate. *Applied Spectroscopy*, 40, 330-336.
- RAO, B. S. M., GANTNER, E., REINHARDT, J., STEINERT, D. & ACHE, H. J. 1990. Characterization of the solids formed from simulated nuclear fuel reprocessing solutions *Journal of Nuclear Materials*, 170, 39-49.

- RHODES & HODGE.JR 1929. Viscosity Relationships in the System Sulfuric Acid-Nitric Acid-Water. *Industrial and Engineering Chemistry* 21, 142-150.
- RICHARDSON & ZAKI 1954a. The sedimentation of a suspension of uniform spheres under conditions of viscous flow. *Chemical Engineering Science*, 3, 65-73.
- RICHARDSON, J. F. & ZAKI, W. N. 1954b. Sedimentation and fluidisation. *Transactions of the Institution of Chemical Engineers*, 32, 35-53.
- RICHARDSON, J. F. & ZAKI, W. N. 1954c. Sedimentation and fluidisation: Part 1. *Transactions of the Institution of Chemical Engineers*, 32, 83-100.
- ROTH, G. & WEISENBURGER, S. 2000. Vitrification of high-level liquid waste: glass chemistry, process chemistry and process technology. *Nuclear Engineering and Design*, 202, 197-207.
- RUSHTON, A., WARD.A & HOLDICH.R 1996. *Solid-liquid filtration and separation technology*, Cambridge, Weinheim.
- SAMOTUS, A., KANAS, A., DUDEK, M., GRYBOS, R. & HORDOROWICZ, E. 1991. 1:1 Molybdenum(VI) citric acid complexes. *Transition Metal Chemistry*, 16, 465-499.
- SCHEETZ, B. E., AGRAWAL, D. K., BREVAL, E. & ROY, R. 1994. Sodium zirconium phosphate (NZP) as a host structure for nuclear waste immobilization: A review. *Waste Management*, 14, 489-505.
- SECRETARY OF STATE FOR TRADE AND INDUSTRY 2006. The Energy Challenge.
- SEGWA, K., NAKATA, S. & ASAOKA, S. 1987. Structure and surface chemistry of crystalline zirconium phosphate catalysts. *Materias Chemistry and Physics*, 17, 181-200.
- SHAW, D. J. 1991. *Colloids and Surface Chemistry*, Butterworth Heinemann.
- SILVER-COLLOIDS.COM. 2012. *The Influence of pH on Zeta Potential* [Online]. Available: <http://www.silver-colloids.com/Tutorials/Intro/pcs18A.html> [Accessed November 2018].
- SKINNER, S. J., STUDER, L. J., DIXON, D. R., HILLIS, P., REES, C. A., WALL, R. C., CAVALIDA, R. G., USHER, S. P., STICKLAND, A. D. & SCALES, P. J. 2015. Quantification of wastewater sludge dewatering. *Water Res*, 82, 2-13.
- SMILES, D. E. 1999. Centrifugal filtration of particulate systems. *Chemical Engineering Science*, 54, 215-224.
- SRIDHARAN & RAO 1973. Mechanisms controlling volume change of saturated clays. *Geotechnical*, 23, 359-382.
- SRILATHA, K., SREE, R., PRABHAVATHI DEVI, B. L., SAI PRASAD, P. S., PRASAD, R. B. & LINGAIAH, N. 2012. Preparation of biodiesel from rice bran fatty acids catalyzed by heterogeneous cesium-exchanged 12-tungstophosphoric acids. *Bioresour Technol*, 116, 53-7.
- STEINOUR, H. H. 1944. Rate of sedimentation. Nonflocculated Suspensions of Uniform Spheres. *Industrial & Engineering Chemistry*, 36, 618-624.
- STOKES, G. G. 1851. On the effect of the internal friction of fluids on the motion of pendulums. *Transactions of the Cambridge Philosophical Society*, 9, 1-86.
- STRICKER, A. E., TAKACS, I. & MARQUOT, A. 2007. Hindered and compression settling: parameter measurement and modelling. *Water Sci Technol*, 56, 101-10.

- STYPKA, A. 1998. Factors Influencing Sludge Settling Parameters and Solid Flux in the Activated Sludge Process. In: P3AZA.E, LEVLIN.B & HULTMAN.B (eds.) *Advanced Wastewater Treatment*. Stockholm: KTH Royal Institute of Technology.
- TABARES, J. O., I. MADRID ORTEGA, J.L. REYES BAHENA, A.A. SANCHEZ LOPEZ, D. VALDEZ PEREZ & VALDIVIESO, A. L. 2006. Surface properties and floatability of molybdenite. *China-Mexico Workshop on Minerals Particle Technology*. San Luis Potosi, Mexico.
- TEOH, S.-H., TAN, R. B. H. & TIEN, C. 2006. A new procedure for determining specific filter cake resistance from filtration data. *Chemical Engineering Science*, 61, 4957-4965.
- TIEN, C. & BAI, R. 2003. An assessment of the conventional cake filtration theory. *Chemical Engineering Science*, 58, 1323-1336.
- TINDLEY, A. 2007. *The Effect Of Electrolytes On The Properties of Titanium Dioxide Dispersions (thesis)*. PhD, The University of Leeds.
- TODD, BATCHELLER, T. A., LAW, J. D. & HERBST, R. S. 2004. Cesium and Strontium Separation Technologies Literature Review. Idaho: Idaho National Engineering and Environmental Laboratory
- TOMAS, J. & REICHMANN, B. 2002. Compression, Permeation and Flow Behaviour of Wet Nanoparticle Cakes, in situ Tested with a Press-Shear Cell. *Chemical Engineering & Technology*, 25.
- TOMKINS, M. R., BALDOCK, T. E. & NIELSEN, P. 2005. Hindered settling of sand grains. *Sedimentology*, 52, 1425-1432.
- TURIAN, MA, HSU & SUNG 1997. Characterization, settling, and rheology of concentrated fine particulate mineral slurries. *Powder Technology*, 93, 219-233.
- TURNNEY, M. A., CHEUNG, M. K., POWELL, R. L. & MCCARTHY, M. J. 1995. Hindered Settling of Rod-Like Particles measured with magnetic resonance imaging. *AIChE Journal*, 41, 251-257.
- UK GOVERNMENT 2008. Climate Change Act 2008.
- USAMI, T., TSUKADA, T., INOUE, T., MORIYA, N., HAMADA, T., SERRANO PURROY, D., MALMBECK, R. & GLATZ, J. P. 2010. Formation of zirconium molybdate sludge from an irradiated fuel and its dissolution into mixture of nitric acid and hydrogen peroxide. *Journal of Nuclear Materials*, 402, 130-135.
- USHER, S., STRUDER.L, WALL.R.C & SCALES, P. J. 2013. Characterisation of dewaterability from equilibrium and transient centrifugation test data. *Chemical Engineering Science*, 93, 277-291.
- VALLEROY, V. & MALONEY, J. 1960. Comparison of the Specific Resistances of Cakes Formed in Filters and Centrifuges. *ALChE Journal*, 6, 382-390.
- VAN OLPHEN 1977. *An introduction to clay colloid chemistry*, New York, J Wiley.
- VARGA, T., WILKINSON, A. P., LIND, C., BASSETT, W. A. & ZHA, C.-S. 2005. Pressure-induced amorphization of cubic ZrMo₂O₈ studied in situ by X-ray absorption spectroscopy and diffraction. *Solid State Communications*, 135, 739-744.
- VERESHCHAGINA, T. A., FOMENKO, E. V., VASILIEVA, N. G., SOLOVYOV, L. A., VERESHCHAGIN, S. N., BAZAROVA, Z. G. & ANSHITS, A. G. 2011. A novel layered zirconium molybdate as a precursor to a ceramic

- zirconomolybdate host for lanthanide bearing radioactive waste. *Journal of Materials Chemistry*, 21, 12001-12007.
- VERWEY, E. J. W. & OVERBEEK, J. T. G. 1948. Theory of the Stability of Lyophobic Colloids. *Elsevier*.
- VESARATCHANON, J. S., NIKOLOV, A. & WASAN, D. T. 2008. Sedimentation of concentrated monodisperse colloidal suspensions: role of collective particle interaction forces. *J Colloid Interface Sci*, 322, 180-9.
- VESILIND, A. 1968. Design of prototype thickeners from batch settling tests. *Water Sewage Works*, 115, 302-307.
- VYAS, MAWSON A, BENNETT R & MARSHALL A 2000. A new method for estimating cake height and porosity during crossflow filtration of particulate suspensions. *Journal of Membrane Science*, 176, 113-119.
- WAITE, T. D., SCHAFER, A., FANE, A. & HEUER 1999. Colloidal Fouling of Ultrafiltration Membranes: Impact of Aggregate Structure and Size. *Journal of Colloid and Interface Science*, 212, 264-274.
- WAKEMAN, R. 2007. The influence of particle properties on filtration. *Separation and Purification Technology*, 58, 234-241.
- WANG, B. H., SHI, E. W. & ZHONG, Z. 1998. Twinning Morphologies and Mechanisms of ZnO Crystallites under Hydrothermal Conditions. *Crystal Research and Technology* 33, 937-941.
- WIESNER, CLARK, J. & MALLEVIALLE J 1989. Membrane filtration of coagulated suspensions. *Journal of Environmental Engineering*, 115, 20-40.
- WINKLER, BASSIN.J.P, KLEEREBZEM.R, VAN DER LANS.R.G.J.M & VAN LOOSDRECHT.M.C.M 2012. Temperature and salt effects on settling velocity in granular sludge technology. *Water Research* 46, 5445-5451.
- WORLD NUCLEAR ASSOCIATION. 2017. *The Nuclear Fuel Cycle* [Online]. Available: <http://www.world-nuclear.org/info/Nuclear-Fuel-Cycle/Introduction/Nuclear-Fuel-Cycle-Overview/> [Accessed November 2018].
- WORLD NUCLEAR ASSOCIATION. 2018a. *Nuclear Power in the United Kingdom* [Online]. Available: <http://www.world-nuclear.org/info/Country-Profiles/Countries-T-Z/United-Kingdom/> [Accessed November 2018].
- WORLD NUCLEAR ASSOCIATION. 2018b. *Processing of Used Nuclear Fuel* [Online]. Available: <http://www.world-nuclear.org/info/Nuclear-Fuel-Cycle/Fuel-Recycling/Processing-of-Used-Nuclear-Fuel/> [Accessed November 2018].
- XUEGANG, L., JIN, C., YANCHAO, Z. & JIANCHEN, W. 2012. Precipitation of Zirconium and Molybdenum in Simulated High-level Liquid Waste Concentration and Denitration Process. *Procedia Chemistry*, 7, 575-580.
- YANG, W.-Y. 2003. *Handbook of Fluidization and Fluid-Particle systems*, CRC Press.
- ZHANG, L., TAKEUCHI.M, KOIZUMI.T & HIRASAWA.I 2013. Evaluation of precipitation behavior of zirconium molybdate hydrate. *Frontiers of Chemical Science and Engineering*, 7, 65-71.
- ZHIRNOV, P. & MOISEENKO, L. V. 1996. Solubility of barium nitrate in highly active raffinate under evaporation conditions. *Atomic Energy*, 81, 751-753.

- ZHOU, Z.-H., WAN H-L & TSAI K-R 1997. Molybdenum(VI) complex with citric acid: synthesis and structural characterization of 1:1 ratio citrato molybdate $K_2Na_4[(MoO_2)_2O(cit)_2].5H_2O$. *Polyhedron*, 16, 75-79.
- ZHU, W., YANG, X.-Y., LI, Y.-H., LI, J.-P., WU, D., GAO, Y. & YI, F.-Y. 2014. A novel porous molybdophosphate-based FeII,III-MOF showing selective dye degradation as a recyclable photocatalyst. *Inorganic Chemistry Communications*, 49, 159-162.

Research Bibliography

Scientific Journal and Conference Paper Contributions

- Shiels J, Harbottle D, Hunter T.N. 2018. Permeability and Compressive Yield Stress Measurements of Spheroidal and Cuboidal Nuclear Waste Simulants. Article in preparation. 2019
- Shiels J, Harbottle D, Hunter T.N. 2018. Synthesis and Physical Property Characterisation of Spheroidal and Cuboidal Nuclear Waste Simulant Dispersions. *Journal of Material Science*,
- Shiels J, Harbottle D, Hunter T.N. 2018. Synthesis and Characterisation of Caesium Phosphomolybdate and Zirconium Molybdate found in the Highly Active Storage Tanks at Sellafield. *Waste Management Conference*, Phoenix, US, 2018.
- Paul N, Biggs S, Shiels J, Hammond R.B, Edmondson M, Maxwell L, Harbottle D, Hunter T.N. 2017. Influence of shape and surface charge on the sedimentation of spheroidal, cubic and rectangular cuboid particles. *Power Technology*, 322, 75-83.

Oral and Poster Presentations Associated with this Thesis

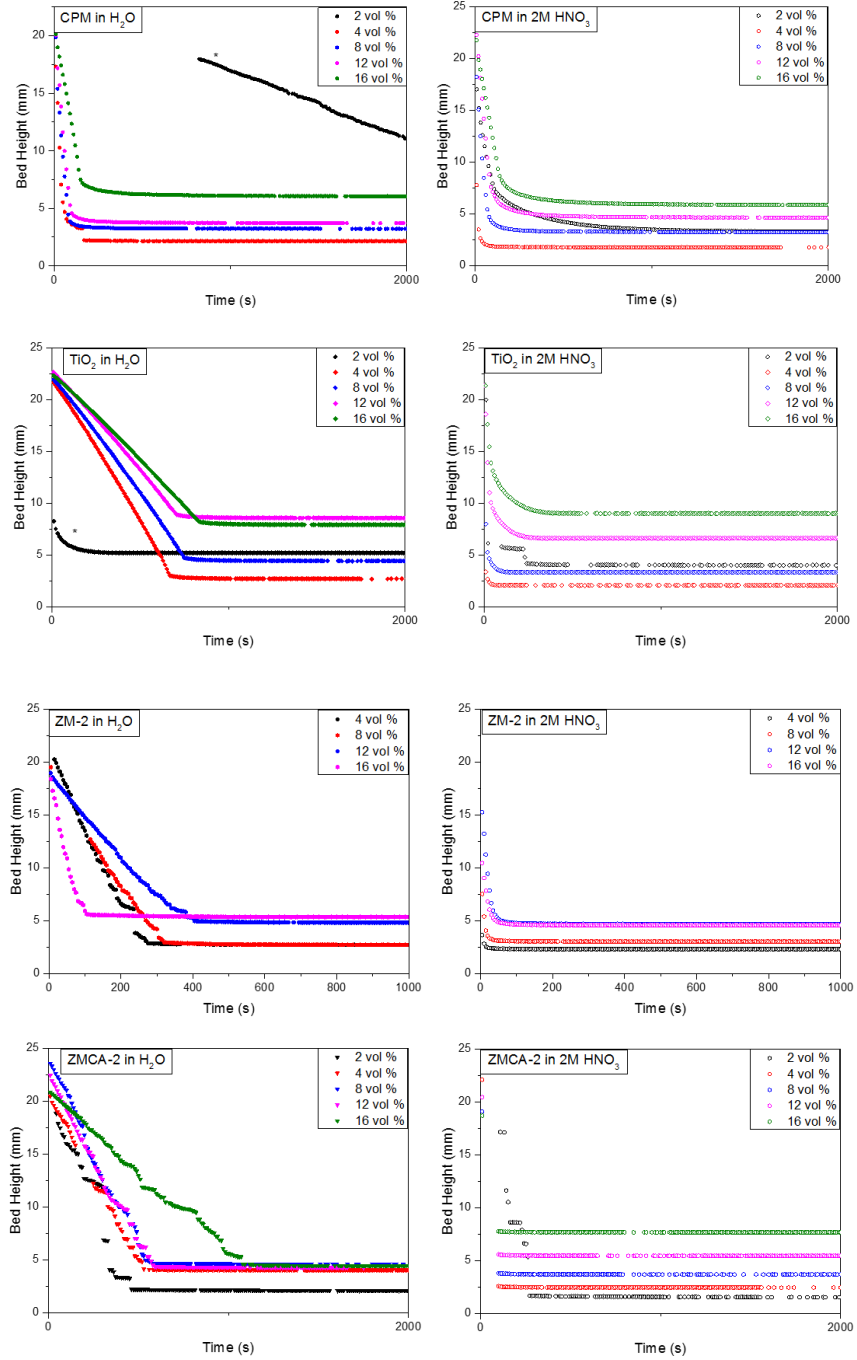
- '*Synthesis and Characterisation of Colloidal Dispersions of Nuclear Waste Simulants with Various Morphologies.*' 16th Conference of the International Association of Colloid and Interface Scientists, Rotterdam, The Netherlands, May 2018, Oral presentation
- '*Synthesis and Characterisation of Caesium Phosphomolybdate and Zirconium Molybdate found in the Highly Active Storage Tanks at Sellafield.*' Waste Management Symposia, Phoenix, US, March 2018, Oral presentation
- '*Cake Permeability of Waste Simulants found in the Highly Active Storage Tanks at Sellafield.*' Waste Management Symposia, Phoenix, US, March 2018, Poster
- '*Particle Sedimentation, Yield Stress Measurements and Permeability Studies of the Nuclear Waste Simulants; Caesium Phosphomolybdate and Zirconium Molybdate.*' International Conference and Workshop Dispersion Analysis & Materials Testing, Berlin, Germany, January 2018, Oral presentation
- '*Synthesis and Characterisation of Highly Active Nuclear Waste Simulants.*' Research Frontiers in Decommissioning and Radioactive Waste Management Conference, Leeds, UK, December 2017, Poster

- '*Synthesis and Characterisation of Highly Active Nuclear Waste Simulants.*' Leeds Association of Women Graduates, Leeds, UK, September 2017, Oral presentation

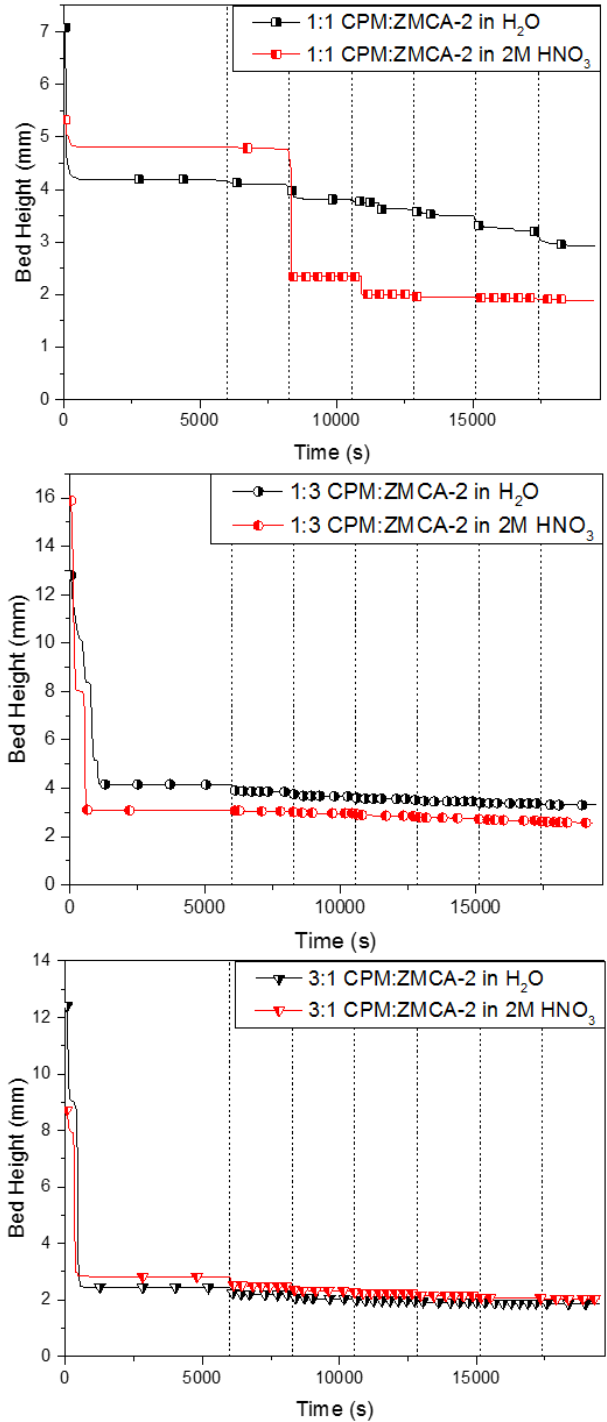
Scholarships and Grants Associated with this Thesis

- The Armourers & Brasiers Gauntlet Trust awarded a £700 travel grant in May 2018 allowing this work to be presented at the 16th Conference of the International Association of Colloid and Interface Scientists in Rotterdam.

Appendix



Appendix Fig. 1 Bed height versus time plots at various concentrations for caesium phosphomolybdate (CPM), titanium dioxide (TiO₂), zirconium molybdate (ZM-2) and zirconium citramolybdate (ZMCA-2) in both Milli-Q water and 2M nitric acid.



Appendix Fig. 2 Compressive yield stress - bed height vs. time plots for mixed systems of caesium phosphomolybdate (CPM) and zirconium molybdate (ZMCA-2) at 1:3, 1:1 and 3:1 weight ratios at 16 vol% in both Milli-Q water and 2M nitric acid.

$$\sigma = \sqrt{\frac{1}{N} \sum_{i=1}^N (x_i - \mu)^2}$$

Appendix Fig. 3 Equation showing standard deviation σ , where N is the total number of values, x represents each individual value and μ is the mean value